THÈSE

Pour l'obtention du grade de

DOCTEUR DE L'UNIVERSITE DE POITIERS

Faculté des Sciences Fondamentales et Appliquées

Diplôme National - Arrêté du 7 Août 2006

ÉCOLE DOCTORALE SCIENCES POUR L'INGENIEUR & AERONAUTIQUE

DOMAINE DE RECHERCHE : MILIEUX DENSES, MATERIAUX ET COMPOSANTS

Présentée par

Vivek Vishwanath Antad

Contrôle de la croissance et de la réactivité de nanoparticules métalliques par spectroscopie optique *in situ*

Directeur de thèse: **D. Babonneau**

Co-direction: **L. Simonot**

Soutenue le 3 novembre 2011

Devant la Commission d'Examen

JURY

Y. Borensztein	Directeur de Recherche au CNRS, INSP, Paris	Rapporteur
M.-C. Saint-Lager	Directeur de Recherche au CNRS, INEEL, Grenoble	Rapporteur
N. Destouches	Professeur d'Université, LHC, Saint-Etienne	Examinateur
G. Abadias	Professeur d'Université, Institut Pprime, Poitiers	Examinateur
D. Babonneau	Chargé de Recherche au CNRS, Institut Pprime, Poitiers	Examinateur
L. Simonot	Maître de Conférence, Institut Pprime, Poitiers	Examinateur

Acknowledgments

The work penned in this Ph.D. manuscript is a yield of three-year research that I have carried out in the research group “Nanoparticules et Nanostructures” from “Département de Physique et Mécaniques des Matériaux” of “Institut Pprime” within the “Université de Poitiers”.

As is always the case, completion of such a profound research work contains numerous direct and/or indirect contributions from the different personalities. Hence, herewith, I would like to take an opportunity to acknowledge these individuals whose ever lasting impression will remain on me and the work that I have been carried out during this Ph.D.

Firstly, I am thankful to Prof. Y. Borensztein, Prof. M.-C. Saint-Lager, and Prof. N. Destouches for accepting the invitation to be in the Panel of Jury for my Ph.D. defense. It was a great honor for me to discuss my Ph.D. work with these distinguished personalities. Their kind nature, command over the different aspects of the subject, and ability to convey the ideas in least complicated manner left a massive impression on me without a doubt. I am equally thankful to Prof. G. Abadias who accepted to be the President of the Jury as well as one of the examiners for my defense. Discussion with him were always informative and his assessments were always fair and square.

Marching with the similar feelings, I owe my deepest gratitude to my thesis director Dr. D. Babonneau and co-director Dr. L. Simonot for their consistent encouragement, guidance, and support, without which this research would have been strangled in its primitive form. Their ability to solve the problems with a particular organized plan and to work as a team are really remarkable. I consistently felt that such virtues are important for a research student who is novice to a particular research domain. Every discussion with them opened interesting insights

about the topic and developed a flexibility in the approach towards the difficulties. In this regard, I am also grateful to Dr. S. Camelio for her valuable advice in the domain of optics, optical instrumentation and optical modelling. It is her ability in explaining a concept with easiest possible ways makes her an effective teacher.

Completion of this thesis would not have been achieved without the assistance given by engineers Dr. F. Pailloux and Dr. P. Guérin. I truly appreciate the help of Dr. Pailloux for carrying out the microscopy measurements and Dr. Guérin for the experiments on the magnetron deposition machine. Their expert opinions and the friendly discussions were always useful in understanding the respective instrument and the related basic concepts. Other than these, I would like thank everyone from administration and technical staff of this laboratory for their swift assistance.

I am indebted immeasurable to many of my friends who were consistently present for filling the void created by the absence of my family due to the geographical differences. Especially, I am heartily thankful to Guillaume and Mathieu for their innumerable help not only with the scientific problems, but also with the personal ones. Both of these amazing friends consistently helped me to come over the language barrier, provided me a social atmosphere, and collected me whenever I felt down. I am also grateful to my friends Eloi and Guo-Ping (with whom I shared the office), for making the research life further interesting. Their absence in the office, even for one day, I really felt which made me appreciate their presence for each day. Moreover, I greatly appreciate the expert solutions provided by Dr. D. Lantiat during the thesis writing. He was the one person I ran to whenever I found myself surrounded by the peculiar problems from LaTeXsoftware.

Furthermore, I was also blessed with some wonderful individuals during this Ph.D. like Cyril, Bertrand, Jean-Batiste, Azzam, William, Clément, Wenbo, Eliot, Julien, Arnaud, Antoine[2], Soundés, Malaz, Alexia, Zhen-yin, Jyoung-ahn, Loukas, Wen-juan, Siranuysh and many more .... It is baffling to have so many friends in the life from different origins, countries, cultures, and thus, making the life rich with numerous social experiences. Moreover, I am also delighted to know many Indian and Pakistani friends that I found here in France who made an ever lasting impression on me with their talents and personalities. Over-all, this thesis was a mind-broadening experience in every possible aspect.

Finally, with all due respect, I heartily treasure the accompaniment provided by my parents and relatives even from thousands of kilometers away. It was their zeal and zest that served me the necessary fire which was sufficient to undertake the tasks for which I might not be capable of in the beginning. My heartiest gratitude also belongs to my wife Priyanka who was with me in the most difficult time a Ph.D. student can come across. Her constant motivation, love,

and respect for my work only helped me to concentrate better without any deviation which is normal under fatigue and stress. In the end, this acknowledgment will remain incomplete without mentioning my friends from India who supported every decision of mine unanimously. They were bold enough to make me aware about my mistakes, praise me for my decisions, backed me without asking a single question, and funny enough to make me laugh during some stressful moments. Off course, during all these years, the things kept running well with the grace of The God.

Vivek Vishwanath Antad. **November 2011, Poitiers, France.**

Contents

Introduction

Nanomaterials are the building blocks of today's nanoscience and nanotechnology. Due to the distinct features of the nanomaterials, their utilization in the application sectors have increased the device miniaturization beyond ones imagination. In this regard, as an example, Moore's law[1] is famous in the domain of semiconductor technologies. However, in nanoscience, as the demand for smaller device sizes is increasing faster and faster, the industries as well as the academic sectors are now facing new challenges and urgent needs to understand the properties of the materials at the nanoscale.

It is well known that, as we move from "bulk" to "nanoscale" dimensions, the material properties change surprisingly. Optical properties of the materials are not an exception to this fact. Applications based on the optical properties of nanomaterials span domains such as, optical detectors, lasers, optical sensors, imaging technologies, screen displays, solar cells, photocatalysis, biomedicine, etc. Especially, in case of noble metal nanoclusters, the optical response is dominated by the phenomenon of surface-plasmon resonance (SPR), classically described as the collective oscillation of the conduction electrons subjected to an electromagnetic excitation, which induces both, a wavelength-selective photon absorption in the visible range and a strong enhancement of the local electromagnetic field around the nanoclusters. As the optical response of the metal nanoclusters strongly depends upon their type, nanostructure (morphology and organization), and surrounding atmosphere, the understanding and control of these parameters are important. In addition, as these metal nanoclusters show remarkable sensitivity for the surrounding atmosphere comparing to their bulk counterparts, they are the current favorites for the nano-sensing applications. Besides, upon covering these metal

[1]Moore's law predicts that the number of transistors per unit area on the integrated circuits will be doubled in every 18 months.

nanoclusters in a protective dielectric matrix, a metal:dielectric nanocomposite structure is formed which has valuable applications in fields of opto-electronics, photonics, plasmonics, and photovoltaics.

In this context, the group called "Nanoparticules et Nanostructures" from "Département de Physique et Mécaniques des Matériaux" of "Institut Pprime" has dedicated its work to understand and control the growth and the optical properties of metal nanoclusters (Ag, Au, and Cu) covered by various dielectric matrices (BN, Si_3N_4, Al_2O_3, Y_2O_3). Extensive studies have been made by this group in the past, which focused on the influence of the nanostructure of the metal nanoclusters on their optical properties[2,3,4], and on the influence of dielectric capping layers in modifying the morphology of the metal clusters, thus altering their optical response accordingly[5,6,7]. In addition to this, significant works have also been done on the understanding of the optical response of self-organized metal nanoclusters, either in dielectric matrices, forming metal:dielectic multi-layer nanostructure systems[8] or on faceted/rippled dielectric surfaces giving rise to well-aligned nanocluster chains [9,10]. For the synthesis purposes, ion-beam sputtering technique was implemented in all above research works, while the optical characterizations of the nanocomposite thin films were carried out by *ex situ* spectroscopic measurements in transmission or in reflection mode. In order to correlate the nanostructure of the metal clusters with their optical properties, *post mortem* structural characterization techniques were used like, high-angle annular dark-field scanning transmission electron microscopy (HAADF-STEM) and grazing-incidence small-angle X-ray scattering (GISAXS).

Compared to previous studies, the work reported in this thesis explores two new approaches to study the properties of nanocomposite thin films. First, the nanocomposite thin films are grown by magnetron sputtering deposition. Second, a home-made *in situ* and real-time surface differential reflectance spectroscopy (SDRS) set-up is mounted on the magnetron sputtering chamber for their optical characterizations.

In the literature, dedicated use of SDRS can be seen for studying the optical properties of metal nanoclusters, but mainly during their growth by thermal evaporation[11]. Such real-

[2] S. Camelio *et al.* Applied Physics B: Lasers and Optics **80**, 89-96 (2005).
[3] S. Camelio *et al.* Journal of Non-Crystalline Solids **352**, 2501-2505 (2006).
[4] J. Toudert *et al.* Journal of Physics D: Applied Physics **40**, 4614-4620 (2007).
[5] J. Toudert *et al.* Journal of Applied Physics **98**, 1-10 (2005).
[6] D. Lantiat *et al.* Journal of Applied Physics **102**, 113518 (2007).
[7] D. Babonneau *et al.* EPJ Applied Physics **44**, 3-9 (2008).
[8] D. Lantiat *et al.* Review Advance Materials Science **15**, 150-157 (2007).
[9] D. Babonneau *et al.* Physical Review B **80**, 155434 (2009).
[10] D. Babonneau *et al.* EPL **93**, 26005 (2011).
[11] R. Lazzari *et al.* Surf. Sci. **482-485**, 823-828, (2001).

time optical diagnostics are extremely important because they not only offer valuable insights during the initial phases of a thin film growth, but also make possible the capture of the "missing-links" during the entire deposition processes that may not be always capable with *post mortem* techniques. Especially, such conditions may arise during the alternate depositions of two materials, or during different physical and chemical treatments of the deposited materials.

This thesis explores such cases sequentially where the optical properties of metal nanoclusters are investigated with *in situ* SDRS in real-time during their deposition on different surfaces, during several physical and/or chemical treatments, and during their capping by a dielectric matrix (Si_3N_4) which not only protects them from the contaminations and aging processes, but also improves their optical properties and "freezes" the modifications in the nanostructure. In order to study the morphology and organization of the nanoclusters, *post mortem* HAADF-STEM and GISAXS are implemented throughout this thesis. The details of the analysis are given in the respective chapters, which are organized in the following order,

- In **Chapter I**, as the properties of the deposited materials sensitively depends on their fabrication process, the advantages of magnetron sputtering deposition used during this work are comparatively discussed with other physical vapor deposition techniques. In this regard, the basic characteristic specifications and the multi-functional operations of our magnetron sputtering machine are presented. Further, different growth modes through which a metal evolves on a dielectric substrate are described in short considering thermodynamic and kinetic aspects.

- *In situ* and real-time SDRS used for the optical study of the nanocomposites during their depositions is first comparatively discussed with other sensitive optical characterization techniques in **Chapter II**. Then, in order to understand the influence of different parameters on the optical properties of the nanocomposites, the Yamaguchi effective medium model[12] is presented briefly. Moreover, the important limitations of optical models in order to obtain the quantitative information are also discussed.

The results achieved during this research work are collected in Chapters III, IV, and V.

- In **Chapter III**, the use of *in situ* and real-time SDRS in studying the optical properties of a dielectric material (Si_3N_4), metals (Ag, Au, and Cu), and their nanocomposites is presented. After studying Si_3N_4 and noble metal depositions individually, real-time variations in the optical properties of Si_3N_4:metal:Si_3N_4 nanocomposites, grown by alternate depositions, are studied. Here, the insightful information given by the SDRS

[12] T. Yamaguchi *et al.* Thin Solid Films **21**, 173-187 (1974).

are discussed thoroughly, as each deposition step modifies the optical properties of the metal nanoclusters accordingly. Furthermore in this chapter, the influence of the metal amount on the structural and optical properties of Si_3N_4:metal:Si_3N_4 nanocomposites is also investigated.

- As Ag nanoclusters show strong reactive properties under gas exposure, **Chapter IV** mainly depicts their reactive interactions with different gases (O_2, N_2, and Ar), which can be introduced in the magnetron chamber either in non-ionized or partially ionized form. As these reactive interactions change the optical properties of Ag nanoclusters, an extensive work is carried out to understand the effects of metal amount, gas flux and type, substrate type, and deposition temperature, on the optical properties of the Ag clusters in real-time. These "gas-reacted" Ag nanoclusters are then subsequently covered by a Si_3N_4 capping matrix and the modifications in the optical properties are registered and discussed along with their structural modifications.

- Finally, the influence of annealing treatments on Ag nanoclusters is presented in **Chapter V**. Here Ag nanoclusters, after their growth on a substrate, are subjected to controlled annealing treatments (either by thermal annealing or by creating a low energy bias plasma around them), and then subsequently capped by a Si_3N_4 capping matrix. As the annealing treatment produces significant modifications in the nanostructure of the Ag clusters, it accordingly alters their optical properties, which can be sensitively captured with the help of *in situ* SDRS.

The important results obtained during this research work are specifically summarized in the general conclusion part, where possible future perspectives are also presented. At the end of this thesis, an appendix part holds extended details of the theoretical concepts related with the reflectance calculations and the Yamaguchi model. In addition to this, the details of image analysis procedures, with which the extraction of the nanostructure information from HAADF-STEM micrographs and GISAXS patterns is possible, are also enclosed.

Chapter I

Nanocomposite thin films: fabrication methods and growth mechanisms

1 Introduction

In the world of materials science, thin films have created path breaking technological advances. These thin films are thin layers of specific materials, which can range from mono-atomic to several micrometers in thickness and can have strikingly different properties than that of their bulk counterparts. Even though Bunsen and Grove first obtained thin films of metals in 1852, their extensive fabrication started in early 1960's when the semiconductor materials found important applications in many electronic devices. Interesting applications of thin films were soon discovered in other areas like solar cells (Si), conductive thin films (ZnO), sensitive high temperature sensors (SiC), high temperature and high mechanical strength nitride thin films (TiN), thin film capacitors (SiO, Ta_2O_5, MnO_2), high temperature superconductor thin films ($YBa_2Cu_3O_7$) etc [1–3].

More specifically, as the optical thin films can guide or modify the light characteristics precisely, it makes them ideal candidates for numerous applications, in opto-electronics, optical sensors, optical multilayer coatings, optical filters etc, e.g. metal thin films (such as, Au, Ag, Cu, Al, Cr etc) and metal-dielectric materials (also known as cermets, like GeSiTe-SiO_2, ZnS-SiO_2, Ag-Si_3N_4 etc) have found important applications in plasmonics and photonics in the form of optical data storage [4–6], optical nano antennas [7, 8], optical waveguides [9], and nanoscale nonlinear optical devices like fast response optical switches [10–12]. In such applications it can be seen that the dielectric materials not only protect the nanoscale metals from aging processes and contaminations, but also improve their respective properties and functioning [13]. Other promising application areas for optical thin films can be in chemical and biochemical sensors, which use nano-scale materials like Au, Ag, with different dielectric substrates such as, Teflon,

TiO_2, SiO_2, ZnO, polymers to influence their sensing properties [14–19]. On the other hand, research interest in nanomaterials like Au, Ag, Sb, Cu, ZnO, ZnS, dye synthesized TiO_2, which constitute basic materials for low cost and efficient solar cells over the traditional silicon-based solar cells, is on high demand [20–25].

As thin films give rise to promising applications, their fabrication techniques are important to address thoroughly. Hence, this part of the thesis is especially dedicated to nanocomposite thin film fabrication techniques. Here, different physical deposition methods are explained with more focus given particularly on the magnetron sputtering deposition technique as it is used in our case to deposit nanocermet thin films consisting of noble metals (Ag, Au, and Cu) and dielectric material (Si_3N_4). In addition to this, different mechanisms through which a thin film grows on a substrate are also discussed in this chapter. On this basis, a detail account is given for the 3D growth of metal nanoclusters on dielectric substrates grown by physical vapor deposition.

2 Thin film deposition techniques

2.1 General schematics of deposition techniques

The act of forming thin layers of any material on a desired surface is known as thin film deposition. The qualities, properties, characteristics of the thin films sensitively depend on the deposition procedure and the technique used during their fabrications. During the deposition process, the materials to be deposited in the form of thin films are called as “target materials” and the surfaces on which the condensation or the deposition of the materials takes place are called as “substrates”. Any thin film deposition process involves three basic steps,

- the production of appropriate atomic species of the target material;
- their proper transport on the substrate;
- their condensation on the substrate surface to form a solid deposit.

A general schematics for the deposition techniques is given in Fig.I.1 below,

Based on the nature of the deposition processes, the thin film deposition techniques can be divided broadly into two categories, namely, physical vapor deposition (PVD) and chemical vapor deposition (CVD).

In PVD techniques, vapors of the desired materials can be generated, either by heating them thermally or by bombarding them with high energy electrons and/or ions in appropriate

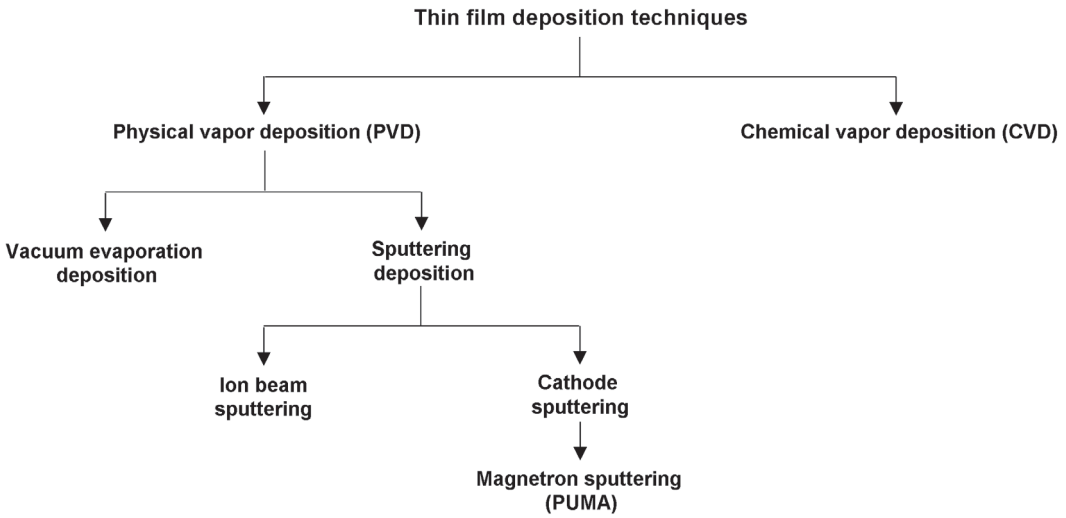

Figure I.1 – Schematics of different thin film deposition techniques.

vacuum conditions. In such deposition methods, vacuum plays an important role in deciding the properties and quality of the thin film, hence the PVD techniques are often called as vacuum deposition techniques [26].

In contrast to this, CVD is a process where a solid material is deposited on the desired surface from its vapor phase during or after chemical reactions. It generally follows the sequence,

$$\text{Gaseous reactants} \rightarrow \text{Stable solid material } (\downarrow) + \text{gaseous products } (\uparrow) \text{ [1, 3]}$$

Here, the CVD relies on the reactive carrier gases that either decompose or react with other gases to produce stable reaction products of the desired materials (↓) on the substrate surface under controlled conditions, while gaseous products are given out of the system (↑). Both PVD and CVD are characteristic deposition methods for a wide range of materials that can be used in numerous applications. Hence, these two techniques are the backbone of the thin film deposition technology. As in our case the depositions were carried out using a physical way, we will stress only on the PVD techniques in detail.

2.2 Vacuum evaporation technique

Vacuum evaporation is one of the simplest and versatile deposition technologies used in thin film fabrications. The first attempt to create thin films with this method was done by Faraday in 1857 for metals and from then on, this technique has been involved in many thin film manufacturing industries [1]. It consists in the vaporization of the materials by heating them to a particular temperature, where the vapor pressure becomes appreciable and atoms or

molecules are lost from the target surface to condense on the substrate surface (e.g. Knudsen tube). This evaporation may be from a liquid surface (i.e. above the melting point) or from a solid surface (i.e. sublimation) [26]. In this deposition method, the vapors are produced from the source material which is heated by direct resistance, radiation or arc discharge. The heating can also be carried out with the help of high energy electrons, which will bombard the surface of the target material that results in the evaporation. During the evaporation, the whole system is kept in a deposition chamber in which necessary vacuum (around 10^{-7} to 10^{-10} mbar) is created. This vacuum plays an important role during the deposition process that allows the evaporated atoms to travel as freely as possible. It is also worth noting that vacuum evaporation is a low-energy process since the deposited material condenses on the substrate surface with a very small kinetic energy around 0.1-0.5eV [1, 3, 27].

2.3 Sputter deposition techniques

Sputtering was originally developed to deposit refractory materials, which were not possible with the vacuum evaporation technique in the early days, but today this technique is a versatile thin film deposition technique for numerous materials that are used for research and industrial purposes [3]. It is a PVD process in which sufficiently energetic ions are used to bombard the surface of the target material. These ions are operated with controlled voltage and appropriate pressure is maintained in the deposition chamber. Due to this ion bombardment, the material atoms "pop out" from the material surface (also known as "sputtered" atoms), and are deposited on the substrate surface in the form of thin films [1, 3]. Sputtering is a non-thermal vaporization process where the surface atoms of the target material are physically ejected by the momentum transfer from the energetic bombarding ions. Hence this method is known as an energetic deposition technique [26, 28]. Sputter-ejected species can have kinetic energies around 5-100eV, which is much more than the thermal energy [1, 3, 27, 29].

In addition, it should be noted that, ion plating deposition also exists as a combination of both, vacuum evaporation and sputtering techniques in which the materials to be deposited are first vaporized by evaporation or sputtering and then bombarded by the atoms or ions of reactive gases. Like other techniques, it is also used for the dense coatings, hard coatings of compound materials on tools, high density optical coatings and coatings on complex surfaces etc ... [26, 30, 31].

2.3.1 Ion beam deposition technique

Ion beam sputtering is generally used for the deposition of uniform thin films and for uniform etching purposes. In this technique, the ions of inert gas (generally plasma of Ar gas, Ar^+) are

generated in a separate ion source chamber (ion gun), and the materials to be deposited on the substrate are directly bombarded by a continuous flux of these ions at low pressures of 10^{-4} mbar [2, 32]. The ions travel with very high energies (in the order of keV) towards the target materials and carry out sputtering processes. Due to the low pressures, the mean free path for the sputtered atoms is higher than in other sputtering deposition techniques explained below and hence, depending on the sputtering voltages, the energies of the sputtered atoms can be in the range of 5-200eV [1, 27, 33].

There are many advantages with this technique, such as the low pressures in the deposition chamber which reduce the irradiations and contaminations in the deposited films. Also, as the substrate is not in contact with the plasma directly, substrate heating effects are reduced efficiently. Moreover, the generation of ions in a separate chamber allows the independency over the current densities and voltages, that extends its flexibilities over a wide range of materials [1, 2].

Even though this technique was less useful for practical depositions in early days due to the small beam size (around 1 cm) and low deposition rate, recent technical adaptations like ion thruster technology, helps to create larger beam sizes (around 10-30 cm) [3].

2.3.2 Cathode sputtering deposition technique

In the cathode sputtering technique, the target materials are subjected to appropriate high voltages upon which, they act as a cathode. Due to this voltage, the gas introduced at the vicinity of the target, converts into a plasma and spreads all over the target surface [3]. These energetic plasma ions collide with the atoms of the target materials with sufficient kinetic energies and the target atoms are ejected out due to such collisions [34]. The mean free path of these sputtered atoms is smaller than other deposition techniques because this technique operates around 10^{-2} mbar and hence, they are deposited with a kinetic energy in the range 5-10eV [29].

In the cathode sputtering technique, there are numerous parameters that have to be controlled precisely for the quality of the deposited thin film. Out of which, vacuum in the deposition chamber and sputtering voltage are the most important parameters along with the "sputtering process" which are described below,

- **Vacuum -** In cathode sputtering, before starting the sputtering process, sufficient vacuum (around 10^{-7} mbar) is created in the sputtering chamber to avoid the gaseous contaminations during the sputtering processes [26]. The mean free path of the sputtered atoms inversely depends on the pressure inside the chamber. If vacuum is not sufficient

and distance between the target and substrate is too large, the mean free path will reduce drastically and the sputtered atoms will not reach at the substrate surface with sufficient energies due to collisions with the gas atoms. The appropriate pressure, the distance between the target-substrate and the substrate temperature, all together decide the quality of the deposited thin film [29, 34, 35].

- **Voltage -** The voltage at the target can be applied in the form of direct current (DC) voltage or radio frequency (RF) voltage. This voltage defines the power during the sputtering. Generally, for the conductors (metallic targets), DC voltage is applied because the free electrons are removed easily and does not accumulate on the target. Voltage (or power) influences the properties and quality of the thin film: e.g. Chan *et al* [36] have shown the effect of DC voltage along with Ar gas pressure on the electrical properties of Cu thin films. In cathode sputtering, the required DC voltage can be in the range of kV.

  On the other hand, RF sputtering is typically useful in the case of high insulating target materials, such as ceramics or oxides. The alternating tension helps the target to be neutral and accumulation of charges on the target surface is avoided [1], which maintains the sputtering rate constant. Even though RF sputtering can produce high quality homogeneous thin films [36], it has relatively slower deposition rates than DC sputtering [29].

- **The "sputtering" process -** After the appropriate pressure formation in the deposition chamber, the target material is subjected to the high voltage and acts as a cathode. Just few moments before this process, a definite flux of sputtering gas is introduced very close to the target surface. Sputtering gases are generally inert to avoid the reactions at target and substrate ends. The sputtering yield can be greater when the mass of the bombarding ions is similar or larger than that of the target atoms [1]. Hence, generally, Ar is the best choice for the sputtering gas but other gases like O_2, N_2 or their mixtures can be used for reactive depositions [37].

  Due to the high voltage, the Ar gas converts into a glow discharge plasma. Then the Ar^+ ions get attracted towards the target rapidly and collide on the target atoms [38, 39]. Due to the sufficient momentum transfer from the Ar^+ ions, the target atoms knock out from the target surface towards the substrate i.e the target is bombarded by Ar^+ ions. During the sputtering, secondary electrons get formed due to the ion bombardment and they play an important role in maintaining the plasma [29, 38]. These target atoms leave the target surface with sufficient energy and get condensed on the substrate [29, 34].

Though this traditional deposition process of cathode sputtering was successful in the beginning, there were lots of limitations. Control over the secondary electrons to maintain the plasma state of the gas during sputtering and low ionization efficiencies in the plasma were the most important, which give rise to low deposition rates. In addition to this, thin film heating effects were also a prime concern due to the uncontrolled plasma formation that may result into modifications in the thin film properties [38]. These problems are reduced efficiently by the introduction of the magnetron sputtering technique where the plasma is well confined by the magnetic lines of forces within the chamber and nearer to the target material.

2.3.3 Magnetron sputtering deposition technique

Even though the first study of low pressure deposition with magnetic field was done by Penning in 1935, the true potential of the magnetron sputtering deposition technique in thin film fabrication was recognized from 1960s [1] Now, it is known as a powerful and flexible technique for the PVD coatings in commercial and scientific fields, and has a wide range of applications for the materials like metals, dielectrics, alloys, oxides, nitrides, composites and so on ... [1, 3, 39]

Though this technique was found to be superior in the thin film deposition, it took a long time to turn it into today's sophisticated magnetron sputtering technique. The biggest problem was the control of the deposition process along with many parameters such as vacuum, voltage, gas flow, plasma control etc ... [39]. But today the magnetron covers the limitations of the cathode sputtering technique and is appreciated for relatively high deposition rates, and low substrate heating effects [1]. In this technique, the controlled plasma of the sputtering gas ultimately controls the whole deposition process.

In magnetron sputtering systems, magnets are used at the base of target (FigI.2). These magnets create magnetic fields parallel to the target surface. The magnetic field lines are sufficiently strong to confine the "glow discharge" plasma at the target surface. The secondary electrons, which are formed due to the electron-ion bombardment, are affected by the combination of electrostatic and magnetic forces and execute helical motion around these magnetic field lines [1, 27, 34, 39]. Such trapped electrons advance in the field lines by collisions and they can have energies in the range of 100eV and hence, their collision with the sputtering gas atoms helps maintaining the plasma at the target surface. This increases the ionization efficiency of the gas resulting in a dense plasma surrounding the target region, which in turn increases the sputtering of the target [1]. This gives a higher sputtering rate at the target and hence a higher

deposition rate at the substrate. The increased ionization efficiency also allows maintaining the discharge glow at high pressures of 10^{-2}-10^{-3} mbar [29] and at lower voltages around 300-500V, compared to the traditional ion-beam sputtering and cathode sputtering, which require high voltages in the order of kV [38, 40].

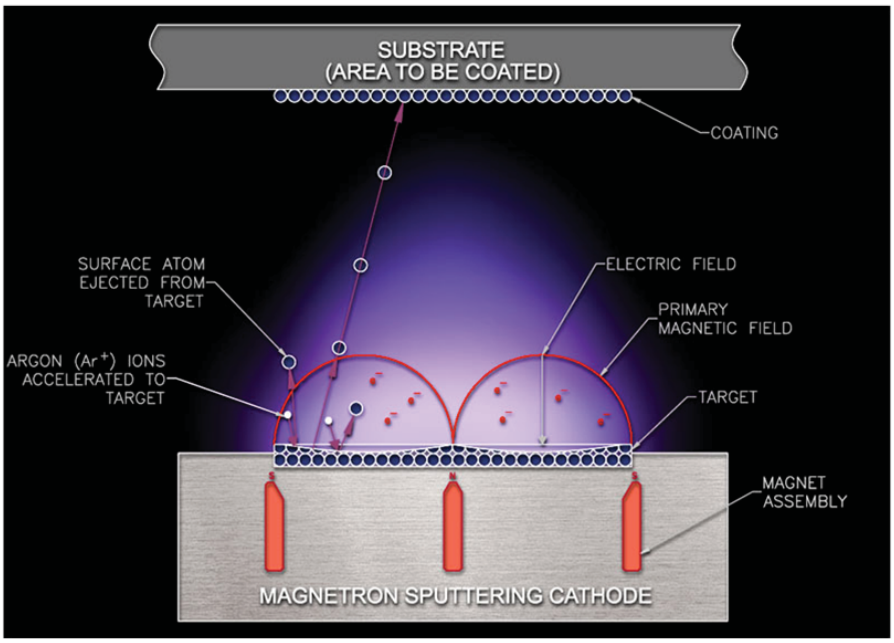

Figure I.2 – A typical magnetron sputtering system [39]. (©*Angstrom Science, 2009*)

2.3.4 PUMA

In this work we have used the magnetron sputtering deposition machine called PUMA (for "Pulvérisation Magnetron") for the depositions of metal-dielectric nanocomposites (AC450 Alliance Concept^{TM}). PUMA (Fig.I.3) is a multi-functional and automatic machine which is used in a "balanced way" with all the magnets having similar pole strength, giving rise to balanced magnetic lines of force that controls the gas plasma. It is a triple-cathode magnetron sputter deposition system. Here, the sputtering or deposition experiments are carried out in a steel vacuum chamber, controlled by a peripheral computer. PUMA has possible application areas in research and development for co-depositions, multilayer depositions, reactive depositions etc ... Sputtering depositions of different metals, nitrides, oxides, semiconductors can be carried out with controlled parameters [37, 41, 42]. The special features of PUMA are:

- **Vacuum -** Cryogenic pump is used to create the ultimate vacuum in PUMA, which can be can be reached around $2\times$ 10^{-8} mbar. But, for the deposition processes, a pressure

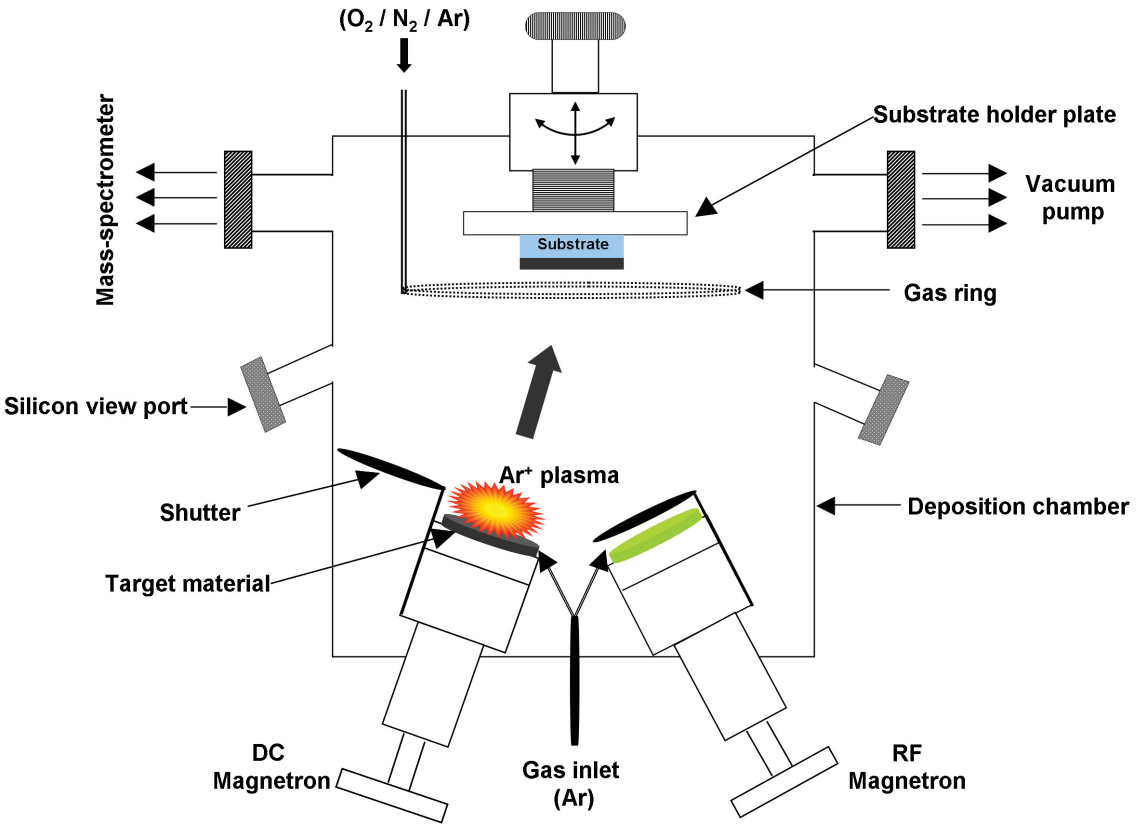

Figure I.3 – Schematics of PUMA. Only two of the three magnetrons are shown for convenience.

around 10^{-2} to 10^{-3} mbar is sufficient which is higher compared to ion beam sputtering ($\sim 10^{-6}$ mbar, respectively) [37].

- **Target Materials -** Three target magnetrons (out of which, only two are shown in Fig.I.3 for convenience,) are mounted inside the deposition chamber with a symmetrical arrangement at 120° and inclined at 25° from the substrate normal. The magnetrons used in PUMA are 3" GencoaTM Vtech target source. Each target is covered by a metal flap (shutter), which is fixed at one end and can semi-rotate in a perpendicular plane over the target. This shutter is helpful during the pre-sputtering of the target material, which prevents the material to be deposited on the substrate and other targets.

  During sputtering, this shutter can slide away from the target automatically and the material deposition on the substrate starts as soon as the appropriate voltage is applied, converting the target material into a cathode. These targets are operated at a voltage range of 300-500V. Generally, RF voltage is used for dielectric materials, while metal targets are sputtered with DC voltage. The maximum power of the supply in RF mode

is 1.2kW, while in DC mode, it is 1.5kW. In PUMA, an appropriate voltage value, a controlled plasma gas, and a correct magnetic field around the target give rise to the desired deposition rate. The currently available targets in our laboratory are Ag, Al, Au, C, Cu, Mo, Ni, Si, Ti, W, Zr, TiAl, NiTi, Y_2O_3, $SrTiO_3$, and Si_3N_4.

- **Gas introduction -** In PUMA, the gases that can be introduced other than Ar are O_2 and N_2. It is possible to introduce the dosage of the single gas flux or gas mixtures with precise control from 0.3 to 20 sccm (standard cubic centimeters per minute) on the target (through a gas inlet) or in the vacuum chamber (through a gas ring). *In situ* and real-time measurements of partial pressures are also possible for all these gases. For that purpose a Vision 1000P-MKS^{TM} quadruple mass spectrometer is used. The range of this mass-spectrometer is 1-200 amu (atomic mass unit) and the detector is made up of dual faraday/secondary electron multilayer. It monitors the process or analyzes the residual gases. More information regarding the gas introductions and the real-time measurements of the gas partial pressures is given in Chapter IV.

- **Substrates -** The substrates are kept at opposite side of the target in an horizontal plane. Generally, depending upon the study, different substrates like glass or Si can be used. These substrates are fixed on a substrate holder along with the carbon coated copper grids if Scanning Transmission Electron Microscopy (STEM) analysis is required. The substrate holder can be fixed or subjected to precise controlled rotations (which is not used in our case) and also, the distance between the substrate and target can be changed. In addition to this, the temperature of the substrate can be changed by controlled heating with the help of infra-red radiations heater and can be measured accurately using a chromel-alumel thermo-couple. An additional discussion regarding the heating arrangement in PUMA can be seen in Chapter V (Section 2)

- **Plasma -** In our case, we use a plasma of Ar gas to sputter the target materials. This Ar gas can be introduced very close to the target surface as well as in the vacuum chamber with a precise flux automatically whenever needed. Here, to confine the Ar plasma during sputtering, balanced magnets are used to create the magnetic field lines of strength not greater than 250 Gauss so that only electrons are better confined to maintain the plasma than the gas ions [27]. Also, in PUMA, it is possible to create a controlled RF plasma of gas at the substrate end (due to the biased voltage maintained at the substrate, hence also known as bias plasma). This feature of PUMA gives an interesting advantage as the plasma in such a configuration is in the vicinity of the substrate (and hence, very close to

the deposited thin film). In this regard, more information on the bias plasma formation can be seen in Chapter V (Section 3).

3 Mechanisms in thin film growth

3.1 A thermodynamic aspect

The growth of a thin film deposited on a substrate prominently depends upon the interactions between the atoms of the deposited material and of the surface of the substrate [43, 44]. The total free energy of the system can be given as,

$$E_{free} = \gamma_M - \gamma_S + \gamma_I, \tag{I.1}$$

where, γ_M is the surface energy of the deposited material on the substrate, γ_S is the surface energy of the substrate, and γ_I is the free energy of the interface between the thin film and the substrate, which is generally small compared to γ_M and γ_S [45]. Based on this thermodynamic relation, the growth of thin films can be modeled into three major mechanisms.

3.1.1 Three-dimensional (3D) or Volmer-Weber (VW) growth

In the VW type growth, 3D growth of the material can be seen on the solid surfaces. $(\gamma_M + \gamma_I)$ greater than the surface energy of the substrate γ_S, i.e.

$$E_{free} > 0. \tag{I.2}$$

Hence, the deposited material has tendency to form 3D clusters on the substrate surface and with the increase in the deposition time, the clusters grow in size (Fig.I.4). In other words, the low affinity of the deposited material towards the substrate leads to a 3D growth [45]. Such a 3D growth mode is seen in case of many metals deposited on insulators, on alkali halides and graphite [44, 45]. Moreover, Campbell [45] has given details on the surface energies for different metals deposited on oxide surfaces.

3.1.2 Two-dimensional (2D) or Frank-Van Der Merwe (FM) growth

In the FM type growth, the materials have totally opposite properties than in the VW growth, i.e.

$$E_{free} < 0. \tag{I.3}$$

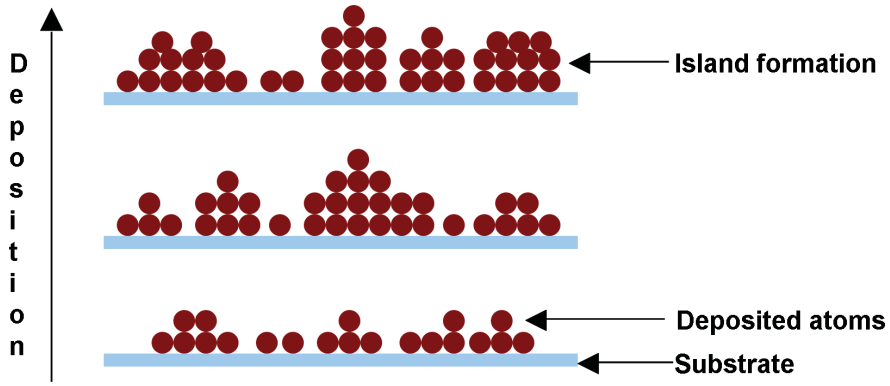

Figure I.4 – A 3D island or VW growth of the material on the substrate surface.

Hence, the atoms deposited on the surface will form a continuous layer. Then, this primary layer of atoms will be covered by the following atoms, and a layer by layer structure will be formed (Fig.I.5).

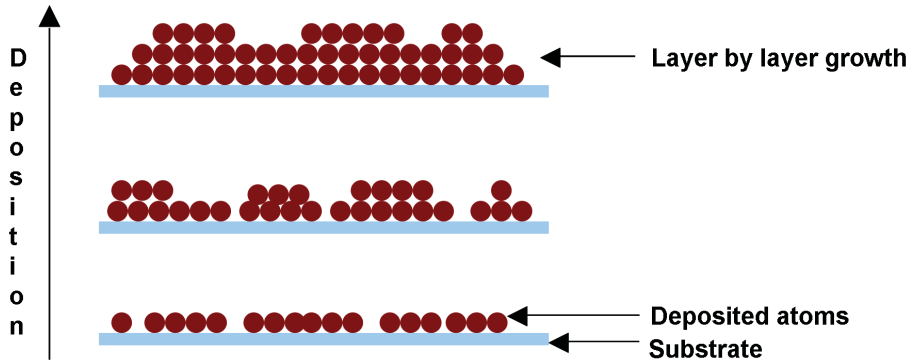

Figure I.5 – A 2D layer by layer or FM growth of the material on the substrate surface.

Such a FM growth mode is generally observed in the deposition of rare gases on graphite or on metals, also in metal-metal systems, and in the growth of semiconductor materials on semiconductor surfaces [43, 44].

3.1.3 Mixed (2D+3D) or Stranki-Krastanov (SK) growth

The SK growth mode is a mixed mechanism of FM and VW type growth. In case of ideal SK growth, a layer by layer growth of a material on a substrate is followed by the 3D growth of clusters or aggregates of the same material (Fig.I.6). Here the role played by the interface energy between the atoms and the substrate is not well known [40, 44].

However, it is worth noting that a Pseudo SK growth can also be seen, where the deposition of the material on the substrate favors a 3D growth up to a critical stage and then, the addi-

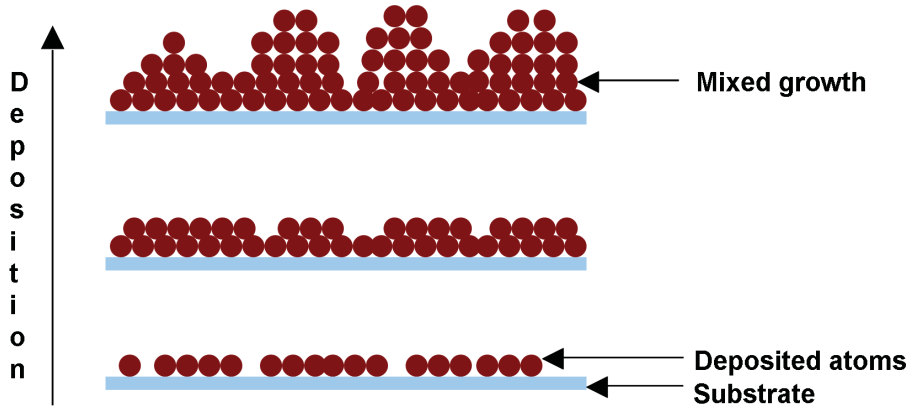

Figure I.6 – An ideal SK growth of the material on the substrate surface.

tionally deposited material grows into an almost layer by layer or FM type growth on the top of these 3D clusters. The uncovered remaining fraction of the substrate surface between these clusters is then filled rather slowly by the additionally deposited material during the deposition [43, 44, 46].

3.2 Movements of atoms on the substrate surface - A surface kinetics aspect

The surface kinetics aspects of the deposited atoms during the thin film deposition are important to understand because even if the system is thermodynamically favored, the kinetic limitations can deny the production of stable structures on the solid surfaces [43, 45].

During the deposition, the atoms of the deposited material condense on the substrate surface due to **adsorption** ***(i)*** with energy E_a. These isolated, individual adsorbed atoms on the surface are called *adatoms*, which are mobile on the substrate under the influence of the surface energies. This adsorption and mobility of the adatoms depend upon the respective materials, deposition rate and the temperature of the substrate. These *adatoms*, undergo different **diffusion processes** ***(ii)*** all over the surface until they are lost or trapped by several processes [44] such as,

- **re-evaporation** ***(iii)*** that takes place if the *adatoms* get sufficient energy to overcome the bonding between atom and substrate;

- trapping in surface defects (a) as the real surfaces can have many imperfections like, vacancies, dislocations, impurities etc, which can give a favorable site for the *adatoms*;

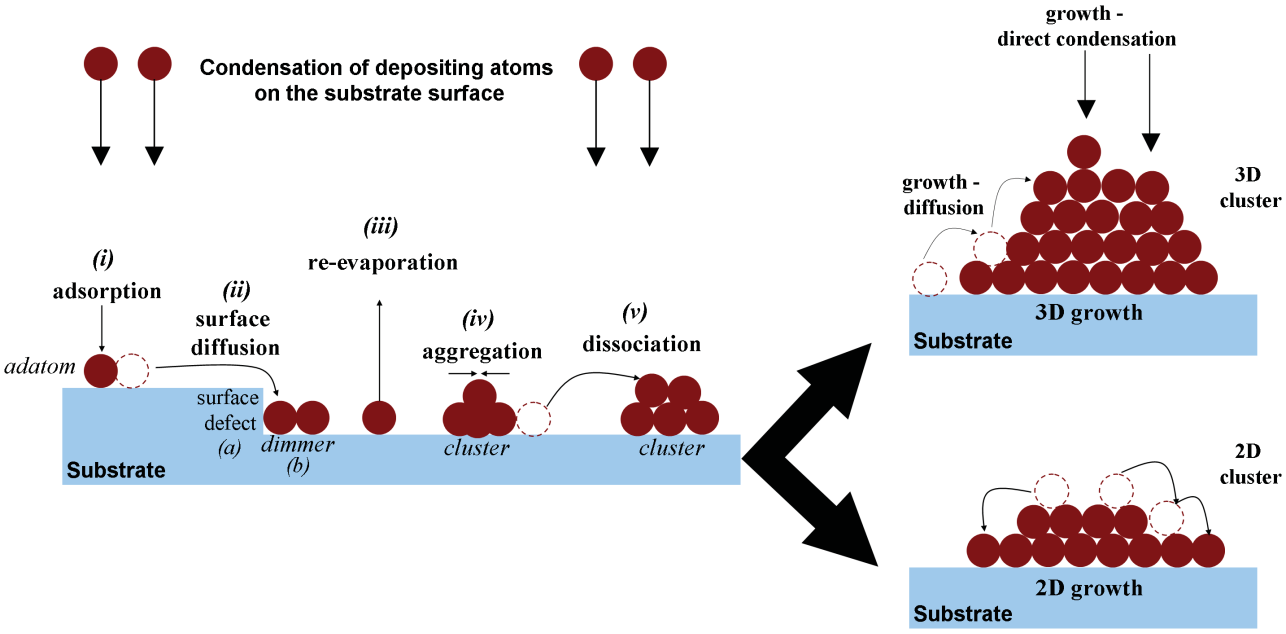

Figure I.7 – Different surface kinetics of atoms during thin film growth.

- trapping in a small group of adatoms called *cluster* (made up of few atoms) or they end up by forming a pair with an other isolated *adatom* and become a *dimmer* (b);

These diffusion processes contribute in the nucleation and growth of nanoclusters. During the diffusion, kinetics in the adatoms lead them towards the **aggregation process** ***(iv)***, where, the individual adatoms can join already existed 2D or 3D *clusters* depending upon the materials, substrates and free energy considerations [40, 46]. Although *cluster* formation is normal in this process, there will be a critical size of *clusters* above which the probability of the *cluster* growth in size will be greater than the probability of their decay. Hence, growth of a *cluster* is a **nucleation** phenomenon and the *clusters* above a critical size are referred as stable *clusters* which can grow in size during deposition process but difficult to decay [43, 44]. In contrast to the aggregation process where *clusters* tend to grow into bigger *clusters*, the process of **dissociation** ***(v)*** can be seen, where the detachment of the *atom(s)* from the *clusters* to substrate surface can take place. In this process, unstable *adatoms* from a *cluster* can dissociate and again diffuse on the substrate or vice versa.

The dissociation can be important if the deposited materials and substrate have same bonding energy, e.g. semiconductor on semiconductor, metal on metal etc... but, desorption of the majority of metal atoms on the oxide materials is negligible if the temperature of the oxide substrate is not near the evaporation temperature of the metal [46].

3.3 Different growth regimes in a metal thin film during their deposition on a dielectric surface

In our case, we are interested in the 3D growth of metals on dielectric substrates, so, it will be interesting to understand the different stages involved in such a process from the beginning of the metal deposition to the formation of a continuous film [47]. We can explain these stages and their features as above.

3.3.1 Nucleation processes to form clusters

This is the first basic step that can be seen during the deposition. Here, the metal atoms with sufficient energy arrive on the dielectric surface, which is maintained at a particular temperature. This growth stage is characterized by the increasing density of the adatoms and their nucleation into 3D clusters on the dielectric surface. This growth step may take place due to two reasons,

- **Nucleation due to the aggregation of the adatoms -** This homogeneous type of nucleation takes place entirely due to the contribution of the adatoms. Here, the nucleating adatoms combine with each other and with other 3D clusters on the substrate surface. Two adatoms may come in influence by accident or by the process of surface diffusion. This aggregation of the adatoms leads them to form stable structures on the oxide surface in the form of 3D clusters. This phase of the thin film growth is sensitive and depends upon the diffusion coefficient of the adatoms, their surface energies, temperature of the substrate, and the deposition rate [48].

- **Nucleation due to the defects on the substrate surface -** This is an heterogeneous type of nucleation, where the defects/imperfections on the surface act as pining points for the adatoms and give rise to nucleation sites on the surface.

3.3.2 Growth of the clusters

During the regime of nucleation, there is always incorporation of new arriving atoms on the surface. Due to this tendency, the metal clusters tend to grow in the size. This growth can be due to the adsorption of the newly added adatoms on the already present stable clusters (growth due to direct condensation or out-of-plane growth) or it may be due to the diffusion among the clusters (in-plane surface diffusion). This atomic mass transport is possible via 2D or 3D cluster diffusion. Such Brownian motions of clusters take place due to various atomic transports across

the substrates as explained in some works in detail [49]. In case of 2D clusters, the growth is governed by the peripheral diffusion, condensation and movement of surface defects e.g. the diffusion of 2D clusters is possible by gliding on the surface as whole cluster [49, 50]. In case of 3D clusters, the rotational and translational movements of the clusters is seen contributing in the growth. Also, diffusion coefficient and temperature take a major role during the growth of 3D clusters [51].

3.3.3 The regime of coalescence

Due to the growth of the clusters, the cluster size increases continuously with the deposition time. After sufficient growth, the clusters coming into the vicinity with each other give rise to the coalescence regime. If two clusters come in contact under favorable thermodynamic conditions then they merge to form a single bigger cluster. During this regime, an increase in the cluster size is accompanied by a decrease in the cluster surface-density [52, 53]. Also, dynamic coalescence can be seen if the high mobility of small clusters contributes to the growth of the bigger clusters [52, 54].

3.3.4 The regime of percolation

With the continuous deposition, further growth of the clusters can be seen. The clusters go on increasing and eventually reach a stage where they start to agglomerate. It is a regime where the coalescence is no more efficient in the particles due to their bigger sizes. Hence, the lateral growth rate of the clusters decreases rapidly. At this stage, the whole cluster system can be treated as one big loosely connected cluster, and the cluster surface density eventually decreases towards zero. This stage in the thin film growth is called percolation and at this point, the properties of the thin film, such as, electrical and optical properties, can alter significantly [55]. Determination of this percolation threshold in the ultra-thin films is thus important and has several applications e.g in thin silver coatings, in charge conducting films etc ... [55, 56].

3.3.5 Continuous or thick layer formation

The last regime in the thin film growth is the formation of a continuous layer. With the continuous deposition of the material, the gap or separation between the percolation areas is filled directly and progressively due to incoming atoms [55]. Generally, the properties of the materials in this regime are similar to their bulk counterparts. The schematics of the cluster density variation with the increasing metal amount in the VW type growth, is given in Fig.I.8.

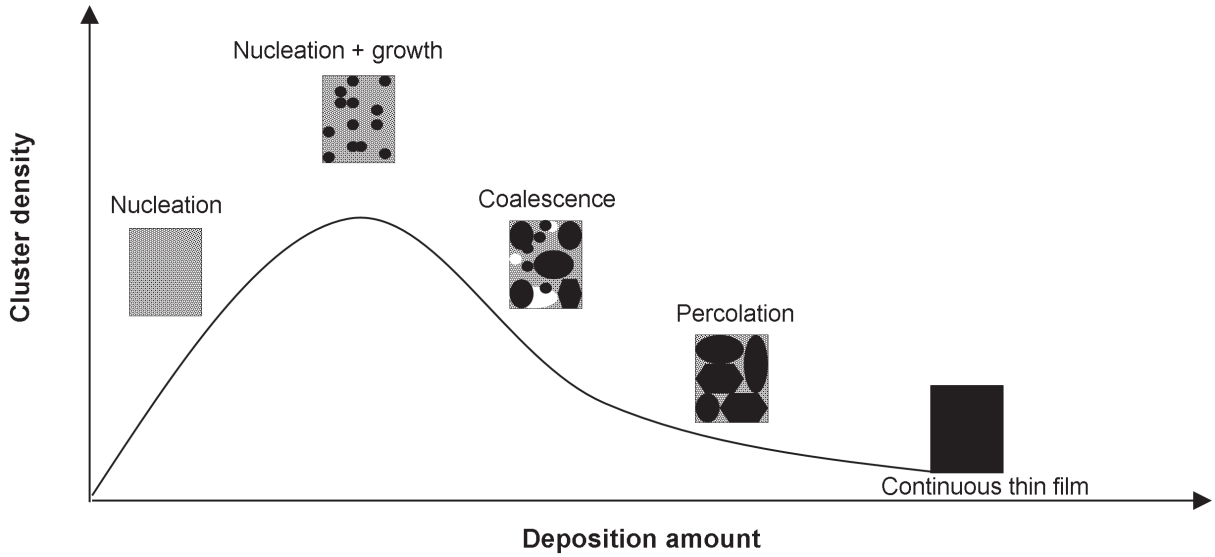

Figure I.8 – Schematics of the cluster density variation with the increasing deposition amount of the metal, showing important regimes of the cluster growth during thin film formation [1, 47].

In summary, during the early steps of deposition, nucleation and growth are prominent in which small clusters are formed rapidly and their number per unit area (areal surface density of the clusters) increases. It is then followed by the coalescence regime, which induces an increase of the cluster size and reduction in the areal cluster density. During the VW growth, this stage form bigger clusters which are distinctly separated from each other. The continuous deposition further imposes a state of percolation where the areal surface density eventually reduced to zero by forming a structure made up of loosely connected bigger clusters. Further deposition then leads to the formation of a continuous layer where the gaps from the percolation regime are eventually filled out by the direct incorporation of the incoming atoms.

4 Summary and conclusions

In this chapter, we have seen a brief overview of thin film fabrication techniques that have been developed over last few decades. Out of these techniques, sufficient stress is given on the magnetron sputtering deposition technique which is used in this research work to fabricate the metal:dielectric nanocomposite thin films. Since with magnetron system we can deposit the materials with different features, such as, automatic deposition process at low pressures, controlled current-voltage configuration, precise introduction of gas flux, real-time partial-pressure measurements, and reliable confinement of gas plasma during deposition, the magnetron deposition technique gives us flexibility over performance during the experiments.

After the fabrication techniques, we have seen different growth mechanisms and surface kinetics through which a thin film can evolve on a substrate surface. As these mechanisms play a vital role in the properties and the qualities of the deposited thin films, their knowledge deserves sufficient account for discussion. Then specifically, the important regimes for metal thin films following the 3D Volmer-Weber growth mode (starting from the nucleation of adatoms to the formation of continuous layer), are explained which give an idea about the metal adatom-cluster behavior during the on-going deposition.

Bibliography

[1] R. F. Bunshah. *Handbook of deposition technologies for films and coatings*. Noyes Publications (1994). 5, 7, 8, 9, 10, 11, 21

[2] K. Wasa and S. Hayakawa. *Handbook of Sputter Deposition Technology - Principles, Technology and Applications*. Noyes Publications (1991). 5, 9

[3] A. Elshabini-Riad and F. D. Barlow-III. *Thin Film Technology Handbook*. McGraw-Hill (1997). 5, 7, 8, 9, 11

[4] S. Park and J. W. Hahn. *Plasmonic data storage medium with metallic nano-aperture array embedded in dielectric material*. Optics Express **17**, 20203–20210 (2009). 5

[5] M. Mansuripur, A. R. Zakharian, A. Lesuffleur, S. H. Oh, R. J. Jones, N. C. Lindquist, H. Im, A. Kobyakov, and J. V. Moloney. *Plasmonic nano-structures for optical data storage*. Optics Express **17**, 14001–14014 (2009). 5

[6] K. P. Chiu, K. F. Lai, and D. P. Tsai. *Application of surface polariton coupling between nano recording marks to optical data storage*. Optics Express **16**, 13885–13892 (2008). 5

[7] B. Lee, I. M. Lee, S. Kim, D. H. Oh, and L. Hesselink. *Review on subwavelength confinement of light with plasmonics*. Journal of Modern Optics 57, 1479-1497 (2010) **57**, 1479–1497 (2010). 5

[8] L. Novotny. *Effective wavelength scaling for optical antennas*. Physical Review Letters **98**, 266802 (2007). 5

[9] J. Homola, S. S. Yee, and G. Gauglitz. *Surface plasmon resonance sensors: review*. Sensors and Actuators, B: Chemical **54**, 3–15 (1999). 5

[10] S. A. Maier, M. L. Brongersma, P. G. Kik, S. Meltzer, A. A. G. Requicha, and H. A. Atwater. *Plasmonics - a route to nanoscale optical devices*. Advanced Materials **13**, 1501–1505 (2001). 5

Bibliography

[11] M. Dragoman and D. Dragoman. *Plasmonics: Applications to nanoscale terahertz and optical devices.* Progress in Quantum Electronics **32**, 1–41 (2008). 5

[12] G. Ma, J. He, and S. H. Tang. *Femtosecond nonlinear birefringence and nonlinear dichroism in Au:Tio$_2$ composite films.* Physics Letters, Section A: General, Atomic and Solid State Physics **306**, 348–352 (2003). 5

[13] F. R. Flory. *Thin Films for Optical System.* Marcel Dekker, Inc, (1995). 5

[14] B. Brian, B. Sepulveda, Y. Alaverdyan, L. M. Lechuga, and M. Kall. *Sensitivity enhancement of nanoplasmonic sensors in low refractive index substrates.* Optics Express **17**, 2015–2023 (2009). 6

[15] B. Liedberg, C. Nylander, and I. Lundstrom. *Biosensing with surface plasmon resonance - how it all started.* Biosensors and Bioelectronics **10**, i–ix (1995). 6

[16] D. J. Sirbuly, A. Too, M. Law, R. Fan, and P. Yang. *Multifunctional nanowire evanescent wave optical sensors.* Advanced Materials **19**, 61–66 (2007). 6

[17] H. Meixner and U. Lampe. *Metal oxide sensors.* Sensors and Actuators B: Chemical **33**, 198–202 (1996). 6

[18] N. E. Stankova, I. G. Dimitrov, P. A. Atanasov, T. Sakano, Y. Yata, and M. Obara. *Nanostructured optical waveguide films of TiO_2 and WO_{3-x} for photonic gas sensors.* Thin Solid Films **518**, 4597–4602 (2010). 6

[19] O. A. Sadik, S. K. Mwilu, and A. Aluoch. *Smart electrochemical biosensors:from advanced materials to ultrasensitive devices.* Electrochimica Acta **55**, 4287–4295 (2010). 6

[20] R. Konenkamp, L. Dloczik, K. Ernst, and C. Olesch. *Nano-structures for solar cells with extremely thin absorbers.* Physica E: Low-Dimensional Systems and Nanostructures **14**, 219–223 (2002). 6

[21] W. E. Vargas and G. A. Niklasson. *Optical properties of nano-structured dye-sensitized solar cells.* Solar Energy Materials and Solar Cells **69**, 147–163 (2001). 6

[22] G. Rothenberger, P. Comte, and M. Gràtzel. *Contribution to the optical design of dye-sensitized nanocrystalline solar cells.* Solar Energy Materials and Solar Cells **58**, 321–336 (1999). 6

[23] A. B. Kashyout, M. Soliman, M. El Gamal, and M. Fathy. *Preparation and characterization of nano particles ZnO films for dye-sensitized solar cells.* Materials Chemistry and Physics **90**, 230–233 (2005). 6

[24] G. Zhao, H. Kozuka, and T. Yoko. *Sol-gel preparation and photoelectrochemical properties of TiO_2 films containing Au and Ag metal particles.* Thin Solid Films **277**, 147–154 (1996). 6

[25] K. Zakrzewska, M. Radecka, A. Kruk, and W. Osuch. *Noble metal/titanium dioxide nanocermets for photoelectrochemical applications.* Solid State Ionics **157**, 349–356 (2003). 6

[26] D. M. Mattox. *The Foundations of Vacuum Coating Technology.* Noyes Publications (2003). 7, 8, 9

[27] R. Bunshah. *Handbook of hard coatings: Deposition technologies, Properties and Applications.* Noyes publications (2001). 8, 9, 11, 14

[28] G. K. Hubler and J. A. Sprague. *Energetic particles in PVD technology: particle-surface interaction processes and energy-particle relationships in thin film deposition.* Surface and Coatings Technology **81**, 29–35 (1996). 8

[29] A. Billard and F. Perry. chapter Pulvérisation Cathodique Magnetron. 8, 9, 10, 12

[30] D. M. Mattox. *Handbook of Physical Vapor Deposition (PVD) processing.* Noyes Publications - USA (1998). 8

[31] M. L. Hitchman and K. F. Jensen. *Chemical Vapor Deposition- Principles and Application.* Academic press limited (1993). 8

[32] H. R. Kaufman. *Technology of ion beam sources used in sputtering.* Journal of Vacuum Science and Technology **15**, 272–276 (1978). 9

[33] P. Martin. *Handbook of deposition technologies for films and coatings (Third Edition).* Elsevier Inc. (2009). 9

[34] www.pvd-coating.co.uk. 9, 10, 11

[35] S. Negi, R. Bhandari, L. Rieth, and F. Solzbacher. *Effect of sputtering pressure on pulsed-DC sputtered iridium oxide films.* Sensors and Actuators B: Chemical **137**, 370–378 (2009). 10

[36] K.-Y. Chan, P.-Q. Luo, Z.-B. Zhou, T.-Y. Tou, and B.-S. Teo. *Influence of direct current plasma magnetron sputtering parameters on the material characteristics of polycrystalline copper films.* Applied Surface Science **255**, 5186–5190 (2009). 10

[37] L. Simonot, D. Babonneau, S. Camelio, D. Lantiat, P. Guérin, B. Lamongie, and V. Antad. *In-situ optical spectroscopy during deposition of Ag:Si_3N_4 nanocomposite films by magnetron sputtering.* Thin Solid Films **518**, 2637–2643 (2010). 10, 12, 13

[38] P. J. Kelly and R. D. Arnell. *Magnetron sputtering: a review of recent developments and applications.* Vacuum **56**, 159–172 (2000). 10, 11, 12

[39] www.angstromsciences.com. 10, 11, 12

[40] D. Lantiat-Baillargue. *Morphologie et auto-organisation de nanoparticles d'argent dispersées dans des matrices diélectriques: influence sue les propriétés optiques.* Thèse de Doctorat, PhyMat - Université de Poitiers, Poitiers (2008). 12, 16, 18

[41] G. Abadias and P. Guérin. *In-situ stress evolution during magnetron sputtering of transition metal nitride thin films.* Applied Physics Letters **93(11)**, 111908 (2008). 12

[42] A. Fillon, G. Abadias, A. Michel, and C. Jaouen. *Stress and microstructure evolution during growth of magnetron-sputtered low-mobility metal films: Influence of the nucleation conditions.* Thin Solid Films **519**, 1655–1661 (2010). 12

[43] J. L. Robins. *Thin film nucleation and growth kinetics.* Applied Surface Science **33/34**, 379–394 (1988). 15, 16, 17, 18

[44] J. A. Venables, G. D. T. Spiller, and M. Hanbucken. *Nucleation and growth of thin films.* Rep Prog Phys **47**, 399–459 (1984). 15, 16, 17, 18

[45] C. T. Campbell. *Ultrathin metal films and particles on oxide surfaces: structural, electronic and chemisorptive properties.* Surface science reports **27**, 1–111 (1997). 15, 17

[46] J. Carrey. *Croissance granulaire d'Or et de Cobalt sur alumine amorphe: caracterisations et Simulations de Monte-Carlo.* Thèse de Doctorat, Orsay - Université de Paris XI, Orsay (2001). 17, 18

[47] J. E. Greene. *Low-energy ion bombardment during film deposition from the vapor phase: Effects on microstructure and microchemistry.* Solid State Technology **30**, 115–122 (1987). 19, 21

[48] G. Hass, A. Menck, H. Brune, J. V. Barth, J. A. Venebles, and K. Kern. *Nucleation and growth of supported clusters at defect sites: Pd/MgO(001).* Physical Review B **61 (16)**, 11105–11108 (2000). 19

[49] S. V. Khare, N. C. Bartelt, and T. L. Einstein. *Diffusion of monolayer adatom and vacancy clusters: Langevin Analysis and Monte-Carlo Simulations of their Brownian Motion.* Physical Review Letters **75**, 2148 (1995). 20

[50] S. C. Wang and G. Ehrlich. *Diffusion of large surface clusters: direct observations on Ir(111).* Physical Review Letters **79**, 4234 (1997). 20

[51] A. Masson, J. J. Metois, and R. Kern. *Migration Brownienne de cristallites sur une surface et relation avec lépitaxie.* Surface Science **27**, 463–482 (1971). 20

[52] C. Templier, S. Muzard, A. Galdikas, L. Pranevicius, J. Delafond, and J. C. Desoyer. *A phenomenological study of the initial stages of film growth.* Surface and Coatings Technology **125**, 129–133 (2000). 20

[53] P. Jensen, H. Larralde, M. Meunier, and A. Pimpinelli. *Growth of three-dimensional structures by atomic deposition onsurfaces containing defects: Simulations and theory.* Surface Science **412/413**, 458–476 (1998). 20

[54] P. Andreazzaa, C. Andreazza-Vignollea, J. P. Rozenbaumb, A.-L. Thomannb, and P. Braultb. *Nucleation and initial growth of platinum islands by plasma sputter deposition.* Surface and Coatings Technology **151 -152**, 122–127 (2002). 20

[55] T. W. H. Oates, L. Ryves, and M. M. M. Bilek. *Dielectric functions of a growing silver film determined using dynamic in situ spectroscopic ellipsometry.* Optics Express **16**, 2302–2314 (2008). 20

[56] T. H. W. Oates and M. M. M. Bilek. *Insulator surface charging and dissipation during plasma immersion ion implantation using a thin conductive surface film.* Journal of Applied Physics **92**, 2980 (2002). 20

Bibliography

Chapter II

In situ optical techniques for real-time thin film characterizations

1 Introduction

In order to study the intrinsic optical properties of materials, optical characterization techniques can be resourceful because of their convenience in application and sensitivity. In this regard, this chapter specially deals with some of the optical characterization probes, which can study the optical properties of variety of materials accurately, in their bulk or thin film form. Sufficient stress is given for the optical techniques which are used for *in situ* and real-time analysis such that during the deposition of thin films.

In addition to optical characterizations, optical models can provide necessary assistance where the influence of different parameters can be studied for practical and/or ideal cases. On this account, a brief review of currently existing optical models for thin films is presented. Further along the same line, optical simulations with the Yamaguchi model, which we have chosen in case of metal nanoclusters buried in a dielectric matrix to form metal:dielectric nanocomposite systems, are discussed. With the help of this model, variations in the intrinsic optical properties of the metal:dielectric nanocomposites are studied in detail for different parameters. Here, first the influence of intrinsic parameters, in the form of dielectric materials and metals, are studied. Then the impact of nanostructure parameters of metal clusters are depicted in detail.

2 Optical characterization of the materials

2.1 A general background

2.1.1 Complex refractive index

Intrinsic optical properties of the materials can be defined by the complex refractive index $(n(\lambda) + ik(\lambda))$ consisting of a real part $n(\lambda)$ and an imaginary part $k(\lambda)$, known as extinction coefficient, which deals with the absorption properties of the materials. This complex refractive index is related to the dielectric function $\varepsilon(\lambda) = \varepsilon_1(\lambda) + i\varepsilon_2(\lambda)$ with the relation,

$$\begin{aligned} \varepsilon_1(\lambda) &= n^2(\lambda) - k^2(\lambda) \\ \varepsilon_2(\lambda) &= 2n(\lambda) \cdot k(\lambda) \end{aligned} \tag{II.1}$$

Fig.II.1 shows the $n(\lambda)$ and $k(\lambda)$ variations for the dielectric materials (SiO_2, Si_3N_4) and noble metals (Ag, Au, and Cu) [1–3] of our interest. Here, spectroscopy ellipsometry (SE) measurements performed with a SOPRA GESP5 instrument are in good aggrement with the tabulated values as shown in case of Si_3N_4 and Ag.

Dielectric materials - The complex refractive indices in case of dielectric materials (Fig.II.1(a-b)) can be described using a Lorentz model which considers the oscillating electrons around the core atoms. As the resonance for the dielectric materials usually lies in the ultra-violet (UV) range, their refractive indices follow a Cauchy law in the visible range, consisting of a slightly decreasing real part $n(\lambda)$ along with $k(\lambda) \approx 0$. Due to this negligible value of $k(\lambda)$ in the visible range (Fig.II.1(b)), the dielectric materials are non-absorbent and appear transparent to eyes. Fig.II.1(a) shows $n(\lambda)$ for some dielectric materials ($\sim$2 for Si_3N_4 and $\sim$1.5 for SiO_2) compared with vacuum ($n(\lambda) = 1$).

Metals - In case of bulk metals, the Drude model [4] explains the complex refractive index on the basis of collision frequency of conduction electrons. Here for higher wavelengths, $n(\lambda)$ reduces to less than 1 and $k(\lambda)$ highly increases, suggesting the prominent absorption of light. In addition to this, in bulk metals, another contribution arises due to the electrons involved in the inter-band transitions. These inter-band transitions, which take place at a certain threshold energy $E > E_{transition}$ or threshold wavelength $\lambda < \lambda_{transition}$, can be seen in Fig.II.1(c-d). For Au and Cu, the inter-band transitions lie in the visible range around 500nm and 590nm [1, 2, 5, 6], respectively, and for Ag in the UV range around 325nm, giving rise to the characteristic colors of these respective metals [1, 5, 6].

Metal:dielectric nanocomposites - In case of granular thin films containing metal nan-

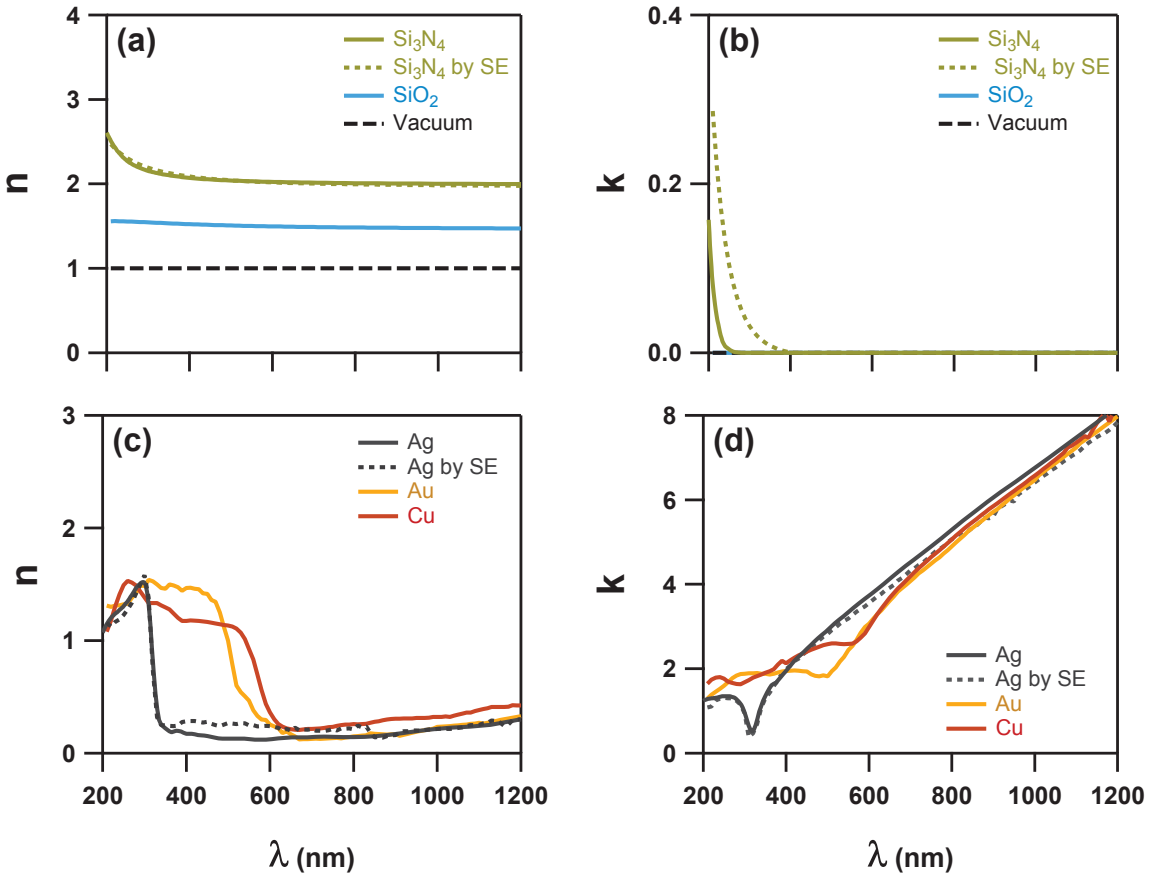

Figure II.1 – Tabulated values (continuous curves) for complex refractive indices $n(\lambda)+ik(\lambda)$ of dielectric materials (a-b) and noble metals (c-d). SE measurements show confirmations of tabulated values in case of Si_3N_4 and Ag (dashed curves).

oclusters embedded in a dielectric matrix, the optical response deviates from the bulk materials and is governed by the phenomenon of surface plasmon resonance (SPR), which is a collective excitation of the electron cloud around the nanoclusters while interacting with the electromagnetic radiations [5]. This SPR is responsible for a strong absorption of light and enhancement of the local electromagnetic field surrounding the nanoclusters. The SPR absorption band is sensitive and strongly affected by the structural properties of the nanoclusters (such as, nature, size, shape, organization, and environment around them) [5, 7].

In practical cases, during the fabrication of nanoclusters using the vacuum deposition techniques explained in Chapter I (Section 2), the assembly of nanoclusters is not ideal (i.e. 3D isotropic organization of spherical nanoclusters) as generally considered in the theoretical models. The non-spherical shape and the two-dimensional organization of the metal nanoclusters can give rise to an anisotropic behavior, which can be described by a diagonal dielectric tensor

given by,

$$\varepsilon_{eff} = \begin{vmatrix} \varepsilon_x & 0 & 0 \\ 0 & \varepsilon_y & 0 \\ 0 & 0 & \varepsilon_z \end{vmatrix} \tag{II.2}$$

whose components are the dielectric functions of the material. For spheroidal nanoclusters with their revolution axis along the z direction and for a uniaxially anisotropic layer $\varepsilon_x = \varepsilon_y = \varepsilon_{xy}$.

2.1.2 Reflectance and transmittance

The above discussed basic optical properties of the materials in the form of complex refractive index, can be studied by means of optical probes in an indirect way, by considering either the transmittance T or the reflectance R of the material (detailed calculations of which are presented in Section 2 of the Appendix). If we consider an interface, as shown in Fig.II.2, made up of two media i and j, having the complex refractive indices n_i and n_j respectively with the respective angles (θ_i and θ_j) in between the normal and the direction of propagation of polarized light (s or p), the Fresnel's complex coefficients r or t can be given as,

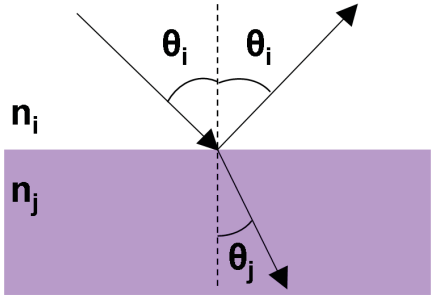

Figure II.2 – Partial reflection and refraction of light at the interface between two media.

$$r_{pij}(\theta_i) = \frac{n_j \cos\theta_i - n_i \cos\theta_j}{n_j \cos\theta_i + n_i \cos\theta_j} \quad \text{and} \quad r_{sij}(\theta_i) = \frac{n_i \cos\theta_i - n_j \cos\theta_j}{n_i \cos\theta_i + n_j \cos\theta_j} \tag{II.3}$$

$$t_{pij}(\theta_i) = \frac{2n_i \cos\theta_i}{n_j \cos\theta_i + n_i \cos\theta_j} \quad \text{and} \quad t_{sij}(\theta_i) = \frac{2n_i \cos\theta_i}{n_i \cos\theta_i + n_j \cos\theta_j} \tag{II.4}$$

where, n_i, n_j and θ_i, θ_j are related by the Snell-Descartes law given as,

$$n_i \sin\theta_i = n_j \sin\theta_j \tag{II.5}$$

From equations II.3, II.4, and II.5, T and R can be obtained as,

$$T_{ij} = \frac{n_j \cos\theta_j}{n_i \cos\theta_i} |t_{ij}|^2 \quad \text{and} \quad R_{ij} = |r_{ij}|^2 \tag{II.6}$$

Further, as shown in Fig.II.3, for a thin film of thickness δ_1 with refractive index n_1 (Medium 1) sandwiched between the two media (Medium 0 and Medium 2), T and R can be given as,

$$T = |t_{012}|^2 = \left| \frac{t_{01}\, t_{12}\, e^{j2\beta_1}}{1 + r_{01}\, r_{12}\, e^{j2\beta_1}} \right|^2 \tag{II.7}$$

and

$$R = |r_{012}|^2 = \left| \frac{r_{01}\, r_{12}\, e^{j2\beta_1}}{1 + r_{01}\, r_{12}\, e^{j2\beta_1}} \right|^2 \tag{II.8}$$

where, $\beta_1 = \frac{2\pi}{\lambda}\delta_1 n_1 \cos\theta_1$, is the dephase created by the single travel of light ray in the thin film material (i.e. medium 1). In case of more complex stratified (multilayer) thin film structures, a matrix formalism can be used for the calculations of T and R [8, 9].

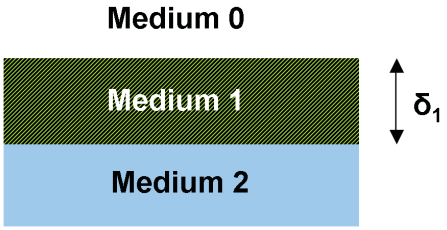

Figure II.3 – Schematics of a thin film layer (medium 1) of thickness δ_1 on a semi-infinite substrate (medium 2).

As the optical properties of thin film materials are prominently different than that of their bulk counterparts, optical characterization techniques, using transmittance and reflectance of light, act as perfect candidates. These optical techniques are surface sensitive, efficient, non-expensive, non-destructive, non-invasive and easy to set-up comparing to other techniques like, electron microscopy or X-ray diffraction and scattering techniques. Thus, optical techniques offer a versatile contribution in the characterizations for a wide range of materials, which can be seen in the form of following factors.

- **Incident light -** Depending upon the material properties to be studied, the incident light can be used in un-polarized (i.e. natural light) or polarized (s or p) form. Moreover, the incident light can be polychromatic (e.g. discharge Xenon lamp) or monochromatic

(such as lasers). In addition to this, the angle of incidence can give another set of freedom where normal or oblique incidence is used during the optical characterization. However, it should be noted that, in oblique incidence, the *s*-polarized light is sensitive to the in-plane information, while *p*-polarized light is sensitive to both, in-plane and out-of-plane information.

- **Analyzed light -** In optical characterization techniques, the information regarding the interaction of light with the materials can be collected in transmitted or reflected mode depending upon the material opacity and the experimental configuration. If the material to be studied contains scattering centers (in volume or at surface), they can be studied using the light in diffused configuration, otherwise specular (or regular) mode is chosen preferably.

For the purpose of *in situ* optical thin film characterizations, we will focus on the specular (regular) reflection mode hereafter. Furthermore, we will assume that the volume or surface scattering, i.e., material heterogeneities to be studied are much smaller in size than the incident light wavelength. Here it is worth noting that, all the characterizations are relative so that the similar responses of the elements (optical source, optical fibers, detectors etc) in the optical path are eliminated [10–12].

2.2 Optical characterization techniques based on specular reflection mode

2.2.1 Spectroscopy Ellipsometry (SE)

Spectroscopy ellipsometry (SE) is a well established technique for studying optical properties of materials (complex refractive index) and for measuring the thin film thickness along with surface roughness or porosity. This sensitive optical characterization technique has been used for variety of bulk and thin film materials, such as metals, semiconductors, minerals, dielectric materials etc [13–17].

In SE, the material surface is illuminated by a polarized light at oblique incidence angle. After the reflection from the surface, light is elliptically polarized and fed to detector through an analyzer. The measured quantities are Ψ and Δ, which are related to the ratio of complex Fresnel reflection coefficients r_p (for *p*-polarized light) and r_s (for *s*-polarized light) with the

following relation,

$$\tan \Psi(\lambda) \cdot e^{i\Delta(\lambda)} = \frac{r_p(\lambda)}{r_s(\lambda)} \tag{II.9}$$

Even though SE can be used at different oblique angles, the measurements at the Brewster's angle[1] of the substrate are popular, where the contrast between the p and s polarization is optimal causing the increase of the sensitivity [17].

However, SE is an indirect method: $n(\lambda)$ and $k(\lambda)$ of the studied material can not be directly deduced from the measured quantities Ψ and Δ. For this, SE requires a model containing optical constants and thickness of the layer system as fitting parameters, with which calculated Ψ and Δ values are determined from Fresnel's equations (II.3 & II.4) and equation II.9. The best matching calculated data with the experimental data provides the correct values of $n(\lambda)$ and $k(\lambda)$ of that material [18].

2.2.2 Reflection anisotropy spectroscopy (RAS)

RAS is a technique based on the same background as that of SE and is useful for the measurement of the surface anisotropy of materials. It is particularly used to study the surface rearrangements and surface contaminations of bulk materials because such factors usually lower the symmetry at the surfaces and lead to optical anisotropy in the plane of the surface, which is a very small, yet measurable quantity [12, 19–23]. RAS is specifically suitable for studying the crystal surface anisotropy by considering the difference in the reflections from the crystal planes [16, 19, 21, 24, 25]. It is also extended for the investigations of organic layers, bio-molecular thin films, metal optical properties, and molecular assembly growth on the metal surfaces [26–28].

RAS uses a polarized light at normal or near-normal incidence during the measurements. It probes the change in the state of polarization upon reflection from the material surface. In RAS, the difference in the reflections of mutually perpendicular polarizations is measured directly and instantly, which is given by [12, 23, 29–32],

$$\frac{\delta r}{r}(\lambda) = 2\left[\frac{r_x(\lambda) - r_y(\lambda)}{r_x(\lambda) + r_y(\lambda)}\right] \tag{II.10}$$

where, r_x and r_y denote the complex reflectivities of the linearly polarized light in orthogonal (x, y) directions [28]. Hence, with such a configuration, an isotropic bulk will produce no output signal (as same signals will be canceled out) in contrast to an anisotropic surface.

[1]For a dielectric material (k(λ)=0), if unpolarized or partially polarized light is incident at the Brewster's angle of that material, the reflected light is totally s-polarized.

The use of two polarizations in SE and RAS, even though increases the surface sensitivity and are used for the wide range of materials, increases the complexity in the device configurations [13–16, 22, 28, 33, 34]. Also, techniques like SE where ratio of polarizations are measured can be inconvenient for instantaneous measurements during depositions because of their slow response and hence difficult to operate with real-time measurements for a broad wavelength range. On the other hand, even though the RAS can produce sensitive instantaneous results, the use of a normal incident mode puts limit on its use.

2.2.3 Direct reflectance spectroscopy

The use of this specular reflection mode can be more convenient for real-time measurements during thin film deposition; so far as a reference measurement for the incident light is available (which is not possible in our case). The optical characterization is then direct in the form of the measured reflectance R from the thin film surface which is given by,

$$R(\lambda) = \frac{I_r(\lambda)}{I_0(\lambda)} \tag{II.11}$$

where, I_r and I_0 are the reflected and incident intensities, respectively.

2.2.4 Surface differential reflectance spectroscopy (SDRS)

SDRS uses a fixed polarization (e.g. s or p) and a fixed oblique angle during the measurements [33, 35]. The relative variation in the reflectance during the measurements is given as [12, 23, 33, 35],

$$\frac{\Delta R(\lambda)}{R_0(\lambda)} = \frac{R(\lambda) - R_0(\lambda)}{R_0(\lambda)} \tag{II.12}$$

where, R_0 and R are the reflectances collected from the bare substrate and deposited thin film, respectively.

The use of only one polarization at a fixed oblique angle during the analysis, reduces the complexity in the measurements comparing to SE or RAS and makes this spectroscopy faster or instantaneous comparing to SE [12, 33]. Moreover, SDRS does not require a special reference measurement of incident light comparing to direct reflectance spectroscopy because the reflectance R_0 is available in the same configuration as R.

3 *In situ* and real-time SDRS

3.1 Implementation in our work

During our study, we have used SDRS in *in situ* configuration for the real-time optical characterization of nanocomposite thin films during their depositions by magnetron sputtering (Fig.I.3). The schematic drawing of the *in situ* SDRS set-up adapted on the magnetron deposition chamber is shown in Fig.II.4, where, a white light source is used in the form of a Xe discharge lamp, powerful enough (150W) to overcome the diffused light emitted by the plasma of Ar^+ during the deposition of the materials. The input and output view ports at the magnetron chambers are made up of pure silica, which allow transmission of the light without blocking UV radiation. Optical fibers are used for the transportation of the light from the source to the polarizer and from the analyzer to the spectrophotometer.

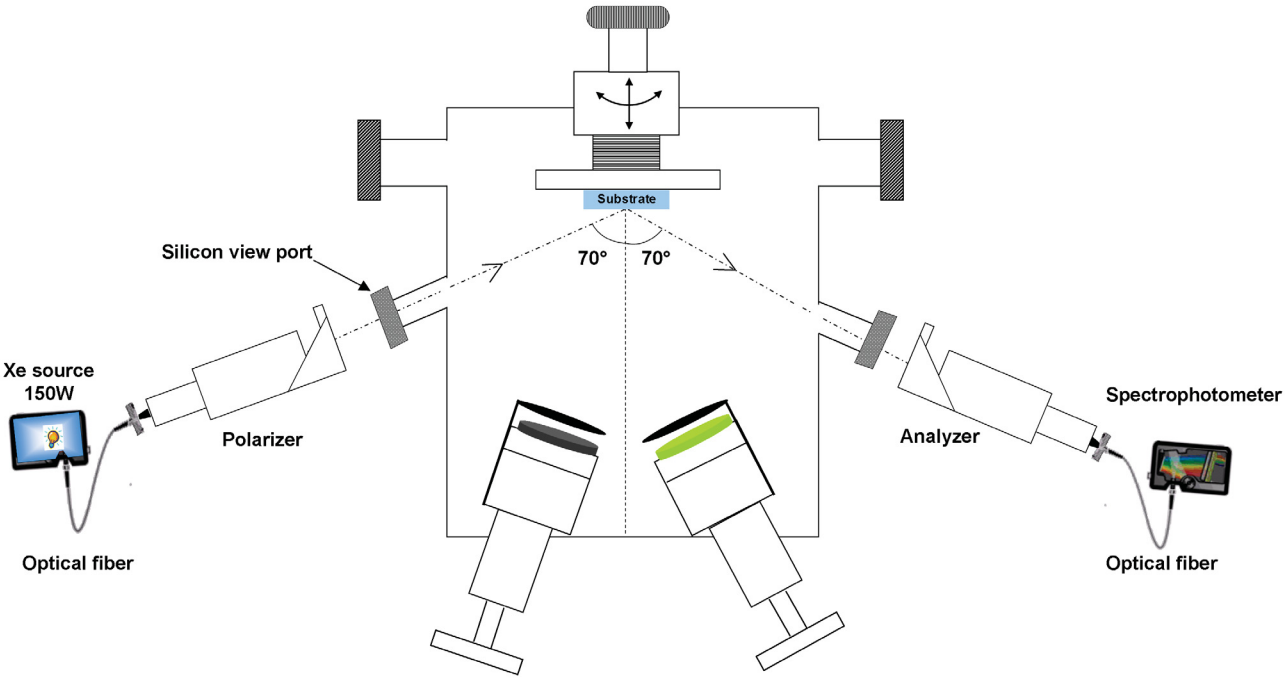

Figure II.4 – Schematics - installation of optical set-up of *in situ* SDRS adapted on magnetron sputtering deposition machine (PUMA).

As the optical systems are situated on two separate ports outside the deposition chamber in a non-intrusive way, the optical characterizations can be continuously performed on the on-going depositions of the thin films, without hampering the vacuum. During the measurements, the sample is illuminated by a *s*-polarized light and focused on the sample surface with the help of

silica lenses at an angle of 70° with respect to the surface normal.[2] The specular polarized light from the specimen surface is collected by a spectrophotometer QE65000 (Ocean Optics^{TM})[3] in which the composite grating allows a wide spectral range (200nm-985nm). However the range of characterization spectra is restricted up to 350-800nm, because below 350nm considerable noise is added in the optical signal due to lack of UV light, and above 800nm the characteristic spectral peaks of the Xe discharge lamp disturb the measurements [10].

The optical measurements start well before the deposition, where the reflectance from the bare substrate surface (R_0) is collected by the detector first. Then, the relative changes in the reflectance due to the on-going deposition of atomic species (R) are measured, as given in equation II.12. In our case, due to the real-time measurements, in addition to the wavelength (λ), the measured reflectance is also a function of the time (t).

3.2 *In situ* SDRS in the literature

A number of research works regarding the use of *in situ* and real-time SDRS can be found in the literature in order to study the optical properties of different materials (see Tables II.1 - II.2). For example, with the help of *in situ* SDRS, Y. Borensztein *et al* [36, 37], M. Roy *et al* [38–40], S. Ohno *et al* [33, 41], C. Goletti *et al* [42], and Selci *et al* [43, 44] have extensively studied the reconstructions and roughening in the semiconductor surfaces due to the oxidation or hydrogenation treatments and high temperature annealing treatments, respectively. H. Proehl *et al* [45] and R. Forker *et al* [46, 47], on the other hand, have used *in situ* SDRS in case of highly ordered organic molecular thin films (such as, PTDCA) deposited on different surfaces to understand the effect of substrates on the film growth. Moreover, A. Gouralnik and S. Dotsenko *et al* [48–51] have extended the real-time SDRS study for the phase determination in magnetic clusters such as FeSi and Fe_3Si during the deposition of Fe on a Si substrate.

In addition to these studies, most of the research works related to the use of SDRS during the growth of metal nanoclusters have been done by a group from INSP (Institute des Nanosciences de Paris) which is mainly focused on the noble or alkali metals deposited on different metallic, semiconductor or oxide surfaces using thermal evaporation technique [35, 53–69] (Table II.2).

Out of this, some of the results [35, 60–69] related to real-time SDRS investigations during the growth of Ag or Au nanoclusters on oxide materials are shown in Fig.II.5. Fig.II.5(a_1- a_2) shows several absorption peaks in p or s polarized spectra, indicating the presence of multi-

[2]The magnetron vacuum deposition chamber was originally designed for SE to be used at a fixed oblique incidence angle of 70° because it is very close to the Brewster's angle of Si.

[3]The detector in the spectrophotometer is Peltier cooled at -10°C which reduces the black noise and the electronic excitations.

Authors	Materials studied	Optical specifications		
		Polarization	Incidence angle	λ range
Borenzstein *et al*, Roy *et al*	Reconstructions on Si-surfaces due to the adsorption of gases or annealing [36–40].	*p-s*	60° or 40°	250-1240nm
Ohno *et al*, Goletti *et al*, Selci *et al*, Chiarotti *et al*, Cricenti *et al*	Oxidation effects on surfaces of Si(111), Ge(111), GaAs(001), InP (110), GaP (110) etc [33, 34, 41–44, 52]	*p-s*	75°	300-4000nm
Proehl *et al*, R. Forker *et al*	PTCDA/Au(111) and PTDCA/mica [45–47]	No	20°	200-1000nm
Gouralnik *et al*, Dotsenko *et al*	Fe/Si or Cr/Si [48–51]	No	17°	450-1550nm

Table II.1 – Literature survey for *in situ* and real-time SDRS.

Authors	Materials studied	Optical specifications		
		Polarization	Incidence angle	λ range
De Crescenzi *et al*, Lopez-Rios *et al*	Ag/Al, Ag/Au [53, 54]	*p*	60° or 70°	250-400nm
Borensztein *et al*	Cu/Ag, Ag/Cu [55, 56]	*p*	45°	250-1240nm
	Pd/Ag [55, 57]		45° - 90°	250-1240nm
	Ag/Si [58]		60°	220-955nm
Beitia *et al*	K/SiO_2 [59, 60]	*p*	60°	410-1240nm
Martin *et al*	Ag/TiO_2 [61, 62]	*p-s*	45°	210-820nm
Lazzari *et al*	Al/Al_2O_3 [63, 64]	*p-s*	45°	210-820nm
	Ag/MgO [64–66]	*p*		250-1240nm
	Ag/Al_2O_3,/ZnO,/TiO_x [67]	*p*		
	Ag/Al_2O_3 [35, 68]	*p-s*		210-820nm
	Ag/Al_2O_3, /TiO_x [63]	*p-s*		
Borensztein *et al*	Au/TiO_2 [69]	No	Diffused configuration	350-800nm

Table II.2 – Literature survey for *in situ* and real-time SDRS during metal nanocluster growth.

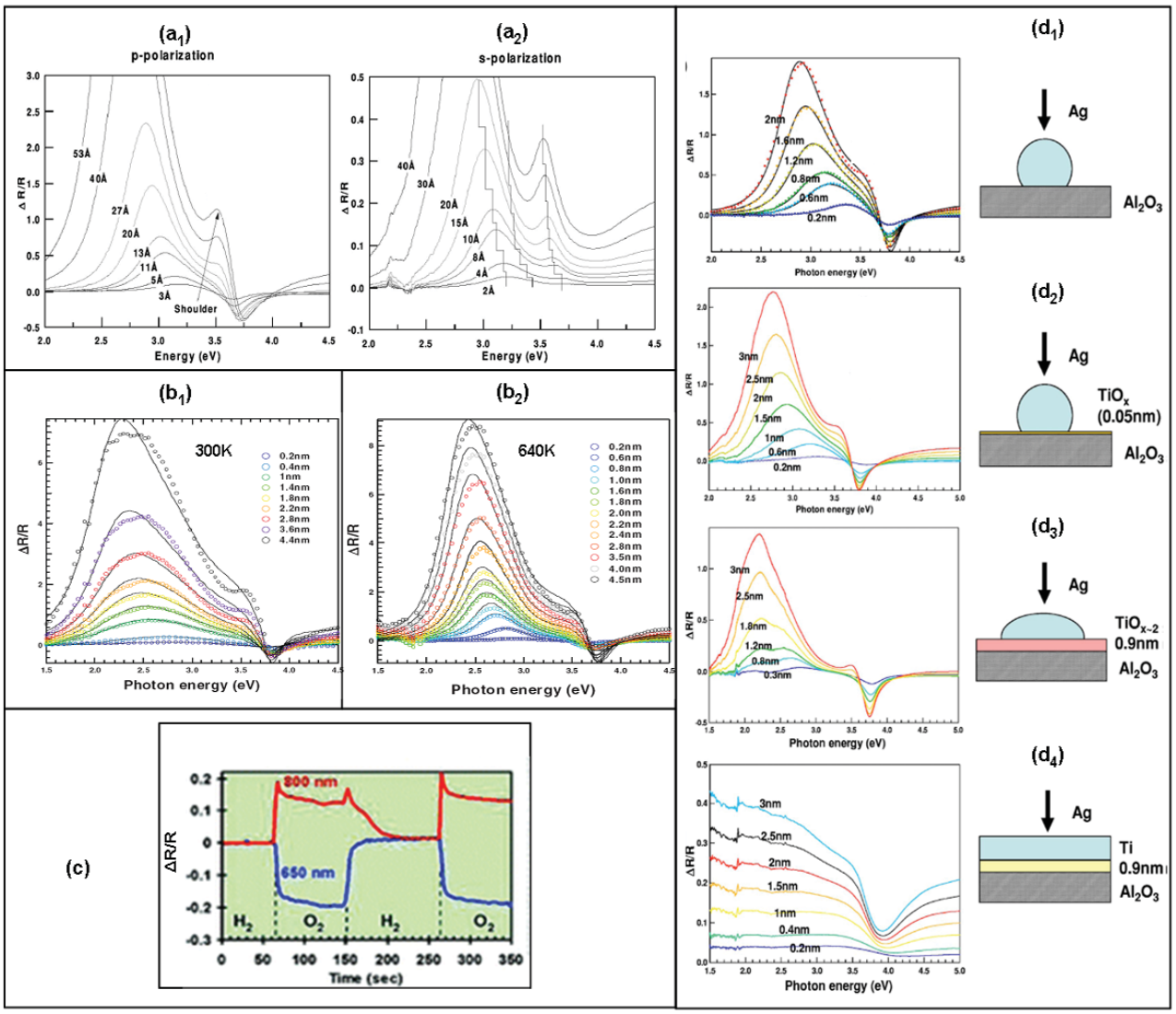

Figure II.5 – *In situ* and real-time SDRS optical investigations during the growth of metal clusters on substrate surfaces. Deposition of Ag on Al_2O_3 at 600K studied with *p* (a_1) and *s* (a_2) polarized light, at 45° [35]. Deposition of Ag on MgO, studied with *p* polarized light at 55°, at 300K (b_1) and 640K (b_2) [66]. (c) Effect of redox atmospheres (H_2/O_2) on the optical properties of Au nanoclusters supported on TiO_2, studied with diffused light for two wavelengths (650nm and 800nm) as a function of time [69]. Deposition of Ag on different substrates (d_1-d_4) at 300K studied with *p* polarized light at 45°, (except d_4 which is studied with *s*-polarized light) [63].

polar resonances from Ag clusters, and an increase in the amplitude with a sharp red-shift of these peaks when the amount of Ag is increased [35]. In Fig.II.5 (b_1-b_2), the influence of the deposition temperature is evident in the form of blue-shifted and sharper SDRS peaks at higher temperature [66]. Fig.II.5(c) shows a real-time optical analysis for the influence of a redox atmosphere (H_2/O_2) on the optical properties of the Au nanoclusters supported on TiO_2

[69]. During the cyclic oxidation-reduction treatments, respective alternate disappearance and reappearance of the optical response of Au nanoclusters (measured in diffused configuration such that incident angle = 40° and reception angle = 0°) can be seen clearly. Furthermore, the influence of different substrates on the optical properties of supported Ag nanoclusters is shown in Fig.II.5(d_1-d_4) [63]. For Ag deposition on oxide substrates at room temperature, prominent maxima and minima in the SDRS spectra are evident due to SPR when studied with *p*-polarized light, indicating the 3D growth of clusters with different contact angles depending on the oxide substrate (Fig.II.5(d_1-d_3)). But, when the oxide substrates are replaced with metal (Ti) (Fig.II.5(d_4)), no more maximum in the SDR spectra can be seen, suggesting the absence of Ag nanoclusters and therefore the 2D growth of Ag on the metal surface.

3.3 *In situ* SDRS specific to our work

As we have seen, research works in the literature support the use of real-time SDRS in characterizing the optical properties of different materials (in general and metal nanoclusters, in particular). Comparing to the literature, as we have used the magnetron sputtering technique for the metal deposition, the nanocluster systems it produces are totally different and hence their optical properties too. Nevertheless, the flexibility of the magnetron deposition technique give us additional advantages.

First of all, as alternate depositions are possible, we can cover the metal nanoclusters by a capping layer of amorphous dielectric material and hence, the influence of the matrix on the optical properties of the metal clusters can be studied in real-time. In addition to this, it is possible to generate a controlled plasma of gas in the magnetron chamber, hence partially ionized gas treatments as well as bias plasma annealing treatments on the deposited metal clusters can be carried out in real-time, which we seldom encounter in the literature. Finally, as we are always keen to put a dielectric capping-layer above them after the respective treatments, it not only reduces the atmospheric contaminations in the metal nanoclusters, but also preserves their nanostructural changes modified due to the respective treatments. Such changes in the nanostructures can be studied later using *post mortem* structural characterization techniques, such as STEM or grazing-incidence small-angle X-ray scattering (GISAXS).

4 Theoretical models for the optical properties of nanocomposite thin films

4.1 Short overview of exiting theoretical models

For any optical spectroscopy, the important limitation of being qualitative can be overcome by constructing a precise theoretical model. In this regard, different authors have developed more or less complex models, which can study the optical response of supported metal nanoclusters and/or nanocomposite thin films (i.e. metal nanoclusters embedded in a dielectric matrix).

Although A. Clebsch [70] and L. Lorentz [71] contributed to this problem by considering the scattering of electromagnetic radiations by a perfectly rigid sphere using potential functions, color effects connected with colloidal gold clusters were treated by Mie using the classical Maxwell equations in 1908 [7, 72]. He proposed that the optical response of metal spheres of various sizes can be calculated within the framework of classical electrodynamics [5, 7].

In recent years, models like discrete dipole approximation (DDA) formalism [73, 74] have been used to compute the optical responses of metal nanoclusters of various sizes and shapes, while quantum approaches [75] have been used to study the finite size effects in the case of very small clusters (diameter < 5nm) where a classical approach may not be appropriate. Even though these theories are proved adequate for an accurate description of the optical response of isolated clusters, they are time and resources consuming and more importantly inadequate to be applied to more complex systems such as nanocomposite thin films containing assembly of interacting metal nanoclusters.

For the common case of nanocomposite thin films in the quasi-static regime, the macroscopic optical response of the heterogeneous material can be described by a homogeneous effective dielectric function. In this context, effective medium theories (EMTs) have been developed in order to link the macroscopic optical properties of the materials to their nanostructures. A complete EMT for a 3D homogeneous organization of the metal nanoclusters within a dielectric matrix has been proposed by Bergman [76]. Other than this, Maxwell-Garnet [77], Garcia [78], and Bruggeman [79] models have been useful in the limiting cases of weakly interacting [80, 81], moderately interacting [78], and strongly interacting nanoclusters [82], respectively. For modeling the effective optical response of a 2D assembly of weakly interacting metal nanoclusters, one of the simplest methods has been proposed by Yamaguchi *et al* [83], which will be used in this research work.

4.2 Optical simulations within the Yamaguchi model

In the Yamaguchi model, the clusters are assumed to be monodisperse, distributed homogeneously on a square lattice and they are spheroidal in shape (with their axis of revolution normal to substrate). These clusters are considered as interacting dipoles and the influence of the substrate is taken into account by image dipole effects. In our case, we have used a slightly modified model adopted to nanoclusters with isotropic distribution. The details of the theoretical calculations used in this modified Yamaguchi model are given in Section 1.2 of the Appendix.

4.2.1 Basic description of the modified Yamaguchi model

For the simulation purpose, we have chosen a metal:dielectric nanocomposite layer, where the metal nanoclusters are completely embedded in the dielectric matrix (Fig.II.6(a)), so that the interactions with the substrate (dipole image) are not taken into account. These nanoclusters are supposed to have a 2D isotropic distribution and an identical spheroidal shape with in-plane diameter D and height H (Fig.II.6(b)).

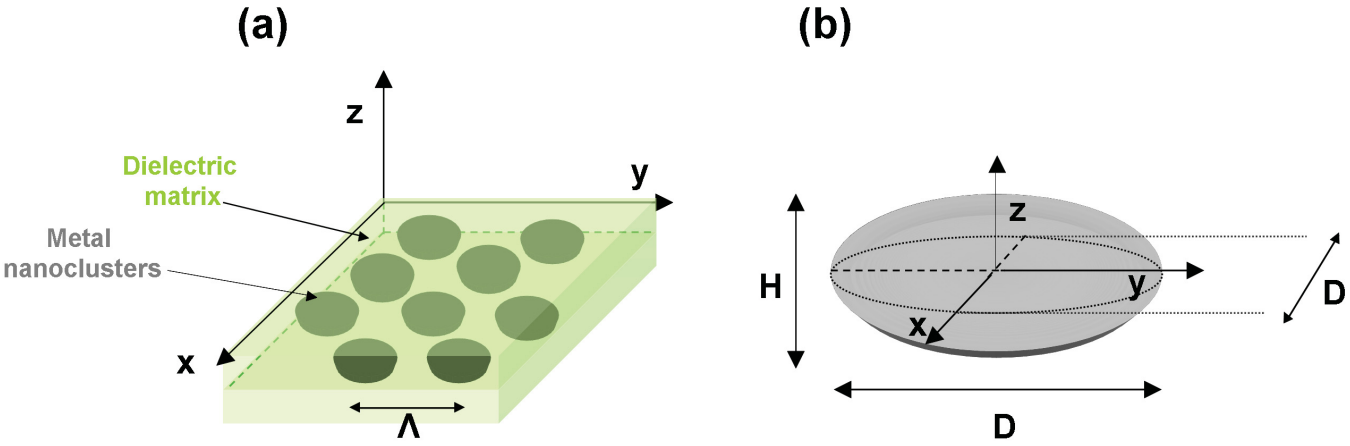

Figure II.6 – Schematics of metal:dielectric nanocomposite layer (a) containing spheroidal shaped metal nanoclusters, having inter-cluster distance Λ, (b) diameter D, and height H.

The effective dielectric function ε_{eff} of the metal:dielectric nanocomposite layer can be given by,

$$\varepsilon_{eff} = \varepsilon_m \left(1 + q\left[\frac{\varepsilon_i - \varepsilon_m}{\varepsilon_m + F\left(\varepsilon_i - \varepsilon_m\right)}\right]\right) \tag{II.13}$$

where,

- ε_m is the dielectric function of the matrix, which acts as a surrounding medium for the embedded metal nanoclusters.

- ε_i is the modified dielectric function of the metal nanoclusters. Here, the dielectric function of the bulk metal is corrected for the nanoclusters [5, 84] by using a phenomenological parameter A, known as amortization or damping constant, which takes into account the cluster size and interface effects on the mean free path of the electrons (see Section 2.4 of Appendix of this thesis for details).

- F is the effective depolarization factor which takes into account the shape of the nanoclusters (via the aspect ratio H/D), and interactions between them (i.e. inter-particle distance Λ).

- q is the volume fraction of the nanoclusters which is also known as metal filling factor. It can be given by $q = NV$, where V is the volume of a nanocluster and N is the number of clusters per unit volume. In case of 2D distribution, assuming that the thickness of the effective layer is equal to the height H of the nanoclusters $N = \frac{d}{H}$, where d is the areal density of the clusters.

Hereafter, the influence of different parameters on the simulated optical response of the nanocomposite layer by using the Yamaguchi model (equation II.13) is presented. For these simulations, the input parameters were fixed with the values collected in Table II.3, except if mentioned.

D (nm)	H/D aspect ratio	Λ (nm)	d (μm^{-2})	A
7	0.75	12	7000	2

Table II.3 – Different morphological and organizational parameters of metal nanoclusters which are chosen as input parameters for optical simulations.

Using Yamaguchi simulations, we will study the optical response in the form of effective in-plane complex refractive index ($n_{xy}+ik_{xy}$), which is related to the effective in-plane dielectric function ε_{xy} (from equation II.1). Hence accordingly, equation II.13 is used by replacing ε_{eff} and F by ε_{xy} and F_{xy}, respectively.

4.2.2 Influence of the materials

The collective in-plane optical response of various metal:dielectric nanocomposites (metals: Ag, Au, and Cu; dielectric: vacuum, SiO_2, and Si_3N_4) is presented in Fig.II.7 in terms of

$n_{xy}+ik_{xy}$. Here it is worth noting that the notation "metal:dielectric" in this chapter represents a nanocomposite made up of metal nanoclusters completely embedded inside the dielectric matrix.

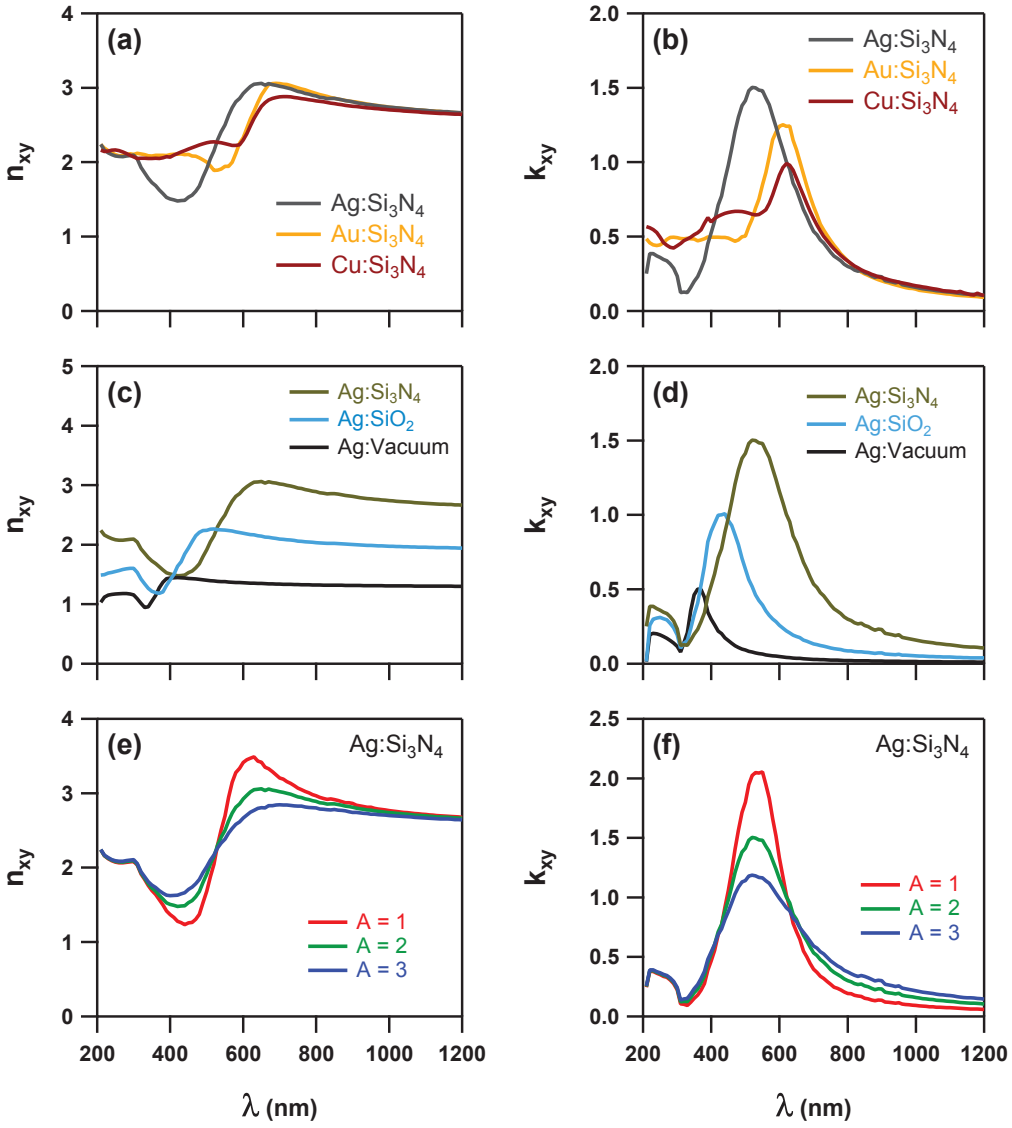

Figure II.7 – Influence of the materials on the effective in-plane complex refractive index of the metal:dielectric nanocomposites, (a-b): metals (Ag, Au, and Cu), (c-d): dielectric matrices (Si_3N_4, SiO_2, and Vacuum), and (e-f): damping constant (A=1,2,3).

From Fig.II.7(a-b), the effect of the metal for Ag:Si_3N_4, Au:Si_3N_4, and Cu:Si_3N_4 nanocomposite systems, is demonstrated. The presence of an absorption peak in Fig.II.7(b) underlines the difference in the optical properties of nanostructures from their bulk counterparts (Fig.II.1(b-d)). Moreover, when the embedded metal in Si_3N_4 changes from Ag → Au → Cu,

the absorption band of k_{xy} is red-shifted from 530nm $\rightarrow$ 610nm $\rightarrow$ 625nm with decreasing amplitude from 1.50 $\rightarrow$ 1.25 $\rightarrow$ 1.00, respectively. Fig.II.7(b) also suggests the sharpness in the optical properties of the Ag:Si_3N_4 nanocomposite where the absorption band is well defined and this makes Ag a suitable candidate for our further works comparing to Au:Si_3N_4 and Cu:Si_3N_4.

Furthermore, the effect of the dielectric material (SiO_2 and Si_3N_4) on the effective optical properties of Ag:dielectric nanocomposites can be seen in Fig.II.7(c-d), and is compared with a virtual situation where the Ag clusters are completely surrounded by the vacuum. Changing the surrounding matrix from vacuum ($n = 1$) $\rightarrow$ SiO_2 ($n = 1.5$) $\rightarrow$ Si_3N_4 ($n = 2$), causes a red-shift of the absorption band of k_{xy} from 360nm $\rightarrow$ 430nm $\rightarrow$ 530nm as well as an increase in the amplitude from 0.5 $\rightarrow$ 1 $\rightarrow$ 1.5, respectively.

Moreover, Fig.II.7(e-f) shows the effect of the damping coefficient A on the optical properties of Ag:Si_3N_4 nanocomposites, which is related with the modified collision rate in case of metal nanoclusters and takes into account the surface effects of the electrons around them. Fig.II.7(f) demonstrates that the increase of A from 1 $\rightarrow$ 3 (i.e. $2A/D$ from 0.29 $\rightarrow$ 0.86) causes a damping in the absorption amplitude from 2 $\rightarrow$ 1.2 without changing the position of the absorption band.

4.2.3 Influence of the morphological and organizational parameters of the metal nanoclusters

The morphological parameters (size and shape) and the organizational parameter (inter-cluster distance or areal density) of the metal nanoclusters, can have significant effects on the collective optical response of the metal:dielectric nanocomposites. Hence, to show these effects on the optical simulations for Ag:Si_3N_4 nanocomposites, only one parameter for the Ag clusters is changed at a time while keeping all the other parameters constant (Table II.3). The influence of each of these morphological and organizational parameters can be seen in Fig.II.8 and Fig.II.9.

- **Size -** Fig.II.8(a-b) show the effect of the Ag cluster diameter D on the optical properties of Ag:Si_3N_4 nanocomposites. Fig.II.8(b) demonstrates the sharp increase in the amplitude of k_{xy} from 0.7 $\rightarrow$ 1.5 $\rightarrow$ 2.5 upon increasing D from 5nm $\rightarrow$ 7nm $\rightarrow$ 9nm, respectively. This increase in D also causes a sharpening of the resulting absorption band. However, the absorption position is weakly red-shifted from 530nm $\rightarrow$ 545nm. The effect of cluster size therefore, is prominent on the absorption amplitude and much smaller on its position, as confirmed in FigII.9(a-b).

- **Shape -** The effect of the Ag cluster shape (i.e. H/D aspect ratio) can be seen in Fig.II.8(c-d). As we move from oblate Ag clusters (with $H/D = 0.5$) to spherical Ag

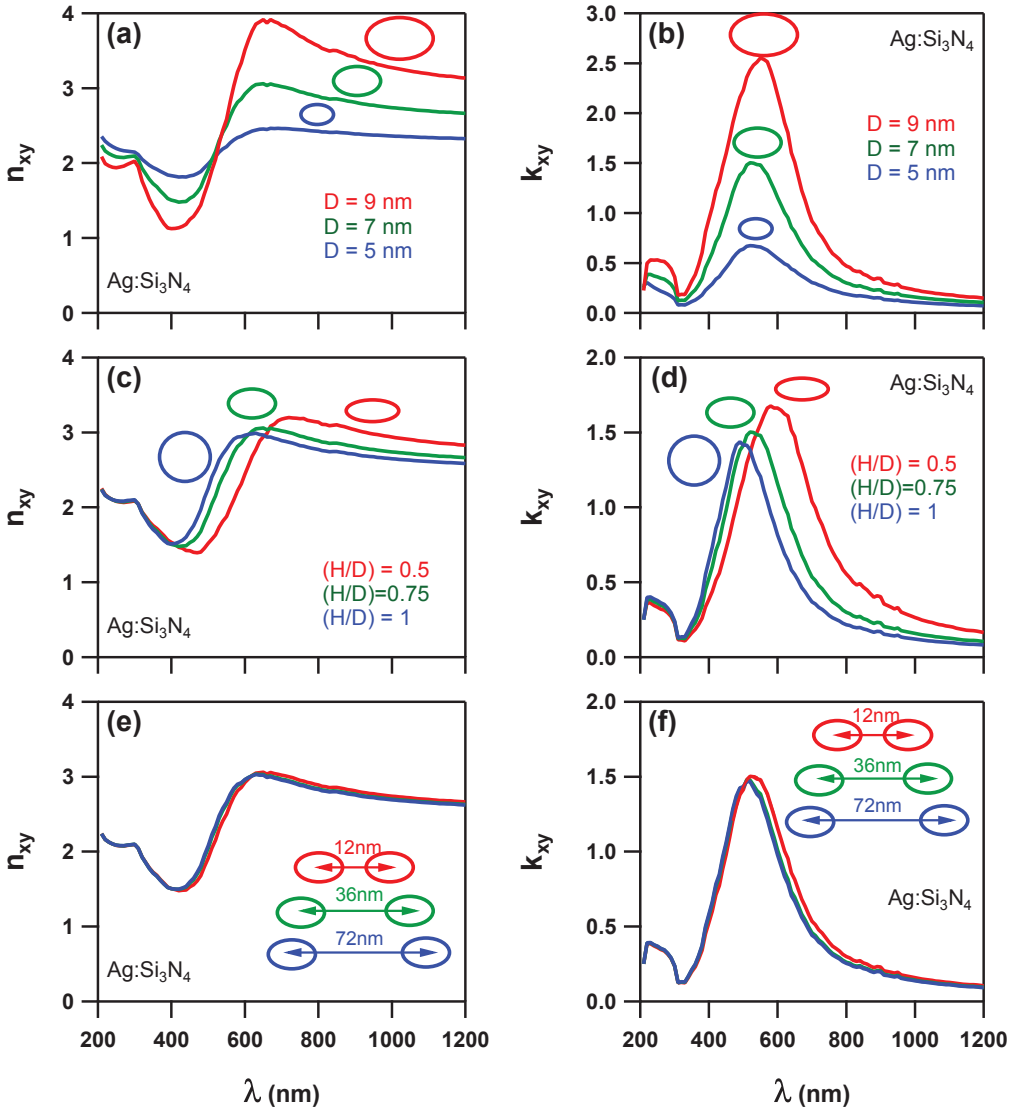

Figure II.8 – Effect of cluster diameter D (a-b), cluster shape H/D (c-d), and inter-cluster distance Λ (e-f), on the effective in-plane complex refractive index of Ag:Si_3N_4 nanocomposites.

clusters (with $H/D = 1$), a blue-shift from 590nm $\rightarrow$ 500nm is evident along with the reduction in the absorption amplitude from 1.70 $\rightarrow$ 1.45, although the volume of the clusters is increased. This gives us an idea that the cluster shape effects are prominent on the position of the absorption band (FigII.9(c-d)) in contrast to the cluster size effects, which modify mainly its amplitude. However it is worth noting that, as shown in the FigII.9(c), even a small increase in the aspect ratio of oblate clusters, causes a larger blue-shift compared to the similar increase for more spherical clusters. For example, when the aspect ratio H/D increased from 0.4 to 0.5, the blue-shift it induces is around

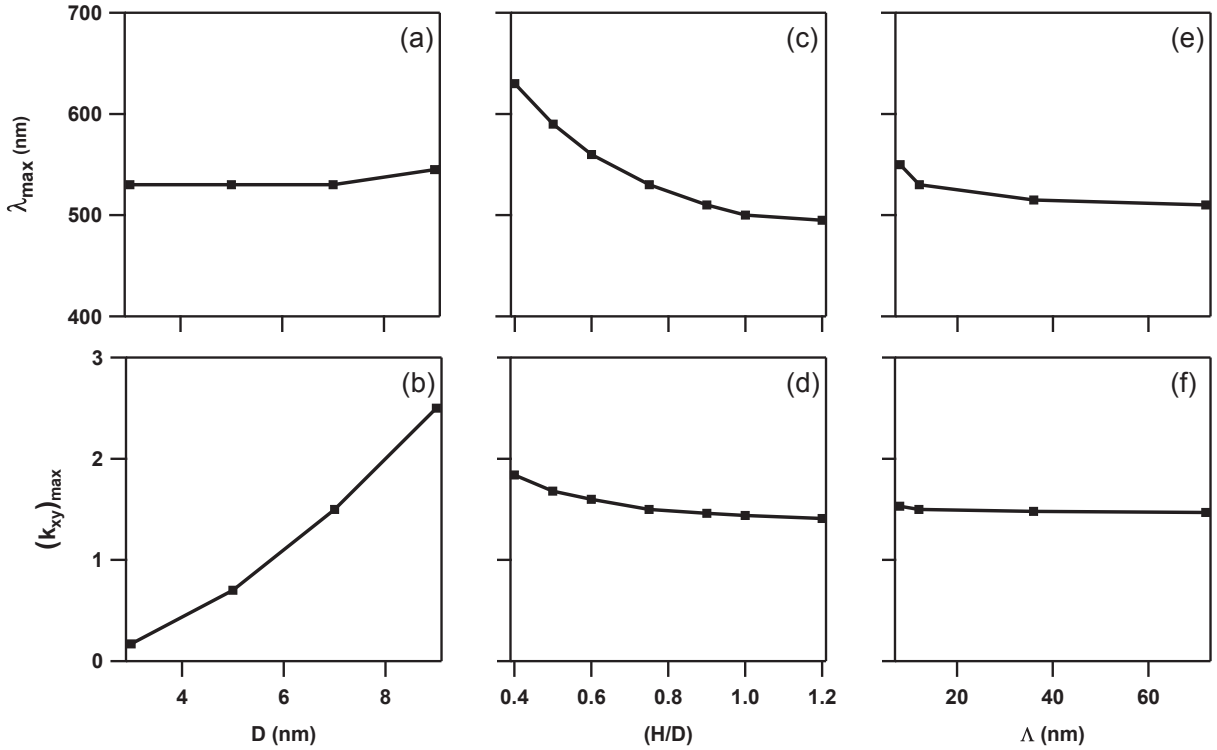

Figure II.9 – Effect of cluster diameter D (a-b), cluster shape H/D (c-d), and inter-cluster distance Λ (e-f), on the position ($\lambda_{\max}$) and amplitude ($(k_{xy})_{\max}$) of k_{xy} maximum for Ag:Si_3N_4 nanocomposites.

-40nm comparing to the increase in H/D from 0.8 to 1, which causes a blue-shift of -20nm (Fig.II.9(c)).

- **Inter-cluster distance -** The inter-cluster distance Λ and the cluster density d define the organization of the nanoclusters. Both are inter-connected with each other such as a decrease in the density always accompanies the increase in the inter-cluster distance ($d \sim 1/\Lambda^2$). As the Yamaguchi model considers the metal clusters as interacting dipoles, the increase in the inter-cluster distance decreases the interactions between the clusters and this shifts the absorption band towards lower wavelengths as seen in Fig.II.8(f). Actually a slight blue shift in the absorption band from 530nm $\rightarrow$ 515nm is seen when the inter-cluster distance changes from 12nm $\rightarrow$ 36nm without much affecting the absorption amplitude of k_{xy}. Further increase in the inter-cluster distance does not affect the optical properties (FigII.9(e-f)). Hence, any changes in the organizational parameters of metal clusters make less impact on the position and even lesser impact on the amplitude of the absorption band comparing to the morphological parameters. Nevertheless, it is worth noting that the Yamaguchi effective medium theory is only valid for rather diluted medium

(low metal clusters densities or small filling factors).

Until now we have changed only one parameter to see its effect on the effective in-plane optical properties of the metal:dielectric nanocomposites. But in the practical situations, some of these parameters can be inter-dependent and prediction of the optical response by changing only one parameter can be ambiguous. Hence, to know the combined effects of inter-dependent parameters, some simulations are presented in Section 2.4 of the Appendix, showing similar results as we have discussed above.

4.3 From effective complex refractive index ($n_{xy} + ik_{xy}$) to the SDRS signal

4.3.1 Comparison between $n_{xy} + ik_{xy}$ and transmittance T or reflectance R of the nanocomposite materials

In previous subsections (4.2.2 and 4.2.3) of this chapter, we have seen the effect of different materials and metal cluster nanostructure on the basic optical properties of metal:dielectric nanocomposite systems in the form of their effective complex refractive index. Now, as already described in Section 2 of this Chapter, the optical properties of the nanocomposites can be studied indirectly using suitable optical characterization techniques that measure the transmittance T or reflectance R.

As a typical example, Fig.II.10(a-b) shows $n_{xy}+ik_{xy}$ of a Ag:Si_3N_4 nanocomposite layer made up of Ag nanoclusters with the parameters gathered in Table II.3. In comparison, Fig.II.10(c-d) displays the corresponding T and R at normal incidence calculated using equations II.6, II.7, and II.8 and assuming the layered structure shown in the inset (Fig.II.10(d)) [4]. In Fig.II.10, it can be seen that T presents a minimum while R presents a maximum and both are located around 550nm, close to the maximum of k_{xy} (530nm) but at a greater wavelength. This shift in the position may be explained by the influence of the maximum of n_{xy} (650nm).

4.3.2 Comparison between reflectance R and the relative reflectance ($\Delta R/R_0$)

In our case, real-time SDRS is implemented to study the optical properties of nanocomposites during their depositions, with which we measure $\Delta R/R_0$ (equation II.12). In this regard, Fig.II.11(a) shows the comparison between the simulated reflectance R and R_0 (where R_0 is the reflectance of bare Si_3N_4 substrate), while Fig.II.11(b) demonstrates the simulated relative

[4] The thickness of the Ag:Si_3N_4 nanocomposite layer is assumed to be equal to the height of the Ag clusters (i.e. 5.25nm).

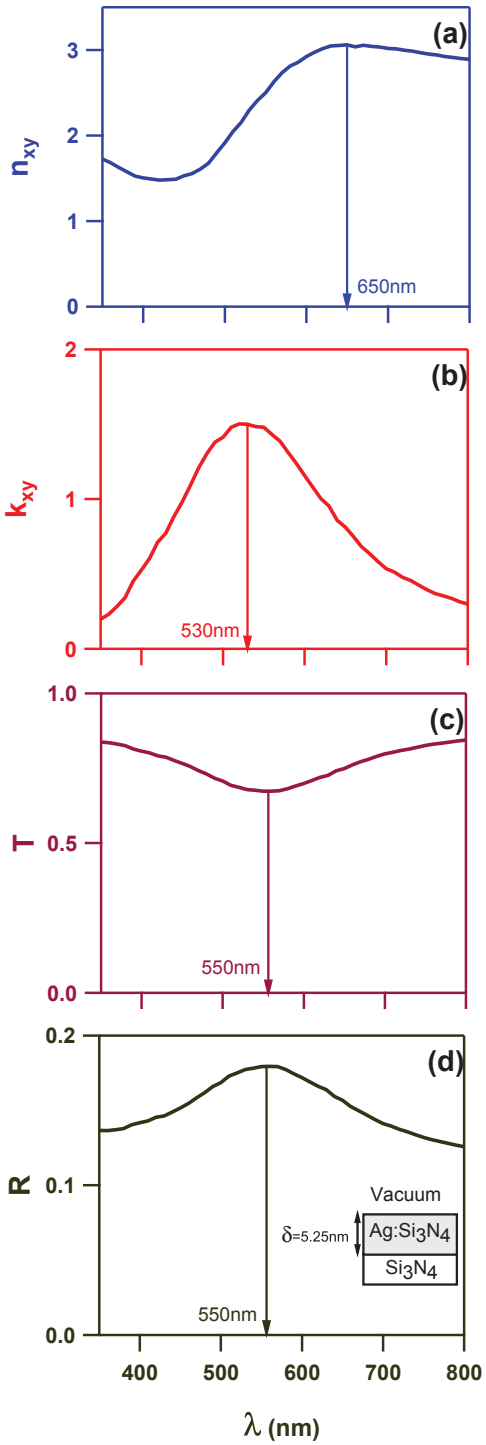

Figure II.10 – The effective in-plane n_{xy} (a) and k_{xy} (b) compared with corresponding transmittance T (c) and reflectance R (d) for a Ag:Si_3N_4 nanocomposite layer of thickness $\delta = 5.25$nm (schematics of which is shown in (d)) at normal incidence angle.

reflectance $\Delta R/R_0$ calculated at normal incidence assuming the same nanocomposite structure as in the Subsection 4.3.1 (Fig.II.10(d)). Even though both R and $\Delta R/R_0$ exhibit a maximum around 550nm, it can be seen that the relative reflectance enhances the signal dynamics. SDRS is therefore more convenient to detect weak modifications.

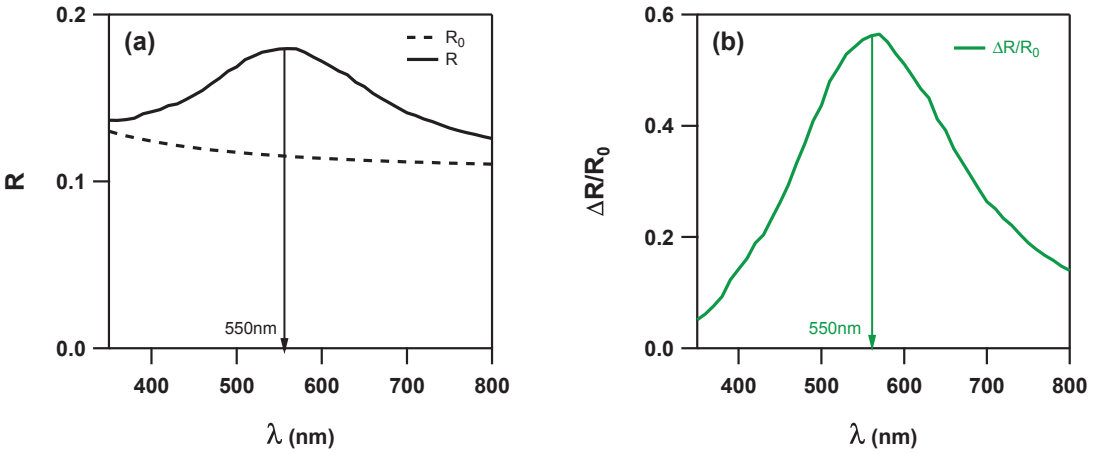

Figure II.11 – Comparison between the reflectance R (a) and relative reflectance $\Delta R/R_0$ (b) at normal incidence angle for a Ag:Si_3N_4 nanocomposite system (attention for the scale). The dashed curve in (a) represents the reflectance R_0 from the bare Si_3N_4 substrate.

4.3.3 Influence of incidence angle and polarization on ($\Delta R/R_0$)

The nanocomposite structure presented in Subsection 4.3.1 (Fig.II.10(d)) is composed of spheroidal nanoclusters with the sample normal as revolution axis. Such a nanocomposite layer is uniaxially anisotrope. For *s*-polarized light, only one SPR mode is visible as the excitation is in the plane of the layer. In Fig.II.12(a), it can be seen that the position of the maximum remains unaffected (550nm) at increasing incidence angles while its amplitude monotonously decreases. For *p*-polarized light[5], the variations with the incidence angle are more complex. At normal incidence, the signal is the same for both polarizations. However, it can be seen in Fig.II.12(b) that the signal amplitude increases with the incidence angle, due to the decrease of the reference reflectance R_0 up to the Si_3N_4 Brewster angle ($\approx 64°$) where $R_0 = 0$. For grazing incidence angles (Fig.II.12(c)), it is worth noting that the maximum around 550nm (with $\Delta R/R_0 > 0$) "becomes" a minimum around the same position (with $\Delta R/R_0 < 0$). However, a second mode appears around 385nm. Indeed, the light can be decomposed into one component in the layer plane and another one parallel to the sample normal. The anisotropy induces

[5]For *p*-polarized light in oblique incidence, the Fresnel coefficients are slightly different to those given in Section 1.1 of the Appendix in order to take into account the layer anisotropy

therefore the presence of two SPR modes: the "in-plane mode" due to k_{xy} and the "out-of-plane" mode due to k_z.

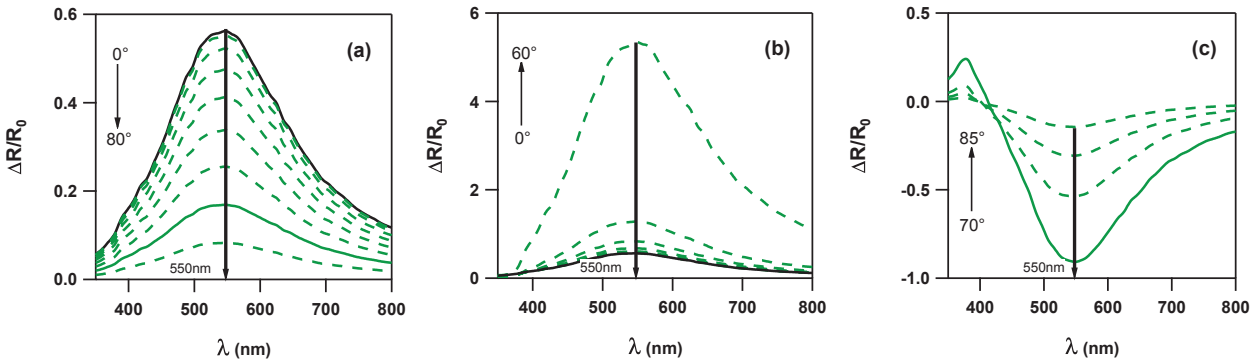

Figure II.12 – Effect of the incidence angle on the simulated $\Delta R/R_0$ for, (a) *s*-polarized light (from 0° to 80°, every 10°), (b) *p*-polarized light (from 0° to 60°, every 10°), and (c) *p*-polarized light (from 70° to 85°, every 5°). The black curves and the continuous green curves represent the simulations at normal incidence (0°) and at 70° (as fixed in our experiments), respectively. (Attention for scale).

In this work, we will limit ourselves to *s*-polarized light measurements, and therefore to the exploration of the SPR in-plane mode.

4.4 Limitations of the optical simulations

As described previously (Subsection 4.1 of the present Chapter), the optical simulations can help us to qualitatively interpret the modifications in the nanocluster morphology or surrounding. Nevertheless, some limitations of the optical models make difficult to perform a quantitative analysis by using only optical means. These restrictions are not only due to some of the limitations of the Yamaguchi effective medium model, but also due to some simplified assumptions (e.g. the nanoclusters are assumed to be identical and spheroidal).

4.4.1 Restriction to the diluted medium

Like most of the effective medium models, the Yamaguchi model [83] is restricted to weakly interacting nanoclusters within the dipolar approximation. Hence it fails to simulate strong inter-cluster interactions at the limit of the percolation regime when cluster shapes are not well defined. Actually, such concentrated systems have been treated mainly in the framework of renormalization theories [85].

4.4.2 Limitation due to the image dipole approximation

In the case of nanoclusters supported on a substrate, the influence of the substrate is taken into account in the Yamaguchi model by image dipole effects, which fail in reproducing the strong cluster-substrate interaction. Fedotov *et al* [86] extended the Yamaguchi model by considering the multipole orders. However, both the Yamaguchi and Fedotov models consider that the nanocluster polarizabilities obey the Laplace equation in a homogeneous medium, despite of the discontinuity at the interface. These problems were solved by Bedeaux & Vlieger [87], whose model permitted a more realistic description of the nanocluster-substrate interaction involving multipole orders and allowed calculations in the case of monodisperse truncated spheroidal nanoclusters. Simulations with this model can be performed with the freely available software GranFilm developed by R. Lazzari and I. Simonsen [88, 89].

It is worth noting that the Bedeaux & Vlieger model [87] is not an effective medium theory. Therefore, it is not possible to compare the effective dielectric functions, but directly the reflectances given by the different models. As an illustration, we calculate $\Delta R/R_0$ for Ag spheroidal nanoclusters on a Si_3N_4 substrate (Fig.II.13(a-c)) with the Yamaguchi, Fedotov, and Bedeaux & Vlieger models (the last one with the help of Granfilm [88]). Simulations are performed for a *s*-polarized light assuming different H/D values (i.e. 1, 0.75, and 0.5, while other parameters are similar to those of Table II.3). The differences between the different models are obvious especially for very oblate nanoclusters (H/D=0.5). In this case, the maximum position $\lambda_{\max}$ is 450nm, 420nm, and 410nm for Yamaguchi, Fedotov, and Bedeaux & Vlieger, respectively.

4.4.3 Restriction to spheroidal and identical nanoclusters

We have already shown that the optical response (especially the SPR wavelength) is very sensitive to the mean shape in the case of identical spheroidal nanoclusters with the Yamaguchi model. The same conclusion could be drawn by considering other nanocluster shapes. As a striking example, we compare in Fig.II.14 the $\Delta R/R_0$ values given by the Bedeaux & Vlieger model (calculated by Granfilm [88]) for spheroidal nanoclusters with $D = 7$nm and $H = 3.5$nm and for hemispherical nanoclusters with radius $R = 3.5$nm. Each individual nanocluster has the same aspect ratio $H/D = 0.5$, the same volume ($V = \frac{\pi D^3}{12}$), and the in-plane projection gives the same disk of diameter D. Despite these strong similarities, the optical responses are very different with $\lambda_{\max} = 410$nm for ellipsoidal nanoclusters and $\lambda_{\max} = 530$nm for hemispherical nanoclusters.

Another study conducted by Toudert *et al* [18] extended the Yamaguchi model to the case of

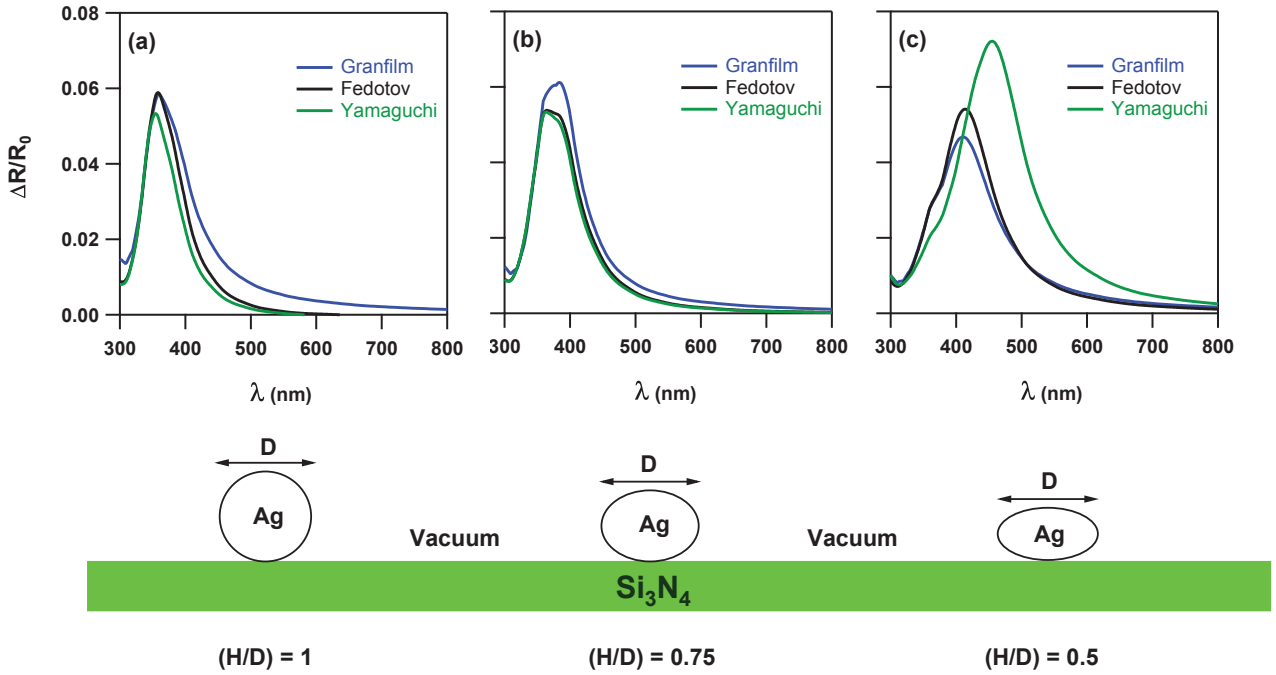

Figure II.13 – Simulations of $\Delta R/R_0$ (for *s*-polarized light and at an incidence angle = 70°) in case of Ag spheroidal nanoclusters supported on Si_3N_4 substrate in vacuum, with different values of H/D ((a) 1, (b) 0.75, and (c) 0.5), by using Yamaguchi, Fedotov, and Bedeaux & Vlieger models.

ellipsoidal nanoclusters embedded in a dielectric matrix (substrate effects can therefore be ruled out) by taking into account the distribution in orientation, size, and shape of the nanoclusters. The broadening of the size and shape distributions - for given mean size and shape - induces a weak shift and a broadening of the absorption band compared to the monodisperse case. By comparing spheroidal and ellipsoidal nanoclusters, this study also confirms that the spectral position of the SPR is mainly governed by the average cluster shape. As it is difficult to know the exact shapes of the nanoclusters and their dispersion, the SPR wavelength cannot be used as a quantitative characterization of the mean shape. This is the reason why, in further chapters, we will use the optical simulations as a qualitative measurement in order to detect nanostructural variations, particularly in the nanocluster morphology.

5 Summary and conclusions

In this chapter, the optical properties of the metals in the form of their complex refractive index $(n + ik)$ are explored, which are interestingly different in their bulk and nanocluster form. Especially in case of metal nanoclusters, the optical response is dominated by surface

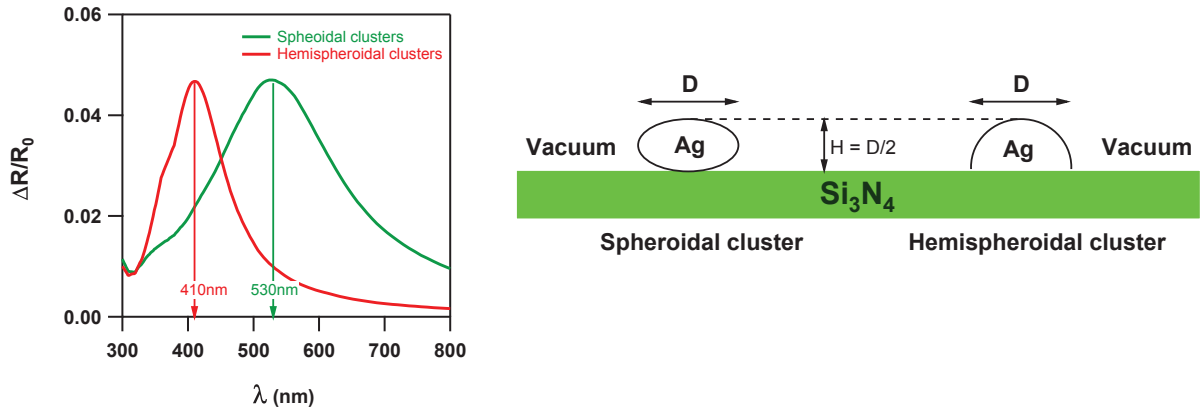

Figure II.14 – Simulations of $\Delta R/R_0$ (for *s*-polarized light and at an incidence angle = 70°) in case of Ag spheroidal nanoclusters surrounded by vacuum on a Si_3N_4 substrate with ellipsoidal or hemispherical shape.

plasmon resonance (SPR), and is sensitive to their nanostructure parameters as well as their surrounding medium. Owing to these features, the effect of different nanocluster parameters (such as, size, shape, and organization) on the simulated optical responses are studied with the help of the Yamaguchi model. Even though this model does not serve us on quantitative basis perfectly, it is nevertheless qualitatively interesting to follow the behavior of the optical signals for understanding the influence of the different parameters. With these simulations it was found that, other than the metal type and refractive index of the surrounding dielectric matrix, the amplitude and position of the SPR are extremely sensitive to the size and shape of the metal clusters, respectively, while, the organizational parameters (areal density or inter-cluster distance) show weak influence. This information will help us to understand the optical variations detected during the optical measurements.

In practical cases, on the other hand, such optical properties of the materials can be studied indirectly with the help of optical characterization techniques in reflection or transmission mode as they offer sensitive and efficient optical measurements, even in real-time. In this regard, in our work, we have implemented an *in situ* and real-time surface differential reflectance spectroscopy (SDRS), which studies the optical properties of the materials in the form of the relative variation in the reflectance ($\Delta R/R_0$), for metal nanoclusters which are surrounded by a dielectric matrix.

Bibliography

[1] E. D. Palik. *Handbook of Optical Constants of Solids*. Academic Press-New York (1985). 30

[2] P. B. Johnson and R. W. Christy. *Optical constants of the noble metals*. Physical Review B **6**, 4370–4379 (1972). 30

[3] P. Winsemius, F. F. v. Kampen, H. P. Lengkeek, and C. G. v. Went. *Temperature dependence of the optical properties of Au, Ag and Cu*. Journal of Physics F: Metal Physics **6**, 1583 (1976). 30

[4] P. Drude. *Zur Elektronentheorie der Metalle*. Annalen der Physik **306**, 566–613 (1900). 30

[5] U. Kreibig and M. Vollmer. *Optical Properties of Metal Clusters*. Springer-Verlag, Berlin (1995). 30, 31, 42, 44

[6] P. G. Etchegoin, E. C. Le Ru, and M. Meyer. *An analytic model for the optical properties of gold*. Journal of Chemical Physics **125**, 164705 (2006). 30

[7] G. Mie. *Beiträge zur Optik trüber Medien, speziell kolloidaler Metallösungen*. Annalen der Physik **3**, 377–445 (1908). 31, 42

[8] R. M. A. Azzam and N. M. Bashara. *Ellipsometry and polarized light*. North Holland Publication Company (1977). 33

[9] F. Abeles. *La theorie generale des couches minces*. Le journal de physique et le radium **11**, 307–310 (1950). 33

[10] L. Simonot, D. Babonneau, S. Camelio, D. Lantiat, P. Guérin, B. Lamongie, and V. Antad. *In-situ optical spectroscopy during deposition of Ag:Si_3N_4 nanocomposite films by magnetron sputtering*. Thin Solid Films **518**, 2637–2643 (2010). 34, 38

[11] J. T. Zettler. *Characterization of epitaxial semiconductor growth by reflectance anisotropy spectroscopy and ellipsometry.* Prog. Crystal Growth and Charact. **35**, 27–98 (1997). 34

[12] I. Herman. *Optical diagnostics for thin film processing.* Academic Press Limited (1996). 34, 35, 36

[13] T. W. H. Oates, L. Ryves, and M. M. M. Bilek. *Dielectric functions of a growing silver film determined using dynamic in situ spectroscopic ellipsometry.* Optics Express **16**, 2302–2314 (2008). 34, 36

[14] T. Tsuru and M. Yamamoto. *In-situ ellipsometric monitor with layer-by-layer analysis for precise thickness control of EUV multilayer optics.* Thin Solid Films **515**, 947–951 (2006). 34, 36

[15] C. Buzea and K. Robbie. *State of the art in thin film thickness and deposition rate monitoring sensors.* Reports on Progress in Physics **68**, 385–409 (2005). 34, 36

[16] C. Liu, J. Erdmann, and A. Macrander. *In situ spectroscopic ellipsometry as a surface-sensitive tool to probe thin film growth.* Thin Solid Films **355-356**, 41–48 (1999). 34, 35, 36

[17] N. Dietz. *Real-time optical characterization of thin film growth.* Materials Science and Engineering B **87**, 1–22 (2001). 34, 35

[18] J. Toudert, D. Babonneau, L. Simonot, S. Camelio, and T. Girardeau. *Quantitative modelling of the surface plasmon resonances of metal nanoclusters sandwiched between dielectric layers: The influence of nanocluster size, shape and organization.* Nanotechnology **19**, 125709 (2008). 35, 53

[19] L. Kipp, D. K. Biegelsen, J. E. Northrup, L. E. Swartz, and R. D. Bringans. *Reflectance difference spectroscopy: Experiment and theory for the model system Si(001):As and application to Si(001).* Physical Review Letters **76**, 15 (1996). 35

[20] R. E. Balderas-Navarroa, K. Hingerl, D. Stifter, A. Bonanni, and H. Sitter. *Reflectance difference spectroscopy during CdTe/ZnTe interface formation.* Applied Surface Science **190**, 307–310 (2002). 35

[21] E. Colas, D. E. Aspnes, R. Bhat, A. A. Studna, M. A. Koza, and V. G. Keramidas. *Reflectance-difference studies of organometallic chemical-vapor-deposition growth transients on (001) GaAs.* Journal of Crystal Growth **94**, 613–618 (1989). 35

[22] C. Kaspari, M. Pristovsek, and W. Richter. *Homoepitaxial growth rate measurement using in situ reflectance anisotropy spectroscopy.* Journal of Crystal Growth **298**, 46–49 (2007). 35, 36

[23] V. G. Bordo and H. G. Rubahn. *Optics and Spectroscopy at Surfaces and Interfaces.* WILEY-VCH-Weinheim (2005). 35, 36

[24] M. Palummo, N. Witkowski, O. Pluchery, R. Del Sole, and Y. Borensztein. *Reflectance-anisotropy spectroscopy and surface differential reflectance spectra at the Si(100) surface: Combined experimental and theoretical study.* Physical Review B - Condensed Matter and Materials Physics **79**, 035327 (2009). 35

[25] K. Gaàl-Nagy, A. Incze, G. Onida, Y. Borensztein, N. Witkowski, O. Pluchery, F. Fuchs, F. Bechstedt, and R. Del Sole. *Optical spectra and microscopic structure of the oxidized Si(100) surface: Combined in situ optical experiments and first principles calculations.* Physical Review B - Condensed Matter and Materials Physics **79**, 045312 (2009). 35

[26] S. D. Silaghi and D. R. T. Zahn. *Monitoring the ordering in biomolecular films on vicinal silicon surfaces by reflectance difference/anisotropy spectroscopy.* Applied Surface Science **252**, 5462–5465 (2006). 35

[27] P. Weightman. *The potential of reflection anisotropy spectroscopy as a probe of molecular assembly on metal surfaces.* Physica Status Solidi (A) Applied Research **188**, 1443–1453 (2001). 35

[28] P. Weightman, D. S. Martin, R. J. Cole, and T. Farrell. *Reflection anisotropy spectroscopy.* Reports on Progress in Physics **68**, 1251–1341 (2005). 35, 36

[29] D. E. Aspnes and N. Dietz. *Optical approaches for controlling epitaxial growth.* Applied Surface Science **130-132**, 367–376 (1998). 35

[30] D. E. Aspnes. *Observation and analysis of epitaxial growth with reflectance-difference spectroscopy.* Materials Science and Engineering B **30**, 109–119 (1995). 35

[31] D. E. Aspnes. *Real-time optical diagnostics for epitaxial growth.* Surface Science **307-309**, 1017–1027 (1994). 35

[32] D. E. Aspnes and A. A. Studna. *Anisotropies in the above-band-gap optical spectra of cubic semiconductors.* Physical Review Letters **54**, 17 (1985). 35

[33] S. Ohno, J. Takizawa, J. Koizumi, F. Mitobe, R. Tamegai, T. Suzuki, K. Shudo, and M. Tanaka. *Real-time observation of electron-stimulated effects on Si(001)-(2 × 1) by optical reflectance spectroscopic methods.* Journal of Physics Condensed Matter **19**, 446008 (2007). 36, 38, 39

[34] G. Chiarotti, P. Chiaradia, F. Arciprete, and C. Goletti. *Sum rules in surface differential reflectivity and reflectance anisotropy spectroscopies.* Applied Surface Science **175-176**, 777–782 (2001). 36, 39

[35] R. Lazzari, S. Roux, I. Simonsen, J. Jupille, D. Bedeaux, and J. Vlieger. *Multipolar plasmon resonances in supported silver particles: The case of Ag/α-Al_2O_3(0001).* Physical Review B - Condensed Matter and Materials Physics **65**, 2354241–23542413 (2002). 36, 38, 39, 40

[36] Y. Borensztein, O. Pluchery, , and N. Witkowski. *Probing the Si-Si dimer breaking of Si(100) 2×1 surfaces upon molecule adsorption by optical spectroscopy.* Physical Review Letters **95**, 1–4 (2005). 38, 39

[37] Y. Borensztein, T. Lopez-Rios, and G. Vuye. *Roughness induced at Si(111) surfaces by high temperature heating.* Applied Surface Science **41-42**, 439–442 (1989). 38, 39

[38] M. Roy and Y. Borensztein. *Optical study of potassium growth on the Si(100) surface.* Applied Surface Science **104-105**, 147–151 (1996). 38, 39

[39] M. Roy, C. Beitia, Y. Borensztein, A. Shkrebtii, C. Noguez, and R. Del Sole. *Optical spectroscopy study of hydrogenation of the Si(111)-7×7 surface.* Applied Surface Science **104-105**, 158–162 (1996). 38, 39

[40] M. Roy and Y. Borensztein. *Hydrogen adsorption on Si surfaces studied by real-time surface reflectance spectroscopy.* Surface Science **331-333**, 453–457 (1996). 38, 39

[41] S. Ohno, J. Takizawa, J. Koizumi, K. Shudo, and M. Tanaka. *The temperature dependence of monolayer oxidation on Si(001)-(2×1) studied with surface differential reflectance spectroscopy.* Journal of Physics Condensed Matter **19**, 446011 (2007). 38, 39

[42] C. Goletti, G. Bussetti, P. Chiaradia, and G. Chiarotti. *Optical transitions and sum rules at clean semiconductor surfaces.* Journal of Physics Condensed Matter **16**, S4289–S4300 (2004). 38, 39

[43] S. Selci, A. Cricenti, A. C. Felici, L. Ferrari, C. Goletti, and G. Chiarotti. *Oxygen chemisorption on cleaved InP(110) surfaces studied with surface differential reflectivity.* Physical Review B **43**, 6757–6759 (1991). 38, 39

[44] S. Selci, F. Ciccacci, A. Cricenti, A. C. Felici, C. Goletti, and P. Chiaradia. *Polarization dependence of optical transitions in GaP(110) and GaAs(110) surfaces studied with surface differential reflectivity.* Solid State Communications **62**, 833–834 (1987). 38, 39

[45] H. Proehl, R. Nitsche, T. Dienel, K. Leo, and T. Fritz. *In situ differential reflectance spectroscopy of thin crystalline films of ptcda on different substrates.* Physical Review B **71**, 165207 (2005). 38, 39

[46] R. Forker, C. Golnik, G. Pizzi, T. Dienel, and T. Fritz. *Optical absorption spectra of ultrathin PTCDA films on gold single crystals: Charge transfer beyond the first*

monolayer. Organic Electronics: physics, materials, applications **10**, 1448–1453 (2009). 38, 39

[47] R. Forker and T. Fritz. *Optical differential reflectance spectroscopy of ultrathin epitaxial organic films*. Physical Chemistry Chemical Physics **11**, 2142–2155 (2009). 38, 39

[48] A. S. Gouralnik, N. G. Galkin, D. L. Goroshko, S. A. Dotsenko, A. A. Alekseev, and V. A. Ivanov. *Growth and magnetic properties of the sandwich structure Fe/magnetic silicide/Si(100) obtained from in situ optic and magneto-optic data*. Solid State Communications **149**, 1292–1295 (2009). 38, 39

[49] D. L. Goroshko, N. G. Galkin, D. V. Fomin, A. S. Gouralnik, and S. V. Vavanova. *An investigation of the electrical and optical properties of thin iron layers grown on the epitaxial Si(111)-(2×2)-Fe phase and on an Si(111)7×7 surface*. Journal of Physics Condensed Matter **21**, 435801 (2009). 38, 39

[50] S. A. Dotsenko, N. G. Galkin, A. S. Gouralnik, and L. V. Koval. *In situ differential reflectance spectroscopy study of early stages of β-$FeSi_2$ silicide formation*. e-Journal of Surface Science and Nanotechnology **3**, 113–119 (2005). 38, 39

[51] S. A. Dotsenk, N. G. Galkin, and L. V. Koval. *Optical properties of magic clusters formed in both reactive and non-reactive systems*. e-Journal of Surface Science and Nanotechnology **4**, 650–655 (2006). 38, 39

[52] A. Cricenti, S. Selci, A. C. Felici, L. Ferrari, A. Gavrilovich, C. Goletti, and G. Chiarotti. *Polarized surface differential reflectivity and oxygen chemisorption on InP(110) surfaces*. Surface Science **251-252**, 281–285 (1991). 39

[53] M. De Crescenzi, T. Lopez-Rios, G. Vuye, N. J. Mansur, and Y. Borensztein. *The reflectance spectroscopy of silver surface layers on gold and aluminium substrates*. Thin Solid Films **57**, 89–92 (1979). 38, 39

[54] T. Lopez-Rios, M. De Crescenzi, and Y. Borensztein. *Contribution of longitudinal polarization waves to the optical properties of Ag surface layers*. Solid State Communications **30**, 755–760 (1979). 38, 39

[55] Y. Borensztein and F. Abelés. *Surface reflectance spectroscopy: Its application to the study of very thin films*. Thin Solid Films **125**, 129–142 (1985). 38, 39

[56] Y. Borensztein, T. Lopez-Rios, and G. Vuye. *Electronic properties of copper and silver adsorbates on metallic surfaces, studied by surface reflectance spectroscopy*. Journal de Physique (Paris), Colloque pages 455–459 (1984). 38, 39

[57] Y. Borensztein. *The growth of palladium on (111) polycrystalline silver surface*. Surface Science **177**, 353–362 (1986). 38, 39

[58] Y. Borensztein, R. Alameh, T. Lopez-Rios, and W. Q. Zheng. *Optical study of Ag overlayers deposited on Si(111)-7×7 as a function of temperature.* Vacuum **41**, 684–686 (1990). 38, 39

[59] C. Beitia, Y. Borensztein, R. G. Barrera, C. E. Romàn-Velàzquez, and C. Noguez. *Multipolar plasma resonances in supported alkali-metal nanoparticles.* Physica B: Condensed Matter **279**, 25–28 (2000). 38, 39

[60] C. Beitia and Y. Borensztein. *Formation and stability of small particles of potassium studied by real-time surface differential reflectance.* Surface Science **402-404**, 445–449 (1998). 38, 39

[61] D. Martin, J. Jupille, and Y. Borensztein. *Silver particle sizes and shapes as determined during a deposit by in situ surface differential reflectance.* Surface Science **402-404**, 433–436 (1998). 38, 39

[62] D. Martin, F. Creuzet, J. Jupille, Y. Borensztein, and P. Gadenne. *2D and 3D silver adlayers on TiO_2 (110) surfaces.* Surface Science. **377-379**, 958–962 (1997). 38, 39

[63] R. Lazzari and J. Jupille. *Wetting and interfacial chemistry of metallic films on the hydroxylated α-Al_2O_3(0001) surface.* Physical Review B - Condensed Matter and Materials Physics **71**, 1–13 (2005). 38, 39, 40, 41

[64] R. Lazzari, I. Simonsen, D. Bedeaux, J. Vlieger, and J. Jupille. *Polarizability of truncated spheroidal particles supported by a substrate: Model and applications.* European Physical Journal B **24**, 267–284 (2001). 38, 39

[65] R. Lazzari, J. Jupille, and Y. Borensztein. *In situ study of a thin metal film by optical means.* Applied Surface Science **142**, 451–454 (1999). 38, 39

[66] R. Lazzari, G. Renaud, C. Revenant, J. Jupille, and Y. Borensztein. *Adhesion of growing nanoparticles at a glance: Surface differential reflectivity spectroscopy and grazing incidence small angle X-ray scattering.* Physical Review B **79**, 125428 (2009). 38, 39, 40

[67] R. Lazzari and J. Jupille. *Silver layers on oxide surfaces: Morphology and optical properties.* Surface Science **482-485**, 823–828 (2001). 38, 39

[68] R. Lazzari, I. Simonsen, and J. Jupille. *Onset of charge localisation on coupling multipolar absorption modes in supported metal particles.* Europhysics Letters **61**, 541–546 (2003). 38, 39

[69] Y. Borensztein, L. Delannoy, A. Djedidi, R. G. Barrera, and C. Louis. *Monitoring of the plasmon resonance of gold nanoparticles in Au/TiO_2 catalyst under oxidative and reducing atmospheres.* Journal of Physical Chemistry C **114**, 9008–9021 (2010). 38, 39, 40, 41

[70] A. Clebsch. *Über die reflexion an einer kugefäche.* Journal für Mathematik **61**, 195–262 (1863). 42

[71] L. Lorenz. *Lysbevaegelsen i og uden for en af plane lysbolger belyst kugle.* Det Kongelige Danske Videnskabernes Selskabs Skrifter **6**, 1–62 (1890). 42

[72] W. Hergert and T. Wriedt. Mie theory 1908-2008: Present developments and interdisciplinary aspects of light scattering. Universität Bremen, Bremen 2008, Martin Luther University Halle -Wittenberg, Halle, Germany., (2008). 42

[73] B. T. Draine and P. J. Flatau. *Discrete-dipole approximation for scattering calculations.* Journal of Optical Society of America A **11**, 1491–1499 (1994). 42

[74] K. L. Kelly, E. Coronado, L. L. Zhao, and G. C. Schatz. *The optical properties of metal nanoparticles: The influence of size, shape, and dielectric environment.* Journal of Physical Chemistry B **107**, 668–667 (2003). 42

[75] J. Lermi, B. Palpant, B. Prével, E. Cottancin, M. Pellarin, M. Treilleux, J. L. Vialle, A. Perez, and M. Broyer. *Optical properties of gold metal clusters: A time-dependent local-density-approximation investigation.* The European Physical Journal D **4**, 95–108 (1998). 42

[76] D. Bergman and O. Levy. *Critical bevhavior of the weakly nonlinear conductivity and flicker noise of two-component composites.* Physical Review B **50**, 3652–3660 (1994). 42

[77] J. C. Maxwell-Garnett. *Colours in metal glasses and in metallic films.* Phil. Trans. R. Soc. Lond. A **203**, 385–420 (1904). 42

[78] M. A. Garcia, J. Llopis, and S. E. Paje. *A simple model for evaluating the optical absorption spectrum from small Au-colloids in sol-gel films.* Chemical Physics Letters **315**, 313–320 (1999). 42

[79] D. A. G. Bruggeman. *Berechnung der elastischen moduln für die verschiedenen texturen der regulären metalle.* Zeitschrift für Physik A Hadrons and Nuclei **92**, 561–588 (1934). 42

[80] J. Toudert, D. Babonneau, S. Camelio, T. Girardeau, F. Yubero, J. P. Espinòs, and A. R. Gonzalez-Elipe. *Using ion beams to tune the nanostructure and optical response of co-deposited Ag:BN thin films.* Journal of Physics D: Applied Physics **40**, 4614–4620 (2007). 42

[81] M. Gilliot, A. E. Naciri, and L. Johann. *Optical anisotropy of shaped oriented cobalt nanoparticles by generalized spectroscopic ellipsometry.* Physical Review B **76**, 045424 (2007). 42

[82] C. G. Granqvist and O. Hunderi. *Optical properties of Ag-SiO_2 cermet films: A comparison of effective-medium theories.* Physical Review B **18**, 2897–2906 (1978). 42

[83] T. Yamaguchi, S. Yoshida, and A. Kinbara. *Optical effects of the substrate on the anomalous properties of aggregated silver films.* Thin Solid films **21**, 173–187 (1974). 42, 52

[84] U. Kreibig and L. Genzel. *Optical absorption of small metallic particles.* Surface Science **156**, 678–700 (1985). 44

[85] P. Gadenne, Y. Yagil, and G. Deutscher. *Transmittance and reflectance in situ measurements of semicontinuous gold films during deposition.* Journal of Applied Physics **66**, 3019–3025 (1989). 52

[86] V. A. Fedotov, V. I. Emelyanov, K. F. MacDonald, and N. I. Zheludev. *Optical properties of closely packed nanoparticle films: Spheroids and nanoshells.* Journal of Optics A: Pure and Applied Optics **6**, 155–160 (2004). 53

[87] D. Bedeaux and J. Vlieger. *Optical properties of surfaces.* Imperial College Press-London (2004). 53

[88] R. Lazzari and I. Simonsena. *GRANFILM: a software for calculating thin-layer dielectric properties and Fresnel coefficients.* Thin Solid Films **419**, 124–136 (2002). 53

[89] http://ln-www.insp.upmc.fr/axe4/oxydes/granfilm/granularfilm.html. 53

Chapter III

Monitoring the optical properties of materials during their deposition

1 Introduction

In the previous chapter, the operation and the utility of real-time SDRS in studying the optical properties of different materials have been discussed. This chapter, in particular, will describe the specific usage of real-time SDRS during the depositions of a dielectric material (Si_3N_4) and noble metals (such as, Ag, Au, and Cu) along with nanocomposites made up of noble metal nanoclusters (Ag or Au) and Si_3N_4. In this regard, first, the optical properties of a transparent (cluster-free) Si_3N_4 layer are studied in detail. Then, a detailed analysis of noble metal optical responses are discussed, which reveals their optical properties right from their nanometric form to the formation of a thick opaque layer (bulk form). Finally, we will focus on the optical properties of tri-layer nanocomposites obtained by alternate deposition of Si_3N_4:Ag:Si_3N_4 or Si_3N_4:Au:Si_3N_4 materials, respectively.

2 Deposition of dielectric material (Si_3N_4)

Silicon nitride (Si_3N_4) is a dielectric ceramic material with excellent thermal stability, remarkable oxidation resistance, and good mechanical properties [1–5]. Moreover, it is chemically inert and transparent in the visible range ($k_{Si_3N_4} \approx 0$) with a high refractive index ($n_{Si_3N_4} \approx 2$) [6, 7]. All these characteristics make Si_3N_4 an ideal candidate for optoelectronic applications [1]. In our case, the fabrication of Si_3N_4 thin films using a magnetron sputtering system is easier comparing to oxide thin films (e.g. Al_2O_3, TiO_2 etc) and is well studied over the years in our group, helping us to set precise deposition parameters for it.

As we have already discussed in chapter II (Section 4.2.2), the surrounding matrix has an

important effect on the optical properties of noble metal nanoclusters. On that basis, Si_3N_4 serves on two purposes: first, the encapsulation of the nanoclusters controls the refractive index of the surrounding medium that enhances the SPR; second, this encapsulation not only protects these clusters from the external environment such as from oxidation, chemical reactions, degradations etc, but also from aging processes [5, 8]. The aspect of encapsulation is important in order to increase the longevity of the nano-optoelectronic devices made up of noble metal nanoclusters because they are very sensitive to the external atmosphere even at room temperature and ambient conditions.

Hence, this section deals with the study of amorphous Si_3N_4 thin films fabricated by magnetron sputtering deposition and their optical properties using real-time SDRS.

2.1 Experimental details

During the fabrication of Si_3N_4 films on glass substrate, a Si_3N_4 target is sputtered using the radio frequency (RF) mode (at 13.56 MHz). The details of the experimental procedure and deposition parameters are given in Table III.1.

Deposition steps		Deposition time (s)	Magnetron power (W)	Ar flow (sccm)	N_2 flow (sccm)
Ignition of Ar^+	(a)	150	88 (RF)	90	–
plasma and	(b)	600	88 (RF)	3	–
Pre-sputtering	(c)	150	132 (RF)	3	0.3
of Si_3N_4	(d)	150	176 (RF)	3	0.3
Si_3N_4 sputtering		3600	176 (RF)	3	0.3

Table III.1 – Experimental procedure for the deposition of Si_3N_4. All steps are performed at 200°C.

Before the actual Si_3N_4 deposition on glass, the Si_3N_4 target is treated with different pre-sputtering steps. Pre-sputtering is an essential stage where the target surface of a material is "cleaned" using an Ar^+ plasma of sufficient energy, confined at the target. During this stage, the target material and the plasma are shuttered with a thin metallic flap to avoid actual deposition on the substrate. As this stage removes the foreign contaminations from the target surface, the later deposited thin film can be practically "contamination-free". Also, pre-sputtering steps allow us to increase the sputtering voltage step by step, so that we can avoid subjecting the dielectric Si_3N_4 target directly to a high voltage which results in large sudden stress and can risk in its breaking.

During the first step of the pre-sputtering, due to the sufficient magnetron power (88W) and high flux of Ar gas (90 sccm), an Ar^+ plasma is created in the vicinity of the Si_3N_4 target

surface. After sufficient time, the Ar^+ plasma kept 'switched ON' at a relatively smaller Ar flux of 3 sccm. In the next pre-sputtering stages, a small flux of N_2 gas (0.3 sccm) is introduced in the deposition chamber with a progressive increase in the magnetron power from 88W to 176W. This N_2 flux plays an important role in preserving the stoichiometry of the deposited Si_3N_4 layer. With the same configuration, at the end of the pre-sputtering stages, the actual deposition of Si_3N_4 starts as soon as the shutter over the target is opened.

During the Si_3N_4 deposition, the partial pressures for gases like Ar and N_2 are always maintained around 10^{-3} and 10^{-4} mbar, respectively, and the deposition was performed at 200°C during 3600s in order to form a relatively thick layer of Si_3N_4 on the glass substrate.

In this regard, the *post mortem* ellipsometry analysis determines the refractive index of this Si_3N_4 film approximated by a Cauchy's law as, $n_{Si_3N_4} = A + \frac{B}{\lambda^2}$ ($k_{Si_3N_4} \approx 0$), with $A = 1.96 \pm 0.02$ and $B = 2.0 \pm 0.5 \cdot 10^4$ nm^2 (Fig.II.1(a-b)). *Post mortem* ellipsometry, along with the X-ray reflectivity, also determines the thickness of the Si_3N_4 layer $\delta_{Si_3N_4}$, as 108 ± 8nm and 110 ± 6nm, respectively, corresponding to a deposition rate $\upsilon_{Si_3N_4}$ as 0.030 ± 0.002nm/s and 0.031 ± 0.002nm/s, respectively.

2.2 *In situ* and real-time SDRS observations

During the Si_3N_4 deposition, *in situ* and real-time SDRS measurements are done using a *s*-polarized polychromatic light to reveal the optical properties and the growth rate of the deposited Si_3N_4 layer (Fig.III.1). A *p*-polarized light in such conditions could be used, but will not be more sensitive than the *s*-polarized light as the refractive indices of the deposited material (Si_3N_4, $n \approx 2$) and the substrate (glass, $n \approx 1.5$), are relatively close to each other along with their Brewster's angles (∼64° and ∼56°, respectively).

As Si_3N_4 is non-absorbing in the visible range, the spectral variations seen in Fig.III.1 are due to the interferences between the successive light rays emerging from the deposited film, which arise from reflection and transmission effects at both air/film and film/substrate interfaces, along with the dephase created in between them during their traveling in the transparent thin layer. Fig.III.1 clearly shows the linear variation of the first wavelength maximum (black dashed line) and first wavelength minimum (white dashed line) with the Si_3N_4 deposition time/thickness. This linear variation can be verified by the calculation with the assumption of a continuous layer of thickness $\delta(t)$ ($= \upsilon_{Si_3N_4} \times t$, with $\upsilon_{Si_3N_4}$ and t being the deposition rate and deposition time, respectively), and refractive index n (considered as real and constant in

the visible range):

$$\begin{aligned} \lambda_{1st-max}(t) &= 4 \cdot \sqrt{n^2 - sin^2\theta} \cdot \delta(t) \\ \lambda_{1st-min}(t) &= 2 \cdot \sqrt{n^2 - sin^2\theta} \cdot \delta(t) \end{aligned} \tag{III.1}$$

By choosing $\theta = 70°$ due to the experimental configuration, $\upsilon_{Si_3N_4} = 0.03$nm/s, and $n = 2$, the calculations are in accordance with the measurements (dashed lines in Fig.III.1).

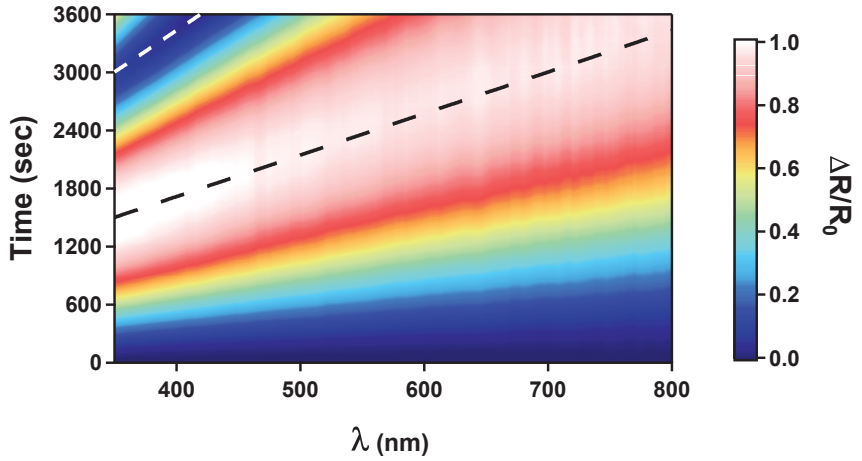

Figure III.1 – SDRS signal for a Si_3N_4 thick film during its deposition for 3600s as a function of wavelength (λ) and time (t). The black and white dashed lines show the linear shift of first maximum and first minimum of interference respectively during the deposition.

Moreover, approximating the Si_3N_4 refractive index by a Cauchy's law, it is possible from reflectance calculations [9] (see Section 1.1 of Appendix) to fit directly the SDRS data $\frac{\Delta R}{R_0}(t, \lambda)$ in the time range of 0-3600s and in the spectral range of 350-800nm by using Cauchy's parameters A, B, and $\upsilon_{Si_3N_4}$ as fitting parameters, thus yielding $A = 1.89 \pm 0.02$, $B = 2.2 \pm 0.2 \cdot 10^4$ nm^2, and $\upsilon_{Si_3N_4} = 0.033 \pm 0.001$nm/s. Using this information for the Si_3N_4 film, Fig.III.2 shows well simulated SDRS signals at different t in the visible range [10].

From onwards, in order to get the same optical properties of Si_3N_4, the experimental deposition parameters will be kept identical through out this work in order to standardize its optical properties.

3 Depositions of noble metals (Ag, Au, and Cu)

In case of noble metals, in contrast to Si_3N_4, the Volmer-Weber type growth leads to the formation of isolated 3D nanoclusters on the dielectric substrates from the beginning of their deposition [11, 12]. These nanoclusters, which exhibit the intrinsic characteristic phenomenon

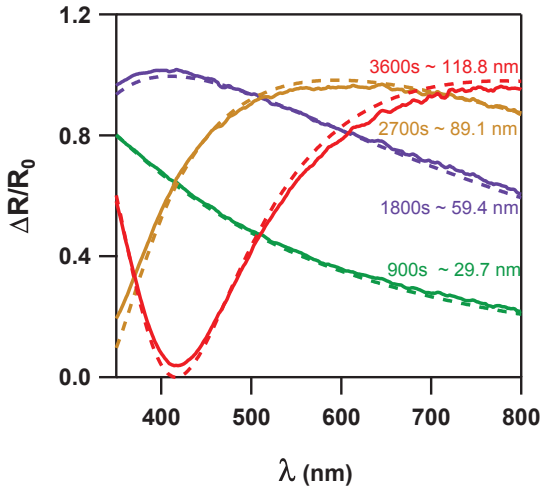

Figure III.2 – Spectral comparison between the SDRS measurements (solid lines) and simulations (dashed lines) during different Si_3N_4 deposition times/thicknesses.

known as surface plasmon resonance (SPR), induce a light absorption in the visible range [13]. Accordingly, depositions of noble metals, such as, Ag, Au, and Cu were studied with SDRS in order to reveal the primary growth stages using optical means. Moreover, the changes in the optical signals were studied with on going deposition, as the discontinuous nanocluster assemblies turn into continuous metallic layers. Finally, relatively thick metallic layers were formed, the optical properties of which resemble that of respective bulk metal.

3.1 Experimental procedure and real-time SDRS observations

Before addressing the optical properties of noble metals using *in situ* SDRS, it is important to see the experimental procedure with which the thick metallic films are deposited on the substrate using the magnetron sputtering technique. In contrast to Si_3N_4 deposition, the noble metals are deposited on the glass substrate using the DC sputtering mode. Nevertheless, before the actual deposition of these noble metals, pre-sputtering is carried out in order to make the metal target surface clean, while the shutter over the target is closed. Pre-sputtering for the noble metals is more direct than for Si_3N_4, and takes a shorter time. During the deposition, the substrate temperature is maintained at 200°C and the partial pressure of Ar is maintained around 10^{-3} mbar. Table III.2 shows the details of deposition parameters used during the sputtering for different metals that give rise to different deposition rates, confirmed by *post mortem* X-ray reflectivity measurements of continuous metal films.

Fig.III.3 shows the SDRS signals obtained during the deposition of thick layers of Ag, Au,

Metal type	Deposition time (s)	Magnetron power (W)	Ar flow (sccm)	Deposition rate (nm/s)
Ag	600	24 (DC)	18	0.10
Au	1000	17 (DC)	18	0.06
Cu	1000	46 (DC)	6	0.09

Table III.2 – Experimental procedure and deposition parameters used during the depositions of the noble metals at 200°C.

and Cu along with the spectral variations during the different deposition stages. These spectral variations can be ascribed to different growth regimes and can be explained with the scheme depicted in Fig.III.4 in case of Au.

3.1.1 3D growth of metal nanoclusters

In contrast to Si_3N_4, a small amount of metal on the substrate in the early deposition step produces a discontinuous thin film comprised of disconnected metal nanoclusters. This fact is evident for all the metals, as shown in Fig.III.3 and Fig.III.4. Here, non-overlapping of the experimental curves (solid curves) with the continuous layer simulation curves (dashed curves) supports the discontinuity in the deposited films. Moreover, the presence of a prominent maximum in the optical signals corresponds to the SPR phenomenon which is responsible for the absorption band in the visible range, verifying the Volmer-Weber type growth. [11–14].

In SDRS, we can define the maximum value of relative reflectivity as $(\Delta R/R_0)_{\max}$ at the corresponding wavelength $\lambda_{\max}$, as shown in Fig.III.5 in case of Ag clusters. These values can be presented as the amplitude and the position of the SDRS signal (black curve), respectively, which is fitted by using a log-normal function (red dotted curve) in a range of 100nm around the maximum of the experimental curve. As seen in Fig.III.3 and Fig.III.4, the increase of the metal deposition time/amount shifts the absorption band towards higher wavelengths (i.e. increment in the $\lambda_{\max}$) and increases $\Delta R/R_0$ progressively. It also causes the red-shift of the region of transparency (where $\Delta R/R_0 \approx 0$) during the early deposition period, which eventually vanishes with further deposition.

Besides, Fig.III.6 shows the SDRS signal measured for Ag, Au, and Cu after the deposition of a same effective thickness of 2nm, from which it is evident that the optical properties are strongly governed by the intrinsic properties of the metals.

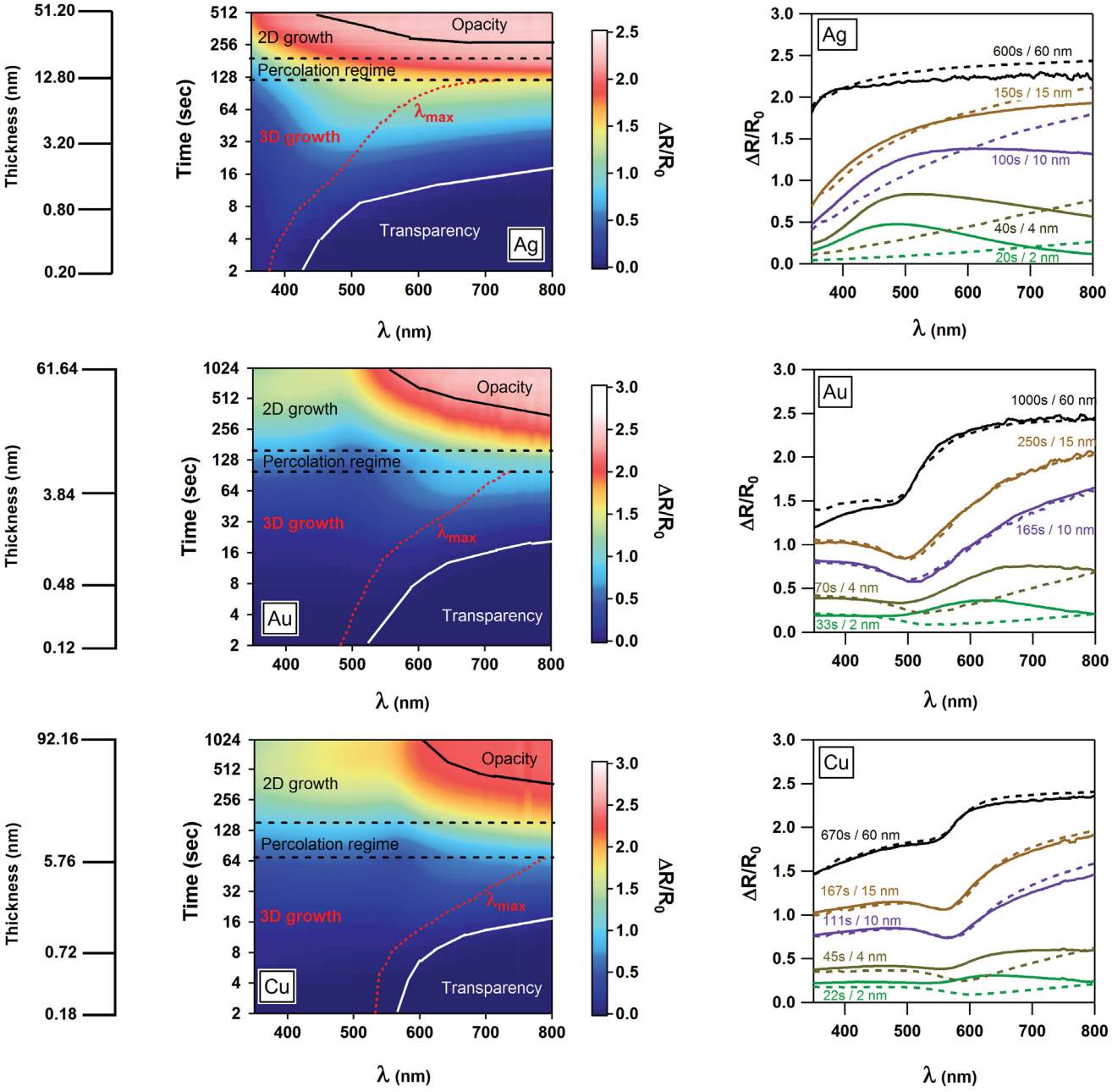

Figure III.3 – SDRS signals as a function of t and λ for the noble metal depositions (Ag, Au, and Cu, respectively) on the left hand side and their spectral variations (solid curves) for different deposition times/film thicknesses compared with continuous layer simulations (dashed curves) on right hand side.

Actually here, the relative reflectivity maximum follows the sequence,

$$\left(\frac{\Delta R}{R_0}\right)^{\mathrm{Ag}}_{\mathrm{max}} > \left(\frac{\Delta R}{R_0}\right)^{\mathrm{Au}}_{\mathrm{max}} > \left(\frac{\Delta R}{R_0}\right)^{\mathrm{Cu}}_{\mathrm{max}} \tag{III.2}$$

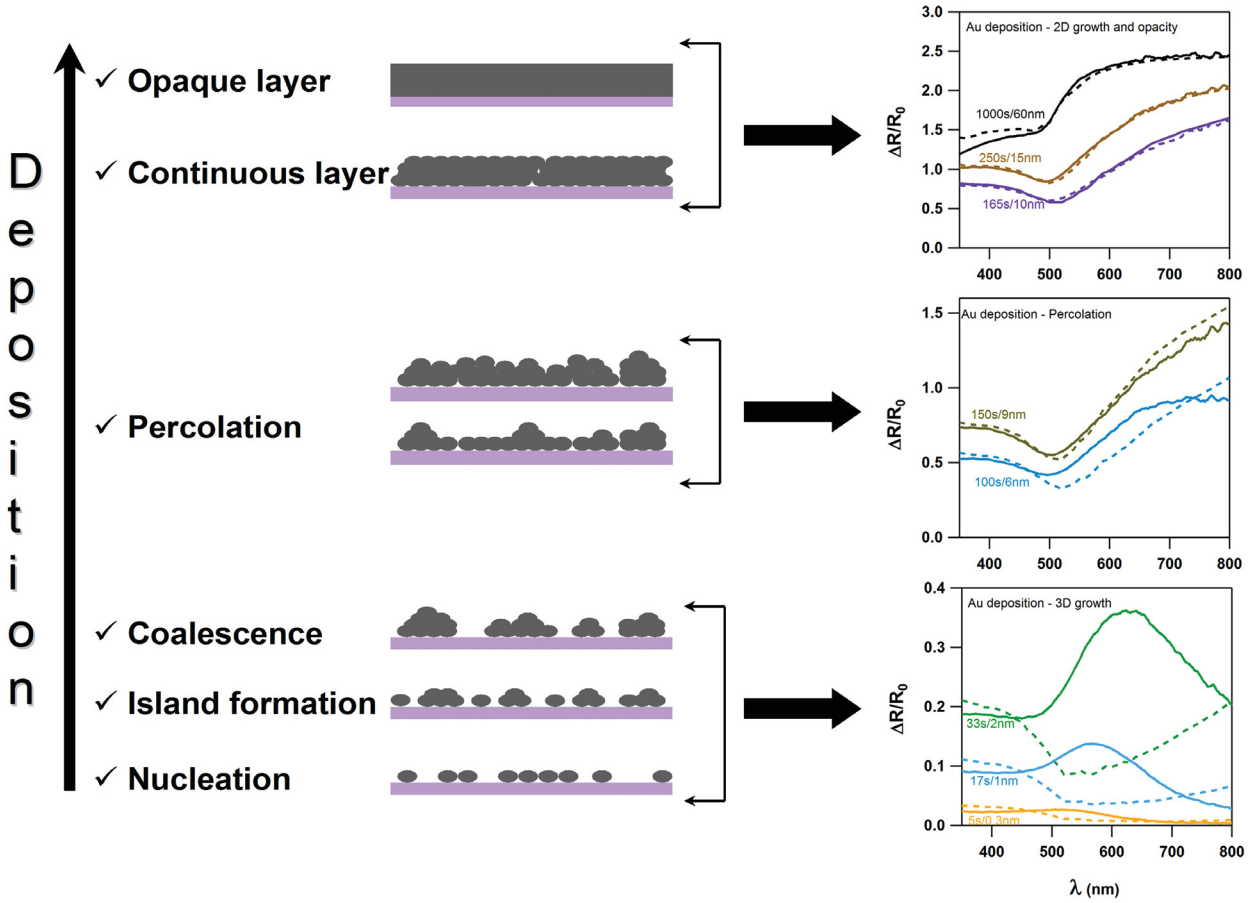

Figure III.4 – Typical schematics showing different growth regimes during the progressive metal deposition on substrate (left hand side), compared with optical measurements (solid lines) and continuous layer simulations (dashed lines) in case of Au deposition (right hand side) (attention for the scale).

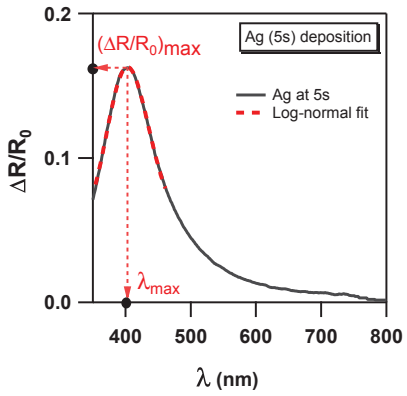

Figure III.5 – A typical SDRS absorption spectrum (black curve) during early Ag (5s) deposition, fitted with a log-normal function (red dotted curve) showing a maximum in the relative reflectivity $(\Delta R/R_0)_{\max}$ at a wavelength position of $\lambda_{\max}$.

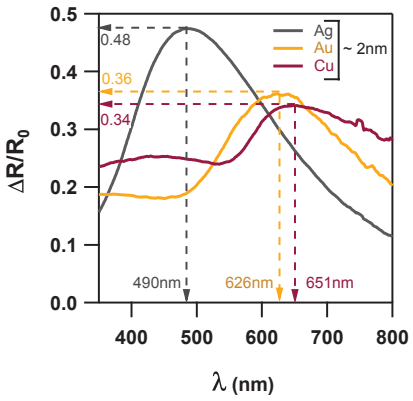

Figure III.6 – SDRS absorption spectra for metal nanoclusters after Ag(20s), Au(33s), and Cu(23s) depositions corresponding to an equivalent effective thickness of 2nm, showing their characteristic $(\Delta R/R_0)_{\max}$ at 0.48, 0.36, and 0.34, along with characteristic $\lambda_{\max}$ at 490nm, 626nm, and 651nm, respectively.

while, the wavelength position of the maximum follows,

$$(\lambda)^{\mathrm{Ag}}_{\max} < (\lambda)^{\mathrm{Au}}_{\max} < (\lambda)^{\mathrm{Cu}}_{\max} \tag{III.3}$$

This behavior was expected from the results presented in the previous chapter (Section 4.2.2, Fig.II.7(a-b), Chapter II), although the cluster size and shape effects cannot be ruled out here (Section 4.2.3, Fig.II.8(a-d), Chapter II). On the other hand, Fig.III.7 confirms that the Ag nanoclusters show a prominent SPR in the visible region, thus it acts as an ideal candidate for studying the optical properties for different effects such as cluster size, shape, and surrounding matrix. In case of Au and Cu, due to the presence of inter-band transitions in the visible range (Section 2.1.1, Fig.II.1(c-d), Chapter II), the presence of the SPR maximum is less obvious during the initial stages of deposition, whereas such inter-band transitions in Ag lie in the UV region, and hence they do not affect the SPR. Moreover, Ag nanoclusters provide a better perspective in studying their sensitivity towards different gases, e.g. for sensing type applications.

3.1.2 Percolation regime in noble metals

After the 3D growth regime, the later regimes can also be seen in Fig.III.3 and Fig.III.4 where, due to the on-going deposition, the growth eventually reaches to a certain limit and the nanoclusters form a percolated layer consisting of loosely connected metal nanoclusters [15, 16]. Here, as the SPR band starts vanishing, the optical curves start appearing flat without a distinct maximum. From Fig.III.8(a), we can see the non-perfect overlapping of the optical curves with the continuous layer simulation curves in the beginning, meaning that the continuous

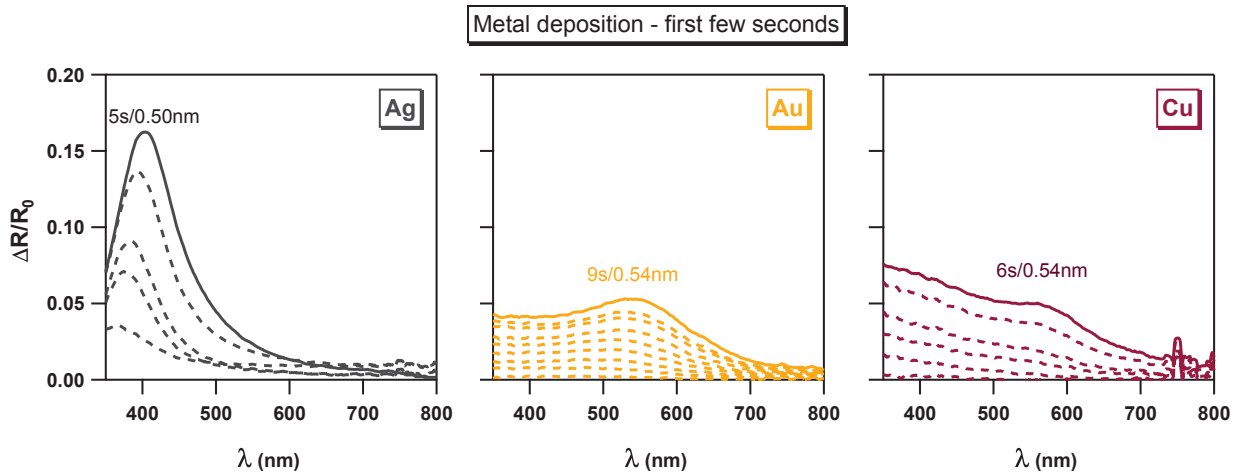

Figure III.7 – SDRS absorption spectra for metal nanoclusters of Ag, Au, and Cu at first few seconds of deposition (but corresponding to $\delta_{\text{metal}} < 0.6$nm) showing strong characteristic optical properties in the Ag clusters comparing to Au and Cu.

layer formation has not been achieved at this stage in all the metals. But later, with the ongoing deposition, the overlapping From Fig.III.8(b) of the experimental and continuous layer simulation curves can be seen, which demonstrates that the continuous layer regime is fast approaching.

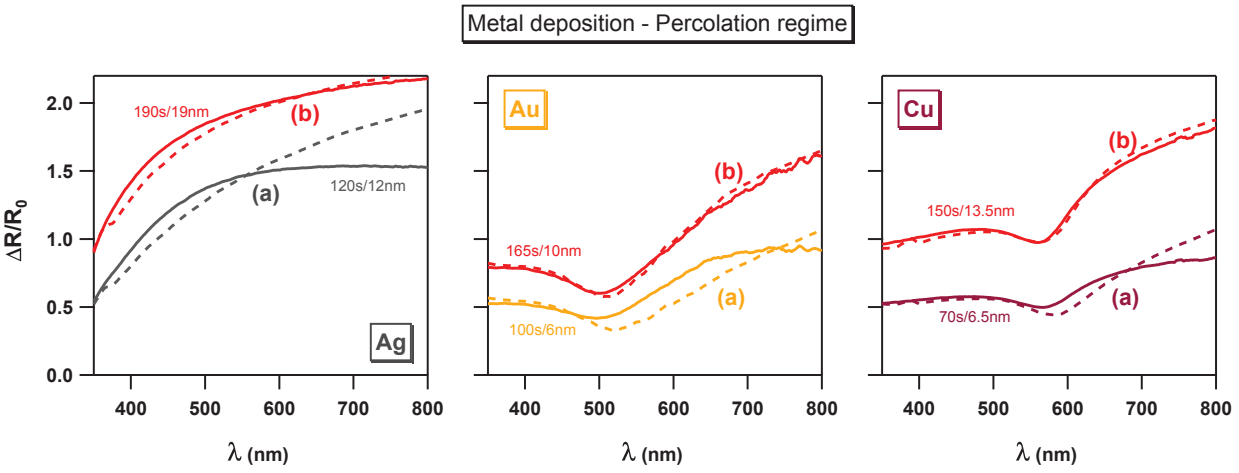

Figure III.8 – SDRS absorption spectra for the metal nanoclusters of Ag, Au, and Cu at the beginning of percolation regime, showing the absence of prominent maximum as well as the non-overlapping (a) of the optical signals (thick lines) with the continuous layer simulations (dotted lines). In the later stages, the prominent maximum remains absent while the experimental and simulated optical curves start to overlap (b).

This percolation regime, even though difficult to spot precisely during the optical characterizations, can be seen in Fig.III.8 as 120s/12nm to 190s/19nm for Ag, 100s/6nm to 165s/10nm

for Au, and 70s/6.5nm to 150s/13.5nm for Cu. A comparative study of Fig.III.8 can lead us to the conclusion that the percolation region starts well before for Au and Cu than for Ag, giving an indication of better surface diffusion processes of Ag atoms on the glass surface (or poor wetting of the glass surface) than that of Au and Cu.

3.1.3 2D growth of noble metals

After the percolation regime, due to the continuous metal deposition, the gaps formed during the percolation start filling up, which eventually leads to the 2D growth of a metal thin film [17]. At this phase, the optical signals overlap the continuous layer simulations as shown in Fig.III.3 and Fig.III.4. Also, after a certain thickness, the metal thin films turn into opaque layers for the visible light, where the optical properties resemble that of the bulk metals. From Fig.III.3, it can be seen that the metallic layer become opaque for the higher wavelengths at a lower thickness owing to the intrinsic property of the metals, which present higher absorption coefficients k for higher wavelengths (Section 2.1.1, Fig.II.1, Chapter II). Since the optical curves overlap with the continuous layer simulations, it is possible to fit the later part of the SDRS data $\Delta R/R_0$ (t, λ) with the assumption of a metal constant deposition rate υ_{metal}. Fixing the complex refractive index ($n_{\text{metal}} + ik_{\text{metal}}$) as determined from *ex situ* ellipsometry spectroscopy (Section 2.1.1, Fig.II.1(c-d), Chapter II) and using υ_{metal} as only fitting parameter, the deposition rates for Ag, Au and Cu were found to be 0.10nm/s, 0.06nm/s, and 0.09nm/s, respectively in agreement with the values determined from *post mortem* X-ray reflectivity measurements.

4 Depositions of Si_3N_4:Ag:Si_3N_4 and Si_3N_4:Au:Si_3N_4 nano-composites

After the individual discussion for the optical properties of Si_3N_4 and noble metal thin films, this part of the chapter is especially dedicated to the implementation of *in situ* and real-time SDRS for studying the optical properties of Si_3N_4:Ag:Si_3N_4 and Si_3N_4:Au:Si_3N_4 nanocomposite tri-layers.

4.1 Experimental procedure during the nanocomposite depositions

To fabricate the nanocomposite tri-layers, metal and dielectric targets are sputtered alternatively. As shown in the schematics (Fig.III.9), a buffer layer of Si_3N_4 (thickness around 20nm) is first deposited on the glass surface. Here it is worth noting that, during the SDRS measure-

ments, R_0 is taken as the reflectance of this Si_3N_4 buffer-layer and not that of the bare glass substrate. Then, a small amount of Ag or Au (effective thickness of about 2nm) is deposited onto the buffer layer in order to obtain metal nanoclusters. After the Ag or Au deposition, sufficient time of around 600s is given to the nanoclusters for their stabilization in the form of a holding time where no action is carried out on the system. Finally, the metal nanoclusters are covered by a Si_3N_4 capping-layer (thickness around 40nm), which not only protects them from the surrounding environment, but also enhances their SPR.

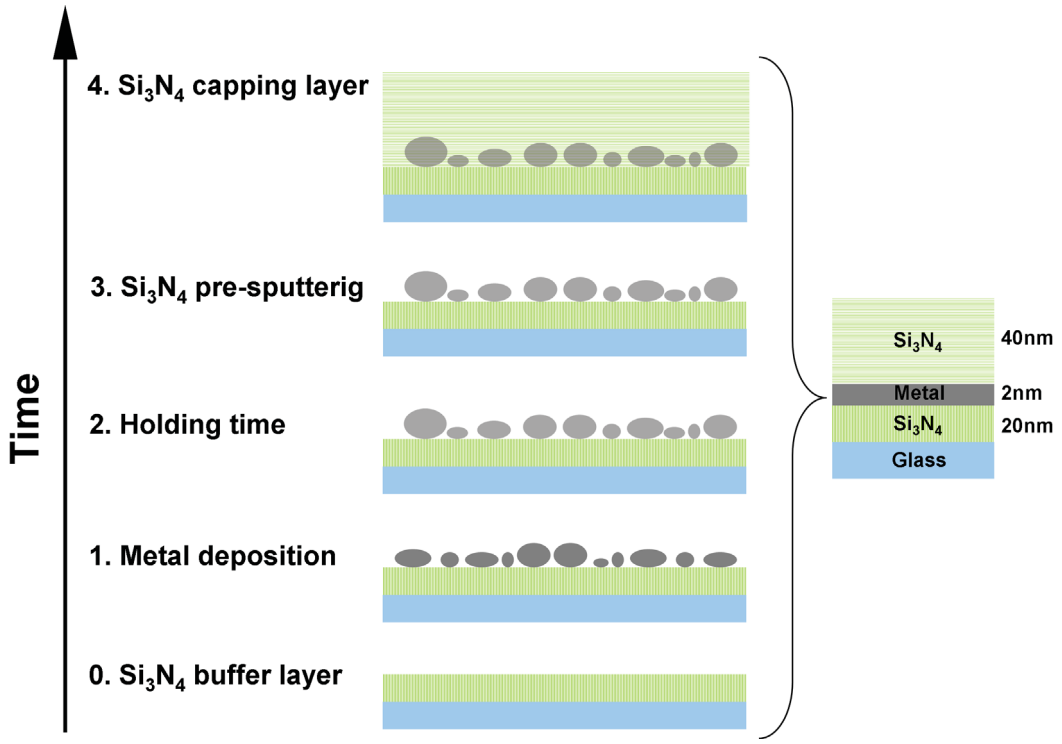

Figure III.9 – Schematics of experimental deposition sequence given in Table III.3 along with the equivalent thickness of respective deposited materials.

This experimental procedure leads to a tri-layer nanostructure where the Ag or Au nanoclusters are sandwiched between two Si_3N_4 layers, i.e. Si_3N_4:Ag:Si_3N_4 or Si_3N_4:Au:Si_3N_4 nanocomposites, respectively. During all the depositions, similar experimental parameters are used in order to reproduce materials with the same properties as studied in Sections 1 and 2 of the present Chapter. The details of this procedure are given in Table III.3.

4.2 *Post mortem* analysis of the nanocomposites

As the optical properties of the nanocomposites are strongly related to their nanostructure, a detailed study of the morphology and organization of the nanoclusters has prime importance.

#	Deposition step		Step duration (s)	Effective thickness (nm)	Magnetron power (W)	Ar flow (sccm)	N_2 flow (sccm)
0.	Si_3N_4 sputtering		600	20	176 (RF)	3	0.3
1.	Ag/Au sputtering		20/33	2	24/17 (DC)	18	–
2.	Holding time		600	–	–	–	–
3.	Ignition and pre-sputtering of Si_3N_4	(a)	150	–	88 (RF)	90	–
		(b)	600	–	88 (RF)	3	–
		(c)	150	–	132 (RF)	3	0.3
		(d)	150	–	176 (RF)	3	0.3
4.	Si_3N_4 sputtering		1200	40	176 (RF)	3	0.3

Table III.3 – Experimental procedure and deposition parameters used during the alternate deposition of Si_3N_4:Ag:Si_3N_4 and Si_3N_4:Au:Si_3N_4 nanocomposites at 200°C.

Hence, in addition to the *in situ* and real-time optical analysis *post mortem* high-angle annular dark-field scanning transmission electron microscopy (HAADF-STEM) and grazing incidence small-angle X-ray scattering (GISAXS) experiments are carried out [18–20]. The details of the analysis methods used for extracting the nanoscale information from the HAADF-STEM micrographs and GISAXS patterns are collected in the Appendix (Section 3) of this thesis. Here, a comparison of HAADF-STEM micrographs and GISAXS patterns in case of Ag and Au nanocomposites is shown in Fig.III.10 along with their SDRS signals collected at the end of the deposition, while the average nanostructure parameters are tabulated in Table III.4.

As shown in Fig.III.10, the presence of polydisperse assemblies of Ag or Au nanoclusters can be seen clearly from the HAADF-STEM micrographs, while the 2D GISAXS patterns show two distinct intensity lobes on either side of the beam-stop due to island-like structures. From Table III.4, slight differences in the morphology and organization of the metal clusters can be seen even though same metal amount (∼2nm) was deposited on the Si_3N_4 buffer-layer.

Nanocomposites	HAADF-STEM analysis					GISAXS analysis	
Si_3N_4:metal:Si_3N_4	d (μm^{-2})	Coverage (%)	D (nm)	σ_D (nm)	Λ (nm)	H/D ratio	H (nm)
Ag(20s/2nm)	6674	34.7	7.6	1.9	12.6	0.73	5.6
Au(33s/2nm)	8174	38.3	7.3	1.9	11.9	0.73	5.3

Table III.4 – The average in-plane nanostructure parameters, such as, areal density d, coverage rate %, diameter D, size-distribution σ_D and the average out-of-plane parameters, such as, aspect ratio H/D and height H of metal nanoclusters from Si_3N_4:Ag:Si_3N_4 and Si_3N_4:Au:Si_3N_4 nanocomposites, studied using *post mortem* HAADF-STEM and GISAXS (Fig.III.10).

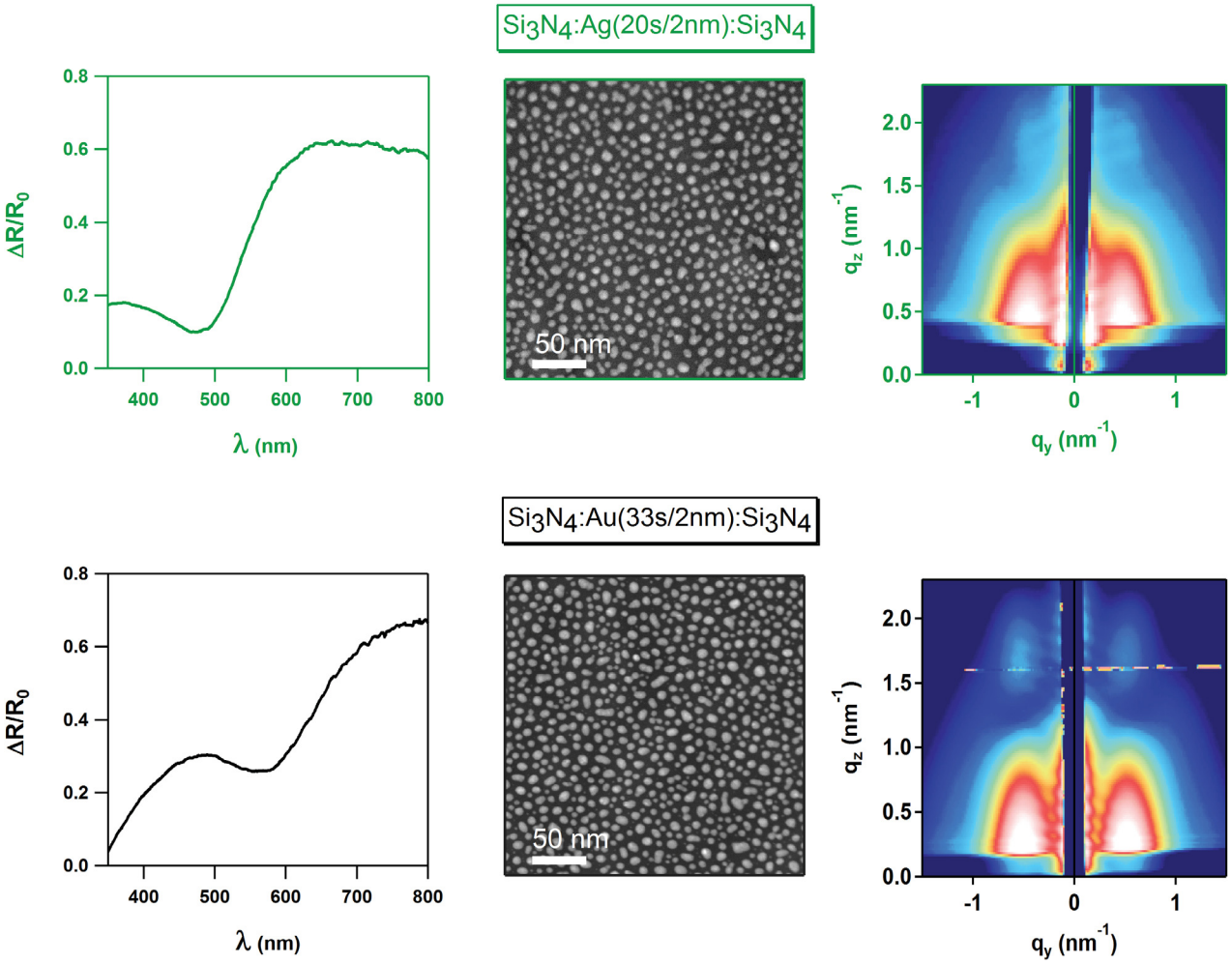

Figure III.10 – A comparison of *post mortem* SDRS signals, HAADF-STEM micrographs and GISAXS patterns of Si_3N_4:Ag(20s):Si_3N_4 and Si_3N_4:Au(33s):Si_3N_4 nanocomposites for similar deposited metal amount (∼2nm). The average structural parameters of respective metal clusters are collected in Table III.4.

The reason behind these small differences, other than intrinsic properties, can be the different deposition rates (0.1nm/s for Ag and 0.06nm/s for Au). Also, the smaller in-plane size D along with the higher areal cluster density d (or lower inter-cluster distance Λ) and coverage rate for the Au clusters suggest a lower surface diffusion of Au than that of Ag. Finally, even though the cluster aspect ratio (H/D, i.e. cluster shape) in both metals is similar and the in-plane nanostructure for both metals are only slightly different, the variations in the optical properties of their nanocomposites at the end of the depositions are dominated by the intrinsic optical characteristics of the metals over the nanostructure of the metal nanoclusters.

4.3 *In situ* and real-time SDRS observations

The real-time SDRS measurements during the deposition of the Si_3N_4:Ag/Au:Si_3N_4 nanocomposites are shown in Fig.III.11. Here, the real-time SDRS parent signals are further separated for the temporal variations of maximum wavelength λ_{max} and amplitude $(\Delta R/R_0)_{max}$ (Fig.III.11), while the spectral signals at the end of each deposition step are shown in Fig.III.12 . This separation allows us to have a "live picture" of the optical response of the nanoclusters during the different deposition steps (i.e. as a function of time t in seconds).

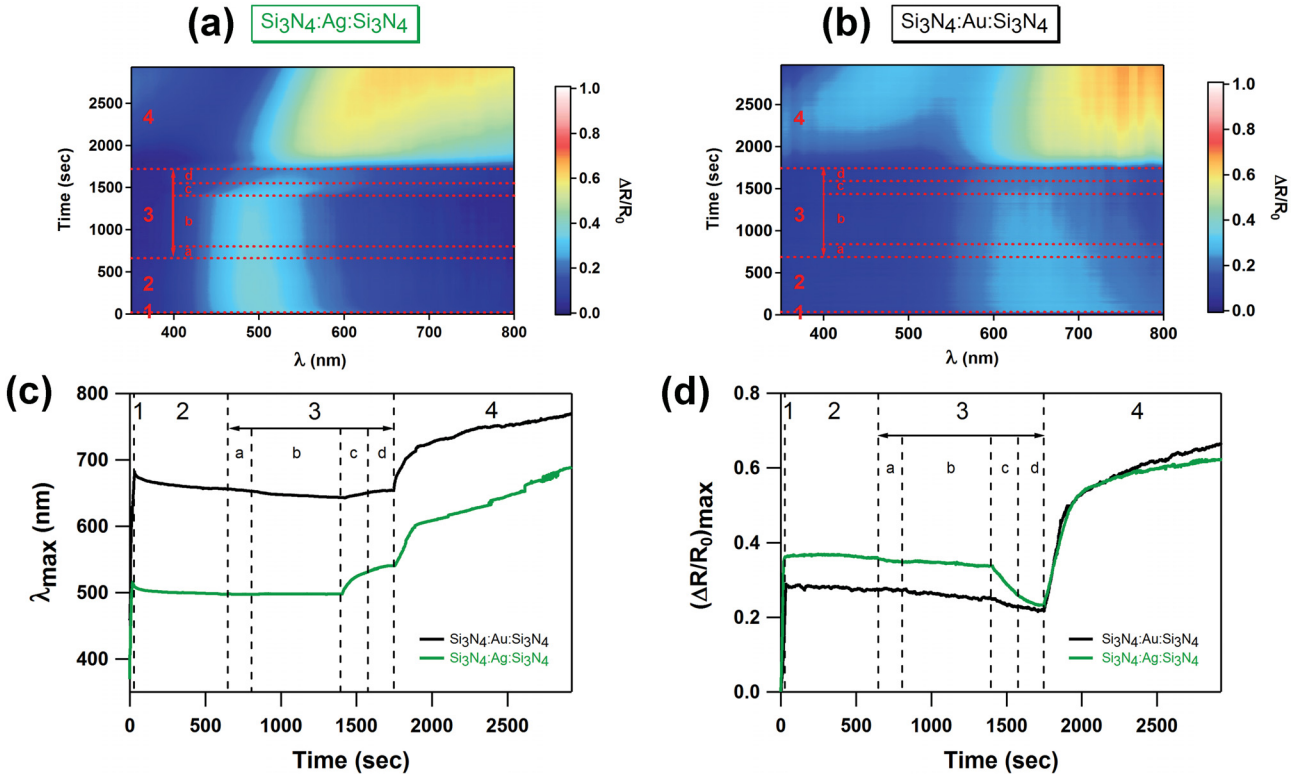

Figure III.11 – Parent SDRS signals $\Delta R/R_0(\lambda, t)$ obtained from Si_3N_4:Ag(20s/2nm):Si_3N_4 and Si_3N_4:Au(33s/2nm):Si_3N_4 nanocomposite depositions (a & b), conveniently separated into maximum wavelength λ_{max} (c) and maximum amplitude $(\Delta R/R_0)_{max}$ (d), expressed in terms of time t (sec).

However, it is worth reminding that the recording of the optical measurements starts from the deposition of the metal (STEP 1) and not from the deposition of Si_3N_4 buffer-layer (Table III.3).

4.3.1 STEP 1: Deposition of Ag or Au on the Si_3N_4 buffer-layer ($t \leq 20/33$sec)

Due to the small deposition durations, STEP 1 appears short in Fig.III.11(1). Nevertheless, Fig.III.12(STEP 1) shows a distinct peak in the optical signals right from the first few seconds

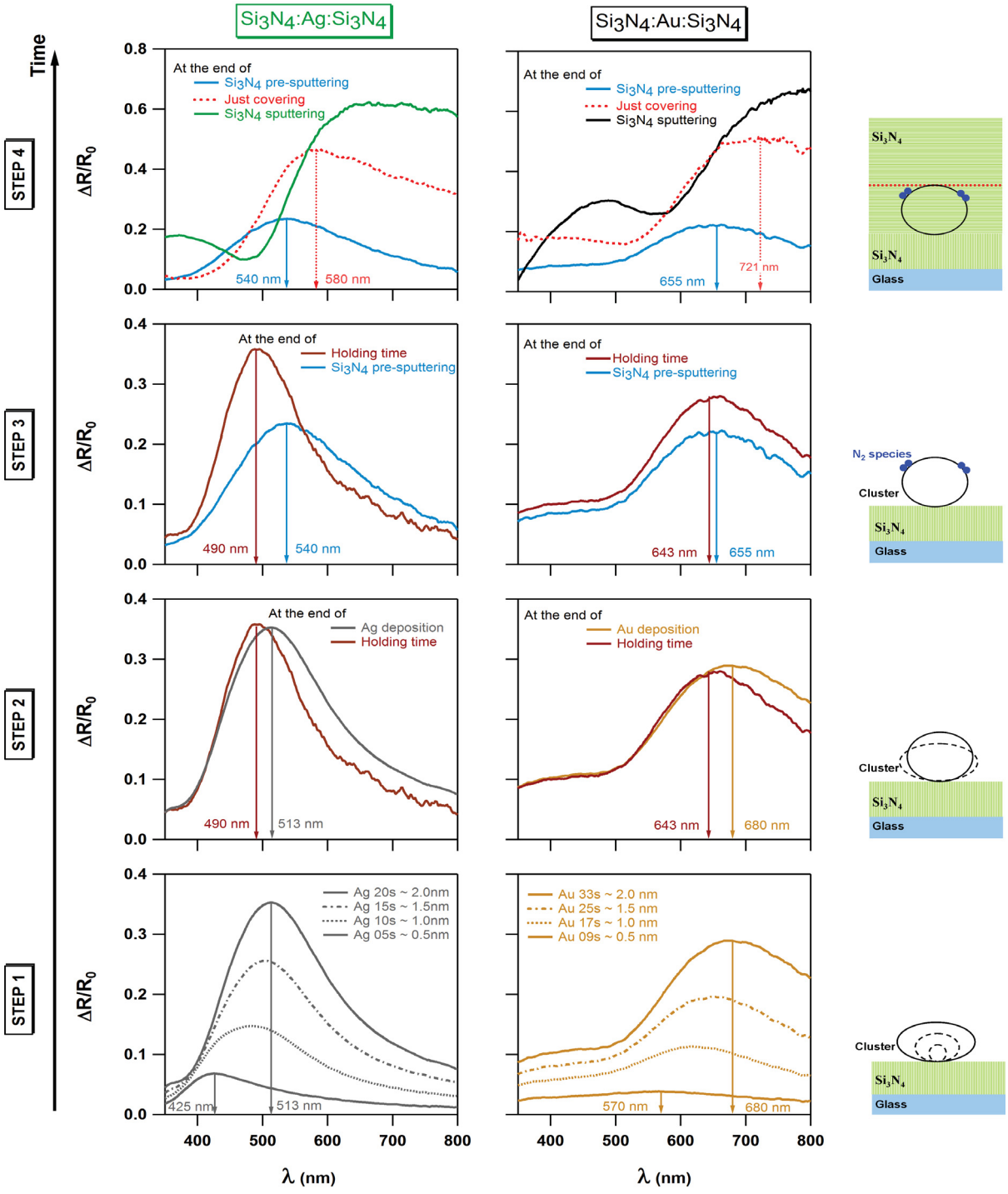

Figure III.12 – Spectral signals for Si_3N_4:Ag:Si_3N_4 (left) and Si_3N_4:Au:Si_3N_4(middle) nanocomposites during different deposition steps as explained in Table III.3. The respective schematics on the right side demonstrate the possible changes in the metal clusters and their surrounding during the alternate deposition of metals and Si_3N_4.

of metal depositions. This peak located in the visible range corresponds to the signature of the SPR phenomenon, indicating the presence of 3D metal nanoclusters [13]. As the deposition time t increases (i.e. deposited metal amount increases), we observe for both Ag and Au an increase of the amplitude and a sharp red-shift of the SPR accompanied by a prominent broadening. These results, which are discussed in the Refs [12, 21, 22], can be ascribed to a decrease of the areal cluster density d, an increase of the average cluster diameter D, and a decrease of the out-of plane aspect ratio H/D, which are typical consequences of a coalescence-type growth. Moreover, Fig.III.12 (STEP 1) also shows the fundamental effect of the metals on the SPR position at the end of their depositions (around 2nm effective thickness), where position of SPR is lower and sharper for the Ag nanoclusters comparing to Au ($\lambda_{\max}^{\mathrm{Ag}} = 513\mathrm{nm} < \lambda_{\max}^{\mathrm{Au}} = 680\mathrm{nm}$).

4.3.2 STEP 2: Holding time after the metal depositions (20/33sec $\leq t \leq$ 620/633sec)

During the holding time (Fig.III.11(2)), no action is taken on the system, which gives nanoclusters sufficient time to stabilize on the buffer-layer surface. However, slight modifications in the optical signals during this step can still be seen, which can be linked to the morphological parameters of the metal nanoclusters.

For both metals, a blue-shift of the SPR together with a narrowing can be observed during this step. Quantitatively, the blue-shift is found to be greater for Au (from 680nm to 643nm) than for Ag (513nm to 490nm), while the amplitudes for both metals remain almost unchanged (Fig.III.12-STEP 2). These results can be ascribed to modifications in the average cluster shape from a metastable oblate shape to a more stable shape, where the in-plane and out-of-plane aspect ratios tend towards 1 (Section 4.2.3, Fig.II.8(c-d), Chapter II) [22].

The optical changes during the holding time show the sensitivity of the SDRS measurements that can capture minute changes in the morphology of metal clusters, which are otherwise difficult to detect.

4.3.3 STEP 3: Pre-sputtering of the Si_3N_4 target (620/633sec $\leq t \leq$ 1670/1683sec)

After the holding time, pre-sputtering of the Si_3N_4 target is carried out (Fig.III.11(3a-3d)). During all the pre-sputtering sub-steps (a to d), a shutter is placed over the Si_3N_4 target in order to avoid the actual deposition of Si_3N_4 on the metal nanoclusters. A detailed experimental description and the necessity of the pre-sputtering steps have been already discussed in Section 2.1 of the present Chapter. The sub-steps (3a) and (3b), where only the Ar^+ plasma is switched on, do not show any significant effects on the optical signals for both metals. In contrast, a

sharp red-shift in the SPR position and a significant damping in the SPR amplitude can be seen as soon as N_2 is introduced in the deposition chamber at sub-step (3c). It should be noted that the optical modifications are immediate upon N_2 introduction. As the Ar^+ plasma is already switched ON (even though the shutter is closed), partially ionized nitrogen species (such as, N^+ or N^{2+}) may get formed and may react with the sensitive metal clusters by hindering the collective electron oscillation responsible for the SPR, and therefore reduce the peak amplitude during the sub-steps 3(c) and 3(d). On the other hand, upon the interaction of energetic partially ionized nitrogen species with the clusters, they may increase the dielectric function of the cluster surrounding, which may explain the immediate red-shift in the SPR position.

Also, Fig.III.12 (STEP 3) clearly shows that the effect of partially ionized nitrogen species is stronger on the Ag clusters than on the Au clusters. Indeed, the SPR position for Ag is red-shifted from 490nm to 540nm with a damping in the amplitude from 3.8 to 2, compared to Au, where a red-shift from 643nm to 655nm and a damping from 2.8 to 2 are evident. This shows that the reactivity of Ag nanoclusters is greater than that of Au nanoclusters. An in-depth analysis of this effect of partially ionized species is given in detail in the following Chapter (IV).

4.3.4 STEP 4: Deposition of the Si_3N_4 capping ($1670/1683\text{sec} \leq t \leq 2870/2883\text{sec}$)

At the end of the pre-sputtering step, as soon as the shutter over the Si_3N_4 target is opened, the deposition of the Si_3N_4 capping-layer starts. During this step, the metal nanoclusters on the Si_3N_4 buffer-layer are progressively embedded in a dielectric Si_3N_4 matrix. The effect of this capping layer is immediate on the SDRS signals and can be seen clearly in Fig.III.11(4). This effect is on both, the SPR position (in the form of a sharp red-shift) and on the SPR amplitude (in the form of strong increase), which can be ascribed to a inter-play between the combined effects as explained below.

First, during the deposition of the Si_3N_4 capping-layer, the refractive index of the medium surrounding the nanoclusters changes from a mix between vacuum ($n = 1$) and Si_3N_4 ($n \approx 2$) to pure Si_3N_4, which is qualitatively in accordance with the simulations already discussed in the previous Chapter II (Section 4.2.2, Fig.II.7(c-d)). Second, studies in the literature have shown that the dielectric capping-layers may modify the shape of metal nanoclusters which is mainly driven by the thermodynamic effects (rather than the kinetic effects) [18, 22]. However, the metal nanoclusters having same buffer and capping-layer, are expected to attain the spherical shape in order to minimize their total interface energy, which in turn should produce a blue-shifted SPR and it is not the case here. Hence, the net red-shift in the SPR of metal nanoclusters in this step, suggests the greater influence of the higher refractive index of surrounding medium

over the cluster shape effects.

By observing Fig.III.11(4), we clearly see two distinct parts in the optical signals for both metals. The first part shows a sharp red-shift (from 540nm to 580nm for Si_3N_4:Ag:Si_3N_4 and from 655nm to 721nm for Si_3N_4:Au:Si_3N_4) and an amplitude increase (from 0.20 to 0.48 for Si_3N_4:Ag:Si_3N_4 and from 0.20 to 0.50 for Si_3N_4:Au:Si_3N_4 (STEP 4)) in the SPR of the metal nanoclusters up to a certain time (around 1900s), which may correspond to the complete capping of the metal clusters (red dotted curves in Fig.III.12 (STEP 4)). At this stage, we get a "true" nanocomposite layer of metal:Si_3N_4 deposited on Si_3N_4. In the second part, the optical signals (λ_{max} and $(\Delta R/R_0)_{max}$) keep increasing continuously but with a lower rate than during the formation of "true" nanocomposite layer, which can be ascribed to the interferences of light in an additional "cluster-free" transparent Si_3N_4 layer (Fig.III.12 (STEP 4)).

In general, this real-time SDRS analysis suggests that the behavior of the optical properties of both metal nanoclusters are similar during their alternate deposition with Si_3N_4, which are dominated by their intrinsic properties rather than their nanostructure (Table III.4). But more specifically, it also indicates that the optical properties of Ag nanoclusters are not only more prominent than that of Au nanoclusters, but also they are more sensitive towards the nitrogen species.

5 Effect of the metal amount on the optical properties of Si_3N_4:Ag:Si_3N_4 nanocomposites

5.1 Experimental procedure

In order to study the effect of metal amount, Si_3N_4:Ag:Si_3N_4 nanocomposites were fabricated by increasing the deposited Ag amount sandwiched between the Si_3N_4 dielectric layers. For this study, five different samples were studied with real-time SDRS during their fabrication and with *post mortem* HAADF-STEM and GISAXS. All the samples were deposited at 200°C and the experimental conditions were kept same for Ag and Si_3N_4, as explained in Table III.3 in order to generate similar optical properties (except for the increase in the Ag deposition time/thickness, which was varied from 5s/0.5nm to 80s/8nm).

5.2 *Post mortem* nanostructure analysis

Fig.III.13 shows the HAADF-STEM micrographs and GISAXS patterns for the five samples. Here, with the increasing deposition time/amount (from left to right), bigger and more distinct Ag nanoclusters are clearly evident from the HAADF-STEM micrographs [19, 20, 23, 24]. On the other hand, the corresponding GISAXS patterns also display the shrinking of the intensity patterns towards origin with the increasing deposition amount, in agreement with the presence of bigger and distinctly separated Ag clusters [19, 20, 25, 26]. Table III.5 represents the nanometric parameters of the embedded Ag nanoclusters from different deposition amounts. Moreover, the variations of the morphological and organizational parameters given in Table III.5 are displayed in Fig.III.14 as a function of the Ag deposition time/thickness.

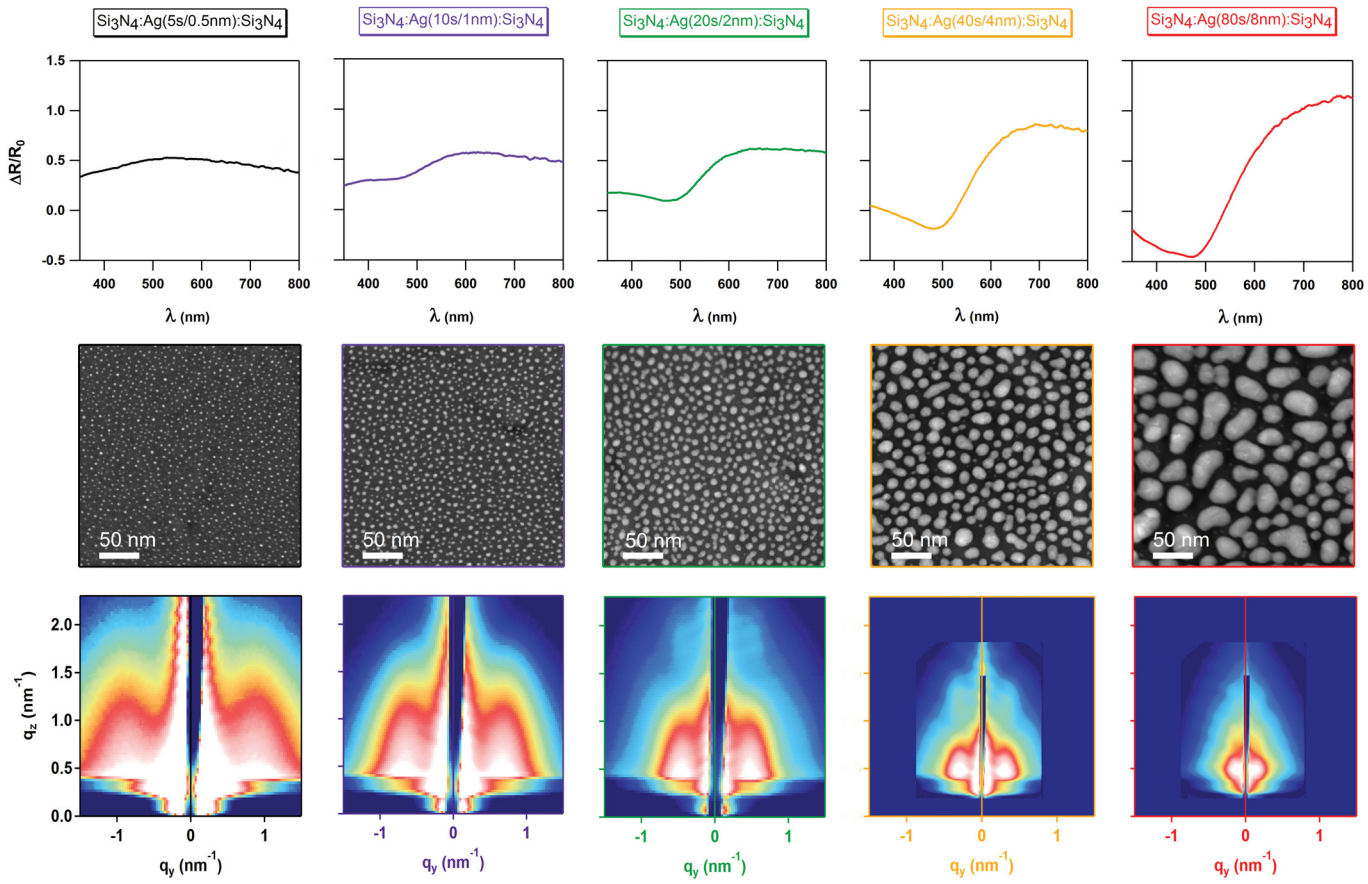

Figure III.13 – Comparison of spectral SDRS signals at the end of the depositions along with the *post mortem* HAADF-STEM micrographs and GISAXS patterns (top to bottom) for Ag nanoclusters from Si_3N_4:Ag:Si_3N_4 nanocomposites, showing their evolution as a function of the Ag deposition time/amount from 5s/0.5nm to 80s/8nm (left to right).

Nanocomposites	HAADF-STEM analysis					GISAXS analysis	
Si_3N_4:Ag:Si_3N_4	d (μm^{-2})	Coverage (%)	D (nm)	σ_D (nm)	Λ (nm)	H/D ratio	H (nm)
Ag(5s/0.5nm)	17942	11.9	2.7	0.8	7.9	0.93	2.5
Ag(10s/1nm)	14464	23.8	4.4	1.4	10.0	0.87	3.8
Ag(20s/2nm)	6674	34.7	7.6	1.9	12.6	0.73	5.5
Ag(40s/4nm)	2094	38.1	13.6	3.6	19.5	0.64	8.7
Ag(80s/8nm)	632	40.9	25.3	7.3	36.0	0.43	10.9

Table III.5 – Morphological and organizational parameters studied using *post mortem* HAADF-STEM and GISAXS for the Si_3N_4:Ag:Si_3N_4 nanocomposites with increasing Ag amount.

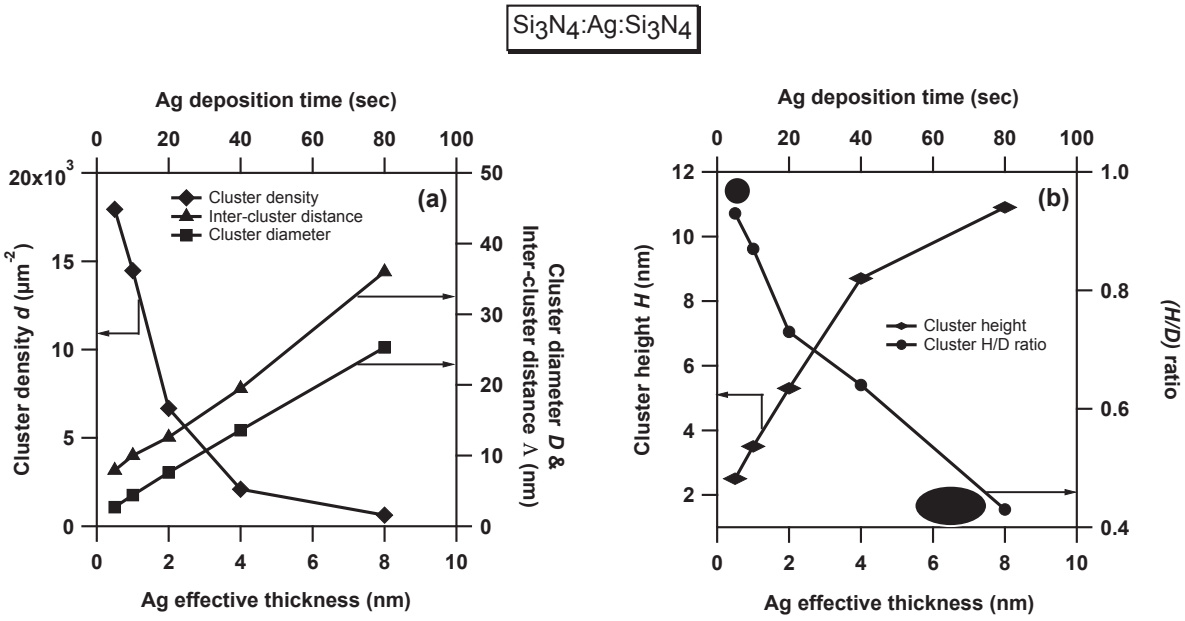

Figure III.14 – Variation of Ag cluster parameters (from Table III.5) embedded in the Si_3N_4 matrix as a function of the Ag deposition time/thickness, (a) - variation of in-plane parameters (d, D, and Λ), (b) - variation of out-of-plane parameter (H/D and H).

- **Cluster density and inter-cluster distance -** From Table III.5 and Fig.III.14(a), the decrease of the areal cluster density d and increase in the inter-cluster distance Λ with increasing the Ag deposition time/thickness prove the prominent coalescence regime in the Ag cluster growth as described in Chapter I (Section 3.3.3). In our case, it is not possible to observe the nucleation and growth regime during the very early deposition period where the cluster density should actually increase with the metal amount. This suggests that the Ag deposition rate (0.10nm/s), even though the slowest possible deposition rate in our case, is still not sufficiently slow.

- **Cluster size and in-plane size distribution -** From Fig.III.14(a), upon increasing the Ag deposition time/thickness, the monotonous increase of the in-plane diameter D of the Ag clusters is evident. Also, from Table III.5, it is clear that with increasing the Ag amount, the in-plane size distribution σ_D of the Ag clusters also broadens monotonously. It is worth noting that the average edge-to-edge distance $(\Lambda - D)$ between the Ag clusters is almost the same, whatever the deposited Ag amount. This may be a typical coalescence growth characteristics of nanoclusters under the considered thickness range.

- **Cluster shape -** Increasing the Ag amount increases both the in-plane size D and the out-of-plane size H of the Ag nanoclusters (Fig.III.14(a-b)). However, from Fig.III.14(b), it is also evident that the out-of-plane aspect ratio H/D decreases dramatically when the deposition time increases [27]. While the vertical growth is driven mainly by direct deposition of atoms on the top of the clusters, their lateral growth is governed by more complex processes including adatom diffusion on the substrate and coalescence [28]. Furthermore, the presence of a 3D Schwoebel barrier[1] may prevent the clusters from reaching their thermodynamically stable shape [12]. Hence, the rate of lateral growth is expected to be higher than the rate of vertical growth, which gives rise to more oblate clusters at higher Ag amounts.

5.3 *In situ* and real-time SDRS observations

After describing the effect of the Ag amount on the structural and optical properties of the Ag clusters *post mortem*, we can discuss the temporal variations of the optical response using real-time SDRS (Fig.III.15). As the different deposition steps have been already described in detail in Section 4.3 of this Chapter for the Si_3N_4:Ag(20s/2nm):Si_3N_4 nanocomposite, the focus of this discussion is preliminary given to a comparative description of the SDRS variations as a function of the Ag amount.

5.3.1 STEP 1: Ag depositions on Si_3N_4 buffer-layers with increasing Ag amounts

The increase in the Ag amount expresses itself at the end of STEP 1 of Fig.III.15(a-b) in the form of a strong red-shift of the SPR from 420nm (for 5s/0.5nm Ag deposition) to 730nm (for 80s/8nm Ag deposition) as well as a sharp increase of its amplitude from 0.05 (for 5s/0.5nm Ag deposition) to 1.13 (for 80s/8nm Ag deposition). The sharp increase of λ_{max} can be associated

[1]The 3D Schwoebel-Ehrlich barrier is defined as the total energy barrier for a metal adatom in diffusing across an edge between two facets (assuming faceted nanocrystals according to the Wulff construction).

to the decrease of the average out-of-plane aspect ratio H/D of the Ag nanoclusters, and the increase of $(\Delta R/R_0)_{max}$ can be related to the increase of their in-plane size D with the increasing Ag amount.

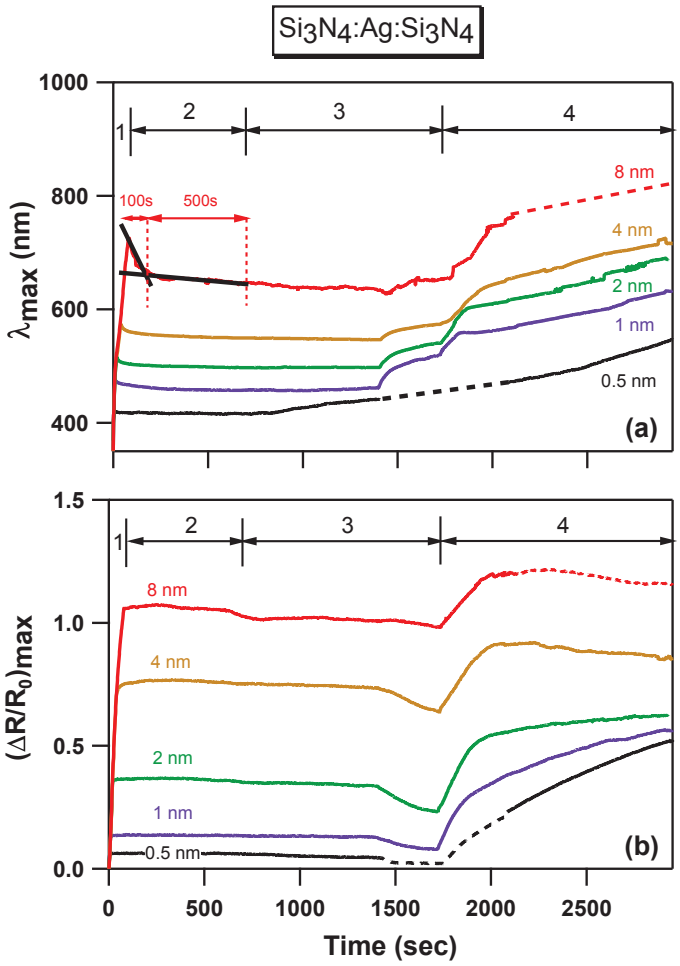

Figure III.15 – SDRS signals of Si_3N_4:Ag:Si_3N_4 nanocomposites studied for different Ag deposition time/amount (5s/0.5nm to 80s/8nm), showing variations in maximum wavelength λ_{max} (a) and maximum amplitude $(\Delta R/R_0)_{max}$ (b) of the SPR during the different deposition steps (1-4). The dashed lines (black and red) in (a) present the periods where the tracing of the λ_{max} was difficult for Ag(5s/0.5nm) and Ag(80s/8nm) samples, the corresponding $(\Delta R/R_0)_{max}$ for which then plotted around 442nm (the black dashed curve) and around 765nm (the red dashed curve), respectively.

5.3.2 STEP 2: Holding time after Ag depositions

During step 2, the holding time stabilizes the system and gives rise to a reshaping of the nanoclusters due to thermodynamic effects, which in turn causes a small blue-shift in the position of the SPR bands. From Fig.III.15(a), it can be seen that the blue-shift is larger for

higher Ag amounts (see $\Delta\lambda_{max}$ in Table III.6), which can be explained by a more important reshaping of the biggest Ag clusters, as the bigger clusters are more oblate comparing to the smaller ones (Fig.III.14(b)). This blue-shift seems to be prominent in the first few tens of seconds and then proceeds at a lower rate with further increase in the holding time duration. As an example, a blue-shift of around -60nm in the first 100s is evident for the Ag(80s/8nm) sample, which further shows a blue-shift of around -23nm in the next 500s (respective horizontal red arrows in Fig.III.15(b)). On the other hand, it can be seen that $(\Delta R/R_0)_{max}$ is constant for the respective samples during this step, which indicates that the loss of Ag metal from the buffer-layer surface is negligible whatever the deposited Ag amount.

Si_3N_4:Ag:Si_3N_4 nanocomposites					
Ag deposition time/thickness	D (nm)	H/D ratio	$\Delta\lambda_{max}$ (nm) after holding time	$\Delta\lambda_{max}$ (nm) after N_2 introduction	% amplitude variation after N_2 introduction
5s/0.5nm	2.7	0.93	-5	–	–
10s/1nm	4.4	0.87	-20	+52	-59
20s/2nm	7.6	0.73	-18	+43	-42
40s/4nm	13.6	0.64	-24	+26	-14
80s/8nm	25.3	0.43	-83	+20	-3

Table III.6 – The shifts in the SPR position ($\Delta\lambda_{max}$) of Ag nanoclusters from Si_3N_4:Ag:Si_3N_4 nanocomposites during the holding time and due to the partially ionized nitrogen species along with the relative variation of the amplitudes for different Ag amounts.

5.3.3 STEP 3: Pre-sputtering of the Si_3N_4 target (effect of N_2 ions)

During the pre-sputtering of the Si_3N_4 target (STEP 3 in Fig.III.15), the effect of partially ionized nitrogen species in the later part is evident in the form of a noticeable red-shift in SPR position along with a small damping in SPR amplitude for all the samples. In this regard, Table III.6 quantifies the reactivity of the Ag clusters with different sizes by gathering the shift in the SPR positions $\Delta\lambda_{max}$ and the relative variation of SPR amplitudes after N_2 introduction (where, the values at the end of holding time (STEP 2) are taken as references). Here, the decrease of both $\Delta\lambda_{max}$ and relative amplitude variation with the increase of the Ag cluster size evidence a reduced sensitivity of the large Ag clusters to ionized species.

However, during this regime, it was difficult to record the SPR position for the 5s/0.5nm sample (black dashed line in Fig.III.15(a)) due to the possible complete reaction of very small Ag nanoclusters (around 2.7nm) with the ionized nitrogen species leading to a strong damping of the SPR. Hence, the $(\Delta R/R_0)_{max}$ signal for Ag(5s/0.5nm) sample during this period was

plotted around 442nm i.e. the last value of λ_{max} traced before the disappearance of the SPR (black dashed curve in Fig.III.15(b)).

5.3.4 STEP 4: Deposition of the Si_3N_4 capping layer

During the deposition of the Si_3N_4 capping-layer (STEP 4 in Fig.III.15), a sharp red-shift in SPR position as well as a strong increase in SPR amplitude are observed. The red dotted line during the optical study of the 80s/8nm sample suggests the impossibility to detect the exact position of the SPR maximum during the real-time analysis as the SDRS signal becomes too flat. However, it should be noted that the SDRS signals for each sample during STEP 4 shows two distinct parts (or two distinct slopes) as shown in Fig.III.16.

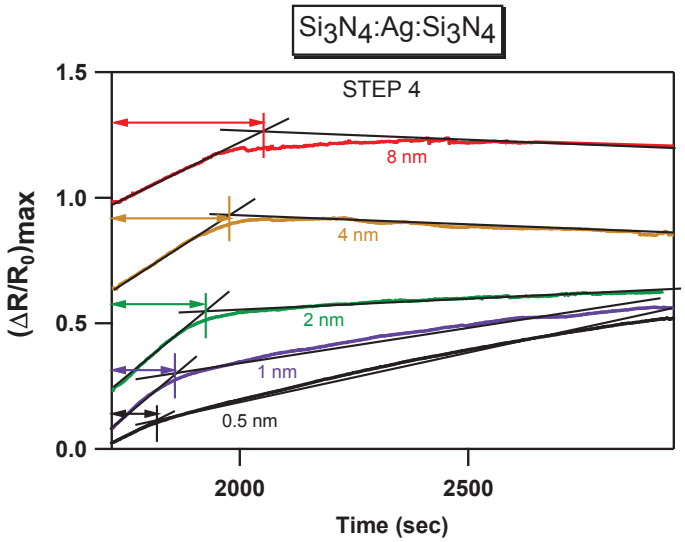

Figure III.16 – Changes in the optical properties of Ag nanoclusters (of different sizes) during their capping by a Si_3N_4 matrix (STEP 4). The horizontal arrows suggests the approximate time duration/thickness at which the respective Ag nanoclusters are just covered by Si_3N_4, giving the distinction between the "true" Ag:Si_3N_4 nanocomposite layers and transparent Si_3N_4 capping layers. These corresponding time durations/thicknesses for respective samples are given in Table III.7.

As already explained in Section 4.3 of this Chapter, these two different parts are the signature of the progressive capping of the Ag nanoclusters (region with high optical variation rate) and of the interference effect of light in the transparent cluster-free Si_3N_4 capping-layer (region with low optical variation rate), respectively. Accordingly, the deposition time at which the Ag clusters are just covered by the Si_3N_4 matrix was estimated from Fig.III.16 (horizontal arrows) and reported in Table III.7. The results show that, with the increasing Ag amount, the time required to just cover the Ag clusters increases and is close to their average height. This fact

Si_3N_4:Ag:Si_3N_4			
Ag deposition time /thickness (sec/nm)	H (nm)	Capping time (sec)	$\delta^{opt}_{Si_3N_4}$ (nm)
5s/0.5nm	2.5	100	3.3
10s/1nm	3.5	140	4.6
20s/2nm	5.3	206	6.8
40s/4nm	8.7	258	8.5
80s/8nm	10.9	333	11.0

Table III.7 – Thickness of Si_3N_4 ($\delta^{opt}_{Si_3N_4}$) to just cover the Ag nanoclusters of different sizes from Si_3N_4:Ag:Si_3N_4 nanocomposites.

shows another benefit of the real-time SDRS optical probe in detecting the interface between the Ag:Si_3N_4 composite layer and cluster-free Si_3N_4 capping-layer during their fabrication.

5.3.5 Comparison of experimental and simulated SDRS signals

To confirm the evolution of the SDRS signals shown in Fig.III.15 and Fig.III.16 during the second part of STEP 4, we carried out optical simulations using the Yamaguchi model described in Chapter II (Section 4.2). The nanoclusters parameters used for these simulations were taken from Table III.5 (i.e. we assume that the morphology and organization of the nanoclusters are frozen during the last part of the capping-layer deposition.) along with a damping constant $A = 1.5$. In this regard, Fig.III.17 shows a comparison of the experimental and simulated SDRS signals for the Si_3N_4:Ag:Si_3N_4 nanocomposites with different Ag amounts as a function of the Si_3N_4 deposition time.

The optical simulations displayed in Fig.III.17(c) and Fig.III.17(d) confirm the overall behavior of the experimental optical signals (Fig.III.17(a) and Fig.III.17(b)) during the deposition of the Si_3N_4 capping-layer on top of the Ag nanoclusters. Simulated λ_{max} and $(\Delta R/R_0)_{max}$ values increase monotonously with both the Ag amount and the capping-layer thickness. Furthermore, it can be seen that the decrease of the slope for $(\Delta R/R_0)_{max}$ as the Ag amount increases is well-reproduced in the simulations in qualitative accordance with the experimental signals. However, it is worth noting that it was not possible to obtain a perfect quantitative agreement between the experimental and simulated data, owing to the discrepancies between the theoretical assumptions and the practical situations. In particular, the experimental and simulated λ_{max} variations (Fig.III.17(a) and Fig.III.17(c)) do not show similar ranges, which may be explained by the ideal consideration of monodispersed spheroidal clusters that is far from the real case (as discussed in Section 4.4 of Chapter II). Nevertheless, although the optical

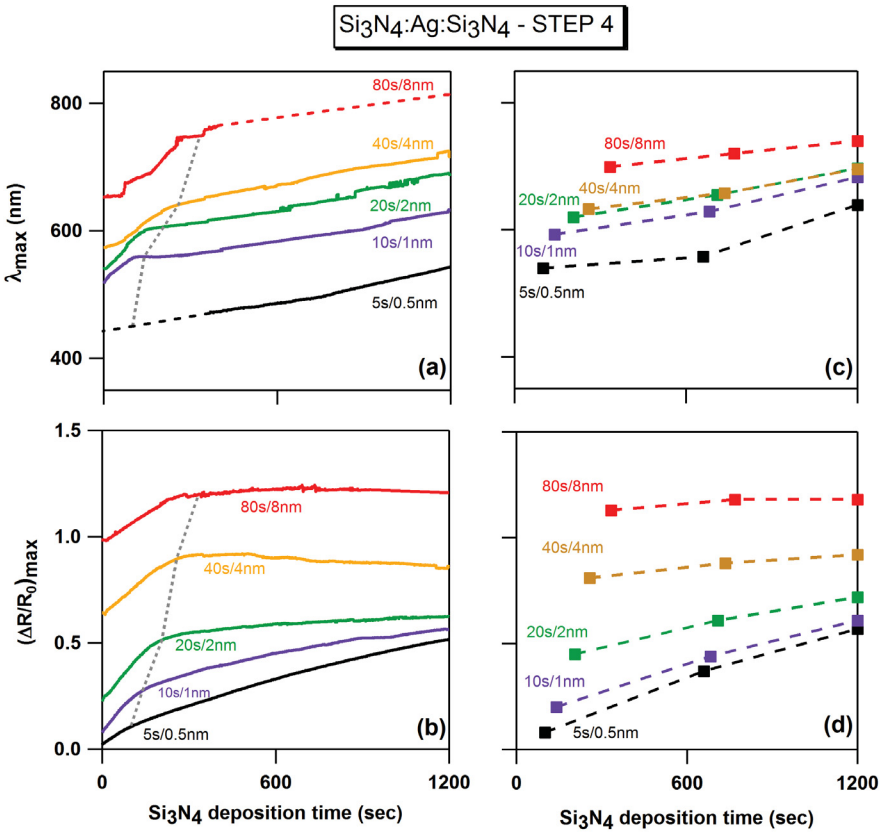

Figure III.17 – Comparison between the experimental optical signals (a-b) and the simulated optical signals (c-d) of Si_3N_4:Ag:Si_3N_4 nanocomposites for different Ag deposition time/thicknesses during the deposition of Si_3N_4 capping layer. The gray dotted curve in (a) and (b) represents the time where the Ag nanoclusters from respective nanocomposites are just covered by the Si_3N_4 capping matrix.

model do not provide an exact quantitative information, it may serve us as a qualitative tool to analyze the overall variations in the experimental SDRS signals.

6 Summary and conclusions

In this chapter, the implementation of *in situ* and real-time SDRS for the sensitive optical characterization of materials has been described. More particularly, we have discussed the possible use of SDRS for studying transparent films and accurately determining their refractive indices along with the deposition rates. In case of noble metals, we have seen the resourceful use of SDRS, which not only gives us an insight for the different growth regimes precisely, but also yields their deposition rates. For noble metal nanoclusters, SDRS allows one to probe modifications in their morphological parameters and chemical surrounding expressing themselves in sharp optical variations. In addition to this valuable information, kinetics of these

modifications and variations can be observed by SDRS, thanks to its real-time operation.

Real-time optical characterization also gives an advantage to study the optical properties of nanocomposites, not only during the depositions of the metal and dielectric material, but also during the intermediate steps (like holding time and exposure to partially ionized species) that can yield very sensitive information regarding the evolution of the metal nanoclusters. These SDRS measurements give insight for each deposition step, characterized by distinct modifications in the optical response arising from the delicate interplay between thermodynamic, kinetic, and chemical effects.

Moreover, we have seen the strength of SDRS in studying the effect of the metal amount on the optical properties of Si_3N_4:Ag:Si_3N_4 nanocomposites. Here, the increase of the Ag amount gives rise to interesting modifications in the optical properties (from the metal deposition step to the capping of the nanoclusters by the Si_3N_4 matrix) owing to different nanostructures of the Ag clusters, which are studied in detail thanks to the complementary *post mortem* structural characterizations by HAADF-STEM and GISAXS. Our study shows that the increase of the Ag deposited amount results in an increase of the in-plane size of the nanoclusters together with a decrease of their out-of-plane aspect ratio, which cause a sharp red-shift and an amplitude increase of the SPR as well as a decrease of the nanoclusters reactivity and of the optical contribution of the dielectric capping-layer.

Hence, such real-time SDRS characterizations not only give a "live picture" of the entire nanocomposite deposition process, but also provide a glance at the sensitive modifications in the metal nanoclusters, which are difficult to detect otherwise.

Bibliography

[1] F. Lebland, Z. Z. Wang, J. Flicstein, C. Licoppe, and Y. I. Nissim. *Bulk and surface properties of RTCVD Si_3N_4 films for optical device applications.* Applied Surface Science **69**, 198–203 (1993). 65

[2] K. S. Grabowski, A. D. F. Kahn, E. P. Donovan, and C. A. Carosella. *Thermal stability of silicon nitride coatings produced by ion assisted deposition.* Nuclear Instruments and Methods in Physics Research Section B: Beam Interactions with Materials and Atoms **39**, 190–193 (1989). 65

[3] S. Guruvenket, J. Ghatak, P. V. Satyam, and G. M. Rao. *Characterization of bias magnetron-sputtered silicon nitride films.* Thin Solid Films **478**, 256–260 (2005). 65

[4] H. Schmidt, W. Gruber, G. Borchardt, M. Bruns, M. Rudolphi, and H. Baumann. *Thermal stability and crystallization kinetics of sputtered amorphous Si_3N_4 films.* Thin Solid Films **450**, 346–351 (2004). 65

[5] E. Byon, T. W. H. Oates, and A. Anders. *Coalescence of nanometer silver islands on oxides grown by filtered cathodic arc deposition.* Applied Physics Letters **82 (10)**, 1634 (2003). 65, 66

[6] B. Canut, A. Ayari, J. Dupuis, M. Lemiti, A. Fave, and S. Ramos. *Swelling and optical properties of Si_3N_4 films irradiated in the electronic regime.* Nuclear Instruments and Methods in Physics Research B **267**, 917–920 (2009). 65

[7] O. P. Agnihotri, S. C. Jain, J. Poortmans, J. Szlufcik, G. Beaucarne, J. Nijs, and R. Mertens. *Advances in low temperature processing of silicon nitride based dielectrics and their applications in surface passivation and integrated optical devices.* Semiconductor Science and Technology **15**, R29–R40 (2000). 65

[8] M. Pattabi, N. Suresh, S. M. Chaudhari, A. Banerjee, D. M. Phase, A. Gupta, and K. Mohan Rao. *Aging studies on discontinuous silver films in ultrahigh vacuum.* Thin Solid Films **322**, 340–343 (1998). 66

[9] R. M. A. Azzam and N. M. Bashara. *Ellipsometry and polarized light*. North Holland Publication Company (1977). 68

[10] L. Simonot, D. Babonneau, S. Camelio, D. Lantiat, P. Guérin, B. Lamongie, and V. Antad. *In-situ optical spectroscopy during deposition of Ag:Si_3N_4 nanocomposite films by magnetron sputtering*. Thin Solid Films **518**, 2637–2643 (2010). 68

[11] J. A. Venables, G. D. T. Spiller, and M. Hanbucken. *Nucleation and growth of thin films*. Rep Prog Phys **47**, 399–459 (1984). 68, 70

[12] C. T. Campbell. *Ultrathin metal films and particles on oxide surfaces: structural, electronic and chemisorptive properties*. Surface science reports **27**, 1–111 (1997). 68, 70, 81, 86

[13] U. Kreibig and M. Vollmer. *Optical Properties of Metal Clusters*. Springer-Verlag, Berlin (1995). 69, 70, 81

[14] R. Lazzari, S. Roux, I. Simonsen, J. Jupille, D. Bedeaux, and J. Vlieger. *Multipolar plasmon resonances in supported silver particles: The case of Ag/α-Al_2O_3(0001)*. Physical Review B - Condensed Matter and Materials Physics **65**, 2354241–23542413 (2002). 70

[15] D. Beysens, C. M. Knobler, and H. Schaffar. *Scaling in the growth of aggregates on a surface*. Physical Review B **41**, 9814–9818 (1990). 73

[16] J. Carrey. *Croissance granulaire d'Or et de Cobalt sur alumine amorphe: caracterisations et Simulations de Monte-Carlo*. Thèse de Doctorat, Orsay - Université de Paris XI, Orsay (2001). 73

[17] T. W. H. Oates, L. Ryves, and M. M. M. Bilek. *Dielectric functions of a growing silver film determined using dynamic in situ spectroscopic ellipsometry*. Optics Express **16**, 2302–2314 (2008). 75

[18] D. Lantiat, D. Babonneau, S. Camelio, F. Pailloux, and M. Denanot. *Evidence for capping-layer effects on the morphology and plasmon excitation of Ag nanoparticles*. Journal of Applied Physics **102**, 113518 (2007). 77, 82

[19] D. Babonneau, S. Camelio, D. Lantiat, L. Simonot, and A. Michel. *Waveguiding and correlated roughness effects in layered nanocomposite thin films studied by grazing-incidence small-angle X-ray scattering*. Physical Review B - Condensed Matter and Materials Physics **80**, 155446 (2009). 77, 84

[20] D. Babonneau. *FitGISAXS: Software package for modelling and analysis of GISAXS data using IGOR Pro*. Journal of Applied Crystallography **43**, 929–936 (2010). 77, 84

[21] C. Templier, S. Muzard, A. Galdikas, L. Pranevicius, J. Delafond, and J. C. Desoyer. *A phenomenological study of the initial stages of film growth*. Surface and Coatings Technology **125**, 129–133 (2000). 81

[22] J. Toudert, S. Camelio, D. Babonneau, M. F. Denanot, T. Girardeau, J. P. EspiÑos, F. Yubero, and A. R. Gonzalez-Elipe. *Morphology and surface-plasmon resonance of silver nanoparticles sandwiched between Si_3N_4 and BN layers.* Journal of Applied Physics **98**, 1–10 (2005). 81, 82

[23] S. Camelio, J. Toudert, D. Babonneau, and T. Girardeau. *Tailoring of the optical properties of Ag:Si_3N_4 nanocermets by changes of the cluster morphology.* Applied Physics B: Lasers and Optics **80**, 89–96 (2005). 84

[24] J. Toudert, D. Babonneau, L. Simonot, S. Camelio, and T. Girardeau. *Quantitative modelling of the surface plasmon resonances of metal nanoclusters sandwiched between dielectric layers: The influence of nanocluster size, shape and organization.* Nanotechnology **19**, 125709 (2008). 84

[25] M.-C. Saint-Lager, A. Bailly, M. Mantilla, S. Garaudée, R. Lazzari, P. Dolle, O. Robach, J. Jupille, I. Laoufi, and P. Taunier. *Looking by grazing incidence small angle X-ray scattering at gold nanoparticles supported on rutile TiO_2(110) during co oxidation.* Gold Bulletin 2008 **41/2**, 159–166 (2008). 84

[26] R. Lazzari, G. Renaud, C. Revenant, J. Jupille, and Y. Borensztein. *Adhesion of growing nanoparticles at a glance: Surface differential reflectivity spectroscopy and grazing incidence small angle X-ray scattering.* Physical Review B **79**, 125428 (2009). 84

[27] T. Wenzel, J. Bosbach, F. Stietz, and F. TrÄger. *In situ determination of the shape of supported silver clusters during growth.* Surface Science **432**, 257–264 (1999). 86

[28] C. Revenant, G. Renaud, R. Lazzari, and J. Jupille. *Growth of Ag on MgO(001) studied in situ by grazing incidence small angle X-ray scattering.* Nuclear Instruments and Methods in Physics Research, Section B: Beam Interactions with Materials and Atoms **246**, 112–117 (2006). 86

Chapter IV

Monitoring the reactivity of Ag nanoclusters for different atmospheres

1 Introduction

The dependency of the optical properties of metal nanoclusters on their morphology and organization as well as on their physical and/or chemical surrounding has been evidenced in the previous chapters. In this regard, we have seen the resourcefulness of real-time SDRS in providing valuable information on reshaping and reactivity effects during and after the formation of the nanoclusters, thanks to the *in situ* configuration. Now, this chapter is devoted to the study of the reactive properties of Ag nanoclusters under the influence of different reactive atmospheres by studying the variations in their optical properties. In this regard, influence of non-ionized gases on the optical properties of Ag nanoclusters are first studied. Here, effect of different parameters (such as cluster size, substrate type, temperature, and gas flux) on the optical properties are documented in real-time and compared with examples present in the literature. Later, the influence of the non-ionized gases are compared with the same partially ionized gases. In addition to this, the structural properties of the Ag nanoclusters are also investigated in detail using *post mortem* HAADF-STEM and GISAXS techniques.

2 State of the art

In case of metal nanoclusters, due to the confinement of valence electrons to the regions smaller than their mean free path, so called quantum confinement effects modify the quantum state of the electrons and introduce modifications in their basic properties, which are totally different than that of their bulk counterparts [1]. Nanoclusters, due to their large surface to volume ratio, show higher reactivity for their surrounding atmospheres, understanding of which

can have potential applications in the field of electro-magnetic devices, photonic devices, gas sensing devices, and in todays catalysis processes. This reactive nature of metal nanoclusters influences their interaction with light and in turn their optical properties. In this regard, Table IV.1 shows a brief summary of research works dedicated to the reactivity of metal nanoclusters for various gases, expressed in terms of their optical response.

Authors	Materials studied	Gas atmosphere	Influence on SPR Amplitude	λ shift	Width
Fernández *et al* [2]	Au/Polyimide,	alcohol vapors,	↑	-	-
& Manera *et al* [3]	Au/TiO_2	dry air,	↓	-	-
		NH_3, NO_2	NE	-	-
Borenzstein *et al*	Au/TiO_2	O_2,	↓	Red shift	↑
[4]		H_2	↑	Blue shift	↓
Brandt *et al* [5]	Na/Quartz,	O_2, N_2O,	↓	Red shift	↑
& Iline *et al* [6]	Na or K/LiF	CO_2,	NE	Blue shift	NE
		N_2	NE	NE	NE
Serna *et al* [1]	Cu/Al_2O_3	O_2	↓	Red shift	↑
Bi *et al* [7] &	Ag/SiO_2, Ag/Quartz,	O_2,	↓	Red shift	↑
Hu *et al* [8, 9]	Ag/Soda-glass	H_2	↑	Blue shift	↓

Table IV.1 – Bibliography survey for reactivity of the metal nanoclusters expressed in terms of their SPR modifications under the influence of different gas atmospheres. (The signs represent usual meanings such that, ↑ = increase, ↓ = decrease, NE = No Effect, and - = no information available.)

From Table IV.1, depending upon the gas, the interaction between gas molecules and the metal clusters can be either reactive/non-reactive, which accordingly affect/do not affect their optical properties. Noble or alkali metal nanoclusters appear non-reactive in presence of gases such as NH_3, NO_2 and N_2. In these systems, unchanged optical properties prove the absence of physical or chemical interactions between the above said gas molecules and the metal nanoclusters [2, 3, 5, 6, 10]. In contrast, reactive gases can cause strong variations in the optical response of metal nanoclusters. These optical variations can be due to the physical and/or chemical interactions of adsorbed gas molecules with the metal clusters, and can be influenced by factors such as cluster nature, substrate nature, temperature etc. In this regard, depending upon the reactive gases, either blue or red-shifted SPR in the metal clusters are observed

together with modifications in the SPR amplitude and width.

Among the reactive gases, organic vapor molecules such as methanol or ethanol, are seen to alter the optical properties of Au nanoclusters [2, 3], which induce an increase in their SPR amplitude without changing the SPR position. Fernández *et al* [2] and Manera *et al* [3] have attributed this improvement in SPR amplitude to Au clusters from Au/TiO_2 systems, which simply act as optical transducers, increasing the refractive index of the surrounding TiO_2 matrix without actually taking major part in the chemical interactions.

In case of gases like CO_2 and H_2, blue-shift of the SPR is more prominent than the modifications in SPR amplitude [4–6, 8, 9]. Brandt *et al* [5] and Iline *et al* [6] have observed this blue-shift in case of alkali metal nanoclusters (such as, Na and K) upon their exposure to CO_2. They have attributed this change to weak physisorption of CO_2 on the cluster surface that modifies the cluster morphology towards a more spherical shape. Another possible reason for such a blue shift can be the charge transfer from CO_2 to the alkali clusters that increases the number of conduction electrons, resulting in a higher energy of the SPR (i.e., resonance shifts to lower wavelengths) [5]. However, they have ruled out this possibility as SPR amplitude and width remain unchanged. On the other hand, in case of H_2, even though blue-shift is evident in the SPR of Ag or Au nanoclusters, the variations in the amplitude can be substrate-dependent along with a confirmed narrowing of the SPR width [4, 8, 9]. These optical modifications not only support possible shape variations in the clusters (towards a more spherical shape) due to adsorbed H_2 molecules, but also possible charge transfer from H_2 molecules to metal clusters.

Out of all above gases, the reactivity of O_2 is found to be stronger with a wide range of metal nanoclusters, such as Na, K, Ag, Au, and Cu, which always causes a sharp red-shift in SPR position, as well as a prominent SPR damping and broadening [1, 4–6, 8, 9]. In a general representation of the O_2 influence on the metal nanoclusters, it can be theoretically explained by a "core-shell" schematics consisting of a metal cluster core surrounded by an oxide shell of that metal (Fig.IV.1) [5, 6]. Such oxide shells around the clusters not only induce modifications in their morphology (size and shape), but also change their surrounding dielectric medium. As such basic parameters regarding the metal clusters change, modifications in their SPR become inevitable. These modifications in the SPR characteristics are discussed below in details along with possible explanations.

The damping in SPR amplitude of metal nanoclusters due to O_2 can be a combined effect. Because adsorption of O_2 molecules on the cluster surface decreases the active metal content, (i.e. less metal amount interacts with light), the SPR amplitude decreases accordingly [5, 6]. Also, charge transfer from the metal clusters to O_2 species is possible, which decreases

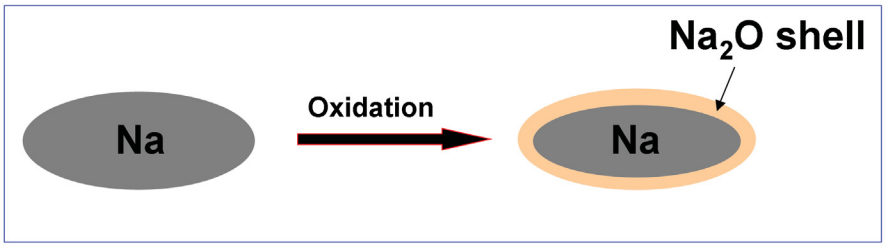

Figure IV.1 – A typical theoretical presentation of the "core-shell" schematics in case of Na clusters surrounded by a Na_2O shell [5]. Note the possible modification in the morphology of the metallic core.

the density of in-phase conduction electrons and in turn reduces the SPR amplitude accordingly [4–6].

Similarly, **the red-shift in the SPR position** can be related to several reasons. One of them is a basic factor such as the cluster shape. O_2 molecules upon adsorption can change the surface energy of the clusters, which in turn can alter their shapes accordingly. Some authors have reported such cluster shape variations, both theoretically and experimentally. For example, with the help of "core-shell" simulations, Brandt *et al* and Iline *et al* have shown a prominent red-shift in SPR position of Na clusters due to the decrease in the cluster aspect ratio with increasing the oxide shell thickness [5, 6]. Y. Borenzstein *et al* [4] have shown with optical simulations that Au clusters become slightly oblate upon their interactions with O_2 species. Similar results are shown using GISAXS structural characterizations by Serna *et al* [1] in case of Cu clusters exposed to O_2. Other than shape variations, importantly, formation of oxide shells can increase the dielectric surrounding of the metal nanoclusters, hence, change the SPR position towards higher wavelengths [5, 6].

Moreover, the **increase in SPR width** can also be related to the interactions of conduction electrons with the adsorbed O_2 species [4–6]. The engaged electrons in oxides can not follow the in-phase electrons of the metal clusters during their interactions with light, hence they disturb the in-phase excitations [4, 5]. This so called "chemical interface damping" increases the SPR width and is more evident in the smaller nanoclusters than in the bigger ones [6, 11].

Hence, due to the reactive nature of the metal nanoclusters under different gas atmospheres, changes in their optical properties can be studied by means of an optical probe efficiently. In this regard, further sections of this chapter will reveal the usefulness of the real-time SDRS for monitoring the optical modifications in metal nanoclusters when they are subjected to different gas atmospheres, either in non-ionized form or in ionized form.

3 Reactivity of the metal nanoclusters for non-ionized gas atmospheres

3.1 Experimental details

In the present work, Ag nanoclusters are chosen as active sites because of their sensitivity towards the surrounding atmospheres. The method and procedure for the fabrication of the Ag clusters is kept same as explained in Chapter III. Furthermore, majority of the work is focused on the O_2 gas, as the modifications it induces in the optical properties of the Ag nanoclusters are prominent and distinct. However, effect of non-reactive gases from literature, such as N_2 and Ar, are also verified during the course of this study. The schematics of the magnetron deposition chamber for studying the nanocluster reactivity for different gases is shown in Fig.IV.2(a).

Pure gases are first filtered for dust, and then a controlled flux (in standard cubic centimeters per minute (sccm)) is introduced in the deposition chamber, either at the target surface through a gas inlet or in the vicinity of the sample by means of a gas ring. Generally, during the pre-sputtering and sputtering steps, Ar is introduced at the target surface for creating an Ar^+ plasma. In contrast, the gas, whose reactivity with Ag nanoclusters is to be studied, is introduced at the sample surface after the formation of the nanoclusters (Fig.IV.2(b)). In that way, the deposited Ag nanoclusters, after sufficient relaxation time, are exposed to gases in a non-ionized form. For *in situ* and real-time SDRS, the data acquisition starts well before the Ag deposition and then the essential modifications in the optical properties due to the reactive interactions of the clusters with the surrounding gas species are captured continuously.

It is worth noting that the partial pressures of all the gases can be measured in real-time thanks to the *in situ* mass-spectrometer. In this regard, a minimum gas flux of 0.3 sccm corresponds to different partial pressures in case of O_2, N_2, and Ar such as 1×10^{-4} mbar, 6×10^{-4} mbar and 9×10^{-4} mbar, respectively. This is because the pumping speed sensitively depends on the respective gas species. The time required for the gas flux to attain a specified value during its injection in the deposition chamber was found to be around 8s. At the end of the reactivity measurements, gases are completely removed from the sputtering chamber by the cryogenic vacuum pump, thus bringing the respective partial pressure back to zero in around 15s.

3.2 Reactivity of Ag clusters under O_2 atmosphere

In this section, Ag nanoclusters supported on a Si_3N_4 buffer-layer are exposed to O_2, which is used as a reactive gas, with the minimum possible flux (i.e., 0.3 sccm $\equiv$ 10^{-4} mbar par-

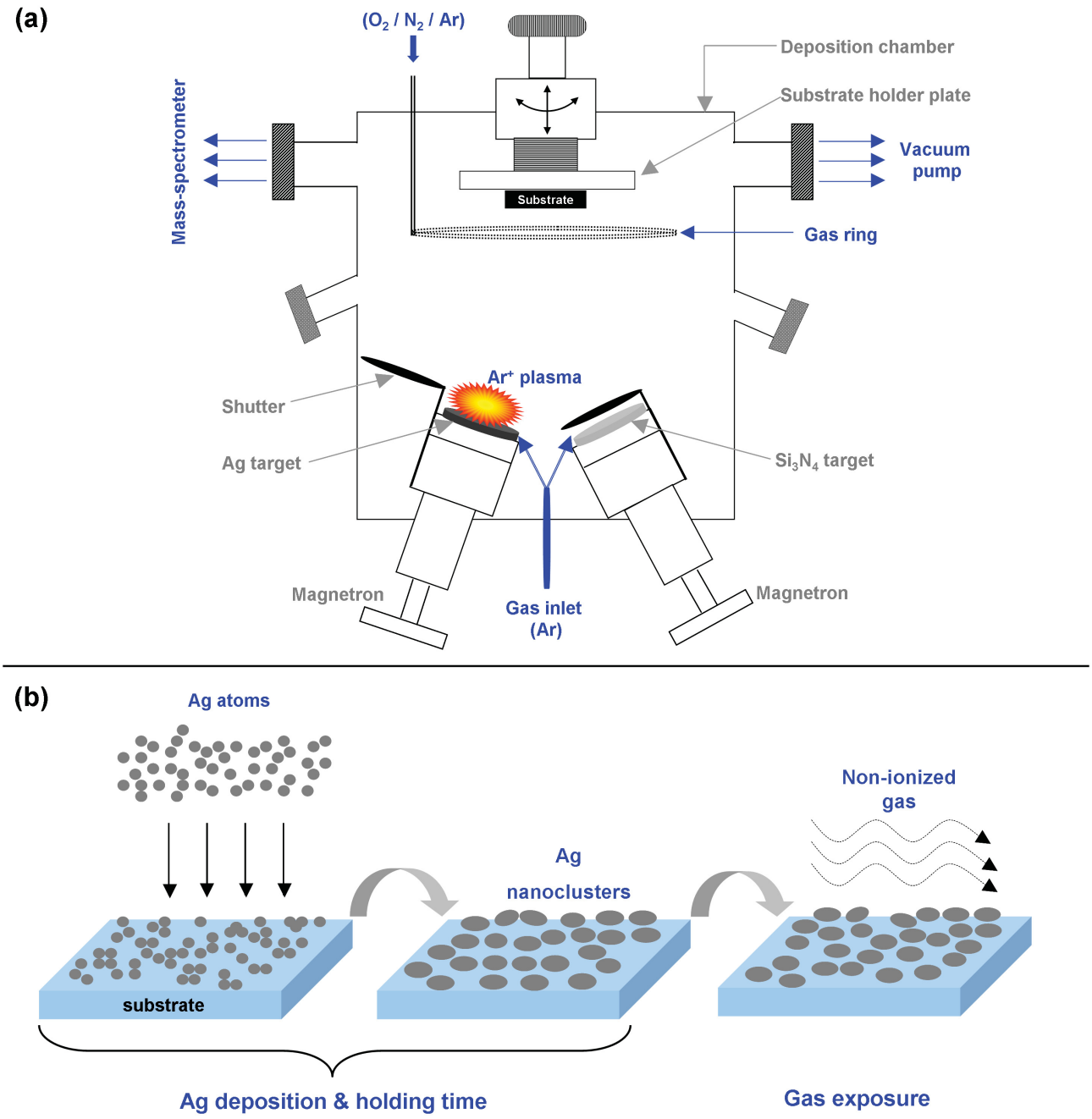

Figure IV.2 – Experimental study for the reactivity of nanoclusters consisting the schematics of: (a) Magnetron deposition chamber, showing possible entrance for the gases, and (b) The experimental steps where, after the Ag deposition and holding time, Ag nanoclusters are exposed to different gas atmospheres.

tial pressure) and sufficient time duration. The oxidized Ag clusters are then covered by a Si_3N_4 capping-layer, in order to form Si_3N_4:Ag(with O_2):Si_3N_4 nanocomposites similar to the Si_3N_4:Ag(w/o O_2):Si_3N_4 nanocomposites tri-layers discussed in the previous chapter. The tem-

perature was maintained at 200°C throughout the deposition. To understand the influence of the O_2 exposure on the nanostructural and optical properties of the Ag clusters, Si_3N_4:Ag(with O_2):Si_3N_4 nanocomposites with different Ag deposition times/effective thicknesses (10s/1nm, 20s/2nm, and 40s/4nm) are studied, as given in Table IV.2. The results are later compared to those obtained from Si_3N_4:Ag(w/o O_2):Si_3N_4 nanocomposites with equivalent Ag amounts.

#	Deposition step		Step duration (s)	Effective thickness (nm)	Magnetron power (W)	Ar flow (sccm)	N_2 flow (sccm)
0.	Si_3N_4 sputtering		600	20	176 (RF)	3	0.3
1.	Ag sputtering		10/20/40	1/2/4	24 (DC)	18	–
2.	Holding time		600	–	–	–	–
3.	O_2 exposure (0.3 sccm)		600	–	–	–	–
4.	Ignition and pre-sputtering of Si_3N_4	(a)	150	–	88 (RF)	90	–
		(b)	600	–	88 (RF)	3	–
		(c)	150	–	132 (RF)	3	0.3
		(d)	150	–	176 (RF)	3	0.3
5.	Si_3N_4 sputtering		1200	40	176 (RF)	3	0.3

Table IV.2 – Experimental parameters during the alternate deposition of Si_3N_4:Ag:Si_3N_4 nanocomposites at 200°C with different Ag deposition time/thickness exposed to a controlled O_2 atmosphere.

3.2.1 *Post mortem* nanostructure analysis

As a typical comparative example, Fig.IV.3 shows the SDRS signals recorded at the end of the depositions together with the corresponding HAADF-STEM micrographs and GISAXS patterns of Si_3N_4:Ag(w/o O_2):Si_3N_4 and Si_3N_4:Ag(with O_2):Si_3N_4 nanocomposites for 10s deposition of Ag. In this case, there is no obvious difference to naked eyes between the sample exposed to O_2 and the non-exposed one. However, as given in Table IV.3 and Fig.IV.4, the quantitative analysis of the HAADF-STEM and GISAXS data shows that the exposure to O_2 causes weak modifications in the nanostructure of the Ag clusters, such as:

- a weak decrease of the areal cluster density d (i.e. inter-cluster distance Λ weakly increases),
- a weak increase of the in-plane cluster size D,
- a weak decrease of the out-of-plane aspect ratio H/D.

These observations are in accordance with the results reported by Serna *et al* [1] and Borensztein *et al* [4], which evidence a weak flattening of the clusters (Cu/Al_2O_3 and Au/TiO_2, respectively) after O_2 exposure along with no dramatic changes in the in-plane structural parameters. Hence, these weak modifications in the nanostructure of the Ag clusters seem to have

no influence on the optical signals at the end of the experiment.

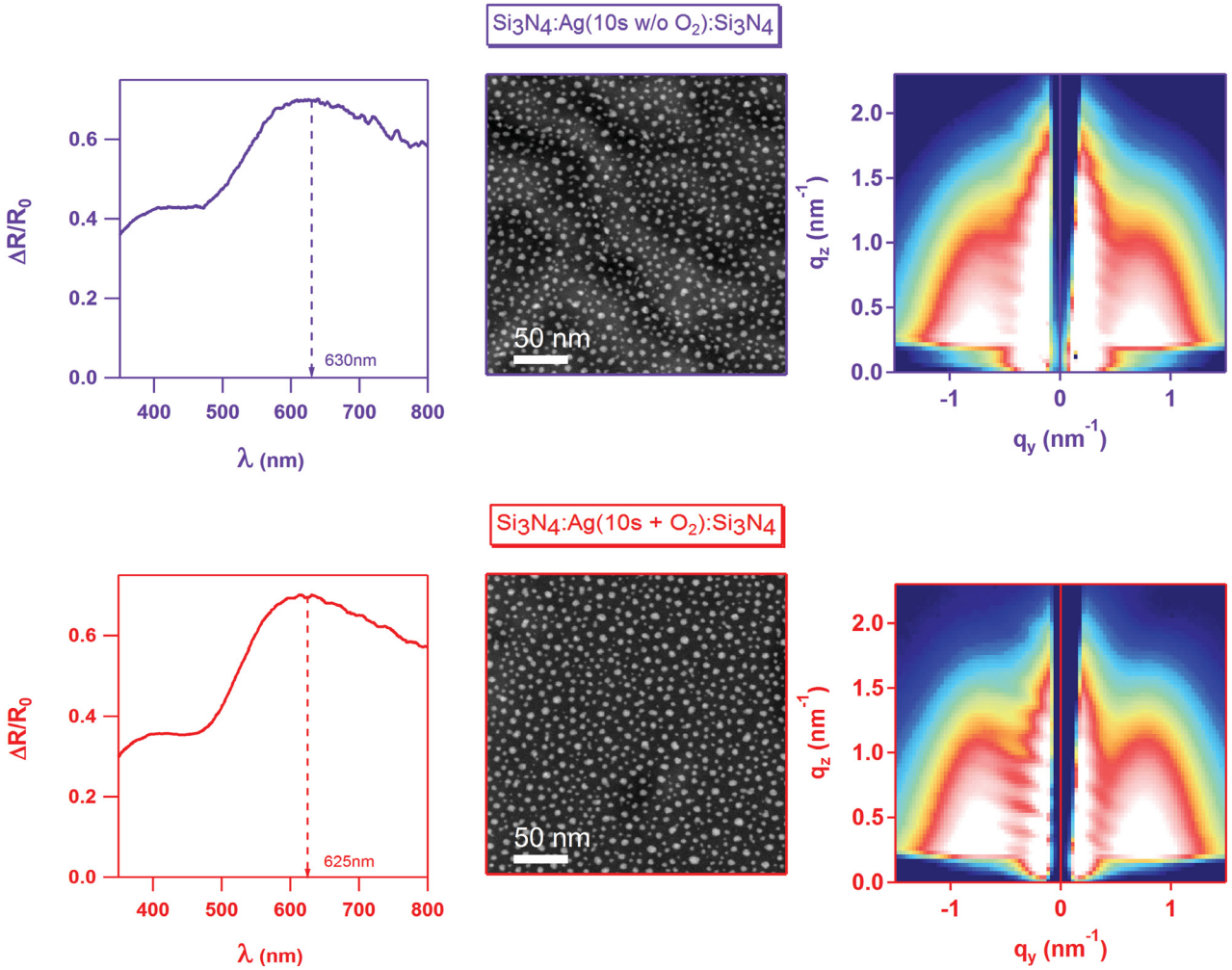

Figure IV.3 – SDRS signals at the end of the deposition, HAADF-STEM micrographs and GISAXS patterns of Si_3N_4:Ag(10s/1nm):Si_3N_4 nanocomposites, Ag nanoclusters of which being non-exposed/exposed to O_2, respectively. The corresponding nanocluster parameters are collected in Table IV.3.

3.2.2 *In situ* and real-time SDRS analysis

A comparison of temporal variations in the SPR amplitude $(\Delta R/R_0)_{max}$ and position λ_{max} for Si_3N_4:Ag(10s+O_2):Si_3N_4 and Si_3N_4:Ag(10s w/o O_2):Si_3N_4 nanocomposites is shown in Fig.IV.5, and the spectral variations at the end of each deposition step are shown in Fig.IV.6.

- **STEP 1 & 2 -** During the Ag deposition and holding time, due to the similar deposited Ag amount, as expected, almost overlapped SDRS signals are observed. At the end of

Si_3N_4:Ag:Si_3N_4 nanocomposites	HAADF-STEM analysis					GISAXS analysis	
Ag deposition time/thickness	d (μm^{-2})	Coverage (%)	D (nm)	σ_D (nm)	Λ (nm)	(H/D) ratio	H (nm)
Ag(10s/1nm) (w/o O_2)	11186	23	4.5	1.6	10.2	0.85	3.8
Ag(10s/1nm) (with O_2)	9906	21	4.8	1.6	11.0	0.81	3.9
Ag(20s/2nm) (w/o O_2)	4318	35	9.0	2.5	15.5	0.61	5.5
Ag(20s/2nm) (with O_2)	3894	34	9.4	2.6	16.5	0.57	5.4
Ag(40s/4nm) (w/o O_2)	1427	42	18.7	5.3	25.8	0.46	8.6
Ag(40s/4nm) (with O_2)	1252	41	18.2	5.5	26.0	0.44	8.0

Table IV.3 – Nanostructural analysis for Ag clusters from Si_3N_4:Ag:Si_3N_4 nanocomposites exposed or not to a controlled non-ionized O_2 atmosphere.

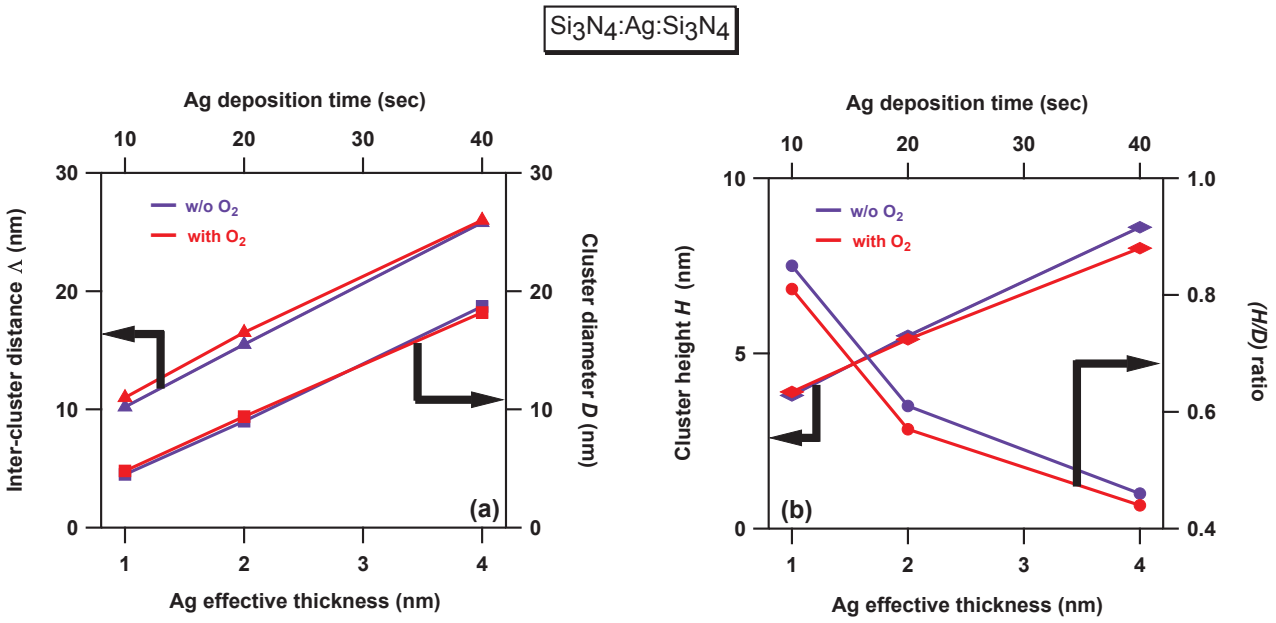

Figure IV.4 – Variations of nanostructure parameters of Ag nanoclusters subjected to O_2 from Si_3N_4:Ag(with O_2):Si_3N_4 nanocomposites as a function of Ag deposition time/thickness, compared with the respective Ag nanoclusters from Si_3N_4:Ag(w/o O_2):Si_3N_4 samples. The respective nanostructure parameters are collected in Table IV.3.

STEP 2, Fig.IV.6(a) shows clearly that the SPR maximum lies around 480nm for both samples.

- **STEP 3 -** During the exposure of the Ag clusters to the non-ionized O_2 flux of 0.3 sccm, λ_{max} strongly increases from 480nm to 560nm while $(\Delta R/R_0)_{max}$ decreases from 0.18 to 0.15 accompanied by an increase of the SPR width (Fig.IV.6(a-b)), comparing to the

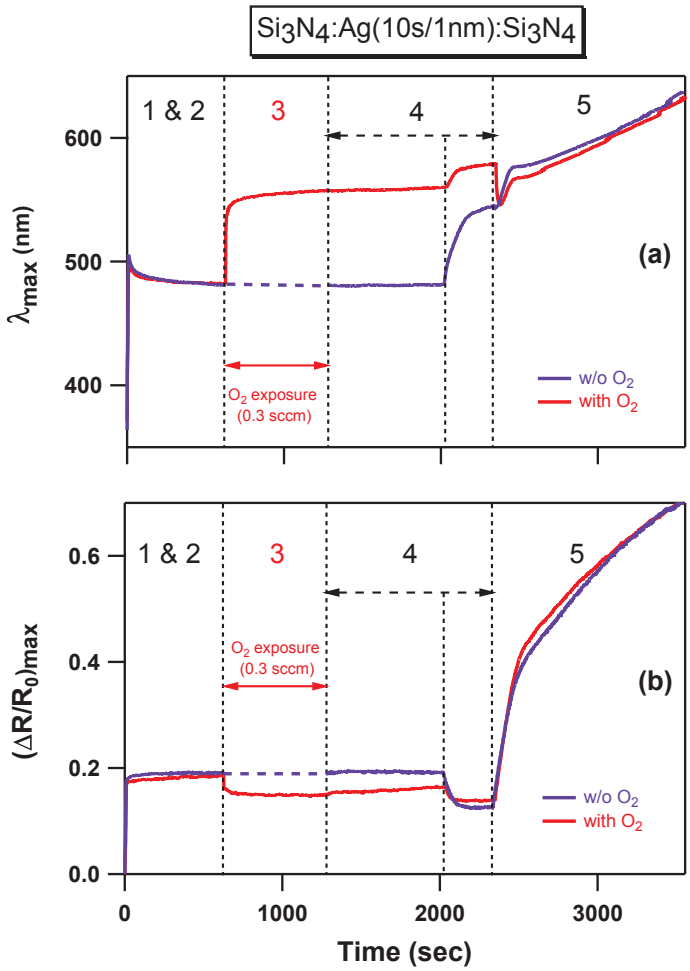

Figure IV.5 – Comparison for temporal variations of λ_{max} (a) and $(\Delta R/R_0)_{max}$ (b) during the deposition of Si_3N_4:Ag(w/o O_2):Si_3N_4 and Si_3N_4:Ag(with O_2):Si_3N_4 nanocomposites. To achieve this comparison, time scale for the nanocomposite without O_2 (w/o O_2) is adjusted accordingly (violet dashed lines). The spectral variations at the end of each deposition steps are shown in Fig.IV.6. The experimental details and discussions for each deposition step are given in the text.

non-exposed sample. These optical modifications are in accordance with the literature [1, 4–6, 8, 9, 12], reasons of which we have already discussed in Section 2 of this Chapter. Moreover, the *in situ* SDRS signals in Fig.IV.5 shows that such prominent optical modifications take place immediately (within first 3s) when the Ag clusters are exposed to O_2. It is worth noting that the optical signals remain constant with increasing exposure time and are persistent even after the removal of O_2 from the deposition chamber, giving an idea about the permanent interactions between the Ag nanoclusters and the adsorbed O_2 species.

- **STEP 4 -** During the ignition and pre-sputtering of the Si_3N_4 target, upon introduction

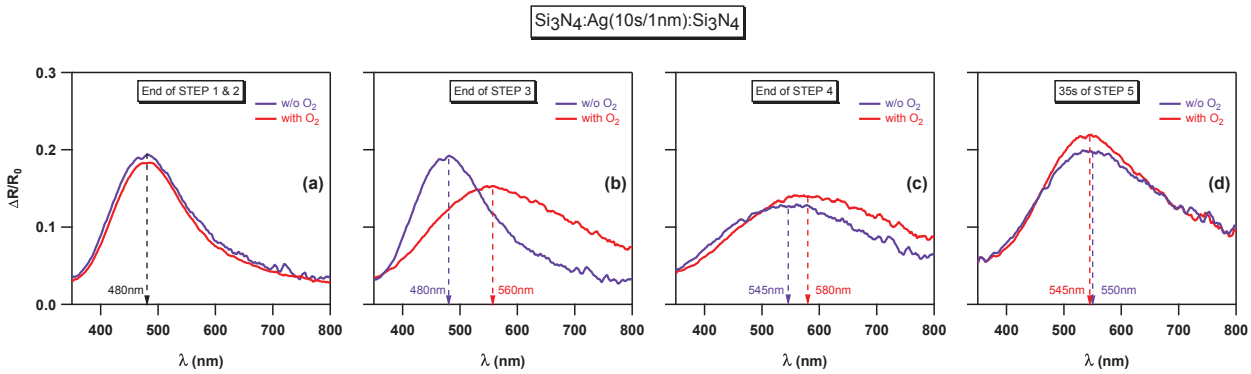

Figure IV.6 – Comparison for spectral variations during the deposition of Si_3N_4:Ag(w/o O_2):Si_3N_4 and Si_3N_4:Ag(with O_2):Si_3N_4 nanocomposites. (a-c): at the end of deposition STEP 2 to 4. (d): after the first 35s of Si_3N_4 deposition during STEP 5. The spectral variations at the end of STEP 5 are already presented in Fig.IV.3.

of N_2 in the deposition chamber, the influence of partially ionized nitrogen species on the Ag clusters leads to a red-shift together with a damping of the SPR, as we have discussed in the previous chapter (Section 5.3.3, Chapter III). However, comparing to the non-oxidized Ag clusters, the effects are less pronounced. This can be seen in Fig.IV.6(b-c) where the SPR position changes from 560nm to 580nm, comparing to the non-exposed sample (from 480nm to 545nm). This reduced affinity of partially ionized nitrogen species with the oxidized Ag clusters again tends to confirm the presence of less Ag metal, and the further charge transfer from oxidized Ag clusters to nitrogen species may be possible.

- **STEP 5 -** At the very beginning of the Si_3N_4 capping-layer deposition (first 35s corresponding to an effective thickness around 1.2nm), the SDRS signals of the Si_3N_4:Ag(w/o O_2):Si_3N_4 and Si_3N_4:Ag(with O_2):Si_3N_4 nanocomposites exhibit very different variations. While a continuous red-shift of the SPR is observed for the non-oxidized clusters (as seen in Section 5.3.4, Chapter III), the SPR of the oxidized clusters is first sharply blue-shifted (from 580nm to 545nm in Fig.IV.6(c-d)), and is then subjected to a progressive red-shift with further increase of the deposition time. Even though the blue-shift effect is ambiguous, it suggests that the Si_3N_4 capping induces a fast desorption of the oxygen species interacting with the oxidized nanoclusters, which in turn causes an opposite effect in terms of SPR shift (comparing to the capping effect on the non-oxidized Ag nanoclusters). In addition, although the determination of the cluster shape at this point of measurement is not possible, an increase of the average out-of-plane aspect ratio owing to modifications of the surface/interface energies cannot be ruled out.

  In contrast to the λ_{max} evolution, the $(\Delta R/R_0)_{max}$ variations are very similar for both

samples, with the SPR amplitude steadily increasing during the Si_3N_4 deposition. As discussed in the previous Chapter (Section 5.3.4), this behavior can be partly ascribed to the increase of the dielectric surrounding of the nanoclusters. The almost identical spectral signals of these two samples at the end of the experiments can be seen in Fig.IV.3.

3.2.3 Effect of Ag amount on the reactivity of the nanoclusters

Fig.IV.7 displays the real-time SDRS signals of the Si_3N_4:Ag(with O_2):Si_3N_4 nanocomposites with different Ag amounts (10s/1nm, 20s/2nm, and 40s/4nm, respectively). The corresponding structural information obtained from *post mortem* HAADF-STEM and GISAXS analysis are gathered in Table IV.3, which shows that the average in-plane cluster size D increases with the deposited Ag amount, whereas the average out-of-plane aspect ratio H/D decreases.

Si_3N_4:(Ag+O_2):Si_3N_4 nanocomposites - STEP 3			
Ag deposition time/thickness	D (nm)	$\Delta\lambda_{\max}$ (nm)	% variation $(\Delta R/R_0)_{\max}$
Ag(10s/1nm)	4.8	+80	-21
Ag(20s/2nm)	9.4	+55	-28
Ag(40s/4nm)	18.2	+35	-7

Table IV.4 – Effect of O_2 (STEP 3) on the optical properties of Ag nanoclusters from Si_3N_4:Ag:Si_3N_4 nanocomposites expressed in terms of variation in λ_{max} ($\Delta\lambda_{\max}$) and % variation of $(\Delta R/R_0)_{\max}$.

After the primary steps, such as Ag deposition (STEP 1) and holding time (STEP 2), the effect of the O_2 exposure (STEP 3) is evident, showing a sharp red-shift (Fig.IV.7(a)) and a damping (Fig.IV.7(b)) of the SPR whatever the deposited Ag amount. However, as seen in Fig.IV.7(c-e) and Table IV.4, the variations of $\lambda_{\max}$ and $(\Delta R/R_0)_{\max}$ upon O_2 exposure tend to be less pronounced when the Ag amount increases. This result confirms that the larger the clusters are, the less reactive they are [7, 13]. Moreover, it can be seen in Fig.IV.7(a) that a fast SPR blue-shift occurs at the beginning of STEP 5 for all the three samples. As explained in Section 3.2.2 (STEP 5) of this chapter, such a blue-shift effect may be due to a delicate interplay between oxygen desorption and cluster reshaping during the deposition of the Si_3N_4 capping-layer. Nevertheless, the fastness of this phenomenon suggests that oxygen desorption is the dominant effect in that case. Also, the blue-shift tends to be less pronounced when the Ag amount increases, which is in agreement with a lower reactivity of the larger clusters compared to the smaller ones.

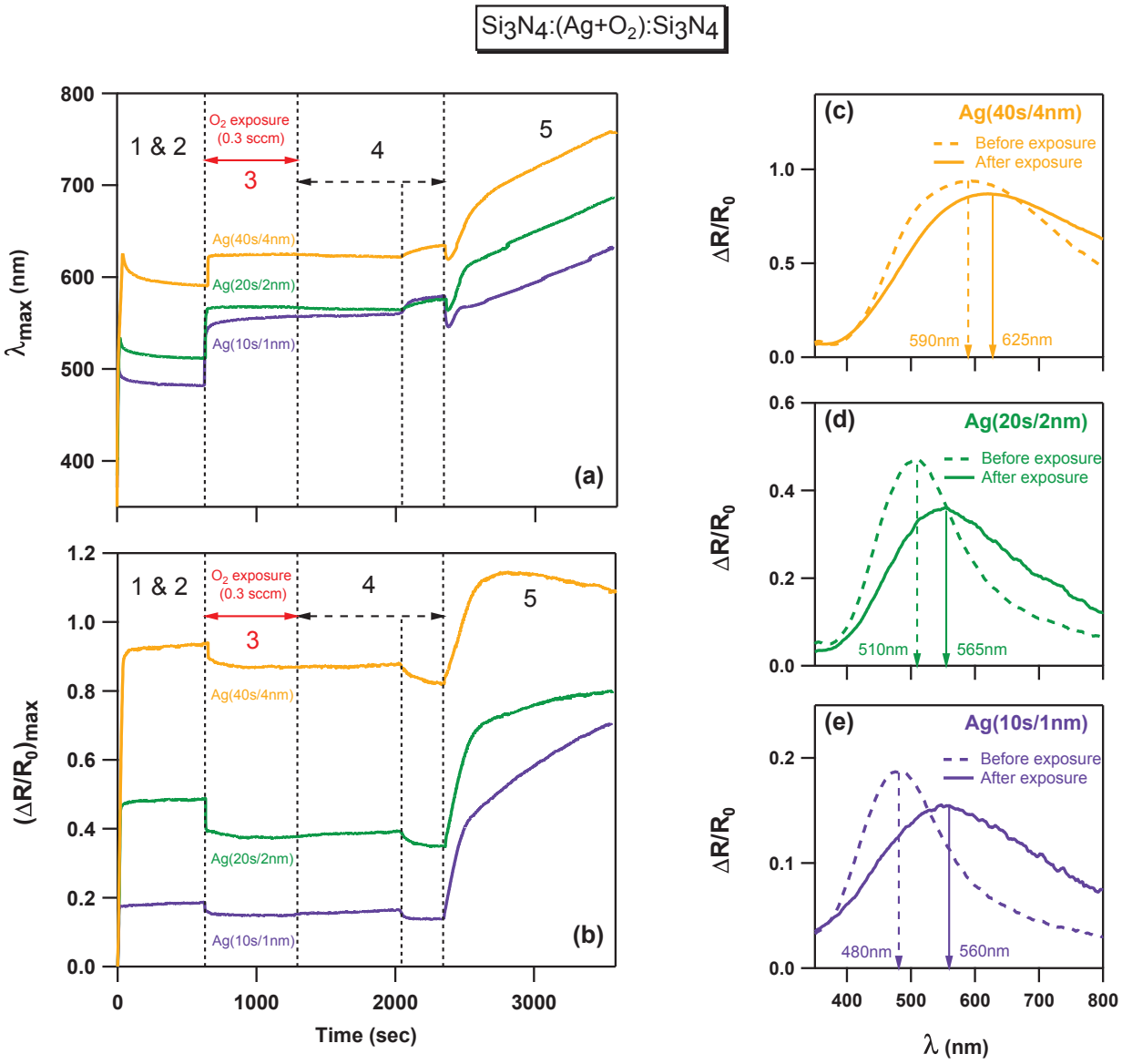

Figure IV.7 – Comparison for temporal variations of λ_{max} (a) and $(\Delta R/R_0)_{max}$ (b) during the Si_3N_4:Ag:Si_3N_4 nanocomposite depositions with increasing Ag deposition time/amount (10s/1nm to 40s/4nm), Ag nanoclusters of which are exposed to O_2.(c-e) represent the spectral variations in the SPR of the Ag nanoclusters before (around 600s - dashed curves) and after (around 1200s - solid curves) the exposure. The experimental details for each deposition step (from STEP 1 to STEP 5) are given in Table IV.2

3.3 Influence of different parameters on the reactivity of Ag nanoclusters with non-ionized gas

After a comparative optical and nanostructural study for O_2 exposed/non-exposed Ag nanoclusters, the influence of different parameters, such as, O_2 partial pressure, substrate type,

and deposition temperature on the reactivity of Ag clusters, are studied. For this purpose, a relatively simple system is chosen in the form of glass-supported Ag nanoclusters, which are exposed to a gas flux ranging from 0.3 sccm ($\equiv 1 \times 10^{-4}$ mbar) to 20 sccm ($\equiv 4.5 \times 10^{-3}$ mbar). The schematics for this experimental procedure is shown in Fig.IV.2(b). Due to the relatively simple Glass:Ag system, the real-time SDRS measurements become shorter than that of the Si_3N_4:Ag:Si_3N_4 nanocomposites. However, it should be noted that, as the Ag nanoclusters are not covered by a dielectric matrix, their *post mortem* HAADF-STEM and GISAXS characterizations were not carried out.

3.3.1 Effect of O_2 partial pressure

In order to understand the effect of the O_2 partial pressure on the optical properties of Ag nanoclusters grown on a glass substrate, a Glass:Ag(20s/2nm) sample was subjected to an increasing O_2 flux from 0.3 to 20 sccm by steps of 2 sccm each 150s. Fig.IV.8(a-b) displays the temporal variations of λ_{max} and $(\Delta R/R_0)_{max}$ along with the variations of the corresponding O_2 partial pressure.

It is clear that the minimum O_2 flux of 0.3 sccm ($\equiv 1 \times 10^{-4}$ mbar) is sufficient to cause an immediate and prominent red-shift as well as a strong damping of the SPR. Even so, as shown in Fig.IV.8(c) (which represents a zoom at the introduction of O_2), it is worth noting here that an overshoot of O_2 flux can be observed which actually corresponds to 2 sccm ($\equiv 7 \times 10^{-4}$ mbar) for around 15s before stabilization to a set-point value of 0.3 sccm. This overshoot is the response by a feedback system of the O_2 flux assigned value. But, as the optical modifications in the Ag nanoclusters are already caused during this period, they may be ascribed to the O_2 flux of 2 sccm and not to the assigned value of 0.3 sccm. Although further increase of the O_2 flux leads to similar red-shift and damping effects, the phenomenon is much weaker and tends towards saturation. In addition to this, Fig.IV.8(a-b) shows that the oxidation effects are irreversible, even when O_2 is completely removed from the deposition chamber, thus confirming strong interaction processes between the Ag clusters and the oxygen species.

3.3.2 Effect of substrate

Fig.IV.9 displays the temporal variations of the SDRS signals showing the influence of O_2 on the reactivity of the Ag nanoclusters grown on glass substrates at 200°C for increasing Ag amounts. The results can be compared with the data obtained after Ag growth on Si_3N_4 buffer-layers as substrates (from previous section, see Fig.IV.7) during the primary steps like, Ag deposition (STEP 1), Holding time (STEP 2), and O_2 exposure (STEP 3).

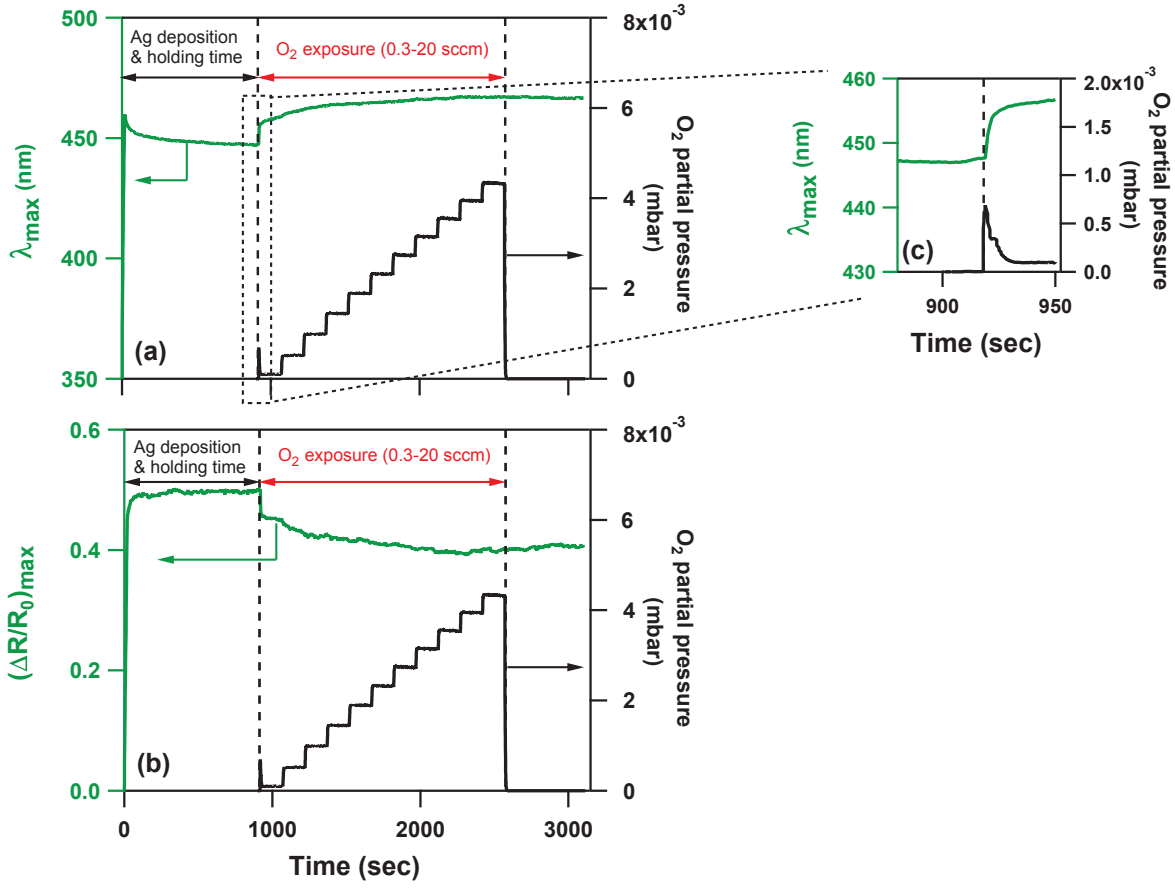

Figure IV.8 – Temporal variations of λ_{max} (a) and $(\Delta R/R_0)_{max}$ (b) during the Ag(20s/2nm) deposition on a glass substrate along with the O_2 partial pressure to which the Ag nanoclusters are exposed. (c) shows a zoom over the time range where O_2 is introduced.

- **Ag deposition and holding time -** The λ_{max} and $(\Delta R/R_0)_{max}$ values determined at the end of the Ag deposition step are compared in Table IV.5 for the glass and Si_3N_4 substrates and different Ag deposition times/amounts. With the increasing Ag amount, the increase of λ_{max} and $(\Delta R/R_0)_{max}$ is obvious for both substrates. Nevertheless, λ_{max} values are significantly lower for glass-supported Ag clusters than for Si_3N_4-supported ones, while $(\Delta R/R_0)_{max}$ values appear to be similar for both substrates. The difference in λ_{max} at the end of the Ag deposition step may arise either from the difference in the refractive indices of the substrates (n_{glass} ~1.5 < $n_{Si_3N_4}$ ~2) [12], or from the presence of more spherical Ag nanoclusters supported on glass than on Si_3N_4 [11].

  In addition to this, during the holding time, smaller SPR blue-shifts for glass-supported Ag clusters are evident comparing to Si_3N_4-supported Ag clusters (Table IV.5). It may be tempting to ascribe this behavior to a reshaping effect more pronounced for Ag clusters

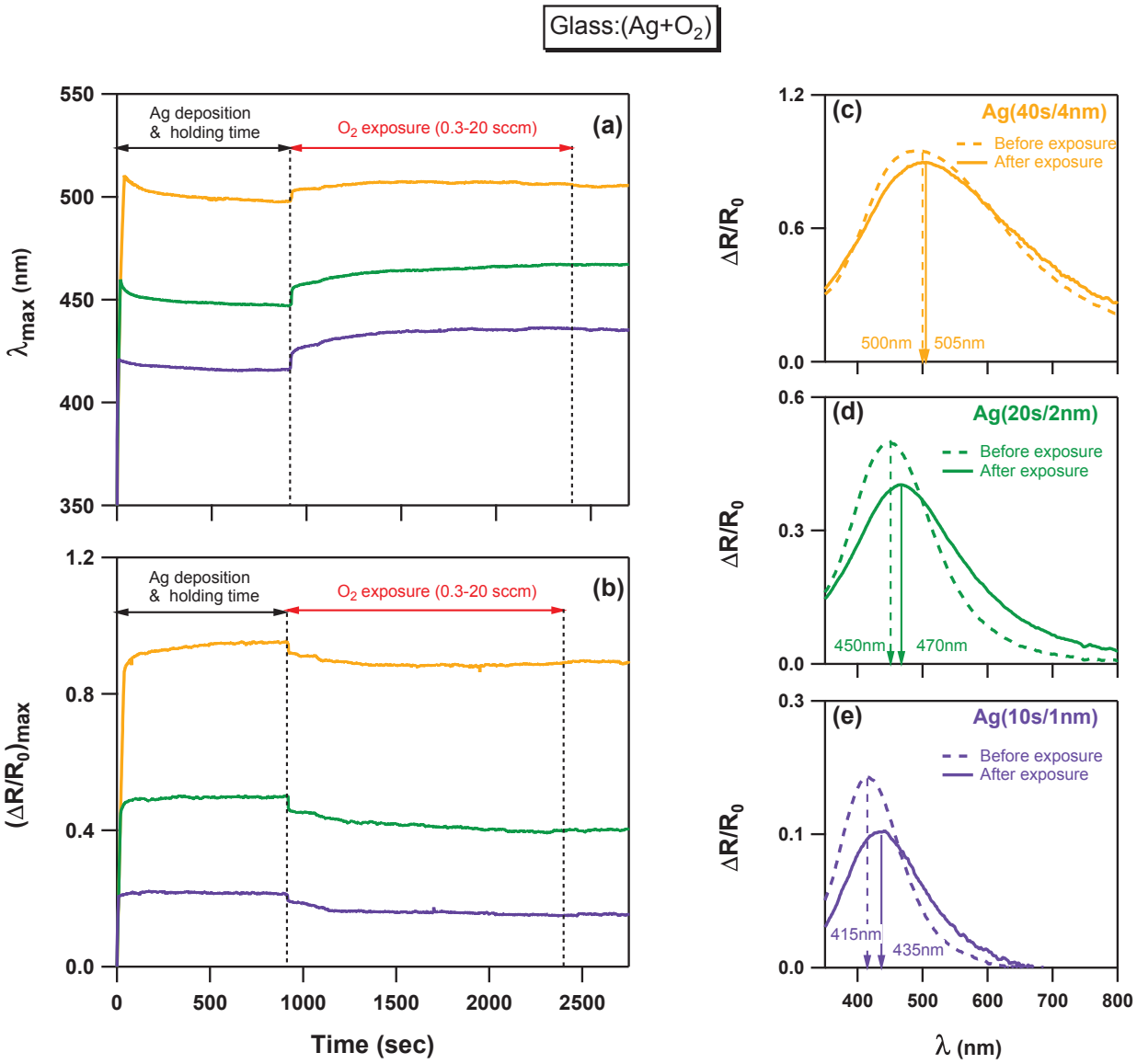

Figure IV.9 – Comparison for temporal variations of λ_{max} (a) and $(\Delta R/R_0)_{max}$ (b) during the deposition of different Ag amounts (10s/1nm, 20s/2nm and 40s/4nm) on glass substrates and their exposure to O_2 flux from 0.3-20 sccm. The experimental parameters for Ag depositions are kept same as given in Table IV.2, except the holding time changed to 900s instead of 600s as in previous cases. (c-e) represents the variation in the SPR of the Ag nanoclusters before (dashed curves) and after (solid curves) their exposure to O_2 gas.

deposited on Si_3N_4, owing to a more oblate shape. However, it should be noted that the wavelength position of the SPR is not expected to vary linearly with the out-of-plane aspect ratio of the nanoclusters (Section 4.2.3, Fig.II.9, Chapter II). Also, as the average size and shape of the nanoclusters deposited on glass and on Si_3N_4 are most likely

different, there is no clear meaning of such different blue-shifts during the holding time.

STEP	At the end of Ag deposition				During holding time	
Ag deposition time/thickness	λ_{max} (nm) on Glass	λ_{max} (nm) on Si_3N_4	$(\Delta R/R_0)_{max}$ on Glass	$(\Delta R/R_0)_{max}$ on Si_3N_4	$\Delta\lambda_{max}$ (nm) on Glass	$\Delta\lambda_{max}$ (nm) on Si_3N_4
Ag(10s/1nm)	420	505	0.20	0.18	-5	-20
Ag(20s/2nm)	460	535	0.45	0.45	-11	-23
Ag(40s/4nm)	510	625	0.87	0.87	-13	-35

Table IV.5 – Comparison for the values of λ_{max} and $(\Delta R/R_0)_{max}$ at the end of respective Ag depositions on glass or Si_3N_4 substrates along with the absolute variations in λ_{max} ($\Delta\lambda_{max}$) during the holding time.

- **O_2 exposure (0.3 - 20 sccm) -** Upon O_2 exposure, the SPR of glass-supported Ag nanoclusters shows an immediate red-shift (within 3s) whatever the deposited Ag amount, as already shown for Ag clusters deposited on Si_3N_4 substrates (Section 3.2.2 of the present Chapter). However, from Table IV.4 and IV.6, it can be seen that the red-shifts ($\Delta\lambda_{max}$) for the glass-supported Ag clusters are much smaller than the corresponding values for the Si_3N_4-supported Ag clusters. It is well-known that the oxidation resistance of Si_3N_4 is remarkable at room temperature [14–16], which may hinder the possible interactions of oxygen species with the Si_3N_4 surface under O_2 exposure. In contrast, due to its non-reducible nature [17–19], adsorption of oxygen species on glass is more likely. Hence, the lower reactivity of glass-supported Ag clusters may be due to the presence of more adsorption sites of O_2 on glass than on Si_3N_4. However, it has been shown before that the reactivity of the clusters strongly depends on their size (Section 5.3, Table III.6, Chapter III). Accordingly, the formation of larger clusters on glass than on Si_3N_4 cannot be ruled out.

O_2 exposure - 0.3-20 sccm		
Glass/ ($Ag+O_2$)	$\Delta\lambda_{max}$ (nm)	% variation $(\Delta R/R_0)_{max}$
Ag(10s/1nm)	+20	-41
Ag(20s/2nm)	+20	-25
Ag(40s/4nm)	+5	-8

Table IV.6 – Effect of O_2 exposure on the optical properties of Ag nanoclusters supported on glass substrates, expressed in terms of absolute variations in λ_{max} ($\Delta\lambda_{max}$) and relative variations in $(\Delta R/R_0)_{max}$ for different Ag deposition time/amount.

In addition to this red-shift, the SPR of the Ag clusters deposited on glass also shows an immediate damping upon O_2 exposure. Comparing the values reported in Table IV.4

and Table IV.6, it is worth noting that the $(\Delta R/R_0)_{\max}$ relative variations seem to be almost similar irrespective of the substrate, with the effect being much stronger at low Ag deposition time. These results confirm again that the larger the clusters are, the less reactive they are. To stress further this point, the reactivity of a continuous Ag layer (160s/16nm) deposited on glass was also studied. Because of the absence of a prominent SPR maximum, the evolution of amplitude $(\Delta R/R_0)$ recorded at the wavelength of 700nm is shown in Fig.IV.10 as a typical example, which evidences the negligible reactivity of such a continuous layer.

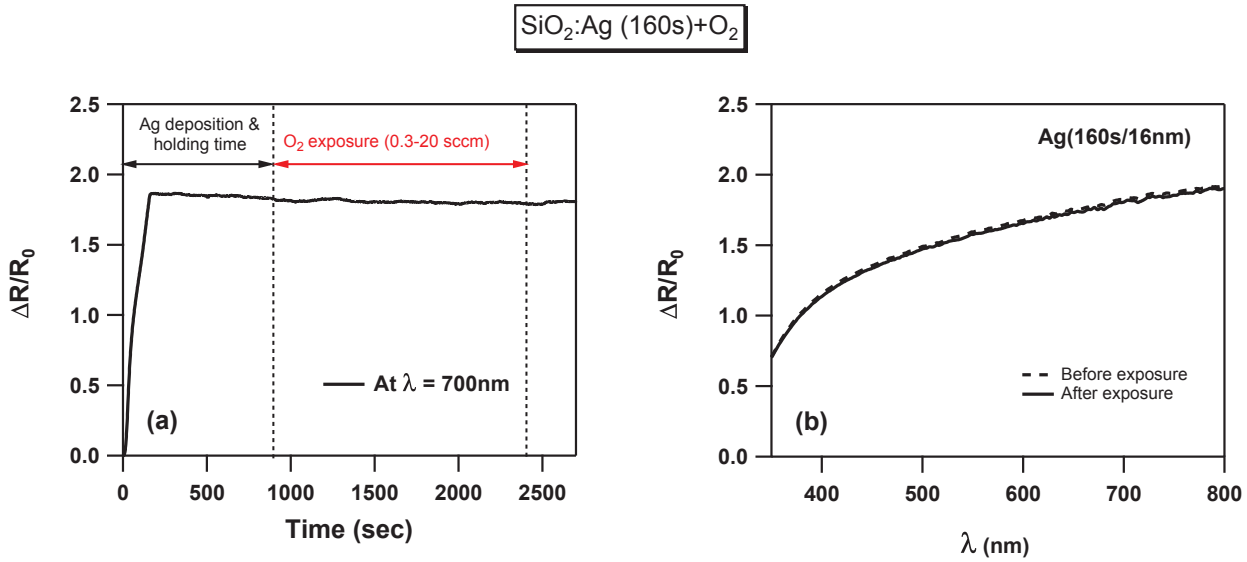

Figure IV.10 – (a) Temporal variation of $(\Delta R/R_0)$ for Ag(160s/16nm) deposition on a glass substrate, showing negligible reactivity with O_2 gas due to the formation of continuous Ag thin film. This temporal variation was traced at $\lambda = 700$nm due to the absence of prominent SPR absorption peak. (b) Spectral variation of SDRS signals before (dashed curve) and after (solid curve) the exposure of the Ag continuous film to O_2 gas.

3.3.3 Effect of deposition temperature

Ag nanoclusters grown on a glass substrate at different temperatures are exposed to an O_2 flux from 0.3 to 20 sccm in order to understand the influence of the temperature on their reactivity. In this regard, Fig.IV.11(a-b) shows the temporal variations of $\lambda_{\max}$ and $(\Delta R/R_0)_{\max}$ observed during the Ag(20s/2nm) deposition at room temperature (RT = 20°C), 200°C, and 400°C.

- **Ag deposition and holding time -** In Fig.IV.11(a) and Table IV.7, at the end of the Ag depositions, a blue-shifted SPR from 520nm to 415nm is clearly evident as the temperature

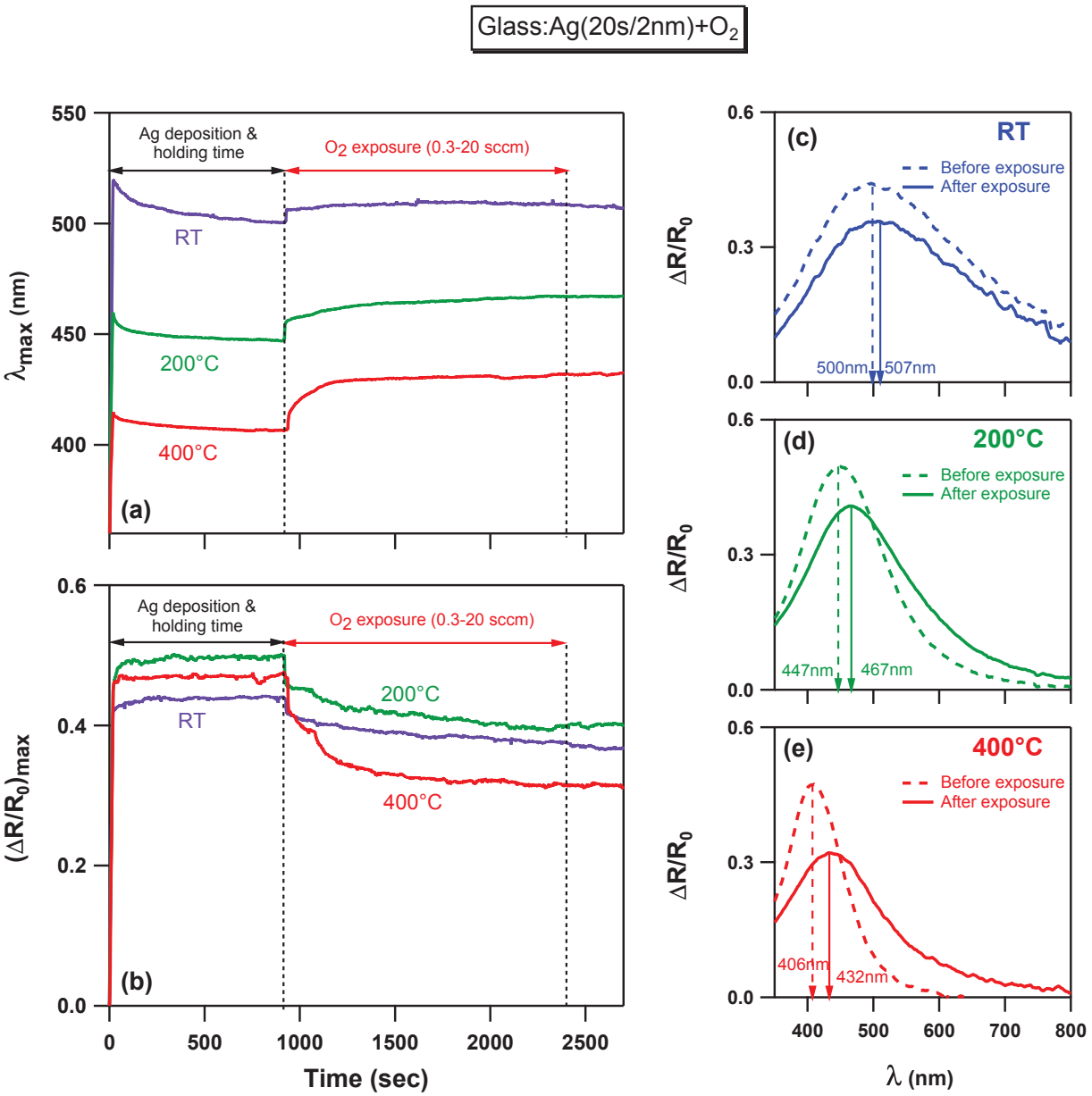

Figure IV.11 – Temporal variations of λ_{max} (a) and $(\Delta R/R_0)_{max}$ (b) for Ag(20s/2nm) depositions on glass substrates, at different temperatures along with corresponding spectral SDRS signals (c, d, e) before (dashed curves) and after (solid curves) the O_2 exposure.

is increased from RT to 400°C. Such a blue-shift can be ascribed to a decreased cluster density and to the formation of more spherical nanoclusters at higher temperature [20]. In contrast, $(\Delta R/R_0)_{max}$ values are very similar (in between 0.42 to 0.45), which indicate that the deposited Ag amounts are equivalent.

In addition, Fig.IV.11(a-b) and Table IV.7 shows that the blue-shift effect due to the

Glass:Ag(20s/2nm)	At the end of Ag deposition		During holding time
Temperature (°C)	λ_{max} (nm)	$(\Delta R/R_0)_{max}$	$\Delta\lambda_{max}$ (nm)
RT	520	0.42	-20
200	459	0.45	-12
400	415	0.45	-8

Table IV.7 – Values of λ_{max} and $(\Delta R/R_0)_{max}$ at the end of Ag(20s/2nm) deposition on glass at different temperatures (RT to 400°C) along with absolute variation in the λ_{max} ($\Delta\lambda_{max}$) during the holding time.

holding time decreases as the deposition temperature increases. As reshaping has less influence on λ_{max} for more spherical nanoclusters (Section 4.2.3, Fig.II.9, Chapter II), this tends to confirm that the nanoclusters grown at higher temperature are more spherical.

- **O_2 exposure (0.3 - 20 sccm) -** After the holding time, the Ag clusters are eventually exposed to O_2 that results into an immediate red-shift and a damping of the SPR at all deposition temperatures. Furthermore, from Fig.IV.11(a-b), it is clear that the optical modifications during the interactions of the Ag nanoclusters with O_2 are persistent at all temperatures even after the removal of O_2 from the deposition chamber. This confirms the permanent partial oxidation of the Ag nanoclusters upon their exposure to O_2. However, the temporal variations reveal that the O_2 effects on the optical properties of the Ag clusters are prominently higher at 400°C (Table IV.8). Moreover it seems that, at higher temperatures, the optical modifications prolong for longer durations before saturation comparing to room temperature exposure. As the formation of smaller clusters at higher temperatures is unlikely [20], these results evidence a thermally enhanced reactivity of the Ag nanoclusters rather than a pure size effect as discussed in Section 3.2.3 of the present Chapter.

Glass:Ag(20s/2nm)+O_2		
Temperature (°C)	$\Delta\lambda_{max}$ (nm)	% varition $(\Delta R/R_0)_{max}$
RT (20)	+7	-16
200	+20	-25
400	+26	-45

Table IV.8 – Effect of deposition temperature on the reactivity of Ag nanoclusters (supported on glass) for O_2 atmosphere, expressed in terms of variations in λ_{max} ($\Delta\lambda_{max}$) and % variations in $(\Delta R/R_0)_{max}$ before and after the O_2 exposure.

3.3.4 (Non)-reactivity of Ag clusters under N_2 and Ar atmospheres

During the course of this reactivity study, we have also verified the non-reactivity of the Ag clusters upon exposure to N_2 or Ar. For this purpose, after 20s/2nm Ag deposition at 200°C on glass, the Ag nanoclusters were subjected to non-ionized N_2 or Ar fluxes (from 0.3-20 sccm), which were introduced in the deposition chamber with the same sequence and procedure as in the case of O_2. As a typical example, the temporal and spectral SDRS measurements during the exposure of Ag nanoclusters to non-ionized N_2 is shown in Fig.IV.12.

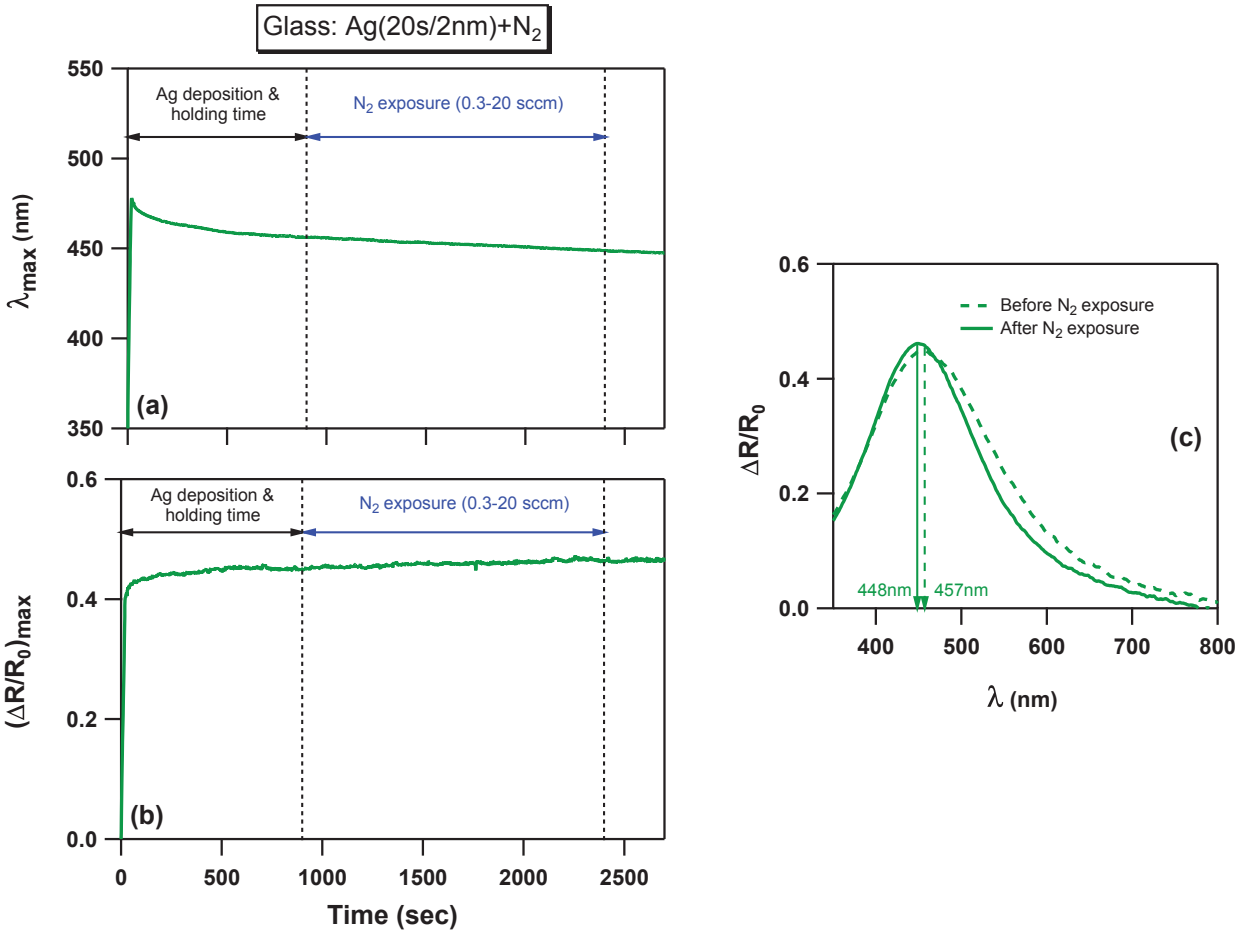

Figure IV.12 – Temporal variations of λ_{max} (a) and $(\Delta R/R_0)_{max}$ (b) during the deposition of Ag(20s/2nm) on glass and the exposure of the Ag nanoclusters to non-ionized N_2. (c) SDRS signals obtained before and after the N_2 exposure.

The non-reactive nature of the Ag clusters is evident from Fig.IV.12 where no sudden change in λ_{max} and $(\Delta R/R_0)_{max}$ is seen upon the introduction of N_2 in the deposition chamber. However, comparing the SDRS signals before and after N_2 exposure during 1500s (Fig.IV.12(c)), a small blue-shift of $\Delta\lambda_{max}$ = -9nm can be seen together with a weak increase of the SPR

amplitude. These effects are similar to those observed during the holding time step (Section 4.3.2, Chapter III). These results suggest that, due to the non-reactivity of the Ag clusters [5, 6, 10], the whole N_2 exposure duration acts as a large holding time, which introduces a further blue-shift of the SPR. As similar results were obtained for non-ionized Ar gas, they are not presented here.

4 Effect of partially ionized gases on the reactivity of Ag nanoclusters

In Section 4.3.3 of Chapter III, we have seen that during the Si_3N_4 pre-sputtering steps, the optical properties of the metal nanoclusters are strongly altered upon the interaction with nitrogen ion species. In this section, in order to understand such an effect, the optical properties of Ag nanoclusters exposed to partially ionized O_2 or N_2 gases are studied in detail using real-time SDRS, while their nanostructure analysis is studied using *post mortem* HAADF-STEM and GISAXS.

4.1 Experimental details

After Ag deposition and holding time, the Ar^+ plasma is switched on at the Si_3N_4 target surface well before the introduction of O_2 or N_2, we call this experiment step as "Plasma ON". For this purpose, the Si_3N_4 target surface is maintained at an appropriate voltage and upon the introduction of Ar at the target surface with a flux of 3 sccm, a confined Ar^+ plasma is formed instantly. After sufficient time (around 300s), a flux of O_2 or N_2 gas (of 20 sccm) is introduced in the vicinity of the sample surface through the gas ring (see Fig.IV.2). Due to the interaction of the molecular gas with the Ar^+ plasma (even though the plasma is confined at the target surface, which is protected with a shutter), a mixture of non-ionized gas and ion species is created in the deposition chamber, which can interact with the Ag clusters supported on the substrate. After a certain duration of O_2 or N_2 exposure, the gas is removed from the deposition chamber, and the Ar^+ plasma at the Si_3N_4 target is switched off by shutting down the magnetron power.

4.2 Effect of partially ionized O_2 on the Ag nanoclusters

For studying the effect of partially ionized O_2 (called $O_2^{(+)}$ for the sake of simplicity in the following text) on the nanostructural and optical properties of the Ag clusters, a typical

Si_3N_4:Ag(20s/2nm):Si_3N_4 nanocomposite system is chosen. The optical and nanostructural modifications caused by $O_2^{(+)}$ are compared with the effects of non-ionized O_2, which are discussed in subsection 3.2.2 (Fig.IV.7) of present Chapter.

4.2.1 *Post mortem* nanostructure analysis

Fig.IV.13 shows a comparative example of the SDRS signals along with the HAADF-STEM micrographs and the GISAXS patterns, obtained after the exposure of the Ag nanoclusters to either non-ionized O_2 or $O_2^{(+)}$.

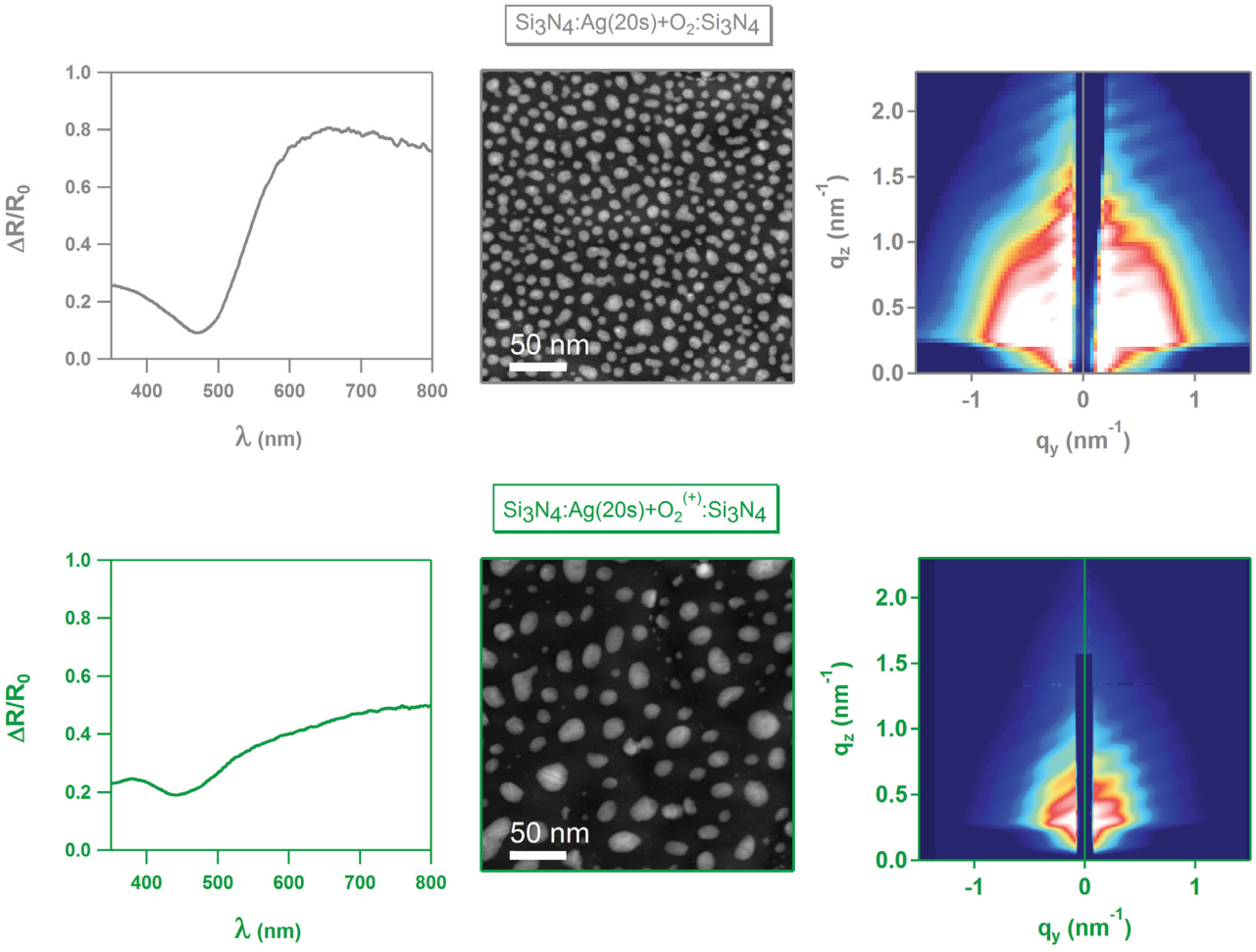

Figure IV.13 – Comparison of SDRS signals, HAADF-STEM micrographs, and GISAXS patterns for Si_3N_4:Ag(20s/2nm):Si_3N_4 nanocomposites: (top) Ag nanoclusters exposed to the non-ionized O_2, and (bottom) to $O_2^{(+)}$.

Here it is worth recalling that, as already discussed in Section 3.2.1 (Table IV.3) of the present Chapter, exposure to non-ionized O_2 does not produce any exceptional changes in

the nanostructural and optical properties of the Ag clusters at the end of the deposition. In contrast, dramatic influence of $O_2^{(+)}$ on the nanostructure of the Ag clusters can be seen with a prominent increase in the cluster size D as well as in the inter-cluster distance Λ along with a decrease in the cluster density d (Table IV.9). In addition to this, a prominent increase in σ_D comparing to the non-ionized O_2, gives an idea of the broad in-plane size distribution for Ag nanoclusters after their exposure to $O_2^{(+)}$. Even though a coalescence-type cluster growth is obviously possible under $O_2^{(+)}$ exposure, many authors have also pointed out the possibility of additional cluster growth by Ostwald's ripening [21–24]. In that case, larger clusters grow at the expense of smaller ones, with the possible transportation of atomic species occurring, either by surface diffusion on the substrate or by vapor-phase transport [22, 24].

Si_3N_4:Ag(20s/2nm):Si_3N_4 nanocomposite							
O_2 exposure	HAADF-STEM analysis					GISAXS analysis	
Form of O_2	d (μm^{-2})	Coverage (%)	D (nm)	σ_D (nm)	Λ (nm)	(H/D) ratio	H (nm)
Non-ionized O_2	3894	33.8	9.4	2.5	16.5	0.57	5.4
Partially ionized O_2 ($O_2^{(+)}$)	1475	20.8	14.1	7.4	34.0	-	-

Table IV.9 – Nanostructural analysis for Si_3N_4:Ag(20s/2nm):Si_3N_4 nanocomposites, exposed to non-ionized O_2/$O_2^{(+)}$ atmospheres. The determination of out-of-plane aspect ratio of the nanoclusters exposed to the $O_2^{(+)}$ is not possible because the GISAXS signal is concentrated in the vicinity of the vertical beam-stop where off-specular scattering arises from the lateral correlation in the surface roughness profile.

On the other hand, following the in-plane nanostructural parameters in the $O_2^{(+)}$ treated Ag nanoclusters, a prominent and largely increased SPR amplitude due to the presence of larger Ag nanoclusters is expected, which is not the case here (in Fig.IV.13). Actually, the SDRS signals at the end of the depositions suggest a strongly damped SPR in the nanocomposite treated with $O_2^{(+)}$ compared to the non-ionized O_2, while the SPR position may lie out of the visible spectral range (in the infra-red region). Hence, it is tempting to correlate such a damped spectral signal to the severe $O_2^{(+)}$ reactivity and to the formation of a thick oxide layer over the Ag nanoclusters. In order to establish the presence or not of silver oxide phases, selected-area electron diffraction (SAED) was performed. Fig.IV.14 shows the zero-loss filtered SAED patterns and averaged profiles taken from plane views of Si_3N_4:Ag(20s/2nm):Si_3N_4 tri-layers with Ag nanoclusters exposed to non-ionized O_2 and to $O_2^{(+)}$. For comparison, the electron diffraction averaged profiles of a cluster-free Si_3N_4 layer and of a Si_3N_4:Ag(20s/2nm):Si_3N_4 tri-layer with non-exposed Ag nanoclusters are also displayed. It is worth noting that, in addition to the signal of the amorphous Si_3N_4 matrix, the SAED patterns of all the nanocomposites exhibit a

set of reflections, which can be indexed as those of face centered-cubic (Fm3m) silver nanocrystallites with random orientation. Even though the presence of other phases in minor quantities cannot be ruled out, these results suggest that the presence of a thick oxide shell around the Ag nanoclusters exposed to non-ionized O_2 or to $O_2^{(+)}$ is unlikely. Hence, the prominently red-shifted but damped SPR in the $O_2^{(+)}$ exposed Ag nanoclusters may be ascribed to their large in-plane and out-of-plane cluster size distributions which give rise to broad resonance bands [25].

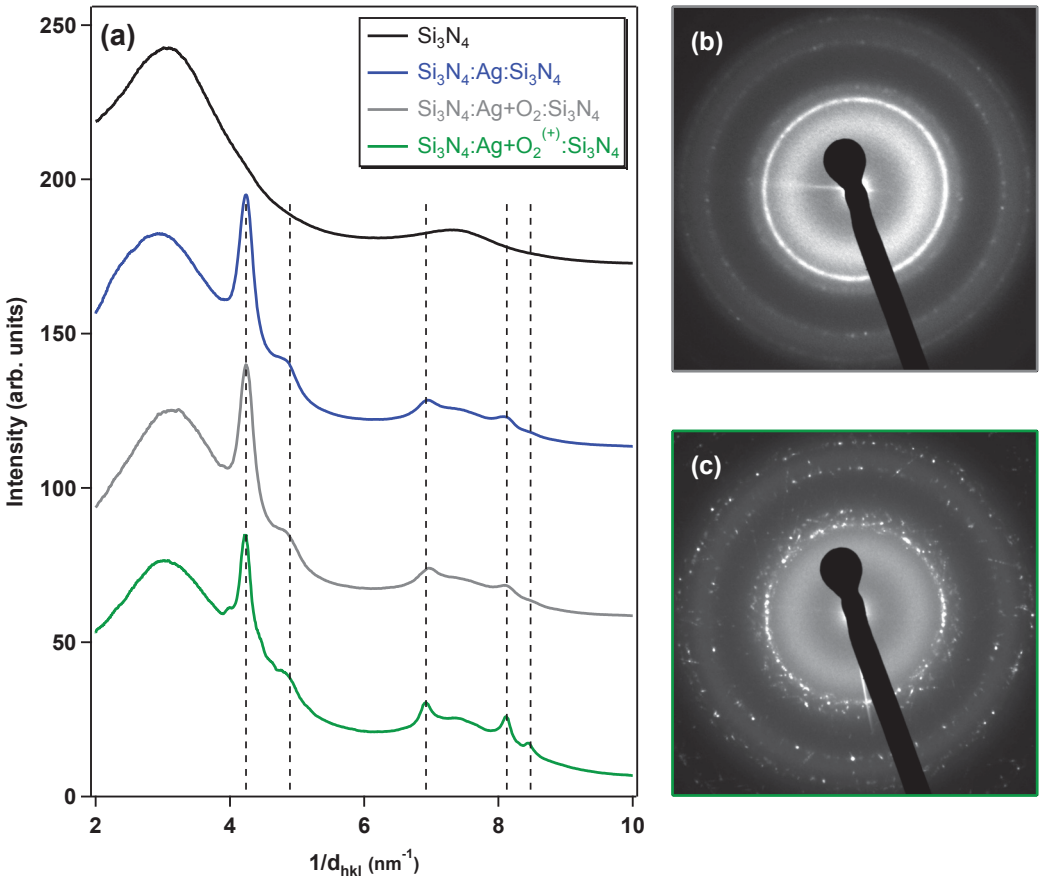

Figure IV.14 – (a) Selected-area electron diffraction (SAED) averaged profiles of Si_3N_4:Ag(20s/2nm):Si_3N_4, Si_3N_4:Ag(20s/2nm)+O_2:Si_3N_4, and Si_3N_4:Ag(20s/2nm)+$O_2^{(+)}$:Si_3N_4 nanocomposite tri-layers. Electron diffraction averaged profile for a cluster-free Si_3N_4 layer is also shown for comparison as well as the position of the main lines expected for pure Ag (dotted lines). SAED patterns of the Si_3N_4:Ag(20s/2nm)+O_2:Si_3N_4 (b) and Si_3N_4:Ag(20s/2nm)+$O_2^{(+)}$:Si_3N_4 samples (c).

4.2.2 *In situ* and real-time SDRS analysis

In order to provide additional information on the reactivity of the clusters to $O_2^{(+)}$, a comparison of the temporal variations in λ_{max} and $(\Delta R/R_0)_{max}$ for the above discussed Si_3N_4:Ag(20s/2nm):Si_3N_4 nanocomposites is shown in Fig.IV.15.

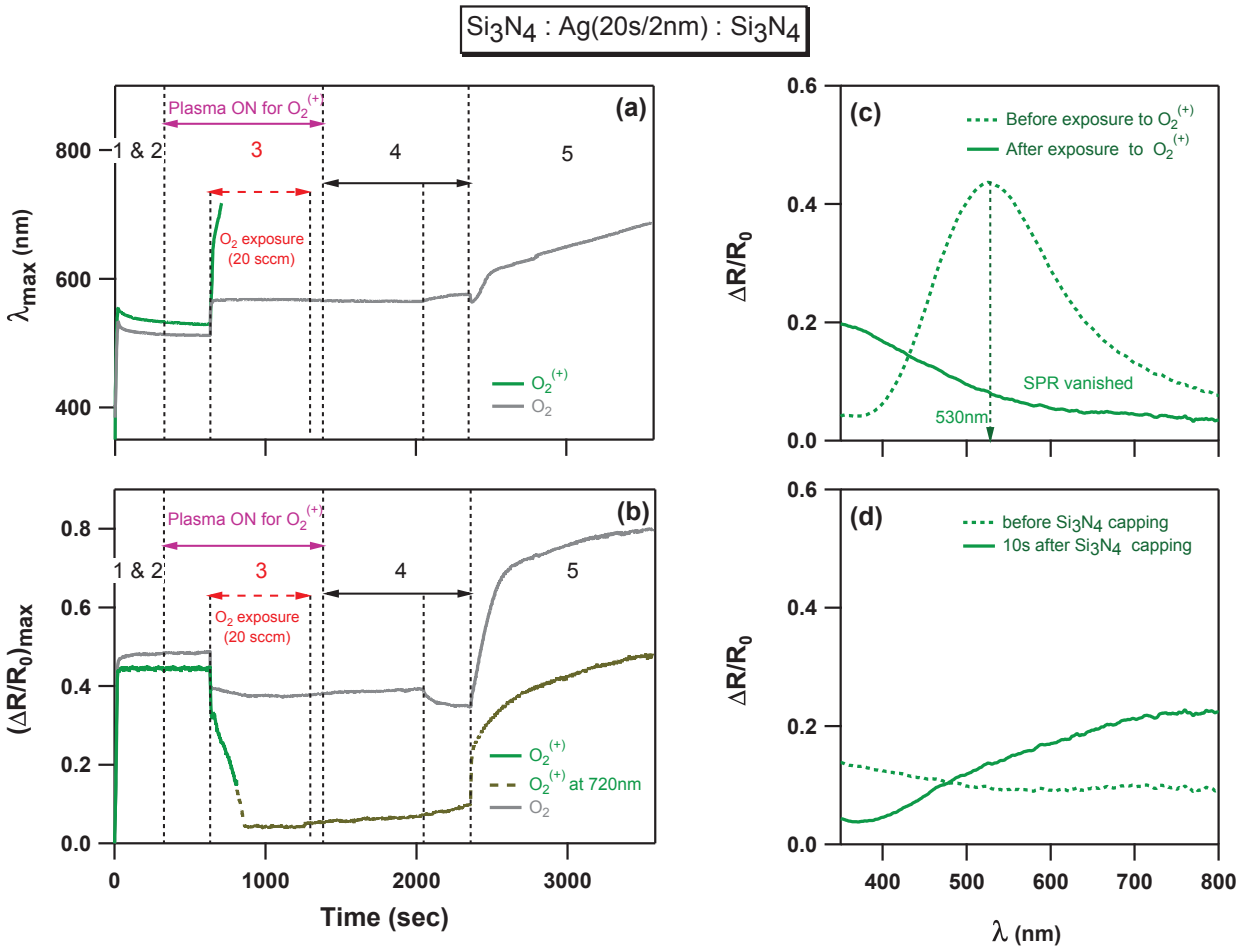

Figure IV.15 – Comparison for temporal variations of λ_{max} (a) and $(\Delta R/R_0)_{max}$ (b) for Si_3N_4:Ag(20s/2nm):Si_3N_4 nanocomposites subjected to either $O_2^{(+)}$ (green curve) or non-ionized O_2 (gray curve). As no prominent SPR maximum is left in Ag nanoclusters due to $O_2^{(+)}$, its $(\Delta R/R_0)_{max}$ curve is further traced at 720nm (olive curve). (c) SDRS signals obtained before and after the exposure of Ag nanoclusters to $O_2^{(+)}$. (d) SDRS signals before and after 10s of capping of $O_2^{(+)}$ treated Ag nanoclusters by Si_3N_4 matrix.

- **STEP 1 & 2 -** During Ag deposition and holding time, as expected, the presence of λ_{max} and $(\Delta R/R_0)_{max}$ curves in the same ranges proves that similar Ag amounts are deposited on the Si_3N_4 buffer layer. After holding time and before introduction of O_2, the

Ar plasma is switched on (Plasma ON) at the Si_3N_4 target surface (while in case of non-ionized O_2, as the Plasma ON step is not required, the holding time progresses further). The ineffectiveness of this step is evident as no modification in λ_{max} and $(\Delta R/R_0)_{max}$ are observed.

- **STEP 3 -** Upon introduction of O_2 (20 sccm), a rapid and strong increase in λ_{max} leading to a SPR red-shift of about 180nm can be noticed in the case of the $O_2^{(+)}$ treatment during the first 75s. On the other hand, during the same time period, a sharp decrease in the $(\Delta R/R_0)_{max}$ signal is also visible. These sudden optical modifications, which are much more pronounced than in the case of the non-ionized O_2 treatment, can be ascribed to the oxygen ion species created due to the Ar^+ plasma and may suggest the formation of a silver oxide shell around the nanoclusters (e.g., Ag_2O [21, 22]), although *post mortem* SAED analysis suggests no crystallized silver oxide after capping by the Si_3N_4 matrix (Fig.IV.14). With further $O_2^{(+)}$ exposure, as no prominent maximum is present in the SDRS signal, determination of $(\Delta R/R_0)_{max}$ is done at the last registered SPR position i.e. around 720nm (olive curve), which remains at a minimum value (below 0.1, but not zero which would have been the case if Ag clusters were completely removed from the Si_3N_4 buffer layer). On the other hand, the determination of λ_{max} is no more possible owing to the complete damping of the SPR. The measurements also show that the SPR damping is permanent even upon removal of O_2 from the deposition chamber and after switching off the plasma of Ar^+, proving the strong chemical interactions between the $O_2^{(+)}$ species and the Ag nanoclusters.

- **STEP 4 -** During the pre-sputtering of the Si_3N_4 target, the SPR of the Ag nanoclusters treated with non-ionized O_2 shows a red-shift and a damping due to the interactions with the $N_2^{(+)}$ species, as discussed in Section 3.2.3 of the present Chapter. With regard to the Ag clusters exposed to $O_2^{(+)}$, the determination of λ_{max} is still not possible owing to the totally damped SPR, while the $(\Delta R/R_0)_{max}$ traced at 720nm, shows a negligible increase.

- **STEP 5 -** At the very beginning of the Si_3N_4 deposition (first 10s corresponding to an effective thickness of about 0.3nm), even though λ_{max} is still not possible to trace, a steep increase in the $(\Delta R/R_0)_{max}$ signal of the $O_2^{(+)}$ treated Ag clusters can be seen (Fig.IV.15(b)). In this regard, Fig.IV.15(d) shows a comparison of the spectral signals before and after 10s of Si_3N_4 capping, where a distinct increase in the SDRS amplitude is seen due to the deposited Si_3N_4. However, a maximum of the signal seems to be out of the visible range (in the infra-red range). This optical change may arise from the desorption

of O_2 due to the Si_3N_4 capping-layer deposition, as already discussed in Section 3.2.2 of this Chapter. This may explain why the presence of silver oxide is not detected by the *post mortem* SAED analysis. With further increase of the Si_3N_4 capping-layer thickness, a monotonous increase in the $(\Delta R/R_0)_{max}$ is evident, which is due to the interferences between the successive light rays emerging from the transparent deposited Si_3N_4 film.

In this way, we have seen that $O_2^{(+)}$ induces dramatic changes not only in the nanostructures of the Ag clusters, but also in their optical properties. The structural characterization techniques show larger nanoclusters under the influence of partially ionized O_2, real-time SDRS reveals the presence of strong chemical interactions between the nanoclusters and the partially ionized O_2 that eventually suppress the SPR, completely. Moreover, similar SPR disappearance has been observed in case of higher Ag amounts where larger Ag clusters are formed on either Si_3N_4 buffer layers or glass substrates. Hence, it can be concluded that the interactions of Ag nanoclusters with partially ionized O_2 are more intense than with non-ionized O_2, whatever the cluster size, the O_2 flux, and the nature of the substrate.

In this regard, it has been demonstrated in the literature [4, 7–10] that when completely oxidized Ag nanoclusters are annealed at temperatures around 500°C for sufficient durations in reducing gas atmospheres, such as H_2, the SPR can reappear. Since the use of H_2 gas in our magnetron system is avoided (mainly due to safety reasons), as an alternate method, we subjected the oxidized Ag nanoclusters to energetic bias Ar^+ plasma treatments. The detail investigation about these bias plasma treatments is presented in the next chapter (V).

4.2.3 Effect of partially ionized N_2

In the previous subsection, we have demonstrated the improved reactivity of Ag nanoclusters in the presence of partially ionized O_2 comparing to non-ionized O_2. Besides, we have already seen that the exposure of Ag nanoclusters to partially ionized nitrogen species during the pre-sputtering of the Si_3N_4 target causes both a red-shift and a damping of the SPR, while their exposure to non-ionized N_2 has no noticeable influence, as expected. In the present subsection, this effect is further investigated from a Glass:Ag(20s/2nm) sample subjected to a $N_2^{(+)}$ exposure at 200°C.

As displayed in Fig.IV.16(a), after the Ag deposition and holding time, an Ar flux of 3 sccm is used to maintain the plasma ON, while gradually increasing the N_2 flux from 0.3 sccm ($\equiv 6 \times 10^{-4}$ mbar) to 20 sccm ($\equiv 6 \times 10^{-3}$ mbar) by steps of 2 sccm each 150s. Then, after pumping the gas from the deposition chamber, the Ar plasma at the Si_3N_4 target is switched off. The corresponding temporal variations of λ_{max} and $(\Delta R/R_0)_{max}$ are exhibited in Fig.IV.16(b-

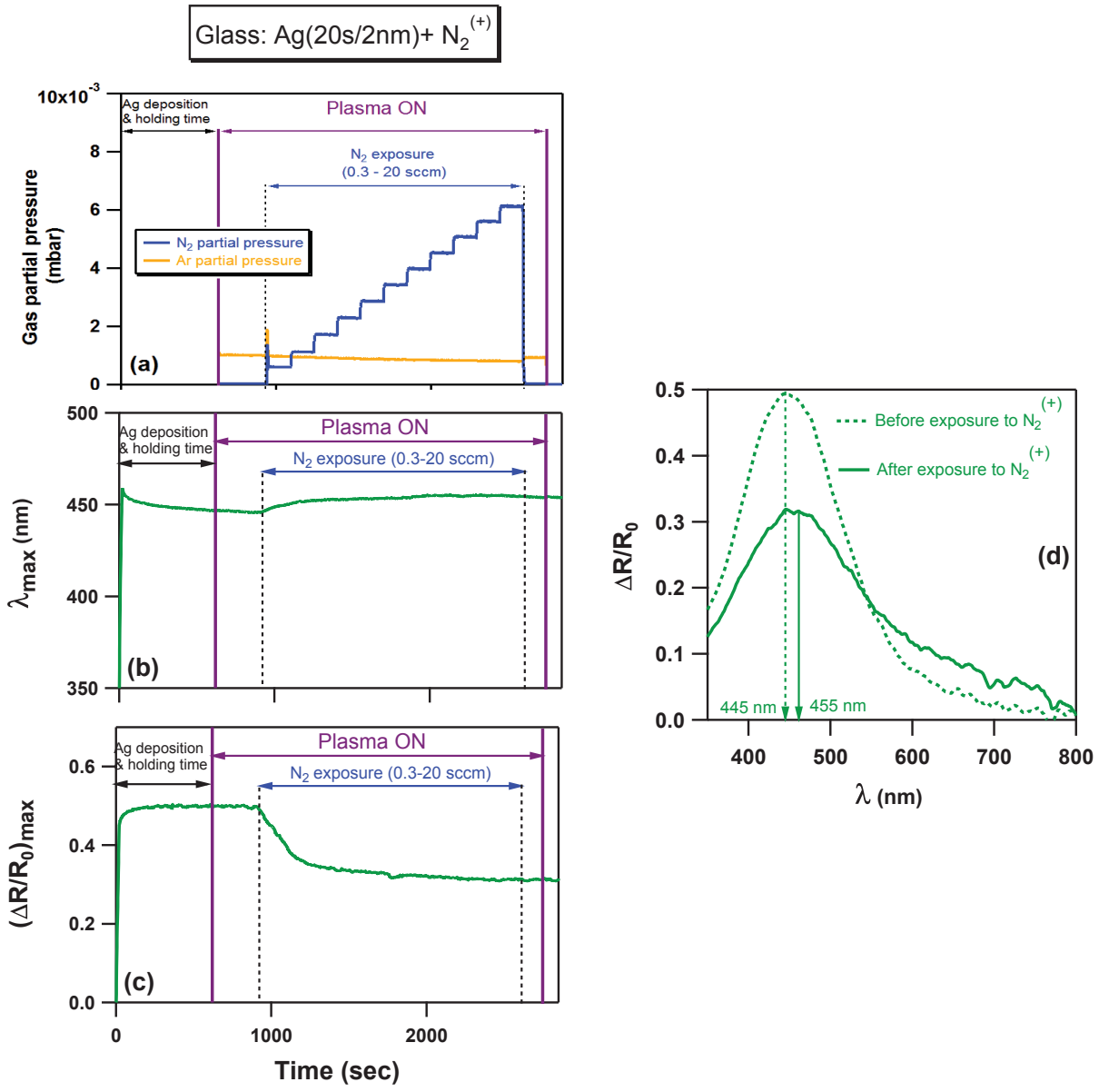

Figure IV.16 – (a): Temporal variation of N_2 partial pressure in the deposition chamber after the ignition of the Ar^+ plasma at the Si_3N_4 target (Plasma ON), (b-c): temporal variations in λ_{max} and $(\Delta R/R_0)_{max}$ of glass Ag nanoclusters during their exposure to $N_2^{(+)}$, (d): the spectral SDRS signals before and after exposure of the Ag nanoclusters to the partially ionized N_2.

c), which show that the kinetics of the red-shift and damping effects due to the interactions between the Ag nanoclusters and the N_2 ion species is much slower than in the case of interactions with non-ionized or partially ionized O_2. Rather than showing almost instantaneous modifications, the variations in the SDRS signals are monotonous with increasing the exposure time and with the N_2 flux up to 2 sccm ($\equiv 1 \times 10^{-3}$ mbar), and then they remain almost

unchanged. Moreover, comparing to partially ionized O_2, interaction of the Ag nanoclusters with nitrogen ion species does not suppress the SPR completely, as seen in Fig.IV.16(d), which also shows an increase of the SPR width. Nevertheless, these optical modifications appear to be permanent even after decreasing the N_2 partial pressure to zero and after switching off the Ar plasma. To the best of our knowledge, such optical modifications of Ag nanoclusters exposed to nitrogen ion species have not been reported in the literature before.

5 Summary and conclusions

In this chapter, the influence of N_2 and O_2 in both non-ionized and partially ionized forms, on the optical properties of Ag nanoclusters has been investigated. The results show that the interactions between the nanoclusters and their surrounding atmosphere can be studied efficiently using *in situ* and real-time SDRS. In addition, it can be concluded that the optical response of the Ag nanoclusters can be tailored by changing their surrounding atmosphere.

While the Ag nanoclusters are found to be non-reactive with non-ionized N_2, their optical properties change sensitively under the influence of non-ionized O_2, causing a sharp red-shift and a strong damping of the SPR without modifying their nanostructure dramatically. The temporal SDRS measurements show that these optical modifications are instantaneous (in few seconds) and strongly dependent on the cluster size, on the nature of the substrate, and on the substrate temperature. Although these effects are permanent (during the exposure period), they become insensitive for further increase or decrease of the O_2 partial pressure. Moreover, our results also suggest that the interaction between non-ionized O_2 and Ag nanoclusters can be suppressed by the Si_3N_4 capping. This desorption of O_2 is found to be dominant during the first 30s of Si_3N_4 capping.

On the other hand, comparing to non-ionized gases optical and nanostructural analysis of Ag clusters under the influence of partially ionized gases show more dramatic changes. More specifically, in contrast to non-ionized N_2, the presence of nitrogen ion species is found to cause a red-shift and a damping of the SPR. While, under the influence of partially ionized O_2, the Ag nanoclusters show a large increase in their in-plane size with accordingly reduced areal cluster density. The real-time optical measurements, however, reveal a completely suppressed SPR indicating a strong reactive effect, whatever the cluster size, the nature of the substrate, and the O_2 partial pressure. But, in this case too, the desorption of O_2 is evident during the first 30s of Si_3N_4 capping, suggesting the possible suppression of O_2-Ag nanoclusters interactions.

Bibliography

[1] R. Serna, D. Babonneau, A. Suàrez-Garcia, and C. N. Afonso. *Effect of oxygen pressure on the optical and structural properties of Cu:Al_2O_3 nanocomposite films.* Physical Review B **66**, 205402 (2005). 97, 98, 99, 100, 103, 106

[2] C. J. Fernàndez, M. G. Manera, and J. Spadavecchia. *Study of the gas optical sensing properties of Au-polyimide nanocomposite films prepared by ion implantation.* Sensors and Actuators B **111-112**, 225–229 (2005). 98, 99

[3] M. G. Manera, J. Spadavecchia, D. Buso, C. d J. Fernández, G. Mattei, A. Martucci, P. Mulvaney, R. Rella J. Pérez-Juste, L. Vasanelli, and P. Mazzoldi. *Optical gas sensing of TiO_2 and TiO_2/Au nanocomposite thin films.* Sensors and Actuators B **132**, 107–115 (2008). 98, 99

[4] Y. Borensztein, L. Delannoy, A. Djedidi, R. G. Barrera, and C. Louis. *Monitoring of the plasmon resonance of gold nanoparticles in Au/TiO_2 catalyst under oxidative and reducing atmospheres.* Journal of Physical Chemistry C **114**, 9008–9021 (2010). 98, 99, 100, 103, 106, 124

[5] T. Brandt, W. Hoheisel, A. Iline, F. Stietz, and F. Träger. *Influence ofmolecular adsorbate layers on the optical spectra of small metal particles.* Applied Physics B **65**, 793–798 (1997). 98, 99, 100, 106, 118

[6] A. Iline, M. Simon, F. Stietz, and F. Trddotager. *Adsorption of molecules on the surface of small metal particles studied by optical spectroscopy.* Surface Science **436**, 51–62 (1999). 98, 99, 100, 106, 118

[7] H. Bi, W. Cai, C. Kan, L. Zhang, D. Martin, and F. TrÄger. *Optical study of redox process of Ag nanoparticles at high temperature.* Journal of Applied Physics **92**, 7491 (2002). 98, 108, 124

[8] J. Hu, W. Cai, Y. Li, and H. Zeng. *Oxygen-induced enhancement of surface plasmon resonance of silver nanoparticles for silver-coated soda-lime glass.* JOURNAL OF PHYSICS: CONDENSED MATTER **17**, 5349–5354 (2005). 98, 99, 106, 124

[9] J. Hu, W. Cai, H. Zeng, C. Li, and F. Sun. *Substrate dependent surface plasmon resonance evolution of Ag nanoparticles treated in atmospheres.* Journal Of Physics: Condensed Matter **18**, 5415–5423 (2006). 98, 99, 106, 124

[10] J. A. Jiménez and M. Sendova. *In situ spectroscopic determination of the activation energies for the growth of silver nanoparticles in silica nanofilms in nitrogen atmosphere.* Solid State Communications **151**, 720–724 (2011). 98, 118, 124

[11] U. Kreibig and M. Vollmer. *Optical Properties of Metal Clusters.* Springer-Verlag, Berlin (1995). 100, 111

[12] D. S. Afanasev, V. F. Anufrienko, S. F. Ruzankin, T. V. Larina, N. I. Kuznetsova, , and V. I. Bukhtiyarov. *Effect of oxygen adsorption on the surface plasmon resonance of oxide-supported silver nanoparticles.* Doklady Physical Chemistry **436**, 23–25 (2010). 106, 111

[13] M.-C. Saint-Lager, A. Bailly, M. Mantilla, S. Garaudée, R. Lazzari, P. Dolle, O. Robach, J. Jupille, I. Laoufi, and P. Taunier. *Looking by grazing incidence small angle X-ray scattering at gold nanoparticles supported on rutile $TiO_2(110)$ during co oxidation.* Gold Bulletin 2008 **41/2**, 159–166 (2008). 108

[14] C. Méthivier, J. Massardier, and J. C. Bertolini. *Pd/Si_3N_4 catalysts: preparation, characterization and catalytic activity for the methane oxidation.* Applied Catalysis A: General **182**, 337–344 (1999). 113

[15] H. Schmidt, W. Gruber, G. Borchardt, M. Bruns, M. Rudolphi, and H. Baumann. *Thermal stability and crystallization kinetics of sputtered amorphous Si_3N_4 films.* Thin Solid Films **450**, 346–351 (2004). 113

[16] S. P. Taguchi and S. Ribeiro. *Silicon nitride oxidation behaviour at 1000 and 1200∘c.* Journal of Materials Processing Technology **147**, 336–342 (2004). 113

[17] M. A. P. Dekkers, M. J. Lippits, and B. E. Nieuwenhuys. *Supported $gold/MO_x$ catalysts for NO/H_2 and CO/O_2 reactions.* Catalysis Today **54**, 381–390 (1999). 113

[18] J. Chou, N. Franklin, S.-H. Baeck, T. Jaramillo, and E. McFarland. *Gas-phase catalysis by micelle derived Au nanoparticles on oxide supports.* Catalysis Letters **95**, 107–111 (2004). 113

[19] K. Qian, Z. Jiang, and W. Huang. *Effect of oxygen treatment on the catalytic activity of Au/SiO_2 catalysts.* Journal of Molecular Catalysis A: Chemical **264**, 26–32 (2007). 113

[20] H. Takele, A. Kulkarni, S. Jebril, V. S. K. Chakravadhanula, C. Hanisch, T. Strunskus, V. Zaporojtchenko, and F. Faupel. *Plasmonic properties of vapour-deposited polymer composites containing Ag nanoparticles and their changes upon annealing.* Journal of Physics D: Applied Physics **41**, 125409 (2008). 115, 116

[21] X. Lai, T. P. St. Clair, and D. W. Goodman. *Oxygen-induced morphological changes of Ag nanoclusters supported on TiO_2(110).* Faraday Discussions **114**, 279–284 (1999). 120, 123

[22] X. Lai and D. W. Goodman. *Structure-reactivity correlations for oxide-supported metal catalysts: new perspectives from STM.* Journal of Molecular Catalysis A: Chemical **162**, 33–50 (2000). 120, 123

[23] P. A. Thiel, M. Shen, D. J. Liu, and J. W. Evans. *Adsorbate-enhanced transport of metals on metal surfaces: Oxygen and sulfur on coinage metals.* Journal of Vacuum Science and Technology A: Vacuum, Surfaces and Films **28**, 1285–1298 (2010). 120

[24] J Tang, A Tserepi, and D Tsoukalas. *Two-dimensional nanoparticle self-assembly using plasma-induced Ostwald ripening.* Nanotechnology **22**, 235306(7pp) (2011). 120

[25] M. Valamanesh, Y. Borensztein, C. Langlois, and E. Lacaze. *Substrate effect on the plasmon resonance of supported flat silver nanoparticles.* Journal of Physical Chemistry C **115**, 2914–2922 (2011). 121

Chapter V

Monitoring the nanostructural and optical changes in Ag nanoclusters during annealing treatments

1 Introduction

In the previous chapter, the reactive properties of Ag nanoclusters under different chemical environments that eventually modify their optical properties, have been presented. In this chapter, we focus on the effects of post-deposition annealing treatments on the metal nanoclusters. Annealing is a process where a system is supplied with sufficient controlled energy for a certain duration in order to alter/modify/improve its physical properties. In the case of supported noble metal nanoclusters, this external supplied energy can provide a suitable assistance for changing their nanostructural and optical properties.

In this regard, effects of thermal annealing on Ag nanoclusters supported onto Si_3N_4 buffer layers are first studied here. Further, a more original approach in the form of bias plasma treatments is also investigated. As both approaches change the morphology and organization of the cluster assemblies distinctly, their related optical properties are subjected to modifications accordingly.

2 Effect of thermal annealing on the Ag nanoclusters

As metal nanoclusters show remarkable dependency on the substrate temperature, thermal annealing can be one of the most efficient and low cost treatments to modify their morphology and organization. Under thermodynamic equilibrium conditions, the cluster shape minimizing the free energy is well described by the Wulff-Kaishew theorem [1]. The stable shape for a

face-centered-cubic (fcc) metal cluster standing on a dielectric surface and being surrounded by vacuum is then expected to be a truncated octahedron, which can be approximated to a truncated sphere with a *H/D* ratio depending on the metal/dielectric and metal/vacuum interface energies. However, nanocluster growth by a physical deposition process is often carried out away from thermodynamic equilibrium, so that the clusters do not reach their equilibrium shape at room temperature [2]. Upon annealing at appropriate temperatures, decrease in the cluster density (or increase in the inter-cluster distance) and increase in the cluster size have been reported as the mobility of the metal adatoms (and dimers, trimers etc ...) is strongly enhanced [3–7]. These changes are the indication of a coalescence-type growth that give rises to narrower cluster size distributions. In addition to this, it has been shown that thermal annealing can also change the shape of the metal nanoclusters, which tend toward a more spherical shape [6, 8, 9]. All these nanostructure modifications obviously alter the basic optical properties of the metal nanoclusters. Hence in this section, efforts are taken to study the thermally induced nanostructural and optical modifications in Ag nanoclusters grown onto a Si_3N_4 buffer layer, using *in situ* and real-time SDRS.

2.1 Experimental details

For the thermal treatments, Si_3N_4:Ag:Si_3N_4 nanocomposite tri-layers with increasing Ag amounts (10s/1nm, 20s/2nm, and 40s/4nm) are studied. The experimental parameters during the nanocomposite depositions are kept similar to those explained in the previous chapters. However, after Ag deposition and holding time of 600s (performed at 200°C), the supported Ag nanoclusters are subjected to thermal annealing at 400°C by using the *in situ* heating system implemented in the magnetron sputtering chamber. Fig.V.1(a) shows the schematics of this heating system consisting of an oven located 2mm above the substrate holder, which is thus heated by infrared radiations. The oven temperature is measured thanks to a chromel-alumel thermocouple, which is not in direct contact with the substrate so that the substrate temperature is always few tens of degrees lower than that indicated by the thermocouple. The schematics of the annealing sequence is displayed in Fig.V.1(b), where it can be seen that the temperature first increases sharply from 200°C to 400°C within ∼300s. Then, after maintaining the system at 400°C during about 3600s, the temperature is allowed to decrease naturally to 200°C so that the thermally annealed clusters can be covered by a Si_3N_4 capping-layer in order to "freeze" their nanostructure and to protect them from the environmental contaminations.

Hereafter, the nanostructural and optical properties of thermally annealed (TA) and non-annealed (NA) Ag clusters are compared from Si_3N_4:Ag:Si_3N_4 nanocomposites with similar

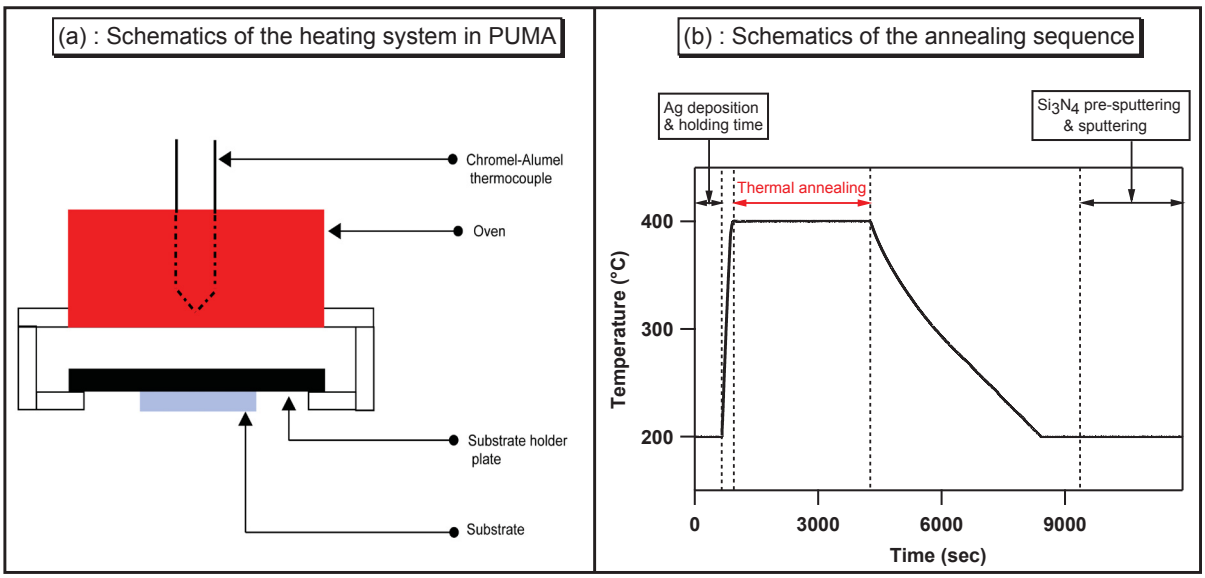

Figure V.1 – (a) Schematics of the heating system used in the magnetron sputtering chamber to perform *in situ* thermal annealing treatments. (b) Schematics of the heating sequence used to study the influence of thermal treatments on the optical properties of the Ag nanoclusters.

Ag amounts. The nanostructure of the Ag nanoclusters is revealed by *post mortem* HAADF-STEM and GISAXS, while their optical response is studied by *in situ* and real-time SDRS. However, it is worth mentioning that the $(\Delta R/R_0)_{\max}$ variations during the annealing treatment are not presented in the following, mainly because thermal dilatation of the substrate and substrate holder at the beginning of the heating step results in strong optical fluctuations, which nevertheless do not affect the $\lambda_{\max}$ values.

2.2 *Post mortem* nanostructure analysis

As a typical example, the SDRS signals recorded at the end of the deposition sequences along with the HAADF-STEM micrographs and GISAXS patterns of TA and NA nanocomposites of Si_3N_4:Ag(20s/2nm):Si_3N_4 are presented in Fig.V.2. Although it is difficult to see the nanostructural differences between the TA and NA samples with naked eyes, general conclusions can be drawn from the quantitative analysis of the HAADF-STEM and GISAXS data gathered in Table V.1. Whatever the deposited Ag amount, thermal annealing of the Ag nanoclusters results in a decrease of the areal cluster density d (or an increase of the inter-cluster distance Λ). Furthermore, it causes a very slight decrease of the in-plane Ag cluster size D, while the in-plane size distribution σ_D remains almost similar. However, distinctly increased out-of-plane aspect ratio H/D and height H of the Ag nanoclusters are clearly evident for the

TA samples. These results are in accordance with the references in literature [3–6, 6–9], (except for the in-plane cluster size D which remains almost similar in our case). Such nanostructural modifications, which can be ascribed to an enhanced Ag mobility promoting coalescence and reshaping processes, also lead to optical changes in the form of a blue-shifted SPR position as well as an increase in the SPR amplitude and a narrowing of the SPR width.

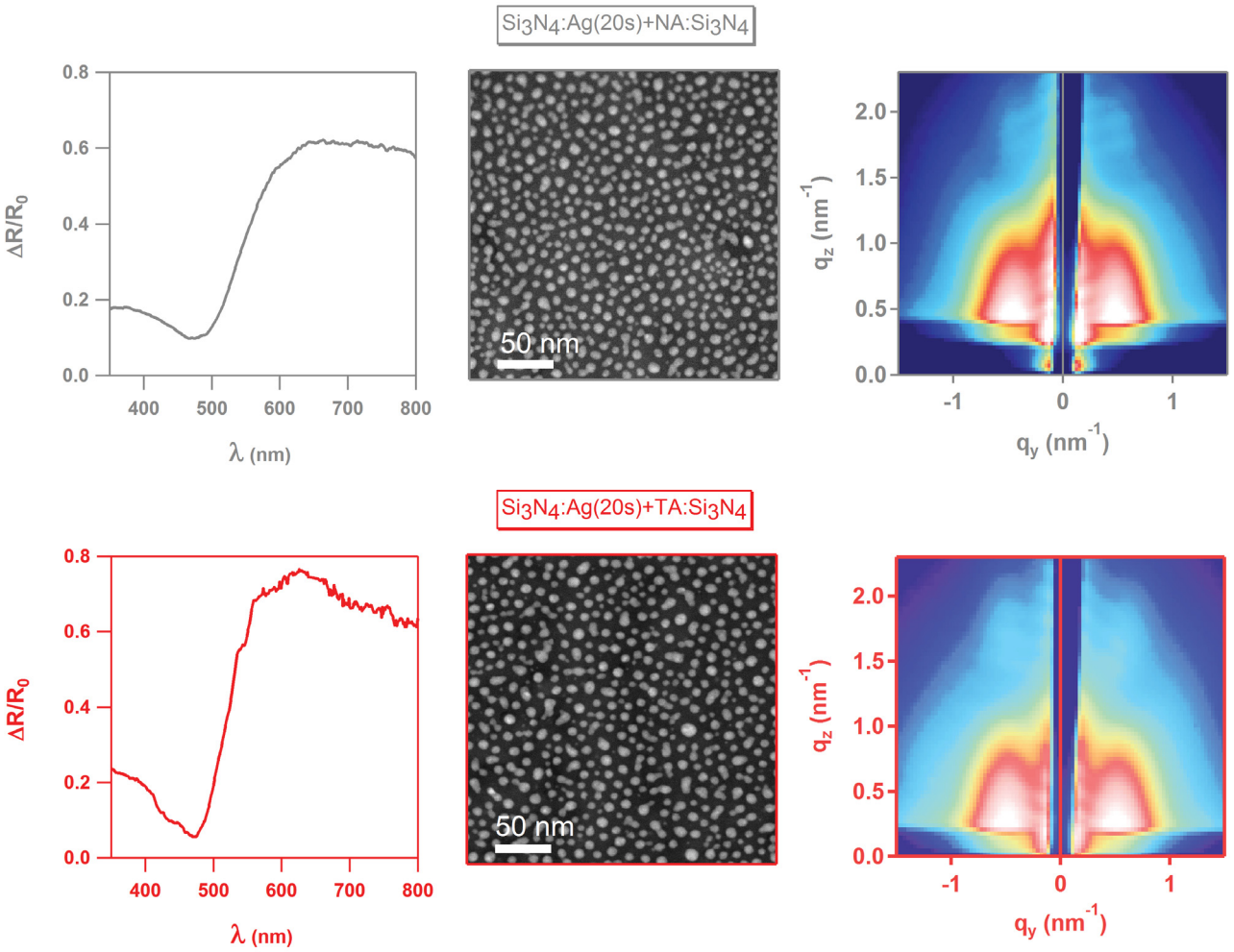

Figure V.2 – Comparison of SDRS signals, HAADF-STEM micrographs and GISAXS patterns for non-annealed (NA) and thermally annealed (TA) Ag nanoclusters from Si_3N_4:Ag(20s/2nm):Si_3N_4 nanocomposites.

2.3 *In situ* and real-time SDRS analysis

As the nanostructure of the Ag clusters changes during the thermal annealing, *in situ* and real-time SDRS can provide sensitive insights into the corresponding optical modifications. In

Si_3N_4:Ag:Si_3N_4 nanocomposites	HAADF-STEM analysis					GISAXS analysis	
Ag deposition time/thickness	d (μm^{-2})	Coverage (%)	Λ (nm)	D (nm)	σ_D (nm)	(H/D) ratio	H (nm)
10s/1nm (NA)	14464	21	10.0	4.4	1.4	0.87	3.8
10s/1nm (TA)	11841	21	11.0	4.3	1.5	0.93	4.0
20s/2nm (NA)	6674	32	12.6	7.6	1.9	0.73	5.5
20s/2nm (TA)	5809	30	14.0	7.2	1.8	0.89	6.4
40s/4nm (NA)	2094	41	19.4	13.6	3.6	0.64	8.7
40s/4nm (TA)	*2387*	40	21.5	13.2	4.2	0.72	9.5

Table V.1 – Structural parameters of "as-prepared" or non-annealed (NA) Ag nanoclusters compared with the thermally annealed (TA) Ag nanoclusters from Si_3N_4:Ag:Si_3N_4 nanocomposites.

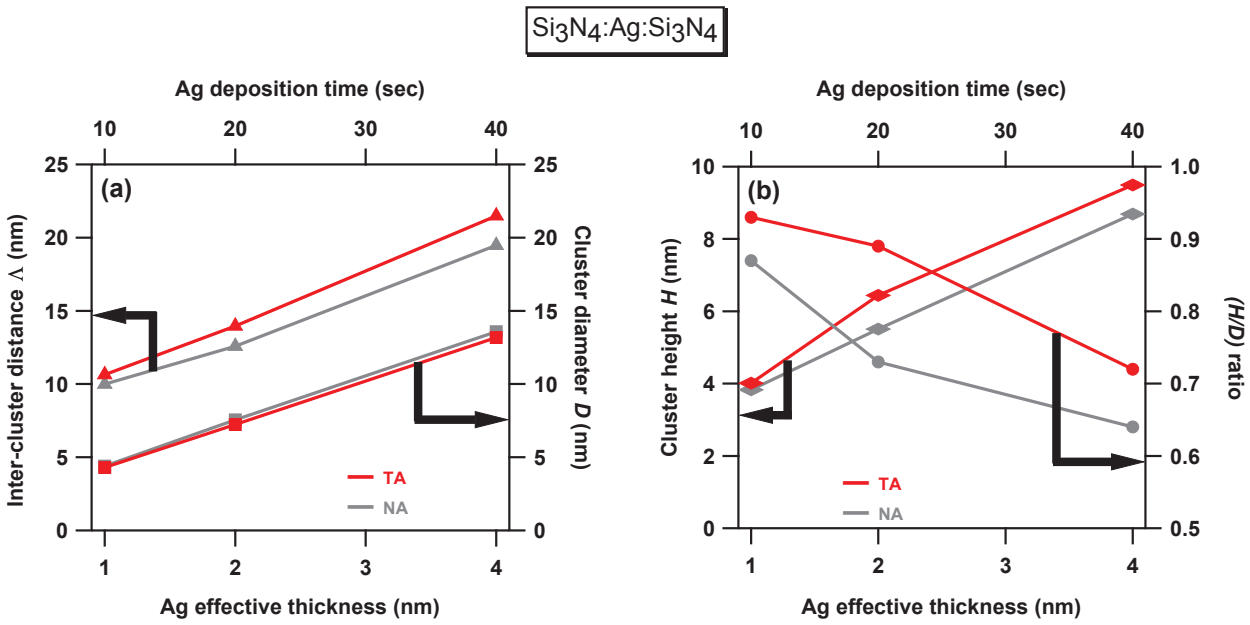

Figure V.3 – Variation of nanostructural parameters of Ag nanoclusters subjected to thermal annealing (TA at 400°C) from Si_3N_4:Ag:Si_3N_4 nanocomposites as a function of the Ag deposition time/thickness, compared with the respective non-annealed (NA) samples.

this regard, Fig.V.4(a-b) shows a comparison of λ_{max} and $(\Delta R/R_0)_{max}$ temporal variations for TA and NA Ag nanoclusters from Si_3N_4:Ag(20s/2nm):Si_3N_4 nanocomposites.

- **Ag deposition and holding time -** A sharp increase of λ_{max} and $(\Delta R/R_0)_{max}$ during the Ag deposition on the Si_3N_4 buffer-layer, and a slight decrease of λ_{max} during the holding time are observed in a similar range for both samples, showing the formation of similar Ag nanocluster assemblies after the growth at 200°C.

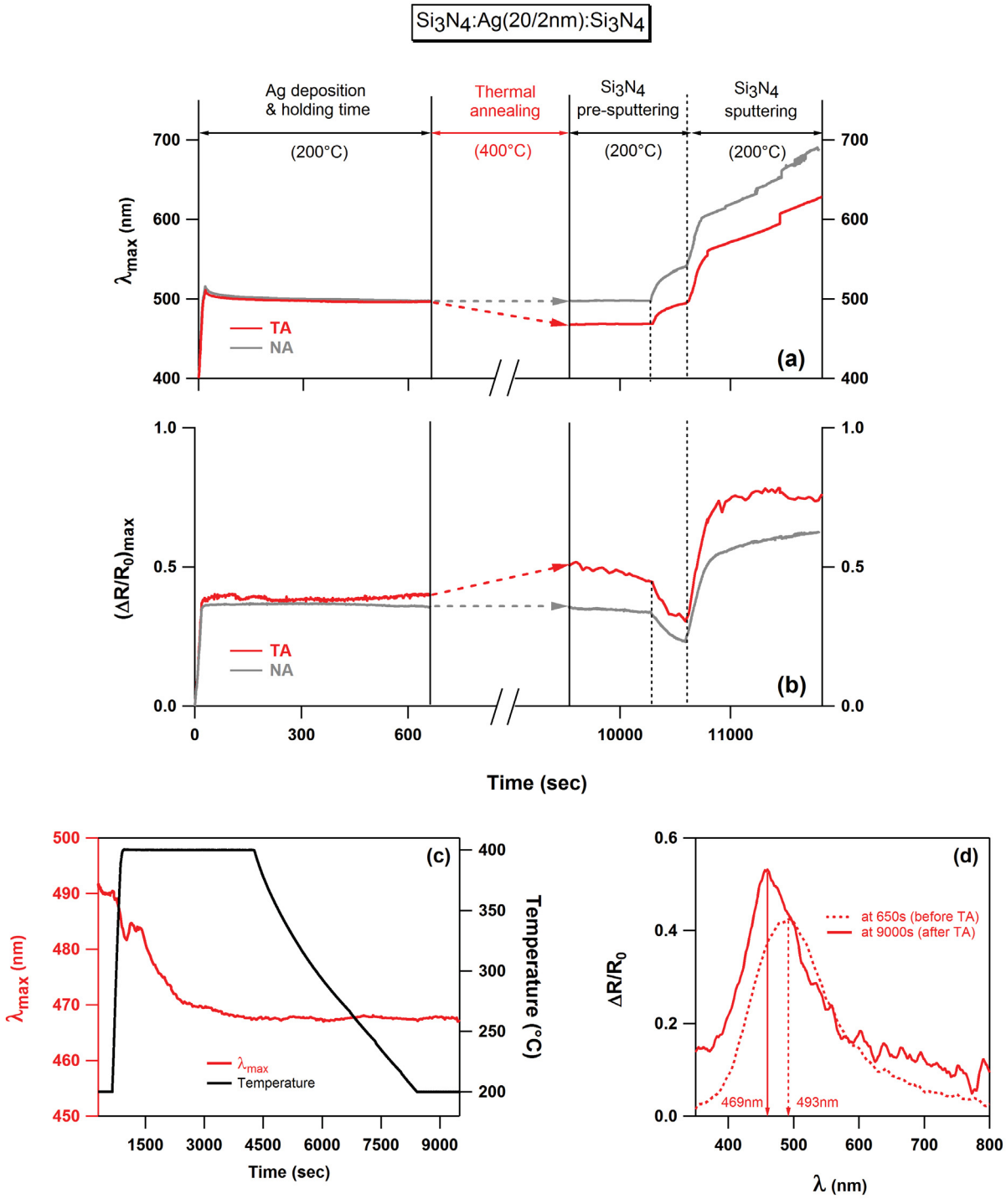

Figure V.4 – Temporal variations of λ_{max} (a) and $(\Delta R/R_0)_{max}$ (b) for TA (red curves) / NA (gray curves) Ag nanoclusters during the deposition of Si_3N_4:Ag(20s/2nm):Si_3N_4 nanocomposites. (c) Variation of λ_{max} during the thermal annealing step at 400°C. (d) Comparison of SDRS signals recorded before and after the heating treatment of the uncovered Ag nanoclusters.

- **Thermal annealing at 400°C -** During the heat treatment, the temporal variations in λ_{max} clearly show an immediate decrease as soon as the annealing temperature is increased (Fig.V.4(c)). This blue-shift further increases with a lower rate for a duration of about 2000s and later remains constant even after diminishing the temperature from 400°C to 200°C, showing that the modifications in the Ag cluster nanostructure are irreversible. From Table V.1, this blue-shifted SPR (from 493nm to 469nm) can be ascribed to the reshaping of the Ag clusters from an oblate shape to a more spherical shape. On the other hand, at the end of the annealing treatment, Fig.V.4(b-d) show that the thermal annealing also causes an increase of $(\Delta R/R_0)_{max}$ from 0.42 to 0.52, along with a slight narrowing of the SPR. These modifications are in aggrement with various works reported in the literature [6, 9–11].

- **Pre-sputtering and sputtering of the Si_3N_4 target -** After annealing and decrease of the temperature to 200°C, the Ag nanoclusters are covered by a Si_3N_4 matrix, which ensures that the pre-sputtering and sputtering conditions during the capping-layer deposition step are similar to those described in the previous chapters. During this capping, as shown in Fig.V.4(a-b), the overall optical behavior of the TA and NA Ag nanoclusters are similar, as explained in the previous Chapters III and IV. From Fig.V.4(a-b), it is clear that the SPR of the NA Ag nanoclusters remains red-shifted and damped in comparison with the SPR of the TA Ag nanoclusters. This results shows that, the modifications induced in the Ag nanostructure during the thermal treatment are well preserved throughout the Si_3N_4 capping process.

Similar optical variations due to the thermal annealing are also seen for different Ag amounts (e.g. Ag(10s/1nm) and Ag(40s/4nm)). Their nanostructure analysis is presented in Table V.1. However, even though the SDRS signals of these thermally annealed samples show distinct blue-shifted SPR compared to the corresponding NA samples, they are not presented here due to the considerable optical fluctuations.

3 Effect of low energy bias plasma treatments

As seen previously, thermal annealing causes modifications in the optical properties of Ag nanoclusters due to enhanced surface atomic mobility. As an alternative to the thermal annealing, plasma treatments can also cause modifications in the nanostructure of the metal nanoclusters, hence accordingly altering their optical properties. In this regard, Table V.2 shows the possible ion energy range in which a nanocomposite thin film can be treated with

energetic ions. At ion energies higher than 2keV, ion implantation processes are dominant, which can produce volume diffusion of atomic species. Such high energy ion treatments are used in the literature to modify nanostructures of embedded noble metal nanoclusters [12–16], which accordingly produce modifications in their optical properties. In addition, for ion energies between 50eV and 2keV, sputtering effects can be significant, causing thin film surface damage [17]. However, ions having energies lower than 50eV can provide us interesting perspectives as both the sputtering and the implantation effects are negligible. In this range, due to the energy exchange between the energetic ions and the atoms at the thin film surface, surface atomic diffusion may take place, leading to modifications in the cluster nanostructure as well as optical properties [18–21].

Ion energy range				
Ion energy	< 50eV	50eV-150eV	150eV-2keV	> 2keV
Dominant process	Energy exchange without sputtering	Energy exchange and sputtering	Sputtering and Implantation	Implantation

Table V.2 – Ion energy ranges and their dominant processes on thin films [22].

Hence in this section, we will focus on the influence of low energy ion treatments (25eV $\leq$ E $\leq$ 80eV) on the structural and optical properties of the Ag nanoclusters, which are either non-oxidized or oxidized by their exposure to a partially ionized oxygen atmosphere.

3.1 Plasma annealing of non-oxidized Ag nanoclusters

3.1.1 Experimental details

In this section, the influence of plasma annealing treatments is first investigated for non-oxidized Ag nanoclusters grown onto a Si_3N_4 buffer-layer. For this purpose, in PUMA, with the help of a RF source and a capacitor, it is possible to establish a bias voltage between the substrate holder (which acts as a cathode) and the surrounding cylinder (which acts as an anode). Due to this versatile provision, as soon as a gas is introduced in the vicinity of the substrate through the gas ring, a plasma of that gas with a controlled energy can be created surrounding the supported Ag nanoclusters (Fig.V.5).

Here, it was found that a minimum ion energy of 25eV can be obtained when an Ar flux of 6 sccm ($\equiv 10^{-3}$ mbar) is introduced through the gas ring at a bias voltage of 25V. The Si_3N_4-supported Ag nanoclusters were thus subjected to low energy Ar^+ plasma (25eV, 50eV, and 80eV) for sufficient duration (around 1200s). The plasma annealed (PA) Ag nanoclusters

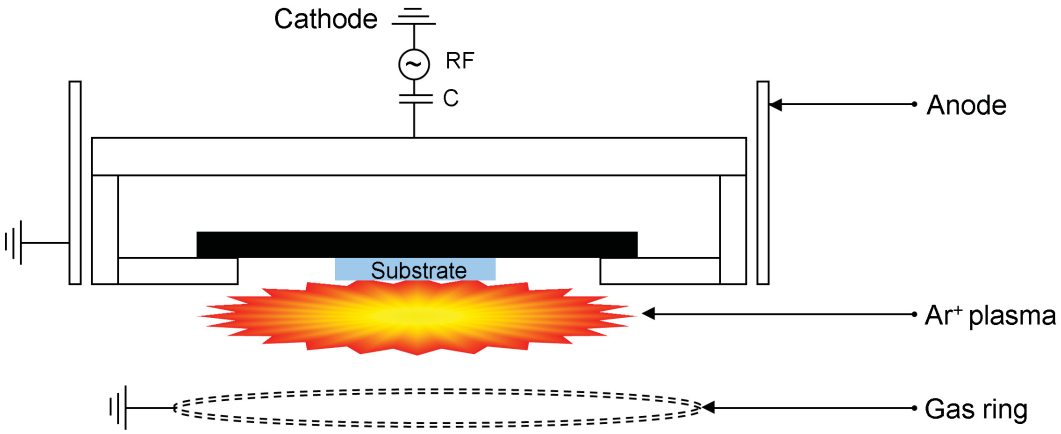

Figure V.5 – Schematics of bias plasma formation in magnetron deposition chamber.

were later covered by a Si_3N_4 capping-layer in order to form Si_3N_4:(Ag+PA):Si_3N_4 nanocomposites. These studies were carried out for different Ag amounts (10s/1nm, 20s/2nm, and 40s/4nm) and compared with the results obtained from non-annealed (NA) or "as-prepared" Si_3N_4:(Ag+NA):Si_3N_4 nanocomposite samples. *post mortem* HAADF-STEM and GISAXS techniques were used for nanostructural analysis of these PA Ag nanoclusters, whereas their optical properties were studied by using real-time SDRS.

3.1.2 *Post mortem* nanostructure analysis

Fig.V.6(a-d) shows typical *post mortem* characterizations for NA and PA Si_3N_4:Ag(20s/2nm):Si_3N_4 nanocomposite tri-layers. Here, comparing to the NA sample, a prominent blue-shifted SPR is evident at the end of the deposition of the nanocomposites treated at 25eV (Fig.V.6(b)) and at 50eV (Fig.V.6(c)). Besides, although it exhibits a maximum in the visible range, the optical signal of the PA nanocomposite treated at 80eV shows no obvious SPR band and resembles more to that of a cluster-free transparent film (Fig.V.6(d)).

Moreover, a gradual decrease of the in-plane cluster size is clearly visible in the HAADF-STEM micrographs of the nanocomposites treated at 25eV and 50eV, while an increase of the scattering lobe separation (i.e., a decrease of the inter-cluster distance) is observed in the corresponding GISAXS patterns. It is also worth noting that, upon treatment at 80eV, no Ag cluster can be seen in the HAADF-STEM micrograph (indicating total Ag re-evaporation by sputtering), and hence no GISAXS measurement was carried out for this sample. This result confirms that the optical signal of this sample (Fig.V.6(d)) is actually due to the contribution of light interferences from a cluster-free transparent Si_3N_4 layer.

The nanostructure parameters retrieved from the quantitative analysis of the HAADF-

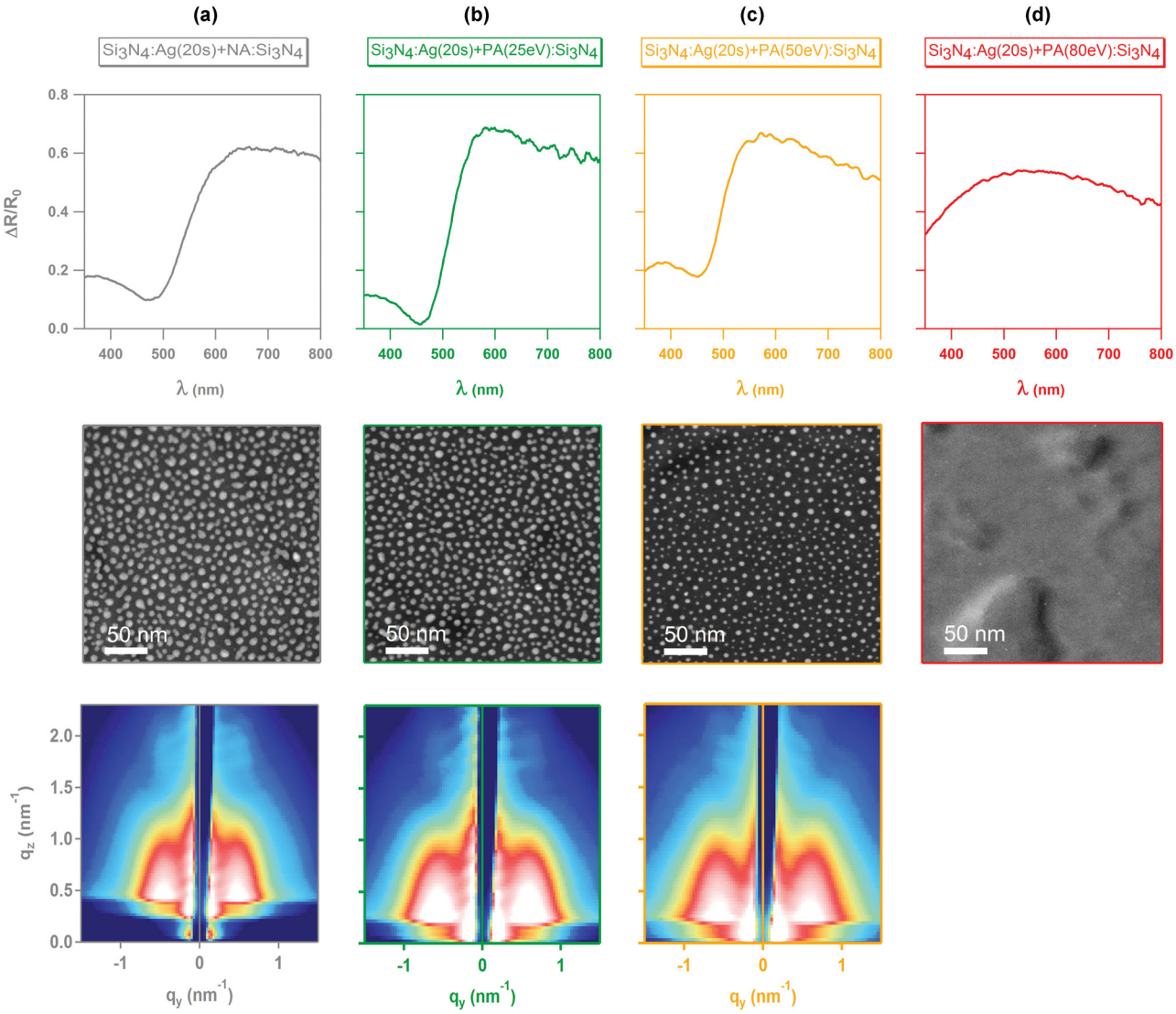

Figure V.6 – Comparison of spectral SDRS signals at the end of the depositions for Si_3N_4:Ag(20s/2nm):Si_3N_4 nanocomposites, along with their respective HAADF-STEM micrographs and GISAXS patterns: (a) non-annealed sample, (b) PA sample at 25eV, (c) PA sample at 50eV, and (d) PA sample at 80eV.

STEM and GISAXS data are reported in Table V.3. It can be observed that the plasma treatment induces a decrease of the in-plane cluster size D and of the metal coverage, associated with an increase of the areal cluster density d and of the out-of-plane aspect ratio H/D along with the cluster height H. Moreover in the PA samples, a clear decrease of the in-plane size distribution σ_D can also be seen comparing to the NA samples. These effects are more pronounced at a bias plasma energy of 50eV than at 25eV. Furthermore, the nanostructural variations are well reproduced for all the samples treated at 25eV (Fig.V.7), with the influence

of the plasma annealing being more or less similar when the deposited Ag amount increases.

Si_3N_4:Ag:Si_3N_4 nanocomposites	Ar^+ plasma annealing	HAADF-STEM analysis					GISAXS analysis	
Ag deposition time/thickness	PA energy	d (μm^{-2})	Coverage (%)	D (nm)	σ_D (nm)	Λ (nm)	(H/D) ratio	H (nm)
10s/1nm	NA	14464	21	4.4	1.4	10.0	0.87	3.8
	25eV	15111	16	3.5	1.2	9.1	1.16	4.1
20s/2nm	NA	6674	32	7.6	1.9	12.6	0.73	5.5
	25eV	7657	29	6.3	1.6	11.9	0.90	5.7
	50eV	8339	16	4.6	1.5	12.1	1.24	5.7
	80eV	-	-	-	-	-	-	-
40s/4nm	NA	2094	41	13.6	3.6	19.4	0.64	8.7
	25eV	2933	41	12.2	3.0	18.7	0.74	9.0

Table V.3 – Nanostructural parameters of plasma annealed (PA) Ag nanoclusters (at 25eV) compared with non-annealed (NA) Ag nanoclusters from Si_3N_4:Ag:Si_3N_4 nanocomposites with different Ag amounts (10s/1nm, 20s/2nm, and 40s/4nm). The Si_3N_4:Ag(20s/2nm):Si_3N_4 nanocomposite sample further treated with additional plasma energies (50eV and 80eV).

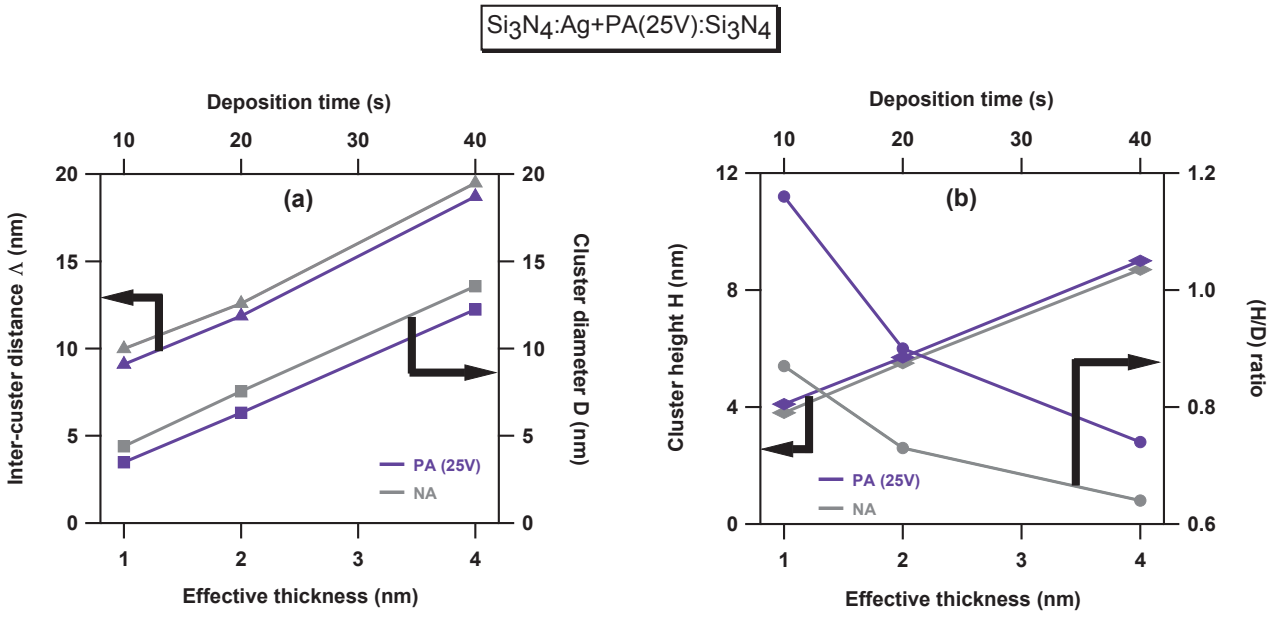

Figure V.7 – Variation of nanostructure parameters of Ag nanoclusters subjected to plasma annealing at 25eV from Si_3N_4:Ag:Si_3N_4 nanocomposites as a function of the Ag deposition time/thickness (violet curves), compared with the respective non-annealed samples (gray curves).

In comparison with the thermal annealing treatment that causes a decrease of the areal clus-

ter density d (Table V.1), our results suggest the absence of coalescence-type growth processes during the plasma annealing of the Ag clusters. In the literature, it has been already reported that upon interactions with a low-energy plasma, surface defects such as vacancies are created on the substrate, which can act as pinpoints or nucleation sites for metal adatoms [23, 24]. This phenomenon associated with sputtering/redeposition effects may explain the increase of d together with the decrease of D after plasma annealing. Nevertheless, both thermal and plasma annealing induce a prominent reshaping of the nanoclusters with an increase of their out-of-plane aspect ratio, which can explain the blue-shift of the SPR band.

3.1.3 *In situ* and real-time optical analysis

The temporal SDRS variations in SPR position λ_{max} and amplitude $(\Delta R/R_0)_{max}$ of the Si_3N_4: Ag(20s/2nm):Si_3N_4 nanocomposites subjected to different plasma annealing conditions and of the Si_3N_4:Ag+PA(25eV):Si_3N_4 nanocomposites with different Ag amounts are displayed in Figs.V.8 and V.9, respectively. For comparison, the SDRS signals of a non-annealed Si_3N_4:Ag(20s/2nm): Si_3N_4 nanocomposite trilayer is also shown in Fig.V.8.

Insofar as the spectral variations during STEPS 1 & 2 (Ag deposition and holding time) have been described in detail in previous chapters, we will focus hereafter on the spectral variations induced during STEP 3 (plasma annealing) and the subsequent steps (pre-sputtering and sputtering of the Si_3N_4 target).

- **STEP 3 -** During plasma annealing, whatever the bias voltage (Fig.V.8 (a-b) & Table V.4) and Ag amount (Fig.V.9), a prominent decrease in both λ_{max} and $(\Delta R/R_0)_{max}$ is evident, which gradually progresses with time and stops as soon as the bias plasma is switched off. This shows that the SPR blue-shift and damping effects induced by the plasma treatment are permanent and irreversible. Moreover, our results clearly indicate that these optical modifications are faster and stronger for higher bias voltages. This phenomenon is highlighted in Fig.V.8(c), which exhibits the SDRS signals of the PA Si_3N_4:Ag(20s/2nm):Si_3N_4 nanocomposites recorded at the end of the plasma annealing at 25eV, 50eV, and 80eV, respectively, and compared with the NA sample. On the other hand, as seen in Fig.V.9 and Table V.4, the influence of the plasma annealing on the optical response of the Ag nanoclusters treated at 25eV tends to weaken for higher deposited Ag amounts (i.e., higher in-plane size D).

  The blue-shift and the narrowing of the SPR after plasma annealing, which are illustrated in Fig.V.9(c-e) for the Si_3N_4:Ag:Si_3N_4 nanocomposite treated at 25eV, are also observed after thermal annealing (see Section 2.3 of this Chapter). However, in contrast to the

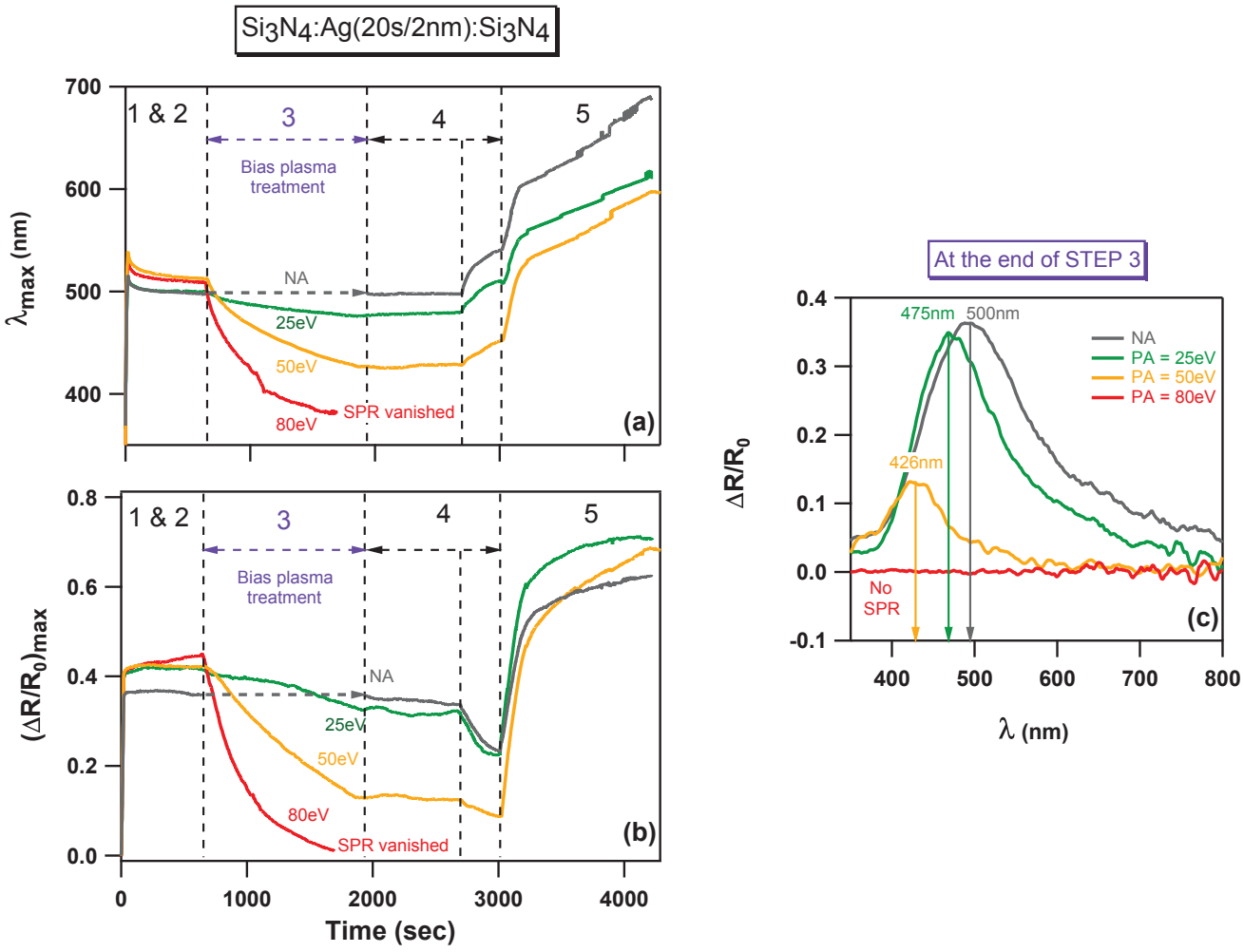

Figure V.8 – Temporal variations of λ_{max} (a) and $(\Delta R/R_0)_{max}$ (b) during the deposition of Si_3N_4:Ag(20s/2nm):Si_3N_4 nanocomposites, Ag nanoclusters of which are subjected to the increasing bias Ar^+ plasma annealing treatments (PA = 25eV, 50eV, and 80eV) and compared with non-annealed (NA) sample, (c) shows the spectral variations for the SPR of Ag nanoclusters at the end of STEP 3 for different bias plasma voltages.

thermal annealing, plasma annealing also induces a decrease of the SPR amplitude, which tends to confirm that sputtering effects contribute to the morphological evolution of the nanoclusters (both, size and shape) subjected to low-energy ion species, even at 25eV. Accordingly, for the nanocomposite treated at 80eV, the complete damping of the SPR (due to total Ag re-evaporation by sputtering) is visible after about 1000s of plasma treatment.

- **STEP 4 -** During the ignition and pre-sputtering of the Si_3N_4 target, upon N_2 introduction, the influence of partially ionized nitrogen species on the Ag clusters leads to a

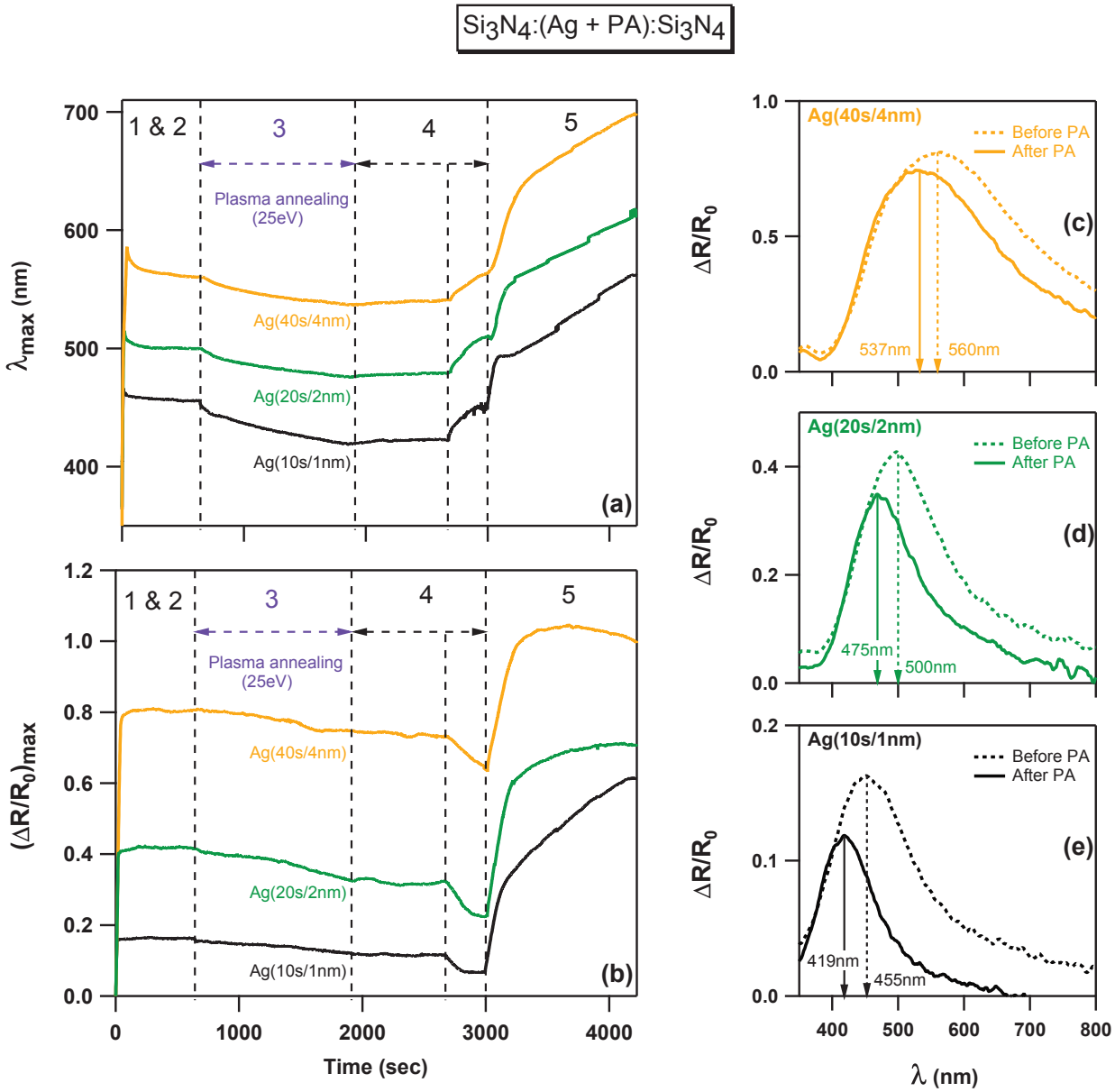

Figure V.9 – Temporal variations of λ_{max} (a) and $(\Delta R/R_0)_{max}$ (b) for plasma annealed (PA at 25eV) Ag nanoclusters during the deposition of Si_3N_4:Ag:Si_3N_4 nanocomposites with increasing Ag amounts (10s/1nm, 20s/2nm, and 40s/4nm). (c-e) represents the spectral variations in the SPR of the Ag nanoclusters before (around 650s - dotted curves) and after (around 1920s - thick curves) the plasma annealing for respective samples during STEP 3 (attention for the scale).

red-shift together with a damping of the SPR, as we have discussed in previous chapters. In Section 5.3.3 of Chapter III, we have seen that smaller Ag nanoclusters show higher reactivity for the nitrogen ion species because of a larger specific surface area. This is in agreement with the results reported in Table V.5, which show a decrease of $\Delta\lambda_{max}$

Si_3N_4:(Ag+PA):Si_3N_4 nanocomposites - STEP 3			
Ag deposition time/thickness	Bias Ar^+ plasma energy	$\Delta\lambda_{max}$ (nm)	% variation $(\Delta R/R_0)_{max}$
Ag(10s/1nm)	PA = 25eV	-36	-36
Ag(20s/2nm)	PA = 25eV	-25	-29
	PA = 50eV	-85	-69
	PA = 80eV	SPR vanished	
Ag(40s/4nm)	PA = 25eV	-23	-8

Table V.4 – Effect of plasma treatment on the optical properties of Ag nanoclusters from Si_3N_4:(Ag+PA):Si_3N_4 nanocomposites, expressed in terms of shifts in λ_{max} ($\Delta\lambda_{max}$) and % variations in $(\Delta R/R_0)_{max}$, for different Ag amounts at the end of bias plasma annealing.

in both NA and PA samples as the deposited Ag amount increases. However, it is also apparent that $\Delta\lambda_{max}$ is smaller in the PA samples than in the NA samples with similar Ag amounts, while plasma annealing induces a decrease of the average cluster size. Furthermore, it can be seen that the SPR red-shift is less pronounced for the Si_3N_4:Ag:Si_3N_4 nanocomposite treated at a bias plasma energy of 50eV than the one treated at 25eV. Although these results are somewhat ambiguous, it should be noted that Borensztein *et al* [25] have shown that spherical Au clusters are less reactive to oxygen than oblate Au clusters. Indeed, for a given volume the specific surface area of an oblate cluster, and therefore its reactivity, decreases upon increasing its aspect ratio. Therefore, our results may arise from a delicate interplay between size and shape effects on the reactivity of the nanoclusters.

Si_3N_4:Ag:Si_3N_4 nanocomposites - STEP 4		
Ag deposition time/thickness	$\Delta\lambda_{max}$ (nm) after N_2 introduction	
	Non-annealed (NA)	Plasma annealed (PA)
Ag(10s/1nm)	+52	+28 (at 25eV)
Ag(20s/2nm)	+43	+29 (at 25eV)
		+24 (at 50eV)
		– (at 80eV)
Ag(40s/4nm)	+26	+22 (at 25eV)

Table V.5 – Shift in λ_{max} ($\Delta\lambda_{max}$) due to the nitrogen ion species in plasma annealed/non-annealed Ag nanoclusters from Si_3N_4:Ag:Si_3N_4 nanocomposites.

- **STEP 5 -** During the capping of the Ag clusters by the Si_3N_4 matrix, the overall optical behavior is similar: λ_{max} and $(\Delta R/R_0)_{max}$ increase sharply in both PA and NA

samples for the same reasons as already discussed in the previous chapters. Furthermore, comparing to the NA sample, the PA samples always show blue-shifted SPR positions (Fig.V.8(a)), indicating that the modifications in the cluster shape induced by the plasma treatment are preserved throughout the Si_3N_4 capping layer deposition.

3.2 Bias plasma annealing of oxidized Ag nanoclusters

It is worth recalling here that the SPR of Ag nanoclusters is completely suppressed upon their interaction with partially ionized oxygen species (Section 4, Chapter IV). In the literature, special attention is paid to the reappearance of the SPR of such oxidized metal clusters in order to find useful industrial applications such as optical switches and chemical sensors [26–28]. For this purpose, many authors have shown the possibility of SPR reappearance by subjecting oxidized Ag nanoclusters to thermal annealing at 500°C in reducing H_2 atmospheres [25, 29, 30], which is not allowed in PUMA for safety reasons. Therefore, as a rarely studied route, we investigated the ability of plasma annealing treatments to induce the reappearance of the SPR of Ag nanoclusters previously oxidized.

3.2.1 Experimental details

In order to study the influence of plasma annealing treatments on oxidized Ag clusters, glass-supported Ag nanoclusters are subjected to a cycle of oxidation/etching treatment. After carrying out Ag(20s/2nm) deposition on glass, the resulting Ag nanoclusters are exposed to a 20 sccm ($\equiv 4.5\times10^{-3}$ mbar) O_2 flux, which is partially ionized ($O_2^{(+)}$), in order to suppress their SPR by complete oxidation. Then, these oxidized clusters are treated with an Ar^+ plasma of 50eV for 600s. Such an oxidation and plasma etching cycle is repeated one more time in order to investigate its reproducibility. Fig.V.10(a-b) shows the variations of λ_{max} and $(\Delta R/R_0)_{max}$ recorded during this sequence.

3.2.2 *In situ* and real-time optical analysis

- **Ag deposition and holding time -** Variations of λ_{max} and $(\Delta R/R_0)_{max}$ during these steps show a classical behavior, as already explained in the previous chapters.

  1st Oxidation-Etching cycle

- **$O_2^{(+)}$ exposure (20 sccm) -** At the beginning of the 1st Oxidation-Etching cycle, the effect of the $O_2^{(+)}$ exposure can be seen immediately in the form of a sharp increase in λ_{max} and a strong decrease in $(\Delta R/R_0)_{max}$. After 90s of exposure, which leads to a red-shift

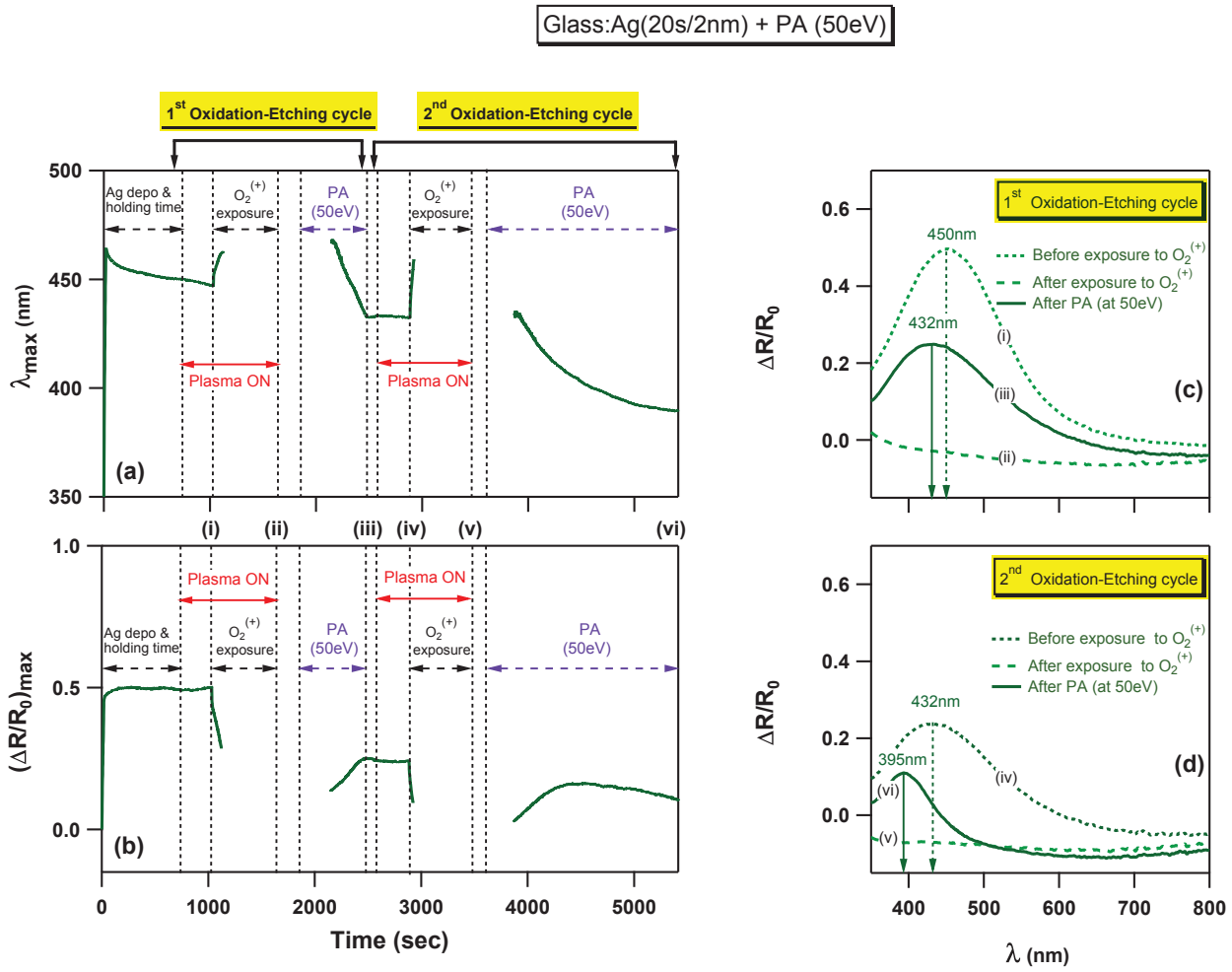

Figure V.10 – Temporal variations of λ_{max} (a) and $(\Delta R/R_0)_{max}$ (b) during the cyclic exposure of glass-supported Ag nanoclusters to partially ionized O_2 ($O_2^{(+)}$) and bias plasma annealing (PA at 50eV). (c-d) represent the SDRS signals at the end of the respective oxidation or PA treatments during the two cycles.

of +16nm, the tracing of the λ_{max} signal becomes impossible due to complete damping of the SPR. In this regard, Fig.V.10(c) clearly shows a totally damped spectral curve at the end of the $O_2^{(+)}$ exposure (dashed curve-(ii)) comparing to the spectral curve measured just before $O_2^{(+)}$ exposure (dotted curve-(i)).

- **Plasma annealing (50eV) -** Upon plasma annealing of the oxidized Ag nanoclusters at 50eV, the SPR reappears after about 290s with a λ_{max} value still significantly higher than before the $O_2^{(+)}$ exposure. However, with further annealing, a gradual blue-shift of the SPR together with an increase of its amplitude are observed as long as the bias Ar^+ plasma surrounding the Ag nanoclusters is maintained. These results suggest that sputtering effects due to the plasma annealing lead to remove oxide species encapsulating

pure Ag nanoclusters. The influence of such sputtering effects may also explain that the $(\Delta R/R_0)_{\max}$ value is much lower after the plasma annealing than before the $O_2^{(+)}$ exposure (solid curve (iii) in Fig.V.10(c)). Furthermore, as seen before in Section 3.1 of the present Chapter, the blue-shifted SPR may be the consequence of energetic interactions between the plasma ions and the Ag nanoclusters that lead to increase the out-of-plane aspect ratio of the clusters.

2nd Oxidation-Etching cycle

- **$O_2^{(+)}$ exposure (20 sccm) -** At the beginning of the 2nd Oxidation-Etching cycle (dotted curve (iv) in Fig.V.10(d)), the PA Ag nanoclusters are again exposed to $O_2^{(+)}$ which accordingly causes a sharp SPR red-shift and a strong SPR damping. Comparing to the first $O_2^{(+)}$ exposure, $\lambda_{\max}$ now increases by +27nm in 38s before total SPR damping as shown in Fig.V.10(d) (dashed curve (v)). Such a greater red-shift in SPR position in a shorter time duration suggests the presence of smaller Ag clusters at the beginning of the "2nd Oxidation-Etching cycle" comparing to the first one, possibly due to the sputtering effect as explained before.

- **Plasma annealing (50eV) -** During the last step, the re-oxidized Ag nanoclusters are again subjected to the plasma annealing at 50eV for a longer time (1800s) comparing to the previous cycle. As expected this leads to the reappearance of the SPR after about 260s. Then, $\lambda_{\max}$ is seen to decrease continuously whereas $(\Delta R/R_0)_{\max}$ first increases before decreasing slowly after about 800s of the plasma annealing. This may indicate that, after complete removal of the oxide shells around the nanoclusters, the sputtering of pure Ag metal starts. Actually, such a slight SPR damping was not observed during the first cycle because its duration was limited to 600s only. Finally, at the end of this "2nd Oxidation-Etching cycle", the SPR appears to be blue-shifted and damped (solid curve (vi) in Fig.V.10(d)) comparing to the SPR recorded at the end of the first cycle (solid curve (iii) in Fig.V.10(c)). These blue-shifts and damping effects are likely the consequence of H/D increase and D decrease, respectively.

In this way, we have seen the ability of the bias plasma annealing treatment in regaining the disappeared SPR from completely oxidized Ag nanoclusters as an alternative route to redox reactions.

4 Summary and conclusions

With the help of real-time SDRS and *post mortem* HAADF-STEM and GISAXS characterizations, the influence of thermal and bias plasma treatments on the optical and nanostructural properties of Ag nanoclusters has been studied. Both thermal and low energy bias plasma annealing lead to the formation of more spherical Ag nanoclusters compared to non-annealed Ag nanoclusters, which accordingly causes a prominent SPR blue-shift. In case of thermal annealing, even though, an increase of the in-plane cluster size D (as suggested in the literature) was absent, a prominent increase of the cluster height H accompanied by a decrease of the cluster-density d are evident, which suggest a coalescence-type growth, thus explaining the increase of the SPR amplitude. On the other hand, contrary to the thermal annealing, the Ag nanoclusters subjected to a low energy bias Ar^+ plasma (of 25eV) show a significant decrease of their in-plane size D, which express itself in a prominently decreased SPR amplitude. The presence of smaller Ag nanoclusters with an increased cluster density indicates the possible etching/re-deposition effects, which distinctly increase with further increment of the bias plasma energy (e.g. at 50eV), and eventually lead to a complete re-evaporation of the supported Ag nanoclusters (at 80eV).

In the later part of this Chapter, disappearance/reappearance of the SPR of Ag nanoclusters is evidenced with the help of alternate oxidation/etching cycles. Even though the reappearance of the SPR of completely oxidized Ag nanoclusters is possible after plasma etching treatment, by re-evaporation/sputtering it results in a prominent SPR damping, thus indicating the loss of Ag metal.

Bibliography

[1] C. R. Henry. *Surface studies of supported model catalysts.* Surface science reports **31**, 231–325 (1998). 131

[2] J. Toudert, S. Camelio, D. Babonneau, M. F. Denanot, T. Girardeau, J. P. EspiÑos, F. Yubero, and A. R. Gonzalez-Elipe. *Morphology and surface-plasmon resonance of silver nanoparticles sandwiched between Si_3N_4 and BN layers.* Journal of Applied Physics **98**, 1–10 (2005). 132

[3] T. Teranishi, S. Hasegawa, T. Shimizu, and M. Miyake. *Heat-induced size evolution of gold nanoparticles in the solid state.* Advanced Materials **13**, 1699–1701 (2001). 132, 134

[4] A. Kolmakov and D. W. Goodman. *In situ scanning tunneling microscopy of oxide-supported metal clusters: Nucleation, growth, and thermal evolution of individual particles.* The Chemical Record **2**, 446–457 (2002). 132, 134

[5] Z. W. Dong, G. J. You, P. Zhou, C. F. Zhang, K. J. Liu, Y. L. Yan, and S. X. Qian. *Heat treatment effect on the ultrafast dynamics and nonlinear optical properties of $Ag:Si_3N_4$ nanocermets.* Journal of Physics D: Applied Physics **39**, 4766–4770 (2006). 132, 134

[6] H. Takele, A. Kulkarni, S. Jebril, V. S. K. Chakravadhanula, C. Hanisch, T. Strunskus, V. Zaporojtchenko, and F. Faupel. *Plasmonic properties of vapour-deposited polymer composites containing Ag nanoparticles and their changes upon annealing.* Journal of Physics D: Applied Physics **41**, 125409 (2008). 132, 134, 137

[7] F. Ruffino, M. G. Grimaldi, C. Bongiorno, F. Giannazzo, F. Roccaforte, and V. Raineri. *Microstructure of Au nanoclusters formed in and on SiO_2.* Superlattices and Microstructures **44**, 588–598 (2008). 132, 134

[8] U. Kreibig and M. Vollmer. *Optical Properties of Metal Clusters.* Springer-Verlag, Berlin (1995). 132, 134

[9] A. Heilmann and J. Werner. *In situ observation of microstructural changes of embedded silver particles.* Thin Solid Films **317**, 21–26 (1998). 132, 134, 137

[10] A. Pan, Z. Yang, H. Zheng, F. Liu, Y. Zhu, X. Su, and Z. Ding. *Changeable position of spr peak of Ag nanoparticles embedded in mesoporous SiO_2 glass by annealing treatment.* Applied Surface Science **205**, 323–328 (2003). 137

[11] J. Sancho-Parramon, V. Janicki, P. Dubcek, M. Karlusic, D. Gracin, M. Jaksic, S. Bernstorff, D. Meljanac, and K. Juraic. *Optical and structural properties of silver nanoparticles in glass matrix formed by thermal annealing of field assisted film dissolution.* Optical Material **32**, 510–514 (2010). 137

[12] F. Garrido, J. C. Dran, L. Thomé, C. Meneghini, F. Gonella, and A. Quaranta. *High-energy ion-beam mixing: A new route to form metallic nanoclusters in a dielectric matrix.* Nuclear Instruments and Methods in Physics Research, Section B: Beam Interactions with Materials and Atoms **115**, 561–564 (1996). 138

[13] G. C. Rizza, M. Strobel, K. H. Heinig, and H. Bernas. *Ion irradiation of gold inclusions in SiO_2: Experimental evidence for inverse Ostwald ripening.* Nuclear Instruments and Methods in Physics Research Section B: Beam Interactions with Materials and Atoms **178**, 78–83 (2001). 138

[14] M. Nikolaeva, M. Sendova-Vassileva, D. Malinovska, Y. Sarov, and J. C. Pivin. *Ion beam assisted formation of Ag nanoparticles in SiO_2 and their optical properties.* Nuclear Instruments and Methods in Physics Research Section B: Beam Interactions with Materials and Atom **193**, 867–870 (2002). 138

[15] S. Camelio, J. Toudert, D. Babonneau, and T. Girardeau. *Tailoring of the optical properties of Ag:Si_3N_4 nanocermets by changes of the cluster morphology.* Applied Physics B: Lasers and Optics **80**, 89–96 (2005). 138

[16] J. Toudert, D. Babonneau, S. Camelio, T. Girardeau, F. Yubero, J. P. Espinòs, and A. R. Gonzalez-Elipe. *Using ion beams to tune the nanostructure and optical response of co-deposited Ag:BN thin films.* Journal of Physics D: Applied Physics **40**, 4614–4620 (2007). 138

[17] P. J. Kelly and R. D. Arnell. *Magnetron sputtering: a review of recent developments and applications.* Vacuum **56**, 159–172 (2000). 138

[18] C. H. Choi, R. Ai, and S. A. Barnett. *Suppression of three-dimensional island nucleation during GaAs growth on Si(100).* Physical Review Letters **67**, 2826 (1991). 138

[19] M. V. Ramana Murty and H. A. Atwater. *Defect generation and morphology of (001) Si surfaces during low-energy Ar-ion bombardment.* Physical Review B **45**, 1507–1510 (1992). 138

[20] N. E. Lee, G. A. Tomasch, and J. E. Greene. *Low-temperature Si(001) epitaxy using low-energy (<E> ≈ 18 eV) Si atoms.* Applied Physics Letters **65**, 3236–3238 (1994). 138

[21] S. H. Lee, H. P. Gillis, and C. Ratsch. *Smoothening mechanism for GaAs(100) surfaces during ion-enhanced plasma etching.* Applied Physics Letters **88**, 161916–161913 (2006). 138

[22] R. Bunshah. *Handbook of hard coatings: Deposition technologies, Properties and Applications.* Noyes publications (2001). 138

[23] S. Esch, M. Bott, T. Michely, and G. Comsa. *Nucleation of homoepitaxial films grown with ion assistance on Pt(111).* Applied Physics Letters **67**, 3209 (1995). 142

[24] S. J. Chey and D. G. Cahill. *Surface defects created by low energy (20 < E < 240 eV) ion bombardment of Ge(001).* Surface Science **380**, 377–384 (1997). 142

[25] Y. Borensztein, L. Delannoy, A. Djedidi, R. G. Barrera, and C. Louis. *Monitoring of the plasmon resonance of gold nanoparticles in Au/TiO_2 catalyst under oxidative and reducing atmospheres.* Journal of Physical Chemistry C **114**, 9008–9021 (2010). 145, 146

[26] B. Liedberg, C. Nylander, and I. Lundstrom. *Biosensing with surface plasmon resonance - how it all started.* Biosensors and Bioelectronics **10**, i–ix (1995). 146

[27] D. J. Sirbuly, A. Too, M. Law, R. Fan, and P. Yang. *Multifunctional nanowire evanescent wave optical sensors.* Advanced Materials **19**, 61–66 (2007). 146

[28] B. Brian, B. Sepulveda, Y. Alaverdyan, L. M. Lechuga, and M. Kall. *Sensitivity enhancement of nanoplasmonic sensors in low refractive index substrates.* Optics Express **17**, 2015–2023 (2009). 146

[29] H. Bi, W. Cai, C. Kan, L. Zhang, D. Martin, and F. TrÄger. *Optical study of redox process of Ag nanoparticles at high temperature.* Journal of Applied Physics **92**, 7491 (2002). 146

[30] J. Hu, W. Cai, Y. Li, and H. Zeng. *Oxygen-induced enhancement of surface plasmon resonance of silver nanoparticles for silver-coated soda-lime glass.* JOURNAL OF PHYSICS: CONDENSED MATTER **17**, 5349–5354 (2005). 146

General conclusion and perspectives

The main objective of this thesis was to study the optical properties of nanocomposite thin films made up of noble metal nanoclusters (Ag) embedded in dielectric matrix (Si_3N_4), during their synthesis using a real-time optical spectroscopy. In this regard, the choice of the magnetron sputtering deposition technique and the non-intrusive *in situ* surface differential reflectance spectroscopy (SDRS), gave us the required flexibilities in studying alternate depositions of Ag and Si_3N_4. Such a simple but robust experimental arrangement efficiently investigates the vital information regarding the optical properties of the composite thin films in real-time with a remarkable sensitivity. As the optical properties of the metal nanoclusters are strongly related to their nanostructure, *post mortem* structural characterization techniques like, HAADF-STEM and GISAXS, are used throughout this research work. Although the literature has witnessed the *in situ* and real-time SDRS characterizations of noble metal nanoclusters, these past research works were almost restricted to the growth of the metal nanoclusters during their depositions. In this regard, we not only study the evolution of the metal nanoclusters during their growth, but also during the post-deposition evolution by subjecting them to different chemical and/or physical treatments, and during their capping by Si_3N_4 in one complete continuous setting.

More specifically, the real strength of *in situ* and real-time SDRS lies in studying the optical properties during alternate depositions of Si_3N_4:Ag:Si_3N_4 nanocomposites, thus giving a "live-picture" of the complete deposition procedures taking place inside the deposition chamber. During the Ag depositions, SDRS captures the evolution of the optical properties that indicates a coalescence-type growth of the Ag nanoclusters. During the holding time, even though no action is taken on the system, the kinetics of the minute modifications in the SDRS signals suggest a slow (in several minutes) and small reshaping of the Ag nanoclusters towards their equilibrium shape. Such sensitive information on the kinetics of reshaping effects are otherwise

difficult to detect with *post mortem* optical and/or structural analysis.

In situ SDRS can also be used to detect gas atmosphere by using nanocomposite materials as the sensitivity and kinetics of the optical modifications are different depending on the atmosphere exposure. Specifically to the magnetron sputtering system, the gas can be non-ionized or partially ionized, which therefore induces modifications in the optical response of the metal nanoclusters. For example, the Ag nanoclusters are found to be reactive to non-ionized O_2, which induces fast modifications (in few seconds) in the SPR characteristics (i.e., strong red-shift and damping of the absorption band), in contrast to non-ionized N_2 and Ar. On the other hand, a complete disappearance of the SPR (in few seconds) of the Ag nanoclusters is evident when they are exposed to partially ionized oxygen species $O_2^{(+)}$, while a significant reactivity of the Ag nanoclusters for partially ionized nitrogen species $N_2^{(+)}$ is evident. Ar is found to be non-reactive with Ag nanoclusters in both non-ionized and partially ionized forms.

The influence of the Si_3N_4 capping matrix on the optical properties of the Ag nanoclusters, clearly shows two successive steps that separate the formation of a "real" Ag:Si_3N_4 nanocomposite layer and the cluster-free (transparent) Si_3N_4 capping-layer, distinctly. Moreover, during the capping of the oxidized Ag nanoclusters, in the very beginning, the optical changes captured by SDRS clearly indicate the possible fast desorption of the O_2 from the Ag nanoclusters (in 10s of seconds). This study seriously exposes the limitations of *post mortem* optical analysis, which do not show such vital modifications in case of Ag nanoclusters exposed to O_2.

On the same line, this research work also explores the influence of physical treatments (like thermal and plasma annealing) on the optical and structural properties of Ag nanoclusters in real-time. Both annealing treatments even though produce prominent blue-shift of the SPR, they give rise to different nanostructure modifications. Thermal annealing is found to reduce the cluster density distinctly without altering the cluster size as reported in the literature frequently. In contrast, the cluster density is increased significantly upon plasma annealing treatment with a reduction of the cluster size. However, *post mortem* GISAXS reveals that both of these annealing techniques give rise to more spherical nanoclusters that explains the observed SPR blue-shifts.

Finally, in this research activity, we have presented different treatments with which we can tailor the SPR of Ag nanoclusters in the visible range, by modulating their SPR characteristics to a great extent. As a striking example, we have demonstrated a combination of oxidation-plasma annealing treatments on Ag nanoclusters where the SPR can disappear or reappear, respectively.

The research work performed during this Ph.D. opens some interesting perspectives. Because of its flexibility, sensitivity, and efficiency, the use of SDRS in an *in situ* configuration on different experimental set-ups could be investigated for the real-time characterization of nanomaterials. As an example, implementation of SDRS on the ion-beam sputtering machine used in our group can be ideal, as it allows the preparation of nanostructured (rippled) surfaces and the self-organized growth of metal nanoclusters[1,2]. The real-time optical diagnostics of such nanocluster patterns can offer insightful information during their synthesis. Furthermore, these nanocluster patterns are expected to have a great potential to be applied for optically dichroic devices using SPR, and also for the detection of molecules by surface enhanced Raman spectroscopy (SERS). In this context, the use of SDRS to monitor the thickness of the dielectric capping-layer above the nanoclusters (see Section 5.3.4, Chapter III) could be very interesting for SERS characterizations, which require precise control of the distance between the buried nanoclusters and the surface adsorbed molecules to separate electromagnetic and chemical effects. Besides, installation of real-time SDRS on the implantor used in our group could yield crucial information on the formation of nanoclusters by implantation of noble metals in dielectric matrices as well as on the formation of nanocavities by implantation of rare gas in metallic matrices.

During this research work we have witnessed that, *in situ* SDRS, even though a sensitive optical probe, gives rise to some ambiguous explanations for the optical analysis related to the metal nanoclusters (e.g., during the capping of Ag nanoclusters by Si_3N_4 matrix, during the annealing treatments, and during the exposure of Ag nanoclusters to partially ionized O_2), as it is not possible to separate the contributions of structural and chemical effects precisely. Considering these ambiguities, in order to resolve the structural effects separately, *in situ* SDRS can be powered with a structural characterization technique, together implemented on a deposition chamber to perform simultaneous optical and structural characterizations in real-time. Such initiatives, even though already started for coupled SDRS-GISAXS characterizations at ESRF[3], are still scarce, and are restricted to the metal nanocluster growth by thermal evaporation technique. On the other hand, to correlate the cluster morphology and their reactivity, implementation of real-time SDRS in combination with real-time GISAXS is also considered at Néel Institute to understand the redox properties of catalysts in the form of very small metal nanoclusters (< 5nm)[4].

[1] S. Camelio *et al.* Physical Review B **80**, 155434 (2009).
[2] D. Babonneau *et al.* EPL **93**, 26005 (2011).
[3] R. Lazzari *et al.* Physical Review B **79**, 125428 (2009).
[4] M.-C. Saint-Lager *et al.* Gold Bulletin **41/2**, (2008).

On the same line, for the quantitative assessments of chemical interactions between the metal nanoclusters and the reactive species, *in situ* SDRS coupled, either with *in situ* X-ray photoelectron spectroscopy (XPS), or with *in situ* X-ray absorption spectroscopy (XAS) may provide useful assistance. Although characterization time for such techniques is not instantaneous like SDRS, their utilization in *in situ* configuration can be resourceful for understanding the details of chemical effects. Out of these, XPS is a sensitive surface chemical analysis technique that can provide a precise quantitative analysis for the element composition and their chemical/electronic states along with the contaminations (if any) at the nanoscale. In a complementary way, XAS which includes, extended X-ray absorption fine structure (EXAFS) spectroscopy and X-ray absorption near edge spectroscopy (XANES), can reveal significant information regarding the nature of core atoms, distance and number of neighboring atoms, their chemical nature, and electronic structure.

Appendix

1 Introduction

In this thesis, majority of the work is focused on the use of surface differential reflectance spectroscopy (SDRS) in studying the optical properties of nanomaterials in real-time. In order to analyze the optical measurements, optical simulations provide an important assistance. In this regard, the first section of the appendix extends some of the theoretical concepts used during this research work. In addition to this, as *post mortem* HAADF-STEM and GISAXS are implemented throughout this research work for the structural characterizations of the Ag nanoclusters, the detailed procedures regarding the extraction of the structural information from the STEM micrographs and GISAXS patterns are also presented in the second section of this appendix.

2 Optical simulations

Here, reflectance calculations in case of thin films are explained first because they construct an important platform for SDRS measurements. Later, a detail account of Yamaguchi model is explained which considers the effective dielectric function of the metal:dielectric nanocomposites, metal nanoclusters from which are supposed to be identical spheroids having 2D distribution in the dielectric matrix (as explained in Chapter II (Section 4.2.1)). Further, with the help of the Yamaguchi simulations and as an extension to Chapter II (Section 4.2.3), the optical response of nanocomposite layers for inter-dependent cluster parameters are studied.

2.1 Reflectance calculations

As seen in the preceding chapters, SDRS measures the relative variations in the reflectance given by,

$$\frac{\Delta R}{R_0} = \frac{R - R_0}{R_0} \tag{1}$$

where, R is the reflectance measured from the deposited material surface and R_0, that of the bare substrate. In case of simulations, these reflectance values can be calculated by considering the Fresnel's complex reflection coefficients, which are developed further in detail.

Consider an incident ray of light on an interface between two media of complex refractive index n_1 and n_2 making an angle θ_1 with the normal (Fig.A.1). The incident light gets reflected and refracted partially in the incident plane at an angle θ_1 and θ_2, respectively with the relation:

$$n_1 \sin\theta_1 = n_2 \sin\theta_2 \tag{2}$$

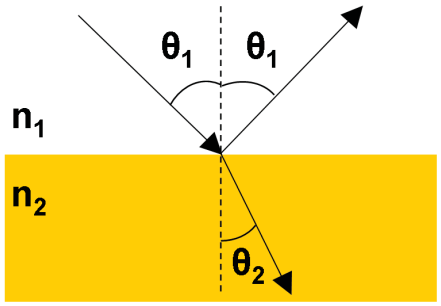

Figure A.1 – Partial reflection and refraction of light at the interface of two media.

In such configuration, Fresnel's complex coefficients r (or t) for reflected (or transmitted) polarized light (p or s) at the interface of two media 1 and 2 can be given as,

$$r_{p12}(\theta_1) = \frac{n_2 \cos\theta_1 - n_1 \cos\theta_2}{n_2 \cos\theta_1 + n_1 \cos\theta_2} \quad \text{and} \quad r_{s12}(\theta_1) = \frac{n_1 \cos\theta_1 - n_2 \cos\theta_2}{n_1 \cos\theta_1 + n_2 \cos\theta_2} \tag{3}$$

$$t_{p12}(\theta_1) = \frac{2n_1 \cos\theta_1}{n_2 \cos\theta_1 + n_1 \cos\theta_2} \quad \text{and} \quad t_{s12}(\theta_1) = \frac{2n_1 \cos\theta_1}{n_1 \cos\theta_1 + n_2 \cos\theta_2} \tag{4}$$

It is worth noting that, the light traveling from medium 2 to medium 1 follows the properties,

$$r_{*21}(\theta_2) = -r_{*12}(\theta_1) \quad \text{and} \quad t_{*21}(\theta_2)t_{*12}(\theta_1) = 1 - r_{*12}^2(\theta_1) \tag{5}$$

where, $*$ denotes the polarization p or s of the light. However in all further calculations in case

of polarized light, we will remove the subscript ($*$, s or p) signs for the sake of simplicity in the notations. Now, from the Fresnel's complex coefficients (equations (3) and (4)), reflectance R and transmittance T can be calculated as,

$$R_{12}(\theta_1) = |r_{12}(\theta_1)|^2 \tag{6}$$

and

$$T_{12}(\theta_1) = \frac{\mathrm{Re}(\mathrm{n_2}\cos\theta_2)}{\mathrm{Re}(\mathrm{n_1}\cos\theta_1)} |t_{12}(\theta_1)|^2 \tag{7}$$

Now, consider a reflection of a polarized light on a thin material layer of thickness δ_1, having complex refractive index n_1, as shown in Fig.A.2. This layer is sandwiched between two non-absorbing media of real refractive index n_0 (e.g. vacuum) and n_2 (e.g. substrate) such that $n_2 > n_0$.

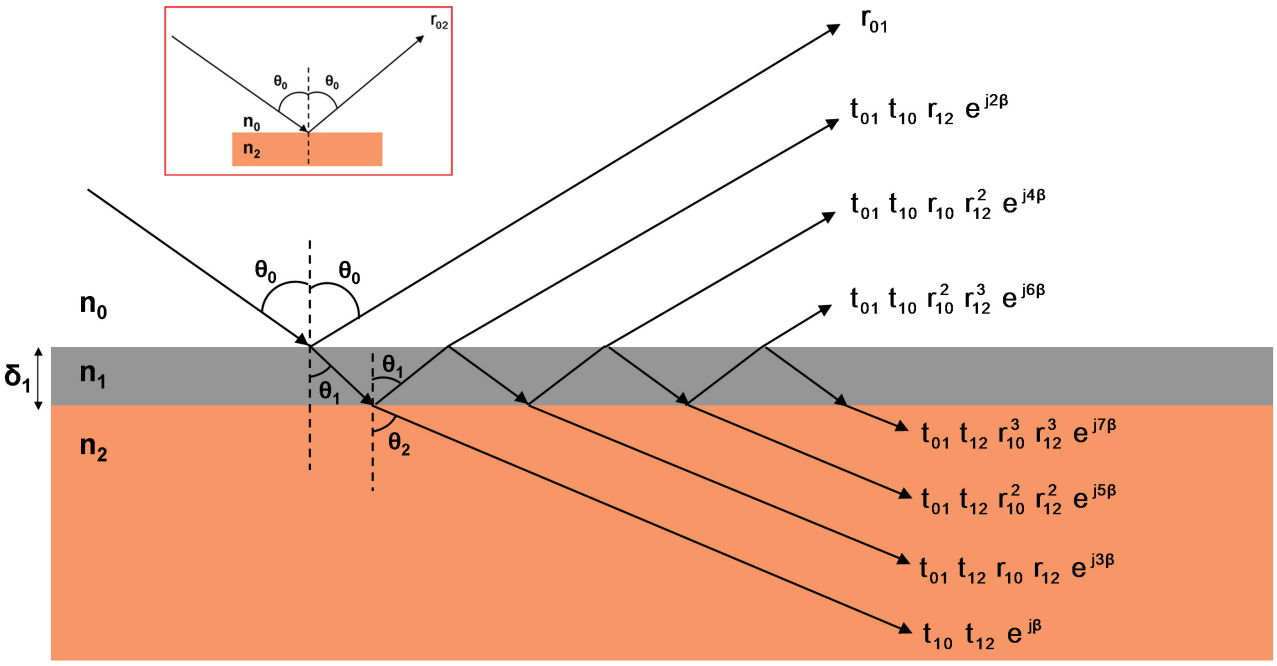

Figure A.2 – Principle for calculation of Fresnel's complex reflection coefficients for the reflected & transmitted light after multiple reflections inside a layer, having refractive index n_1 and thickness δ_1. Inset shows the Fresnel's complex reflection coefficient in case of absence of that layer.

Here, by Snell-Descartes law we can write,

$$n_0 \sin\theta_0 = n_1 \sin\theta_1 = n_2 \sin\theta_2 \tag{8}$$

and the dephase created by a single traveling of light inside the thin layer can be given by,

$$\beta = \frac{2\pi}{\lambda}\delta_1 n_1 \cos\theta_1 \tag{9}$$

Now, if we consider the reflected and transmitted complex amplitudes, r_{012} and t_{012} of reflected and transmitted light, respectively, they can be calculated considering the multiple reflections inside the thin material layer. In this case, the calculations for the reflected light can be given as,

$$\begin{aligned} r_{012} &= r_{01} + t_{01}\, t_{10}\, r_{12}\, e^{j2\beta} + t_{01}\, t_{10}\, r_{10}\, r_{12}^2\, e^{j4\beta} + t_{01}\, t_{10}\, r_{10}^2\, r_{12}^3\, e^{j6\beta} + \cdots \\ &= r_{01} + t_{01}\, t_{10}\, r_{12}\, e^{j2\beta}\left[\sum_{k=0}^{\infty} r_{01}^k\, r_{12}^k\, e^{j2k\beta}\right] \end{aligned} \tag{10}$$

From equation (5), the final form of the Fresnel's reflection coefficient r_{012} can be written as,

$$r_{012} = \frac{r_{01} + r_{12}\, e^{j2\beta}}{1 + r_{01}\, r_{12}\, e^{j2\beta}} \tag{11}$$

Similarly, the Fresnel's transmitted coefficient t_{012} can be given by,

$$t_{012} = \frac{t_{01} + t_{12}\, e^{j\beta}}{1 + r_{01}\, r_{12}\, e^{j2\beta}} \tag{12}$$

In case of multilayer stratified systems, these Fresnel's complex coefficients for the reflection or transmission can be generalized by the Abeles matrix formalism [1, 2]. However in absence of the material layer (as shown in inset of Fig.A.2), the Fresnel's complex coefficient of the reflected wave from the bare substrate will be simply r_{02}.

Now, as in case of SDRS we only study the reflectance, we restrict ourselves here in the reflection configuration. In this regard, from equation(6) the Fresnel's complex reflection coefficient r_{012} gives rise to the reflectance R as,

$$R = |r_{012}|^2 = \left|\frac{r_{01} + r_{12}\, e^{j2\beta}}{1 + r_{01}\, r_{12}\, e^{j2\beta}}\right| \tag{13}$$

and the reflectance R_0 of the bare substrate will be,

$$R_0 = |r_{02}]^2 \tag{14}$$

These two equations (13 and 14) allows one to calculate the relative variations in the reflectance given by the equation (1). However, such calculations (using equation (13)) are

generally restricted to a continuous and homogeneous medium. Hence in case of homogeneous medium having heterogeneities at the nanoscale, we have to consider the effective medium models. In such models, the basic aim is to consider a hypothetical homogeneous medium which has same optical response that of the inhomogeneous medium. In this regard, among the effective medium theories, we have adopted Yamaguchi model.

2.2 Yamaguchi model

In case of Yamaguchi model [3], as shown in Fig.A.3, metal nanoclusters of dielectric function ε_i are considered to be identical spheroids and supposed to have 2D isotropic distribution inside a matrix of dielectric function ε_m, and are supported on the substrate of dielectric function ε_{sub}.

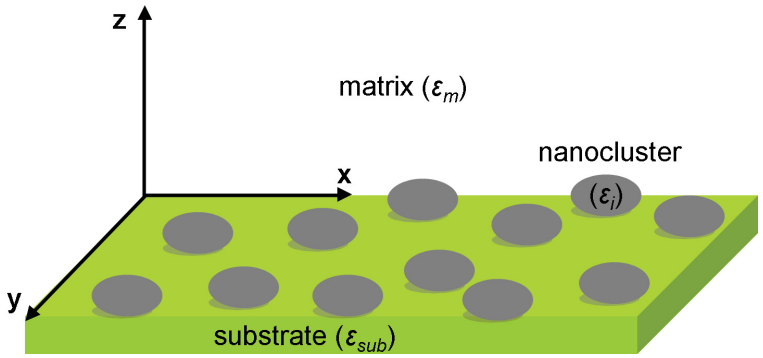

Figure A.3 – Assembly of identical spheroidal metal nanoclusters supported on a substrate, with the axis of rotation perpendicular to the substrate surface (in the direction of z axis) and having 2D random distribution.

Under the influence of external electric field $\mathbf{E}$, each nanocluster is supposed to act as a dipole and hence, only dipole interactions are taken into account. Here, expressing the macroscopic polarization $\mathbf{P}$ of the total composite assembly as a function of dipolar moments $\mathbf{p}$ of the nanoclusters, we obtain the effective dielectric function ε_{eff} of the composite material, which characterize its macroscopic optical response.

2.2.1 Macroscopic response of the nanocomposite system

The macroscopic polarization $\mathbf{P}$ of the nanocomposite system is assumed to be linearly related with $\mathbf{E}$ such that,

$$\mathbf{P} = \varepsilon_0 \left[\varepsilon_{eff}\right] \mathbf{E} - \varepsilon_0 \varepsilon_m \mathbf{E} = \varepsilon_0 \left(\left[\varepsilon_{eff}\right] - \varepsilon_m\right) \mathbf{E} \tag{15}$$

where, ε_0 and $[\varepsilon_{eff}]$ are the permittivity of the free space and the tensor form of the dielectric

function of the composite material, respectively. In the (x,y, and z) axes system, $[\varepsilon_{eff}]$ can be written in the form of a diagonal tensor as,

$$[\varepsilon_{eff}] = \begin{bmatrix} \varepsilon_{eff,xy} & 0 & 0 \\ 0 & \varepsilon_{eff,xy} & 0 \\ 0 & 0 & \varepsilon_{eff,z} \end{bmatrix} \tag{16}$$

2.2.2 Microscopic response of the nanoclusters

Due to the external applied electric field $\mathbf{E}$, a local electric field $\mathbf{E_{loc}} = \begin{vmatrix} E_{loc,x} \\ E_{loc,y} \\ E_{loc,z} \end{vmatrix}$ is formed at a spheroidal nanocluster, giving rise to its dipole moment $\mathbf{p} = \begin{vmatrix} p_x \\ p_y \\ p_z \end{vmatrix}$ given by,

$$\mathrm{p_u} = \varepsilon_0 \varepsilon_m V \alpha_u \mathrm{E_{loc,u}} \tag{17}$$

where, V is the volume of the spheroidal cluster and α_u is the volumic polarizability of the cluster for u(=x,y or z) component and is defined as,

$$\alpha_u = \frac{(\varepsilon_i - \varepsilon_m)}{\varepsilon_m + L_u\,(\varepsilon_i - \varepsilon_m)} \tag{18}$$

Here, an important factor comes in to picture in the form of depolarization factor (L_u) [4, 5], which is a shape dependent factor.

For a prolate cluster ($D < H$), the in-plane depolarization factor L_{xy} and out-of-plane depolarization factor L_z can be given by,

$$L_{xy} = \frac{1-e^2}{e^2}\left(-1 + \frac{1}{2e}\ln\left[\frac{1+e}{1-e}\right]\right) \text{ and } L_z = 1 - 2L_{xy} \tag{19}$$

where, e is the eccentricity of that cluster and is related to its in-plane (x,y) diameter D and out-of-plane (z) height H, such that $e = \left[1 - (D/H)^2\right]^{1/2}$.

For a spheroidal cluster ($D > H$), L_{xy} and L_z are given by,

$$L_{xy} = \frac{1}{2}\left[1 - \frac{1+e^2}{e^3}(e - \arctan(e))\right] \text{ and } L_z = 1 - 2L_{xy} \tag{20}$$

where, $e = \left[(D/H)^2 - 1\right]^{1/2}$.

Moreover, as we consider the identical spheroidal nanoclusters has isotropic 2D distribution, equation (17) can be written in the tensor form as,

$$\begin{bmatrix} p_{xy} \\ p_{xy} \\ p_z \end{bmatrix} = \varepsilon_0 \varepsilon_m V \begin{bmatrix} \alpha_{xy} & 0 & 0 \\ 0 & \alpha_{xy} & 0 \\ 0 & 0 & \alpha_z \end{bmatrix} \begin{bmatrix} \mathrm{E}_{\mathrm{loc,xy}} \\ \mathrm{E}_{\mathrm{loc,xy}} \\ \mathrm{E}_{\mathrm{loc,z}} \end{bmatrix} \tag{21}$$

where, α_{xy} is the polarizability of spheroidal clusters in x-y direction, with corresponding depolarization factor L_{xy}, and α_z that of in the z-direction with depolarization factor L_z (from equation (18)).

2.2.3 Relation between macroscopic and microscopic responses

The macroscopic polarization $\mathbf{P}$ of the nanocomposite system can be linked to the identical microscopic dipole moments $\mathbf{p}$ of the metal nanoclusters as,

$$\mathbf{P} = N\mathbf{p} \tag{22}$$

where, N is the number of metal clusters per unit volume.

Now from equations, (15) to (22) we get a relation between the applied external electric field and the local electric field in horizontal (x-y) plane and vertical (z) plane of the nanocomposite material as,

$$\begin{aligned} (\varepsilon_{eff,xy} - \varepsilon_m)\,\mathbf{E_{xy}} &= q\varepsilon_m \left(\tfrac{\varepsilon_i - \varepsilon_m}{\varepsilon_m + L_{xy}(\varepsilon_i - \varepsilon_m)} \right) \mathbf{E_{loc,xy}} \\ (\varepsilon_{eff,z} - \varepsilon_m)\,\mathbf{E_z} &= q\varepsilon_m \left(\tfrac{\varepsilon_i - \varepsilon_m}{\varepsilon_m + L_z(\varepsilon_i - \varepsilon_m)} \right) \mathbf{E_{loc,z}} \end{aligned} \tag{23}$$

where, q denotes the volume-density of the nanoclusters (i.e. $q = NV$) and

$$\mathbf{E_{loc,xy}} = \begin{bmatrix} E_{loc,xy} \\ E_{loc,xy} \\ 0 \end{bmatrix}, \mathbf{E_{xy}} = \begin{bmatrix} E_x \\ E_y \\ 0 \end{bmatrix}, \mathbf{E_{loc,z}} = \begin{bmatrix} 0 \\ 0 \\ E_{loc,z} \end{bmatrix}, \text{ and } \mathbf{E_z} = \begin{bmatrix} 0 \\ 0 \\ E_z \end{bmatrix}.$$

2.2.4 Calculation of local electric field $\mathbf{E_{loc}}$

In order to find the components of the effective dielectric tensors, it is necessary to calculate the local electric field "seen" by the nanocluster and putting its value back in the equation (23). Here, for the calculation of $\mathbf{E_{loc}}$, we only consider the dipolar interactions between the clusters.

In case of dipolar approximation we recall that, as shown in Fig.A.4, the expression for the electric field created at $\mathbf{O}_\mathrm{k}$ by a dipole moment $\mathbf{p}$ of dipole $\mathbf{O}$ is,

$$\mathbf{E} = \frac{1}{4\pi\varepsilon_0\varepsilon_m}\left[\frac{3\left(\mathbf{p}\cdot\mathbf{u_r}\right)\mathbf{u_r}-\mathbf{p}}{r^3}\right] = \frac{1}{4\pi\varepsilon_0\varepsilon_m}\left[\frac{3p\cos\varphi\mathbf{u_r}-\mathbf{p}}{r^3}\right] \tag{24}$$

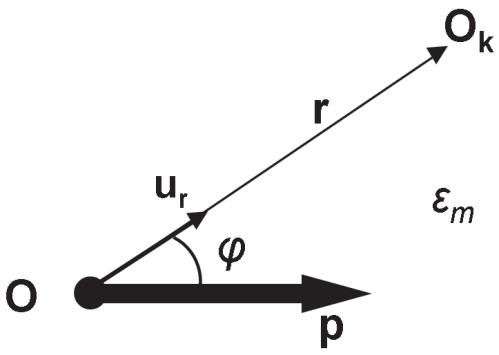

Figure A.4 – Schematics for the field created at $\mathbf{O_k}$ by a dipole moment $\mathbf{p}$ at $\mathbf{O}$ situated at a distance r

where, $\mathbf{u_r}$ is the unit vector in the direction $\mathbf{OO_k}$, such that, $\mathbf{OO}_\mathrm{k} = r\mathbf{u_r}$ and φ is the angle between the dipole moment $\mathbf{p}$ and $\mathbf{OO_k}$.

As the metal nanoclusters are considered as interacting dipoles, the local electric field $\mathbf{E_{loc,k}}$ at the metal nanocluster $\mathbf{O}_\mathrm{k}$ is a result of the following three contributions (25): the macroscopic external applied electric field ($\mathbf{E}$), the electric field created by the dipole image, induced by the substrate ($\mathbf{E_{img,k}}$), and the electric field of interaction created at the dipole under consideration ($\mathbf{O}_\mathrm{k}$) by other dipoles and their dipole images ($\mathbf{E_{int,k}}$), i.e.

$$\mathbf{E_{loc,k}} = \mathbf{E} + \mathbf{E_{img,k}} + \mathbf{E_{int,k}} \tag{25}$$

- **Calculation of $\mathbf{E_{img,k}}$ -** In the consideration of the dipole image interaction, as shown in Fig.A.5, a nanocluster in a dielectric medium (ε_m) supported on a substrate (ε_{sub}) can be replaced by a dipole $\mathbf{O}_\mathrm{k}$ of that cluster with its image $\mathbf{O}'_\mathrm{k}$ created due the substrate.

  In such condition, the in-plane dipole moment ($\mathbf{p}'_{\mathrm{k,xy}}$) and out-of-plane dipole moment ($\mathbf{p}'_{\mathrm{k,z}}$) of the dipole image can be related to the dipole moment ($\mathbf{p}_\mathrm{k}$) of the dipole by the

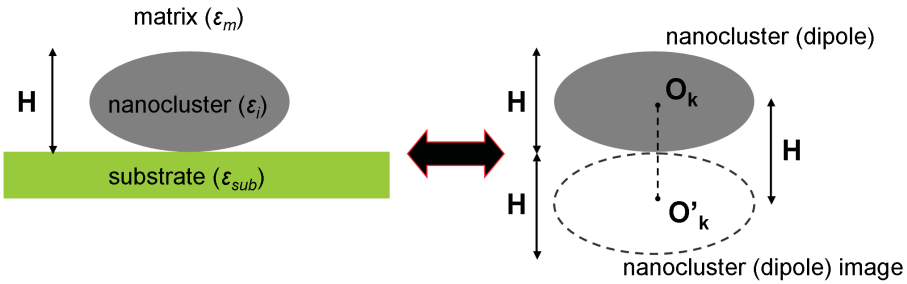

Figure A.5 – The assumption of replacement of substrate supported nanocluster by the equivalent dipole and its dipole image.

relations,

$$\mathbf{p}'_{\mathbf{k,xy}} = -\frac{\varepsilon_{sub} - \varepsilon_m}{\varepsilon_{sub} + \varepsilon_m}\mathbf{p}_{\mathbf{k,xy}} \quad \text{and} \quad \mathbf{p}'_{\mathbf{k,z}} = \frac{\varepsilon_{sub} - \varepsilon_m}{\varepsilon_{sub} + \varepsilon_m}\mathbf{p}_{\mathbf{k,z}} \tag{26}$$

It is worth noting that the dipole moment and its mirror image can be in the same or opposite directions according to the applied electric field (normal or parallel to the substrate surface) [3].

Now, from Fig.A.5, if we consider the distance between the center of the dipole $\mathbf{O}_\mathrm{k}$ and the center of its image $\mathbf{O}'_\mathrm{k}$ equivalent to the height H of the nanocluster, then from equations (24) and (26), the in-plane (x-y) and out-of-plane (z) electric field created by the dipole image $\mathbf{O}'_\mathrm{k}$ at $\mathbf{O}_\mathrm{k}$ can be given by the following equations.

$$\mathbf{E}_{\mathbf{img,xy}} = \frac{1}{4\pi\varepsilon_0\varepsilon_m H^3}\left[\frac{\varepsilon_{sub} - \varepsilon_m}{\varepsilon_{sub} + \varepsilon_m}\right]\mathbf{p}_{\mathbf{k,xy}} \tag{27}$$

and

$$\mathbf{E}_{\mathbf{img,z}} = \frac{2}{4\pi\varepsilon_0\varepsilon_m H^3}\left[\frac{\varepsilon_{sub} - \varepsilon_m}{\varepsilon_{sub} + \varepsilon_m}\right]\mathbf{p}_{\mathbf{k,z}} \tag{28}$$

- **Calculation of $\mathbf{E}_{\mathbf{int,k}}$ -** The electric field due to the interactions $\mathbf{E}_{\mathbf{int,k}}$ takes into account the interactions of the other dipoles and their images with the dipole under consideration ($\mathbf{O}_\mathrm{k}$). It can be given directly by the sum of the electric field created by all the dipoles and their images (from the equations (24)-(26)).

  Now, if the distance between the nanoclusters in the horizontal direction $\mathrm{r_j}$ is much greater than that of the distance in vertical direction H (i.e. $\mathrm{r_j} \gg H$), we can assume $\mathbf{u_{rj}} = \mathbf{u}'_{\mathbf{rj}}$

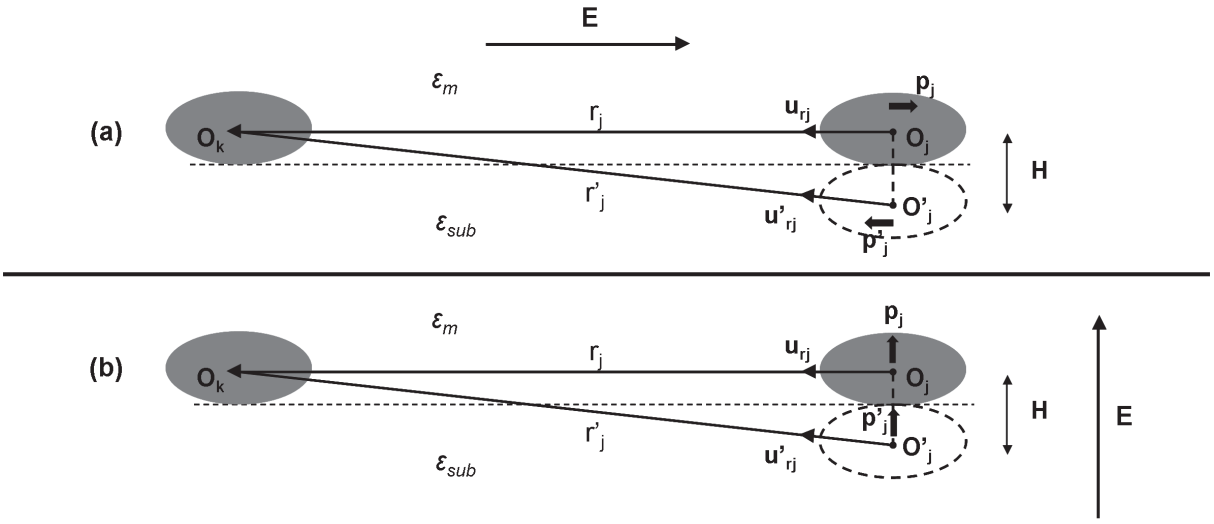

Figure A.6 – Schematics for the (a) in-plane (x-y) and (b) out-of-plane (z) field created by the dipole ($\mathbf{O_j}$) and its image $\mathbf{O_j^{'}}$ at the dipole under consideration ($\mathbf{O_k}$).

and $\mathbf{r_j} = \mathbf{r_j^{'}}$ (Fig.A.6(a-b)). Hence with the help of equation (26), the resulting dipole moment $\mathbf{p_j^{''}} = \mathbf{p_j} + \mathbf{p_j^{'}}$, can be written as,

$$\mathbf{p_{j,xy}^{''}} = \frac{2\varepsilon_m}{\varepsilon_{sub} + \varepsilon_m}\mathbf{p_{j,xy}} \tag{29}$$

and

$$\mathbf{p_{j,z}^{''}} = \frac{2\varepsilon_{sub}}{\varepsilon_{sub} + \varepsilon_m}\mathbf{p_{j,z}} \tag{30}$$

Moreover, with the help of equation (24) the electric field due to the interaction $\mathbf{E_{int,k}}$ can be written in terms of effective dipole moment $\mathbf{p_j^{''}}$ as,

$$\mathbf{E_{int,k}} = \frac{1}{4\pi\varepsilon_0\varepsilon_m}\sum_j \left[\frac{3\left(\mathbf{p_j^{''}}\cdot\mathbf{u_{rj}}\right)\mathbf{u_{rj}} - \mathbf{p_j^{''}}}{r_j^3}\right] \tag{31}$$

From equation (29), equation (31) becomes,

$$\mathbf{E_{int,k,xy}} = \frac{1}{4\pi\varepsilon_0\varepsilon_m}\frac{2\varepsilon_m}{\varepsilon_{sub} + \varepsilon_m}\sum_j \left[\frac{3\left(\mathbf{p_{j,xy}}\cdot\mathbf{u_{rj}}\right)\mathbf{u_{rj}} - \mathbf{p_{j,xy}}}{r_j^3}\right] \tag{32}$$

Assuming the isotropic distribution of the nanoclusters in the in-plane (x-y) direction (Fig.A.6(a)), the distribution of the vectors $\left(\mathbf{p_{j,xy}}\cdot\mathbf{u_{rj}}\right)\mathbf{u_{rj}}$ from the above equation (32)

is reduced to the projection following $\mathbf{p_{j,xy}}$. Hence we get,

$$\mathbf{E_{int,k,xy}} = \frac{1}{4\pi\varepsilon_0\varepsilon_m}\frac{2\varepsilon_m}{\varepsilon_{sub}+\varepsilon_m}\sum_j\left[\frac{3\cos^2\varphi_j - 1}{r_j^3}\mathbf{p_{j,xy}}\right] \tag{33}$$

where, φ_j is the angle between the dipole moment $\mathbf{p_{j,xy}}$ and the direction $\mathbf{O_jO_k}$ (not shown in Fig.A.6(a)). In out-of-plane (z) direction (Fig.A.6(b)), from equation (30), equation (31) can be written as,

$$\mathbf{E_{int,k,z}} = \frac{1}{4\pi\varepsilon_0\varepsilon_m}\frac{2\varepsilon_{sub}}{\varepsilon_{sub}+\varepsilon_m}\sum_j\left[\frac{-\mathbf{p_{j,z}}}{r_j^3}\right] \tag{34}$$

In this way, the local electric field "seen" by the nanocluster in (x,y) direction can be given using equations (27) and (33) in the equation (25) as,

$$\mathbf{E_{loc,k,xy}} = \mathbf{E_{xy}} + \frac{1}{4\pi\varepsilon_0\varepsilon_m H^3}\left[\frac{\varepsilon_{sub}-\varepsilon_m}{\varepsilon_{sub}+\varepsilon_m}\right]\mathbf{p_{k,xy}} + \frac{1}{4\pi\varepsilon_0\varepsilon_m}\frac{2\varepsilon_m}{\varepsilon_{sub}+\varepsilon_m}\sum_j\left[\frac{3\cos^2\varphi_j - 1}{r_j^3}\mathbf{p_{j,xy}}\right] \tag{35}$$

Similarly, the local electric field in (z) direction can be given using equations (28) and (34) in the equation (25) as,

$$\mathbf{E_{loc,k,z}} = \mathbf{E_z} + \frac{2}{4\pi\varepsilon_0\varepsilon_m H^3}\left[\frac{\varepsilon_{sub}-\varepsilon_m}{\varepsilon_{sub}+\varepsilon_m}\right]\mathbf{p_{k,z}} + \frac{1}{4\pi\varepsilon_0\varepsilon_m}\frac{2\varepsilon_{sub}}{\varepsilon_{sub}+\varepsilon_m}\sum_j\left[\frac{-\mathbf{p_{j,z}}}{r_j^3}\right] \tag{36}$$

As it is assumed that the nanoclusters are identical, they "see" the same local field and they have similar dipolar moment (i.e. $\mathbf{E_{loc,k}} = \mathbf{E_{loc}}$, $\mathbf{p_k} = \mathbf{p}$; $\forall\ \mathbf{k}$). Hence we can write the equations (35) and (36) as,

$$\mathbf{E_{loc,xy}} = \mathbf{E_{xy}} + \left(\frac{1}{4\pi\varepsilon_0\varepsilon_m H^3}\left[\frac{\varepsilon_{sub}-\varepsilon_m}{\varepsilon_{sub}+\varepsilon_m}\right] + \frac{1}{4\pi\varepsilon_0\varepsilon_m}\frac{2\varepsilon_m}{\varepsilon_{sub}+\varepsilon_m}\sum_j\left[\frac{3\cos^2\varphi_j - 1}{r_j^3}\right]\right)\mathbf{p_{xy}} \tag{37}$$

and

$$\mathbf{E_{loc,z}} = \mathbf{E_z} + \left(\frac{2}{4\pi\varepsilon_0\varepsilon_m H^3}\left[\frac{\varepsilon_{sub}-\varepsilon_m}{\varepsilon_{sub}+\varepsilon_m}\right] + \frac{1}{4\pi\varepsilon_0\varepsilon_m}\frac{2\varepsilon_{sub}}{\varepsilon_{sub}+\varepsilon_m}\sum_j\left[\frac{-1}{r_j^3}\right]\right)\mathbf{p_z} \tag{38}$$

Expressing the dipolar moments in terms of local electric fields with the help of equation

(17), we can correlate the local electric field $\mathbf{E_{loc}}$ with the external electric field $\mathbf{E}$ as,

$$\begin{aligned} \mathbf{E_{loc,xy}} &= \frac{\mathbf{E_{xy}}}{1+\varepsilon_0\varepsilon_m V\alpha_{xy}\beta_{xy}} \\ \mathbf{E_{loc,z}} &= \frac{\mathbf{E_z}}{1+\varepsilon_0\varepsilon_m V\alpha_z\beta_z} \end{aligned} \tag{39}$$

with,

$$\beta_{xy} = -\left(\frac{1}{4\pi\varepsilon_0\varepsilon_m H^3}\left[\frac{\varepsilon_{sub}-\varepsilon_m}{\varepsilon_{sub}+\varepsilon_m}\right] + \frac{1}{4\pi\varepsilon_0\varepsilon_m}\frac{2\varepsilon_m}{\varepsilon_{sub}+\varepsilon_m}\sum_j\left[\frac{3\cos^2\varphi_j - 1}{r_j^3}\right]\right) \tag{40}$$

and

$$\beta_z = -\left(\frac{2}{4\pi\varepsilon_0\varepsilon_m H^3}\left[\frac{\varepsilon_{sub}-\varepsilon_m}{\varepsilon_{sub}+\varepsilon_m}\right] + \frac{1}{4\pi\varepsilon_0\varepsilon_m}\frac{2\varepsilon_{sub}}{\varepsilon_{sub}+\varepsilon_m}\sum_j\left[\frac{-1}{r_j^3}\right]\right) \tag{41}$$

2.3 Calculation of effective dielectric function $\varepsilon_{eff,u}$

With the help of equations (39) and (23) it is now possible to find the components of the effective dielectric function of the composite as,

$$\varepsilon_{eff,xy} = \varepsilon_m\left(1 + q\frac{\varepsilon_i - \varepsilon_m}{\varepsilon_m + F_{xy}\left(\varepsilon_i - \varepsilon_m\right)}\right) \tag{42}$$

and

$$\varepsilon_{eff,z} = \varepsilon_m\left(1 + q\frac{\varepsilon_i - \varepsilon_m}{\varepsilon_m + F_z\left(\varepsilon_i - \varepsilon_m\right)}\right) \tag{43}$$

where, the coefficients F_{xy} and F_z are the factors of effective depolarizations which can be given by,

$$\begin{aligned} F_{xy} &= \left(\frac{\varepsilon_0\varepsilon_m^2\alpha_{xy}\beta_{xy}}{\varepsilon_i-\varepsilon_m} + L_{xy}[1+\varepsilon_0\varepsilon_m\alpha_{xy}\beta_{xy}]\right) \\ F_z &= \left(\frac{\varepsilon_0\varepsilon_m^2\alpha_z\beta_z}{\varepsilon_i-\varepsilon_m} + L_z[1+\varepsilon_0\varepsilon_m\alpha_z\beta_z]\right) \end{aligned} \tag{44}$$

These effective depolarization factors F_{xy} and F_z take in to account the shape of the clusters (in the form of L_{xy} and L_z), the interactions between the clusters and with the substrate (in the form of β_{xy} and β_z). Hence, in particular conditions such as, if the nanoclusters are diving in the homogeneous medium completely (i.e. no contact with the substrate, $\mathbf{E_{img}} = \mathbf{0}$) and if they are infinitely far away from each other (i.e. $\mathbf{E_{int}} = \mathbf{0}$) then the factors of effective depolarization (F_{xy} and F_z) will reduce to the intrinsic depolarization factors (L_{xy} and L_z).

2.4 Modified dielectric function of metal nanoclusters (ε_i)

As discussed in Chapter II (Section 2.1.1), the dielectric function of bulk metals ε_m can be explained with Drude model [6] and is given by,

$$\varepsilon_m(\omega) = 1 + \chi_{core} - \frac{{\omega_p}^2}{\omega(\omega + i\Gamma_0)} \tag{45}$$

where, the term χ_{core} is related with the interband transitions of electrons that take place between the core d bands and the conduction $s-p$ bands. While, $\omega_p = \sqrt{n_e e^2/\varepsilon_0 m_e}$ is the bulk volume plasmon frequency of that metal, with n_e, e, and m_e representing the volume density, charge, and effective mass of electrons in the conduction band respectively. The term Γ_0 is considered as an amortization parameter (also called as collision frequency of electrons) and is defined by,

$$\Gamma_0 = \frac{\nu_f}{l} \tag{46}$$

where, ν_f is the velocity of Fermi electrons in the bulk metals with l being taken as the mean free path of the electrons which is of the order of 50nm for Ag and 40nm for Au in the bulk form.

Correction term for the dielectric function of metal

In case of metal nanoclusters, in order to take into account the effects due to their size and interfaces, a correction term is introduced in the amortization Γ_0 [7, 8] in the form of,

$$\Gamma = \Gamma_0 + A\frac{\nu_f}{R} \tag{47}$$

where, R is the radius of the nanocluster, while A is the amortization or damping constant. This damping constant A actually has two contributions,

$$A = A_{size} + A_{interface} \tag{48}$$

The factor A_{size} considers the different diffusion processes at nano-dimensions such as, collisions of electrons with the nanocluster surfaces and their interactions with the clusters/matrix (size effects), and the other factor $A_{interface}$ considers the chemical effects at the interface (interface effects) [9–12]. Among these contributions, even though the theoretical value of A_{size} lies in between 0.1 to 1, due to the presence of $A_{interface}$ effects, the total value of damping constant A is seen to be exceed up to 3 [12].

2.5 Influence of inter-dependent cluster parameters on the simulated optical response

With the help of equation (42), in Chapter II (Section 4.2.3), we have presented the optical simulations for complex refractive index of Ag:Si_3N_4 nanocomposites where Ag nanoclusters are supposed to be buried completely inside a Si_3N_4 dielectric matrix. Here we have discussed the effects of the individual nanostructure parameters on the effective in-plane complex refractive index ($n_{xy} + ik_{xy}$). From the simulations, it was evident that the amplitude of absorption band of k_{xy} is sensitive to the average in-plane cluster size D and its maximum position is sensitive to the cluster shape (i.e. H/D aspect ratio), while the influence of organizational parameter (such as, inter-cluster distance Λ) found to have weak impact. However it is worth noting that, the influence of cluster parameters studied here are individual, which may not be the case in practical situations. In practical cases, cluster parameters are strongly inter-dependent e.g. for constant deposited metal amount, increase in the in-plane cluster size D cause relative increase in the inter-cluster distance Λ (or relative decrease in the cluster density d). Hence in this part of the appendix, influence of such inter-dependent cluster parameters on the simulated $n_{xy} + ik_{xy}$ are studied.

2.5.1 Influence of the morphological parameters (D and H/D) at same cluster organization (Λ = constant)

FigA.7(a-b) shows influence of cluster shape H/D and in-plane cluster size D on the optical properties of Ag:Si_3N_4 nanocomposites when the deposited Ag amount (effective thickness t_{Ag}) along with the inter-cluster distance Λ, are supposed to be constant i.e. average volume of the cluster remains constant. By following this condition, at Λ = constant, it is possible to express D as a function of cluster aspect ratio H/D as,

$$D = \sqrt[3]{\frac{6t_{Ag}\Lambda^2}{\pi(H/D)}} = f(H/D) \tag{49}$$

From FigA.7(b), as we move from (i) to (iii), an identical blue-shift from 590nm $\rightarrow$ 500nm can be seen in the absorption bands Ag:Si_3N_4 nanocomposites as in Fig.II.8(d) (from Chapter 3, Section 3.2.3). The reason for this blue-shift is attributed to the shape change in the Ag clusters from oblate to spherical. However in FigA.7(b), the decrease in the amplitude (from 2.2 $\rightarrow$ 1.2), is sharper in contrast to Fig.II.8(d) (from 1.70 $\rightarrow$ 1.45). It is due to the decrease in the average in-plane cluster size D (from 8nm to 6nm) as demonstrated in Fig.II.8(b).

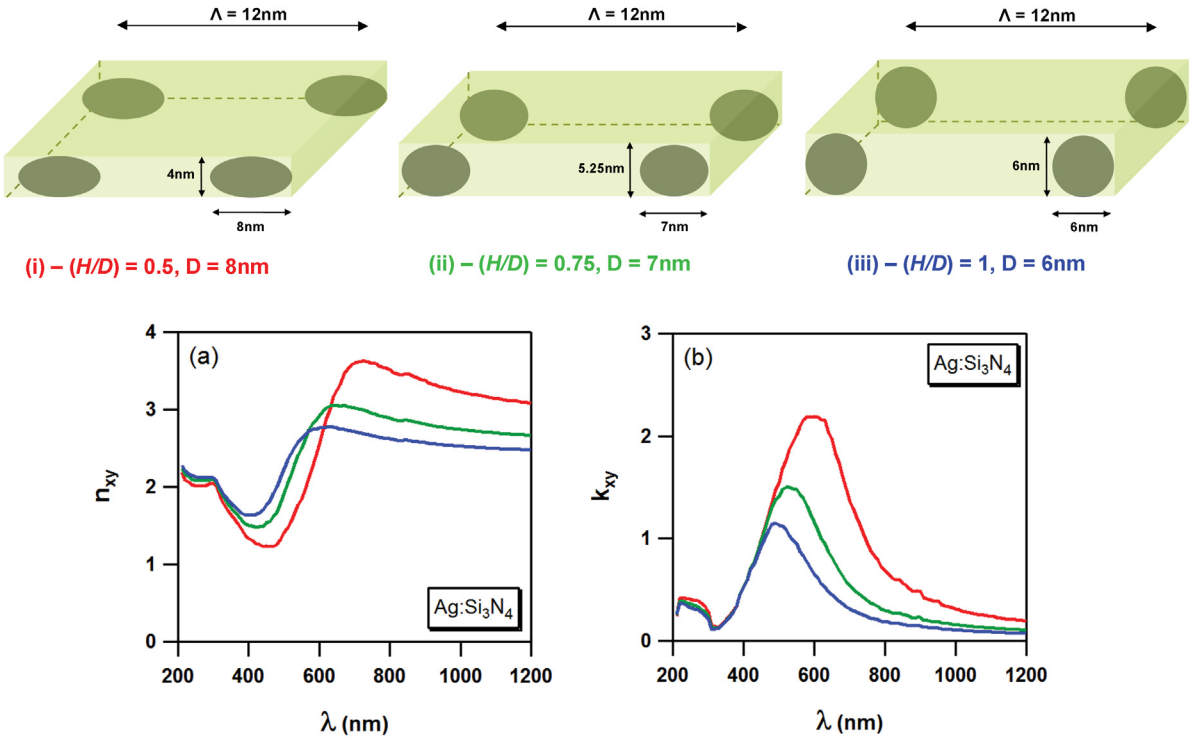

Figure A.7 – Effect of cluster shape H/D and cluster size D (i to iii) on the effective in-plane complex refractive index of $Ag:Si_3N_4$ nanocomposites (a-b), considering the deposited Ag amount t_{Ag} and the inter-cluster distance Λ are constant.

2.5.2 Influence of cluster size and inter-cluster distance for same cluster shape

Fig.A.8(a-b) show another set of simulations, where, the effective in-plane optical properties of the nanocomposites are simulated by increasing the average cluster size D with increasing the average inter-cluster distance Λ. But, while doing so, we kept the deposited metal effective thickness t_{Ag} constant along with the average aspect ratio of the clusters i.e. $(H/D = 0.75)$ which help us to express Λ as a function of average in-plane cluster size D using the relation from equation (50),

$$\Lambda = \sqrt{\frac{\pi D^3 (H/D)}{6 t_{Ag}}} = f(D) \tag{50}$$

In this regards, Fig.A.8(b) shows the increase in cluster size increases the amplitude of effective k_{xy} (from $0.7 \rightarrow 2.5$) without making significant change in the absorption position (from 530nm $\rightarrow$ 545nm). These results are similar to that of in Fig.II.8(b), where impact of increasing cluster size D is much more on the maximum amplitude than on the position, while increase in inter-cluster distance Λ shows no significant influence on the amplitude as well as

on the maximum position (Fig.II.8(f)).

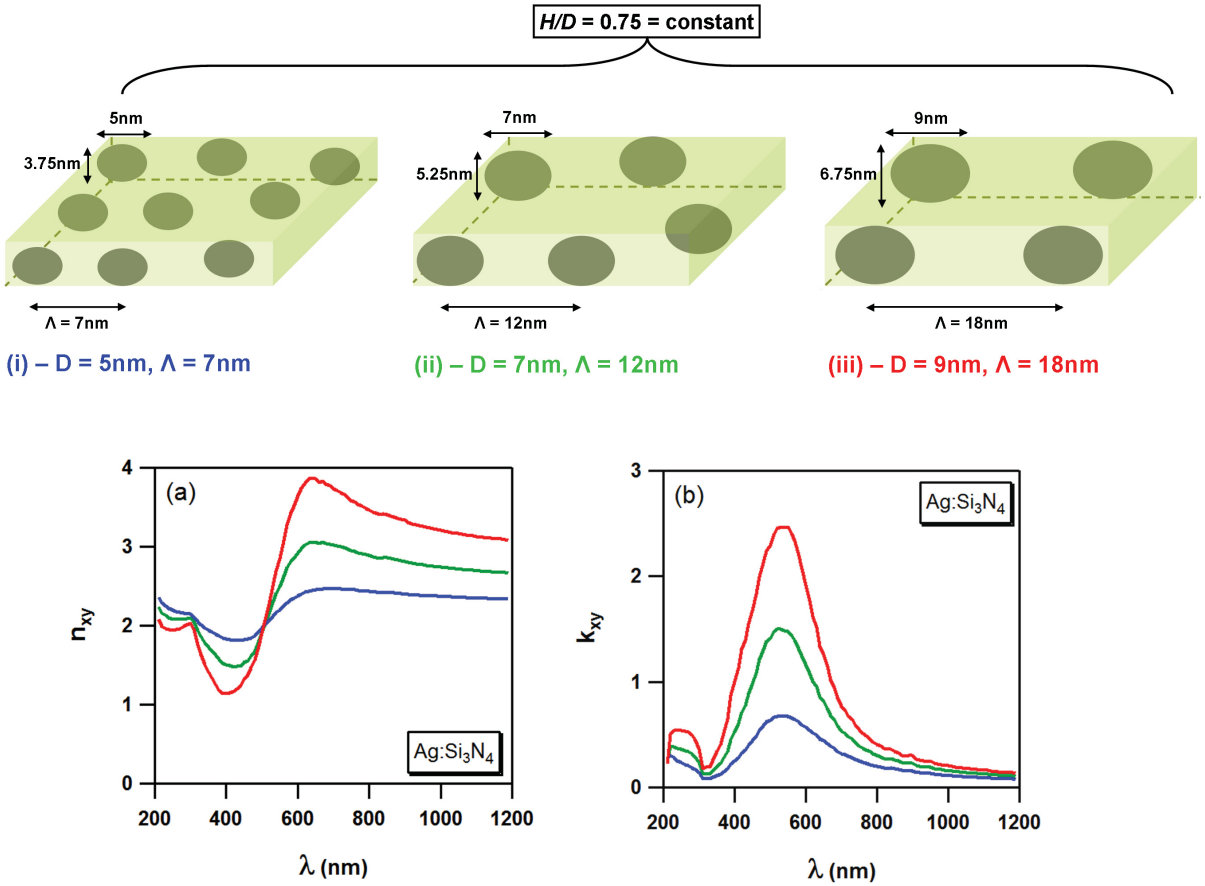

Figure A.8 – Effect of cluster size D and inter-cluster distance Λ (i to ii) on the effective in-plane complex refractive index of Ag:Si_3N_4 nanocomposites (a-b) considering the deposited Ag amount t_{Ag} constant along with the average cluster shape i.e. H/D ratio (i to iii).

3 Determination of cluster parameters using *post mortem* structural characterization techniques

In this work, the *post mortem* structural characterization techniques, such as high-angle annular dark-field scanning transmission electron microscopy (HAADF-STEM) and grazing-incidence small-angle X-ray scattering (GISAXS), are used to determine the nanostructure of the metal clusters. Only the metal nanoclusters completely embedded inside a Si_3N_4 dielectric matrix are selected for the structural analysis. For this purpose, in case of HAADF-STEM analysis, alternate depositions of Si_3N_4:metal:Si_3N_4 nanocomposites were carried out onto carbon-coated copper grids during their fabrications, while for GISAXS characterizations, the tri-layer

nanocomposite system deposited on the glass substrates is used. Here, as a typical example, nanostructure analysis procedures in case of Ag nanoclusters from a Si_3N_4:Ag(20s/2nm):Si_3N_4 nanocomposite are given in detail (which we have studied in Section 4.2 of Chapter III).

3.1 HAADF-STEM analysis

HAADF-STEM imaging method consists in collecting the high-angle scattered electrons with an annular detector, so that almost only incoherent Rutherford scattering contributes to the image formation and the image intensity is approximately proportional to the square of the atomic number (Z-contrast imaging) and atomic column occupancy. In this regard, the HAADF-STEM characterizations were performed using a JEOL 2200FS microscope operated at 200keV using a probe size of 0.7nm and an inner collection angle of 50mrad.

A representative in-plane micrograph image obtained by this method is shown in Fig.A.9(a), which exhibits a polydisperse assembly of Ag nanoclusters (bright regions) embedded in the light transparent Si_3N_4 matrix (dark background). From the quantitative analysis of this in-plane HAADF-STEM micrograph by image processing techniques, such as thresholding, it is possible to determine the average in-plane nanostructure parameters of Ag clusters i.e., areal cluster-density d, coverage rate of the Ag metal, and cluster-size D of Ag nanoclusters along with their size distribution σ_D. A detail insightful description regarding the image analysis and the cluster-parameter extraction are given in Refs [13–16].

Thresholding operation allows one to create a binarized image as seen in Fig.A.9(b). However, it is worth noting that, a perfect thresholding can be difficult to apply because if the thresholding is done to respect the biggest clusters, the smaller clusters will appear with a size lower than their actual size, whereas the smallest of them will simply disappear.

After thresholding, the in-plane projected perimeter of Ag nanoclusters is taken equivalent to an ellipse with a short axis a_n and a large axis b_n, thus giving rise to an average in-plane cluster size $D_n = \sqrt{a_n b_n}$. In this regard, Fig.A.9(c) shows an in-plane size histogram of the Ag nanoclusters, which is accurately fitted with a Gaussian distribution function specified by the mean value, $D = 7.6$nm and $\sigma_D = 1.9$nm.

In addition to this, inset of Fig.A.9(a) shows a auto-correlation function (ACF) of the HAADF-STEM micrograph, which is the cross correlation of the micrograph with itself. This symmetric circular ACF with the presence of intensity maximum suggests that the in-plane organization of the Ag clusters is isotropic over a long distance and their orientation is random. This also indicates that a short range ordering between the nanoclusters exists with an average distance between the nearest neighbors (i.e mean inter-cluster distance) $\Lambda = 12.6$nm.

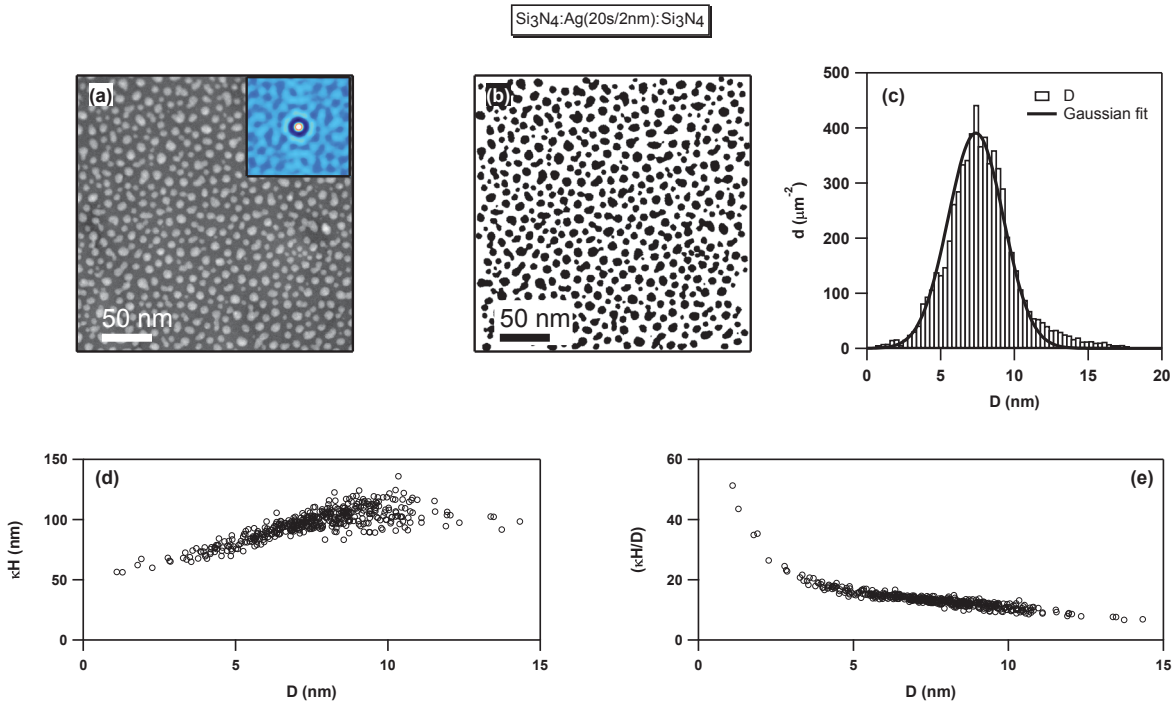

Figure A.9 – HAADF-STEM analysis for Si_3N_4:Ag(20s/2nm):Si_3N_4 nanocomposite. (a) In-plane HAADF-STEM micrograph and central part (50×50 nm^2) of the corresponding autocorrelation function (inset), (b) Binarized image, (c) In-plane size distribution of Ag nanoclusters fitted with a Gaussian function specified by mean $D = 7.6$nm and $\sigma_D = 1.9$nm, (d) Correlation between the in-plane cluster-diameter D and cluster-height H of each of Ag nanoclusters, with κ being an experimental constant, (e) Correlation between the height-to-diameter ratio (H/D) of Ag nanoclusters with their in-plane diameter D.

Furthermore, HAADF-STEM can also provide a reliable information on the height H_n of the individual embedded nanoclusters without cross-section sample characterizations. The quantification of the intensity distribution is necessary here. For this purpose, the intensity collected at the pixel p is the sum of individual atomic scattering contributions given by,

$$I^{(p)} = I^{(p)}_{\mathrm{Ag}} + I^{(p)}_{\mathrm{buffer}} + I^{(p)}_{\mathrm{cap}} + I^{(p)}_{\mathrm{C}} = I^{(p)}_{\mathrm{Ag}} + I^{(p)}_{\mathrm{B}} \tag{51}$$

where, $I^{(p)}_{\mathrm{Ag}}$ is proportional to the number of Ag atoms, i.e. thickness of the Ag column $t^{(p)}_{\mathrm{Ag}}$ and $I^{(p)}_{\mathrm{B}} = I^{(p)}_{\mathrm{buffer}} + I^{(p)}_{\mathrm{cap}} + I^{(p)}_{\mathrm{C}}$ is a constant that can be considered as the background signal of the image (assuming that the thickness of Si_3N_4 buffer layer, capping layer, and the carbon substrate are homogeneous). Accordingly, $I^{(p)} - I^{(p)}_{\mathrm{B}} = \kappa t^{(p)}_{\mathrm{Ag}}$ and the volume of V_n of a nanocluster n extended over m pixel is given by

$$\kappa V_n = A \sum_{p=1}^{m} (I^{(p)} - I^{(p)}_{\mathrm{B}}), \tag{52}$$

where, κ is an unknown experimental HAADF-STEM constant and A is the pixel area. By assuming that the Ag nanoclusters are hemispheroidal (with $V_n = \pi D_n^2 H_n/6$), and from equation (52), the height κH_n and aspect ratio $\kappa H_n/D_n$ of the nanocluster n can be given by,

$$\kappa H_n = \frac{6}{\pi D_n^2}\left[A\sum_{p=1}^{m}(I^{(p)} - I_{\mathrm{B}}^{(p)})\right], \tag{53}$$

and

$$\frac{\kappa H_n}{D_n} = \frac{6}{\pi D_n^3}\left[A\sum_{p=1}^{m}(I^{(p)} - I_{\mathrm{B}}^{(p)})\right], \tag{54}$$

In this regard, Fig.A.9(d-e) shows the variation of κH_n and $\kappa H_n/D_n$ with D_n, where it can be seen that, the nanoclusters with larger diameters, even though posses larger height, have smaller aspect ratios (i.e. larger nanoclusters are flatter).

3.2 GISAXS analysis

3.2.1 GISAXS theory

Let us consider a plane wave $E_0^-(\vec{r},t) = A_0^-(\vec{r})e^{i(\omega t - \vec{k}_0^-\vec{r})}$ impinging on the surface ($z_1 = 0$) of a stratified medium consisting of $N-1$ layers supported by a semi-infinite substrate, as illustrated in Fig.A.10(a). The air and the substrate are labeled as medium 0 and N, respectively, and their refractive indices are $n_0 = 1$ and $n_N = 1 - \delta_N - i\beta_N$ [16]. Each layer j ($1 \leq j \leq N-1$) is characterized by its refractive index $n_j = 1 - \delta_j - i\beta_j$ and its thickness t_j. The roughness of the interface z_j between the $j-1$ and j layers is σ_j. In the grazing incidence geometry (Fig.A.10(b)), the incident and scattered waves in air are described by wave vectors $\vec{k}_0^{\mathrm{i}}$ and $\vec{k}_0^{\mathrm{f}}$, which are defined by the angle of incidence (α_{i}) and by the in-plane ($2\theta_{\mathrm{f}}$) and out-of-plane (α_{f}) angles in emergence. The scattering vector in air $\vec{q} = (q_{\mathrm{x}}, q_{\mathrm{y}}, q_{\mathrm{z}})$ is then defined by

$$\vec{q} = \vec{k}_0^{\mathrm{f}} - \vec{k}_0^{\mathrm{i}} = \frac{2\pi}{\lambda}\begin{bmatrix}\cos(2\theta_{\mathrm{f}})\cos(\alpha_{\mathrm{f}}) - \cos(\alpha_{\mathrm{i}})\\ \sin(2\theta_{\mathrm{f}})\cos(\alpha_{\mathrm{f}})\\ \sin(\alpha_{\mathrm{f}}) + \sin(\alpha_{\mathrm{i}})\end{bmatrix}. \tag{55}$$

The incident and scattered waves propagating into the stratified medium are refracted and reflected at each interface so that the perpendicular component of the scattering vector in layer j is complex and defined by

$$\widetilde{q}_{z,j} = \widetilde{k}^{f}_{z,j} - \widetilde{k}^{i}_{z,j} = \frac{2\pi}{\lambda}\left[\sqrt{n_j^2 - \cos^2(\alpha_f)} + \sqrt{n_j^2 - \cos^2(\alpha_i)}\right], \tag{56}$$

and the complex amplitude of the scattered wave by an object located at the interface z_{j+1} is given by

$$\mathcal{A}_j(\vec{q}) = \frac{k_0^2}{4\pi}\left(n_j^2 - \nu_j^2\right)\Phi_j(\vec{q}), \tag{57}$$

where ν_j and $\Phi_j(\vec{q})$ are the refractive index and the form factor of the scattering object, respectively.

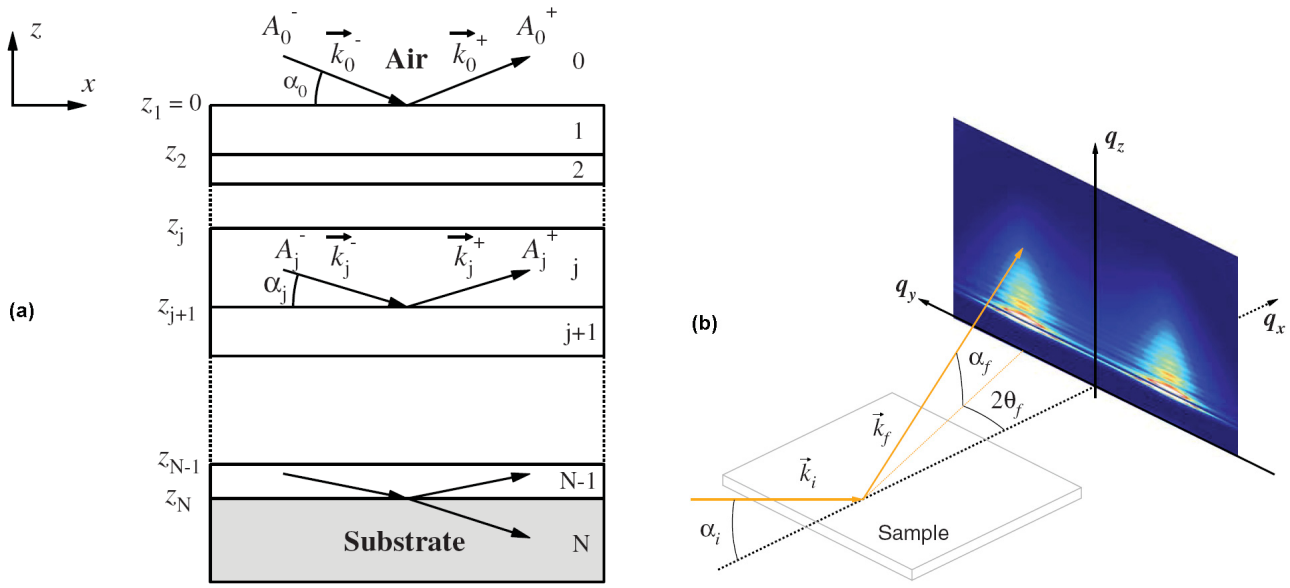

Figure A.10 – (a) Sketch of a plane wave propagating into a stratified medium. The z axis is perpendicular to the surface and its origin lies on the surface at $z_1 = 0$. The signs + (upward) and − (downward) label the direction of propagation of the wave. (b) Schematic drawing of the GISAXS geometry. α_i is the angle of incidence, while $2\theta_f$ and α_f are the in-plane and out-of-plane angles of emergence, respectively [16].

In order to describe the grazing angle effects both in incidence and in emergence, the form factor $\Phi_j(\vec{q})$ can be expressed within the distorted wave-Born Approximation (DWBA) as [16, 17],

$$\begin{aligned}\Phi_j\left(q_\parallel, q_z\right) &= A_j^-\left(\alpha_i\right) A_j^-\left(\alpha_f\right) F_j\left(q_\parallel, \widetilde{k}_{z,j}^f - \widetilde{k}_{z,j}^i\right) \\ &+ A_j^+\left(\alpha_i\right) A_j^-\left(\alpha_f\right) F_j\left(q_\parallel, \widetilde{k}_{z,j}^f + \widetilde{k}_{z,j}^i\right) \\ &+ A_j^-\left(\alpha_i\right) A_j^+\left(\alpha_f\right) F_j\left(q_\parallel, -\widetilde{k}_{z,j}^f - \widetilde{k}_{z,j}^i\right) \\ &+ A_j^+\left(\alpha_i\right) A_j^+\left(\alpha_f\right) F_j\left(q_\parallel, -\widetilde{k}_{z,j}^f + \widetilde{k}_{z,j}^i\right), \end{aligned} \tag{58}$$

where $q_\parallel = \sqrt{q_x^2 + q_y^2}$ is the in-plane component of the scattering vector and $F_j(\vec{q})$ is the Fourier transform of the shape of the object (*i.e.*, its form factor calculated in the Born approximation). In Eq. 58, $A_j^+(z_{j+1})$ and $A_j^-(z_{j+1})$ are the complex amplitudes of the upward and downward propagating waves at the interface z_{j+1} between the j and $j+1$ layers, which can be calculated by applying the Abélès matrix formalism [1].

Finally, assuming a two-dimensional assembly of monodisperse scattering objects located at the interface z_{j+1}, the GISAXS intensity can be calculated as,

$$\mathcal{I}\left(\vec{q}\right) = \mathcal{K}\mathcal{S}\left(q_\parallel\right)\left|\mathcal{A}_j\left(\vec{q}\right)\right|^2, \tag{59}$$

where $\mathcal{K}$ is a scaling factor and $\mathcal{S}(q_\parallel)$ is the structure factor due to the spatial correlation.

3.2.2 Experimental method and quantitative analysis

GISAXS experiments were performed under vacuum with the small-angle scattering setup of the D2AM beamline at the European Synchrotron Radiation Facility (Grenoble, France), in collaboration with Dr. J.-P. Simon. The focus of the incident x-ray beam on the sample was 0.4mm (H)×0.1mm (V) (Full Width at Half Maximum, FWHM) and the energy of 9.8keV was selected to measure the samples with an incidence angle $\alpha_i \approx 0.25°$. The transmitted and specularly reflected beams were masked by a vertical beam-stop, and the scattered intensity was collected with a 2D charge-coupled device (CCD) detector placed either at 715mm or at 1960mm from the sample in order to give access to different q ranges depending on the average size of the nanoclusters. Before quantitative analysis, raw data were corrected for the background and nonuniform sensitivity of the CCD. The experimental data were analyzed with the *FitGISAXS* package [18] developed within the IGOR Pro analysis software (WaveMetrics, Inc.).

As a typical example, Fig.A.11(a) shows the 2D GISAXS pattern of a Si_3N_4(20nm):Ag(20s/2nm):Si_3N_4(40nm) tri-layer, which exhibits scattering lobes oriented parallel to q_z typical of a 2D distribution of nanoclusters with short-range order.

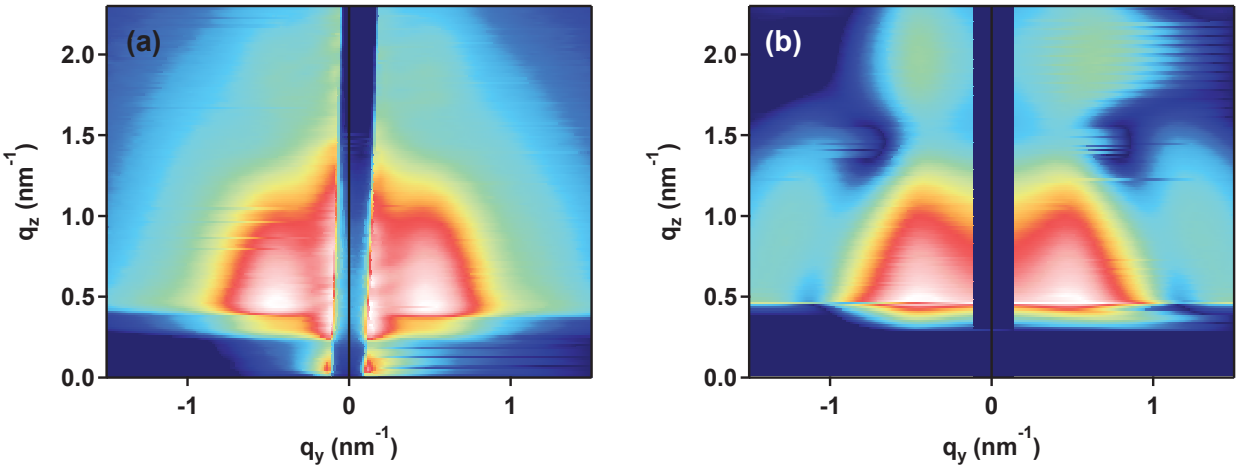

Figure A.11 – (a) Experimental and (b) simulated 2D GISAXS patterns of a Si_3N_4(20nm):Ag(20s/2nm):Si_3N_4(40nm) tri-layer nanocomposite sample.

To analyze quantitatively such a pattern, we consider a stratified medium consisting of two Si_3N_4 layers (with thicknesses of 40nm and 20nm, respectively) deposited onto a semi-infinite glass substrate where the Ag nanoclusters are located at the interface $z_2 = 40$nm. The structure factor $S(q_\parallel)$ is calculated within the Percus-Yevick approximation for hard spheres [19] with 2D short-range order as,

$$S\left(q_\parallel\right) = \left[1 + 24\frac{\eta_{\rm hs} G\left(q_\parallel D_{\rm hs}\right)}{q_\parallel D_{\rm hs}}\right]^{-1}, \tag{60}$$

where

$$\begin{aligned} G(A) &= \alpha(\sin A - A\cos A)/A^2 + \beta[2A\sin A + (2-A^2)\cos A - 2]/A^3 \\ &+ \gamma\{-A^4\cos A + 4[(3A^2-6)\cos A + (A^3-6A)\sin A + 6]\}/A^5, \end{aligned}$$

and

$$\begin{aligned} \alpha &= (1+2\eta_{\rm hs})^2/(1-\eta_{\rm hs})^4 \\ \beta &= -6\eta_{\rm hs}(1+\eta_{\rm hs}/2)^2/(1-\eta_{\rm hs})^4 \\ \gamma &= \eta_{\rm hs}\alpha/2. \end{aligned}$$

In Eq. 60, the hard spheres are assumed to have a packing fraction η_{hs} and a diameter D_{hs}. Moreover, assuming hemispheroidal Ag nanoclusters with in-plane diameter D and height H, the form factor $F_2(\vec{q})$ can be expressed as

$$F_2(q_{\parallel}, q_{\text{z}}) \quad = \quad 2\pi \int_0^H R_{\text{z}}^2 \frac{J_1\left(q_{\parallel} R_{\text{z}}\right)}{q_{\parallel} R_{\text{z}}} \exp\left(-i q_{\text{z}} z\right) dz, \tag{61}$$

where $R_{\text{z}} = \frac{D}{2}\sqrt{1 - \frac{z^2}{H^2}}$.

Finally, by fixing D to the average in-plane diameter value determined from HAADF-STEM, the experimental 2D GISAXS pattern shown in Fig.A.11(a) can be fitted using Eqs. 59–61 and only 4 free parameters, i.e. η_{hs}, D_{hs}, H, and $\mathcal{K}$. As seen in Fig.A.11(b), the simulated data using the best-fit values given in Table A.1 show an overall good agreement with the measured data.

Nanocomposite	GISAXS analysis			
Si_3N_4:Ag:Si_3N_4	η_{hs}	D_{hs} (nm)	H (nm)	$\mathcal{K}$
Ag(20s/2nm)	0.2	10.6	5.6	5.9×10^8

Table A.1 – The morphological and organizational parameters for the metal nanoclusters from Si_3N_4:Ag(20s/2nm):Si_3N_4 nanocomposite, studied using ex-situ STEM-HAADF and GISAXS.

Bibliography

[1] F. Abeles. *La theorie generale des couches minces.* Le journal de physique et le radium **11**, 307–310 (1950). 162, 179

[2] R. M. A. Azzam and N. M. Bashara. *Ellipsometry and polarized light.* North Holland Publication Company (1977). 162

[3] T. Yamaguchi, S. Yoshida, and A. Kinbara. *Optical effects of the substrate on the anomalous properties of aggregated silver films.* Thin Solid films **21**, 173–187 (1974). 163, 167

[4] C. F. Bohren and D. R. Huffman. *Absorption and scattering of light by small particles.* Wiley-Interscience Publication (1983). 164

[5] S. Berthier. *Optique des milieux composites.* Polytechnica (1993). 164

[6] P. Drude. *Zur Elektronentheorie der Metalle.* Annalen der Physik **306**, 566–613 (1900). 171

[7] U. Kreibig and L. Genzel. *Optical absorption of small metallic particles.* Surface Science **156**, 678–700 (1985). 171

[8] U. Kreibig and M. Vollmer. *Optical Properties of Metal Clusters.* Springer-Verlag, Berlin (1995). 171

[9] U. Kreibig and Fragstein. *The limitation of electron mean free in small silver particles.* Zeitschrift für Physik **224**, 307–323 (1969). 171

[10] P. Apell and D. Penn. *Optical properties of small metal spheres: Surface effects.* Physical review letters **50**, 1316–1319 (1983). 171

[11] H. Hövel, S. Fritz, A. Hilger, and U. Kreibig. *Width of cluster plasmon resonances: bulk dielectric functions and chemical interface damping.* Physical Review B **48**, 24 (1993). 171

[12] U. Kreibig, G. Bour, A. Hilger, and M. Gartz. *Optical properties of cluster-matter: Influences of interfaces.* Physica Status Solidi (A) Applied Research **175**, 351–366 (1999). 171

[13] D. Lantiat, D. Babonneau, S. Camelio, F. Pailloux, and M. Denanot. *Evidence for capping-layer effects on the morphology and plasmon excitation of Ag nanoparticles.* Journal of Applied Physics **102**, 113518 (2007). 175

[14] D. Babonneau, D. Lantiat, S. Camelio, J. Toudert, L. Simonot, F. Pailloux, M. F. Denanot, and T. Girardeau. *Gold and silver nanoparticles embedded in dielectric-capping layers studied by HAADF-STEM.* European Physical Journal Applied Physics **44**, 3–9 (2008). 175

[15] D. Lantiat-Baillargue. *Morphologie et auto-organisation de nanoparticles d'argent dispersées dans des matrices diélectriques: influence sue les propriétés optiques.* Thèse de Doctorat, PhyMat - Université de Poitiers, Poitiers (2008). 175

[16] D. Babonneau, S. Camelio, D. Lantiat, L. Simonot, and A. Michel. *Waveguiding and correlated roughness effects in layered nanocomposite thin films studied by grazing-incidence small-angle X-ray scattering.* Physical Review B - Condensed Matter and Materials Physics **80**, 155446 (2009). 175, 177, 178

[17] S. Narayanan, D. R. Lee, R. S. Guico, S. K. Sinha, and J. Wang. *Real-time evolution of the distribution of nanoparticles in an ultrathin-polymer-film-based waveguide.* Physical Review Letters **94**, 145504 (2005). 178

[18] D. Babonneau. *FitGISAXS: Software package for modelling and analysis of GISAXS data using IGOR Pro.* Journal of Applied Crystallography **43**, 929–936 (2010). 179

[19] J. K. Percus and G. J. Yevick. *Analysis of classical statistical mechanics by means of collective coordinates.* Physical Review **110**, 1–13 (1958). 180

Un système de spectroscopie de réflectance différentielle de surface est adapté sur un bâti de déposition par pulvérisation magnétron afin de suivre *in situ* et en temps réel les propriétés optiques de films nanocomposites métal:diélectrique. Cette technique permet notamment d'étudier les toutes premières étapes de formation de nanoparticules de métaux nobles dont la réponse optique est dominée par la résonance de plasmon de surface. Cette résonance est sensible à l'environnement des nanoparticules ainsi qu'à leur morphologie et à leur organisation. Pour établir la corrélation entre les propriétés optiques et les nanostructures, des analyses *post mortem* sont effectuées par microscopie électronique en transmission, en mode balayage, avec un détecteur annulaire champ sombre à grand angle (HAADF-STEM) et par diffusion rayons X aux petits angles obtenue par illumination en incidence rasante (GISAXS). Le suivi *in situ* de la résonance de plasmon de surface permet d'interpréter les mécanismes de croissance mais aussi les effets de différents traitements classiques - exposition des nanoparticules à des gaz (O_2, N_2), recuit thermique - ou plus originaux en utilisant certaines possibilités de la machine de dépôt - exposition des nanoparticules à des gaz (O_2, N_2) partiellement ionisés ou à un plasma d'Ar à basse énergie. Enfin les effets d'un recouvrement par une matrice protectrice de Si_3N_4 sont également étudiés. La spectroscopie optique *in situ* est donc une technique qui permet de contrôler toutes les étapes de fabrication de films nanocomposites. Couplée avec des analyses *post mortem*, elle permet en outre de comprendre les phénomènes mis en jeu à l'échelle nanométrique, et d'en quantifier les cinétiques.

Mots clés: Dépôt par pulvérisation magnétron, spectroscopie de réflectance différentielle de surface, résonance de plasmon de surface, croissance, réactivité, HAADF-STEM, GISAXS, recuit thermique

A non-intrusive *in situ* surface differential reflectance spectroscopy (SDRS) is adapted on a magnetron sputtering deposition technique in order to study the optical properties of metal:dielectric nanocomposites in real-time during their alternate depositions. SDRS is helpful in studying optical properties of metal nanoclusters which are dominated by the surface plasma resonance (SPR), which is sensitive, not only to the morphology and organization of the nanoclusters, but also to their physical and/or chemical surroundings. Hence, to establish the correlation between the optical properties of nanoclusters and their nanostructure, *post mortem* high-angle annular dark-field scanning transmission electron microscopy (HAADF-STEM) and grazing-incidence small-angle X-ray scattering (GISAXS) techniques are implemented. Following the signature SPR in real-time helps us not only to understand the different growth regimes through which the metal nanoclusters evolve, but also to study the effects caused by the physical and/or chemical treatments (such as, exposure of nanoclusters to different gases, either non-ionized or partially ionized, thermal annealing, and low-energy plasma annealing). Finally, the influence of a dielectric (Si_3N_4) capping matrix on the optical properties of the metal nanoclusters is equally studied after each physical and/or chemical treatment. In this way, the *in situ* optical spectroscopy allows us to monitor the optical properties of nanocomposites thin films during all the deposition steps and the additional *post mortem* structural characterization techniques help us to understand the different phenomena taking place at the nanoscale.

Keywords: Magnetron sputtering deposition technique, *in situ* surface differential reflectance spectroscopy, surface plasmon resonance, nanocluster growth, reactivity of nanoclusters, HAADF-STEM, GISAXS, annealing treatments